THE UNIVERSITY OF TULSA

THE GRADUATE SCHOOL

EXPERIMENTS, CFD SIMULATION AND MODELING OF ESP PERFORMANCE UNDER GASSY CONDITIONS

By
Jianjun Zhu

A dissertation submitted in partial fulfillment of

the requirements for the degree of Doctor of Philosophy

in the Discipline of Petroleum Engineering

The Graduate School

The University of Tulsa

2017

THE UNIVERSITY OF TULSA

THE GRADUATE SCHOOL

EXPERIMENTS, CFD SIMULATION AND MODELING OF ESP PERFORMANCE UNDER GASSY CONDITIONS

By
Jianjun Zhu

A DISSERTATION

APPROVED FOR THE DISCIPLINE OF

PETROLEUM ENGINEERING

By the Dissertation Committee:

______________________________________, Chair
Hong-Quan Zhang

____
Siamack Shirazi

____
Mauricio Prado

____
Baojun Song

COPYRIGHT STATEMENT

ABSTRACT

Jianjun Zhu (Doctor of Philosophy in Petroleum Engineering)

Experiments, CFD Simulation and Modeling of ESP Performance under Gassy Conditions

Directed by Dr. Hong-Quan (Holden) Zhang

232 pp., Chapter 5: Conclusions and Recommendations

(272 words)

Experimental measurements of pump boosting pressure under liquid and gas-liquid flow conditions are conducted on a 3-inch two-phase flow loop with a 14-stage radial-type electrical submersible pump (ESP). The stage-by-stage pressure increment with varying flow conditions is measured. Effects of intake pressure, gas volumetric fraction (GVF), rotational speeds, and surfactant presence on the ESP pressure increment are investigated. Two schemes of experimental testing are carried out to evaluate the pump behavior at different operational conditions, including surging tests (constant liquid flow rate) and mapping tests (constant gas flow rate). Experimental results reveal that the boosting pressure of ESP deteriorates with GVF increase. The gas tolerance of ESP improves significantly with surfactant injection, especially at higher intake GVFs.

Three-dimensional (3D) computational fluid dynamics (CFD) is used in this study to investigate multiphase flow behavior related to ESP boosting pressure. Compared with experimental measurements, the numerical prediction error for high-viscosity fluid flows is within ±15%. For gas-liquid flow, the numerically simulated ESP pressure increment is found to match experimental results well by incorporating a newly-developed bubble size model. The CFD simulation results of the in-situ gas void fraction (α_G) are used to validate the newly developed model for predicting in-situ α_G in a rotating ESP impeller.

Based on the basic conservation equations for mass and momentum, a mechanistic model for predicting flow patterns and hydrodynamics in two-phase ESP flow is developed and validated with experimental results. The model predicted ESP stage pressure increment agrees well with experimental measurements in both trends and values. The discrepancy in model predictions can be improved by improving the closure relationships, including bubble size model, and drag coefficient correlation.

ACKNOWLEDGEMENTS

I want to thank my advisor, Dr. Hong-Quan Zhang, for accepting me as a graduate student and providing me the opportunity to conduct the doctoral research at Tulsa University Artificial Lift Projects (TUALP). His guidance, encouragement, and support throughout this study are highly appreciated. I am also grateful for his scientific attitude and professionalism during the formation of this dissertation, without which my Ph.D. study completion would not have been possible.

I am also grateful for the support and help of the TUALP team, especially to Mr. Bryan Sams for his technical assistance with the facility assembly and to Mrs. Donna Trankley for her efficient administrative work and grammar check in my publications. I appreciate the helps from TUALP visiting scholars, Dr. Xiaozhe Guo and Dr. Fachun Liang, during design and build up of experimental facilities.

My deep gratitude also goes to many colleagues and friends, from whom I have gained enormous support and encouragement during this memorable time of my life. I want to thank Dr. Zhiyuan Wang, Dr. Hongfang Gu, Dr. Zhenyan Xia, Dr. Junqi Wang, Dr. Xuhui Liu and Dr. Kun Bo for discussions on my research; Haiwen Zhu, Jiecheng Zhang, Hattan Banjar for helping me with experiments; Bailian Chen, Yuandao Chi and Jianchun Xu for our friendship to stand together stronger when confronting difficulties.

I wish to thank Dr. Siamack Shirazi, Dr. Mauricio Prado and Dr. Baojun Song for serving in my doctoral committee. Their important comments and encouragement regarding my dissertation are very much appreciated. Special gratitude is given to the friends of Agape Chinese Baptist Church (ACBC) for their help, especially during the first year after my arrival.

At last, my love goes to my parents, Yuechun Zhu and Shengqin Yao. I spent most my time studying and researching, and have given you so little. However, I sincerely wish you understand how much gratitude I forever owe you not only for bringing me to the world and raising me, but also for supporting me with endless love. I thank my brother Weizhong Zhu who offered invaluable support and humor over the years.

TABLE OF CONTENTS

LIST OF FIGURES

LIST OF TABLES

INTRODUCTION

The electrical submersible pump (ESP), as a mean of high-efficiency downhole equipment for converting kinetic energy to hydraulic pressure head, has improved significantly since it was invented in the 1910's by a Russian engineer, A. Arutunoff. Globally, there are more than 100,000 ESP installations, making ESP the second most widely used artificial lift method in oil production (Barrios, 2007). ESPs excel in producing crude oil with much higher flow rates, but they have to be operated within a narrow application window. Issues such as gas involvement, changing production rate and high oil viscosity, greatly impede the ESP boosting pressure (Takacs, 2009).

Previous studies showed that the presence of gas would cause ESP hydraulic head degradation. The flow behaviors inside ESPs under gassy conditions, such as pressure surging and gas pockets, further deteriorate ESP boosting pressure. Surging may result in vibrations and short service life, and gas pockets may severely limit liquid production rates (Zhou et al., 2010). Although handling gas-liquid mixture has gradually become common for ESPs, the physical mechanism of two-phase flow affecting ESP hydraulic performance is not well understood. The gas bubble formation, coalescence and breakup inside ESPs, critically affecting the two-phase flow characteristics, are still unclear. Due to the compact and complex geometries of ESPs, the visualization of internal flow structures and bubble movement is very difficult.

The main objectives of this research are to understand the mechanism that dominates ESP's ability to handle gas-liquid mixture, and to study the surfactant effects on

ESP two-phase flow behaviors. In previous studies, the use of surfactant was found to be a possible alternative during operating ESP under gassy conditions. The surfactants could extend the ESP operating envelope and avoid the pump surging or gas locking. Gamboa (2008) did a preliminary study on ESP two-phase boosting pressure with isopropyl alcohol (IPA) being injected. A delay of pressure surging to a higher inlet gas void fraction (GVF) was observed. Since various surfactants may exist in crude oil and cause foamy gas-liquid flow, the ESP performance in foamy oil production should also be investigated.

In this study, the ESP performance under gas-liquid two-phase flow is tested in a semi-closed 3-inch diameter flow loop. The tested flow conditions include liquid and gas flow rates, intake pressure, rotational speed, and surfactant concentration. Gamboa (2008) testing matrix is adopted. Experiments are first conducted under both water and air-water flows without presence of surfactants. Then, tests are run again with injection of surfactants. CFD simulations are carried out to better understand the internal two-phase flow structures, especially the bubble behavior. Finally, a comprehensive mechanistic model for predictions of representative bubble size, in-situ gas void fraction inside a rotating ESP, flow pattern transition boundary and stage pressure increment is developed.

CHAPTER 1

LITERATURE REVIEW

Many studies on ESP performance under gassy conditions have been conducted experimentally. However, CFD simulations and mechanistic modeling studies of ESP overall performance with gas-liquid mixture are few. So is study on the surfactant effects, which change the gas-liquid interfacial tension and cause significant variance in dispersion characteristics. In this chapter, the literature review is presented with following topics: basic concepts, experimental studies, CFD simulations, and finally, mechanistic modeling.

1.1 Basic Concepts

ESPs are widely used in petroleum industry to increase the hydrocarbon fluid production rates, especially for off-shore deep-water oil fields. Normally, multistage ESP is assembled (Figure 1.1) in series with each stage comprising of the rotating impeller and stationary diffuser (Figure 1.2). The impeller is the dominant part of ESP since it forces the fluid flow and adds kinetic energy to the fluids by spinning the blades. At the outlet of impeller, the main part of kinetic energy in the fluid is converted to pressure potential by diffuser vanes, which are fixed and work as the guiding channels for the impeller of the next stage (Croce, 2014).

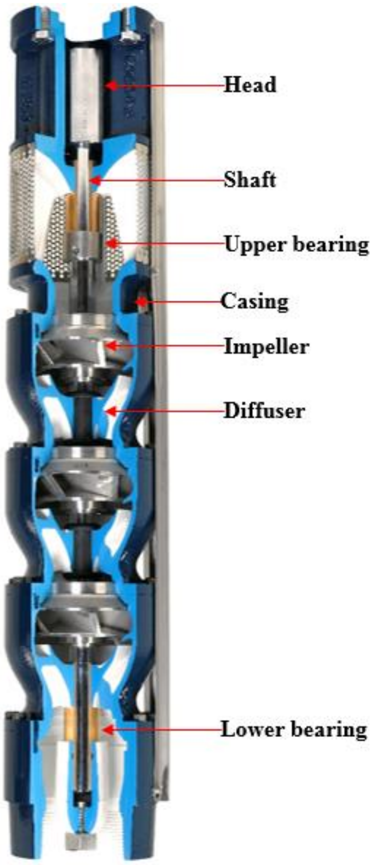

Figure 1.1 Main components of an electrical submersible pump (ESP)
(http://www.franklinwater.com)

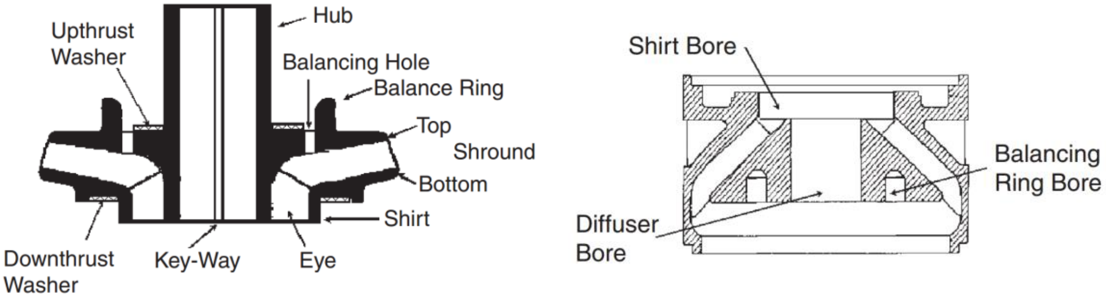

(a) Impeller (b) Diffuser

Figure 1.2 Components of ESP impeller and diffuser in front views, (a) impeller and (b) diffuser (Takacs, 2009)

As a type of centrifugal pumps, ESPs can be classified into three different categories: radial, axial and mixed types based on the dimensionless specific speed (N_S). The non-dimensional N_S is given by

$$N_S = \frac{\Omega Q^{1/2}}{\left(gH\right)^{3/4}}\,, \tag{1.1}$$

where Ω is the rotational speed (*rad*/*s*), Q is liquid flow rate (m^3/s), g is local gravitational acceleration (m/s^2), H is pump head (m). The pump industry uses a more practical expression for the specific speed N_S as below:

$$N_S = \frac{N\sqrt{q}}{h^{0.75}}\,, \tag{1.2}$$

where N, q and h are rotational speed (rpm), flow rate (gpm) and pump head (*ft*), respectively. Based on such definition, centrifugal pumps are categorized as shown in Figure 1.3. The radial type corresponds to low N_S, and the axial type corresponds to high N_S, while the mixed type is located in the middle between the radial and axial types.

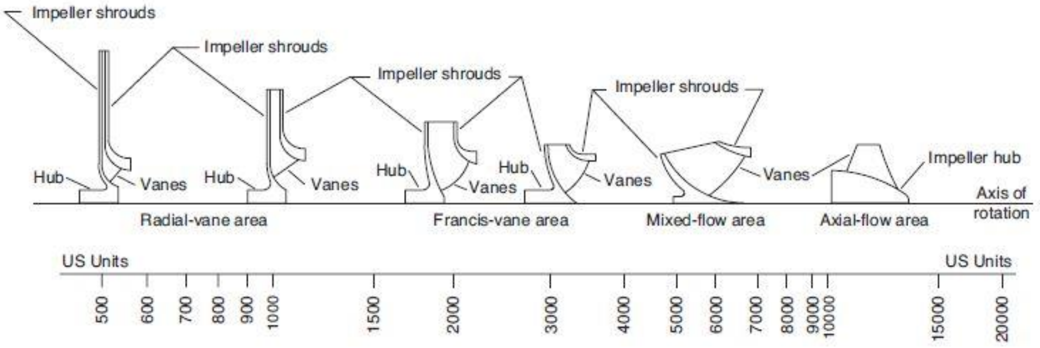

Figure 1.3 Classification of centrifugal pumps according to specific speed (http://www.pumps.com)

The radial pumps usually fall in the range $500 < N_S < 1800$, while the mixed pumps can reach a maximum $N_S = 4500$. However, as discussed by Takacs (2009), the specific speed N_S has no practical importance and is only used to compare different centrifugal pump designs.

For a centrifugal pump, there are three important variables to characterize its hydraulic and mechanical performance, namely: pumping head (H), efficiency (η) and brake horsepower (BHP). Figure 1.4 below shows the typical pump performance curves provided in the product brochure, which are obtained experimentally using tap-water.

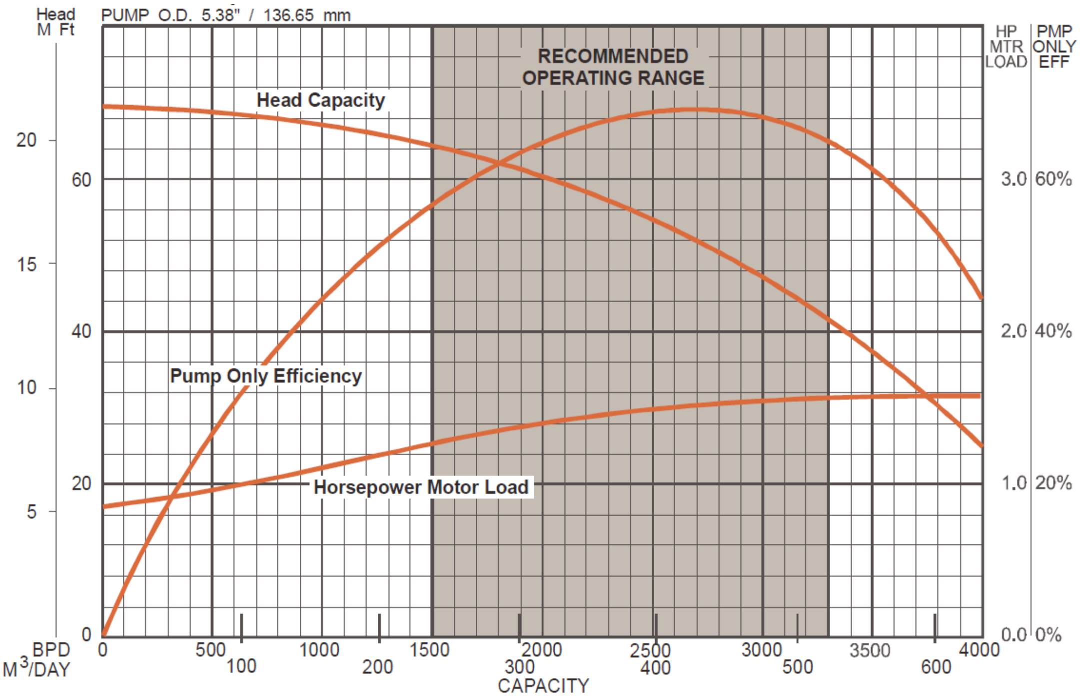

Figure 1.4 Typical ESP pump performance curves (Wood Group ESP, Inc., 2004)

With the liquid flow rate increase, the ESP performance curves exhibit different trends. The horsepower and pumping head and render a monotonic increasing and decreasing trend versus flow rates, respectively, whereas the efficiency is in a semi-quadratic relationship with the pump capacity. The best efficiency point (BEP), corresponding to the highest efficiency of 68.9% at Q = 2700 bpd, N = 3500 rpm in Figure 1.4 is an important concept in characterizing the ESP overall performance. In this study, the main objective is to investigate ESP hydraulic boosting pressure under various two-phase flow conditions.

1.2 Experimental Studies

The ESP boosting pressure suffers from many hydraulic factors, including fluid properties, downhole environmental conditions, as well as multi-phase flow conditions. In recent years, with more and more installations of ESP in oil production systems, the effects of fluid viscosity and gas entrainment on ESP's pressure boosting ability have been a focal area of research interests.

Ippen (1945) conducted over 200 performance tests for oil viscosities up to 10,000 SSU (Saybolt Second Universal) on four variants of centrifugal pumps. The experimental results were summarized by plotting the ratio of oil head to water head, brake horsepower and efficiency against a Reynolds-type dimensionless number, based on which the general correction factors for specific speeds from 800 to 2200 were proposed to correlate pump's boosting pressure under viscous fluid flow.

Hydraulic Institute (1948) provided a typical empirical approach with correction factors to estimate the conventional centrifugal pump boosting pressure for viscous liquid flow if the water performance were known. However, the accuracy of this approach was questioned by Gülich (1999a, 1999b) and Li (2002) since the experiments carried out by Hydraulic Institute were within a narrow range of the pump specific speeds. Unreasonable errors were found if extrapolation was beyond that range.

Stepanoff (1957) proposed a similar Reynolds-type number by using only one correction factor to get the new *H-Q* curves if the water performance were known. A more general model based on the evaluation of viscous dissipation for disk and hydraulic frictions to predict the boosting pressure of centrifugal pumps was proposed by Gülich. The friction losses on disk and in flow passage, as the author claimed, were dominating factors impairing centrifugal pump's ability to handle high viscosity fluids. Compared with available data, Gülich also pointed out that friction losses were affected significantly by pump geometry, fluid properties and thermal conditions. More recent experimental studies conducted by Amaral et al. (2009) and Solano (2009) further revealed that the Hydraulic Institute charts and empirical correlations available in literature were unable to give appropriate correction factors to predict the ESP boosting pressure for viscous oil flow. The contradictory results between experimental measurement and predictions by existing correlations or charts can be found in Barrios et al. (2012), Banjar et al. (2013).

Solano (2009) tested a seven-stage mixed type ESP with oils flowing at different temperatures so that the fluid viscosities were adjusted. The stage-by-stage pressures of ESP at three different specific speeds were investigated. A dimensionless analysis based on the conservation equations of momentum was adopted to verify the experimental data. His work proved that ESP's hydraulic head could be correlated by three dimensionless variables

$$\psi = f\left(\mathrm{Re}, N_S\right), \tag{1.3}$$

where ψ is the head coefficient, and N_S is the pump specific speed. The definitions of ψ and Re are

$$\psi = \frac{\Delta P}{\rho D_2^2 \omega^2}, \tag{1.4}$$

and

$$\mathrm{Re} = \frac{\rho D_2^2 \omega}{\mu}, \tag{1.5}$$

where ΔP is the stage pressure increment (*Pa*), D_2 is the impeller diameter (*m*), ω is the rotational speed (*rad*/*s*), ρ is the fluid density (*kg/m*^{3}), and μ is the fluid viscosity (*Pa·s*). For practical applications it is more appropriate to relate the pump performance to that of water at 3600 rpm. Hence, the normalized form of Eq. (1.3) is

$$\psi_n = f_2\left(\mathrm{Re}_n, \varphi_n\right), \tag{1.6}$$

where the subscript *n* denotes normalized values. Thus, ψ_n, φ_n and Re_n are

$$\psi_n = \frac{H}{H_{w,60Hz}^{shut-in}}\left(\frac{3600}{N}\right)^2, \tag{1.7}$$

$$\varphi_n = \frac{q}{q_{w,60Hz}^{3600}}\frac{3600}{N}, \tag{1.8}$$

$$\mathrm{Re}_n = \frac{\mu}{\mu_w}\frac{\rho_w}{\rho}\frac{3600}{N}. \tag{1.9}$$

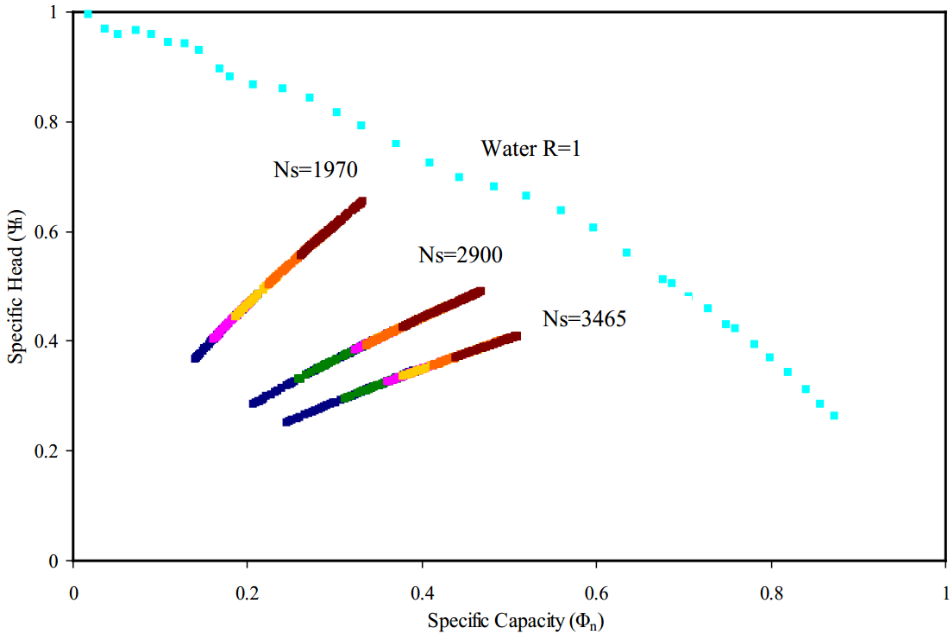

Figure 1.5 Normalized ψ_n vs. φ_n (Solano, 2009)

With a database of more than 80,000 points obtained from experimental measurements, Solano summarized the results in Figure 1.5, in which the light blue points correspond to water flow at $N = 3600$ rpm, and the colored points show experimental results of ESP pressure increment with viscous fluid flow. As it can be seen, ψ_n and φ_n are in a semi-liner relationship if N_S is fixed.

The pioneering experimental studies conducted by Murakami and Minemura (1974, 1st and 2nd reports) investigated centrifugal pump performance with gas entrainment. By employing a semi-opened impeller pump with a transparent casing, they experimentally observed the behavior of entrained air bubbles. The decreasing total head of the pump caused by air admission and the work consumed for air delivery were reported. Since then, the investigators have conducted more experimental measurements and mathematical modeling on centrifugal pump performance under gassy flow conditions.

Experimental research of ESP performance under gas-liquid flow conditions was carried out by Cirilo (1998), Pessoa (2001), Beltur (2003), Duran (2003), Zapata (2003), Barrios (2007), Gamboa (2008), and Salehi (2012), among others. Cirilo built the experimental flow loops for testing ESP performance at the TUALP. Using water and air as the working fluids, he measured both the water and air-water performances of three different types of ESPs as a function of GVFs, intake pressure and rotational speeds. The obtained data indicated that the mixed type pumps were able to handle much higher GVFs (> 30%) than radial type pumps (< 10%). With necessary modifications of the same testing flow loops, Pessoa conducted experimental investigations of two-phase performance of ESP using a 22-stage GC-6100 pump. By monitoring the stage-by-stage pressure increment, his results revealed that the ESP average behavior was significantly different from that observed per stage. Also, phenomena like surging and gas locking were observed and their boundaries were mapped. Additionally, a second region after pressure surging was observed in mapping test curves, where the slope of pressure increment versus flow rate changed again.

Using the same experimental flow loop of Pessoa, Beltur, Duran, Zapata and Salehi conducted extensive experimental measurements of ESP performance under both liquid- and gas-liquid flow conditions. Beltur focused on ESP performance deterioration with the presence of gas for varying intake GVFs and pressure. Data analysis revealed that the intake GVF is the most important factor in affecting ESP boosting pressure under gassy flow. A higher deterioration of pumping head occurs with GVFs above 6%. Duran and Zapata developed empirical correlations for predicting the pressure increment across the stage and the flow regime boundaries. Zapata also carried out further measurements with a wide range of rotational speed to study its effects on the average efficiency of ESP. Salehi did similar measurements using a 14-stage TE-2700 ESP, on which the effects of the stage number, intake pressure and fluid properties were investigated. It was found that ESP two-phase boosting pressure varied stage by stage only when the GVF exceeded a certain value, below which the deterioration was mild and independent of stage number. However, the degradation of pumping head became more prominent and affected by the stage number if the GVF reached a critical value, at which the pump boosting pressure of the downstream stage is better than upstream ones.

By visualizing the ESP internal flow, Barrios (2007), Barrios and Prado (2011) observed that bubbles enlarged when inlet GVFs increased and pump rotational speeds decreased. Such enlargement corresponding to the poorer pump performance indicated that bubble behaviors played a significant role in ESP's ability of handling gas-liquid mixtures. In addition, visualization experiments also showed different flow patterns prevailing inside ESP channels at higher GVFs.

In Figure 1.6, λ_G denotes the intake GVF. It is evident that flow behaviors inside ESP impeller altered significantly with flow conditions. From Figure 1.6(a) to 1.6(b), the GVF increase caused formation of larger bubbles and gas pockets, which in turn choked the flow passage for liquids and decreased the pump hydraulic head. Moreover, the flow patterns prevailing in ESP impeller at a specific value of λ_G, are comparable to that of gas-liquid two-phase flow in pipelines.

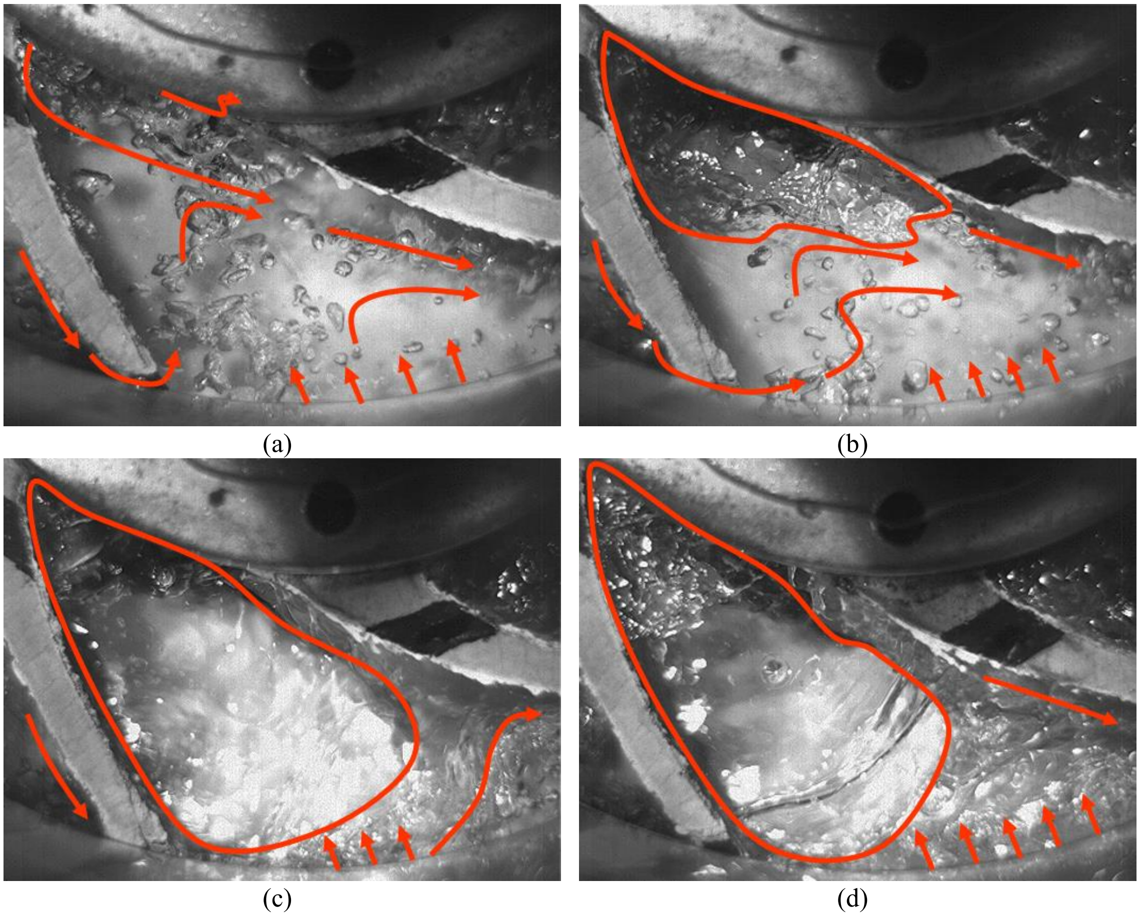
(a) (b) (c) (d)

Figure 1.6 Impeller channel flow behavior at N = 600 rpm and Q_L = 174 bpd with various gas flow rates, (a) λ_G = 0.15%, (b) λ_G = 0.23%, (c) λ_G = 0.39%, (d) λ_G = 1.05% (Barrios, 2007)

As proposed by Estevam (2002) and Estevam et al. (2003), the flow patterns in a rotating ESP impeller were categorized as bubbly flow, transition flow, and elongated-bubble flow. A more thorough experimental study on flow pattern recognition of two-phase flow in ESP impeller was done by Gamboa (2008), Gamboa and Prado (2011). Under a given flow condition, the typical flow pattern map from their visualization experiments is shown in Figure 1.7. The curves in Figure 1.7 denoted by different markers represent the transition boundaries between flow patterns, namely homogenous flow, bubbly flow, gas-pocket formation, and segregated flow. From the perspective of mechanistic modeling, each flow regime corresponds to the specific governing equations for flow characteristics, such as bubble size (d_b), in-situ gas void fraction (α_G), slippage velocity (V_{slip}) between gas and liquid phases. Figure 1.7 is important to understand the two-phase flow mechanisms in ESP.

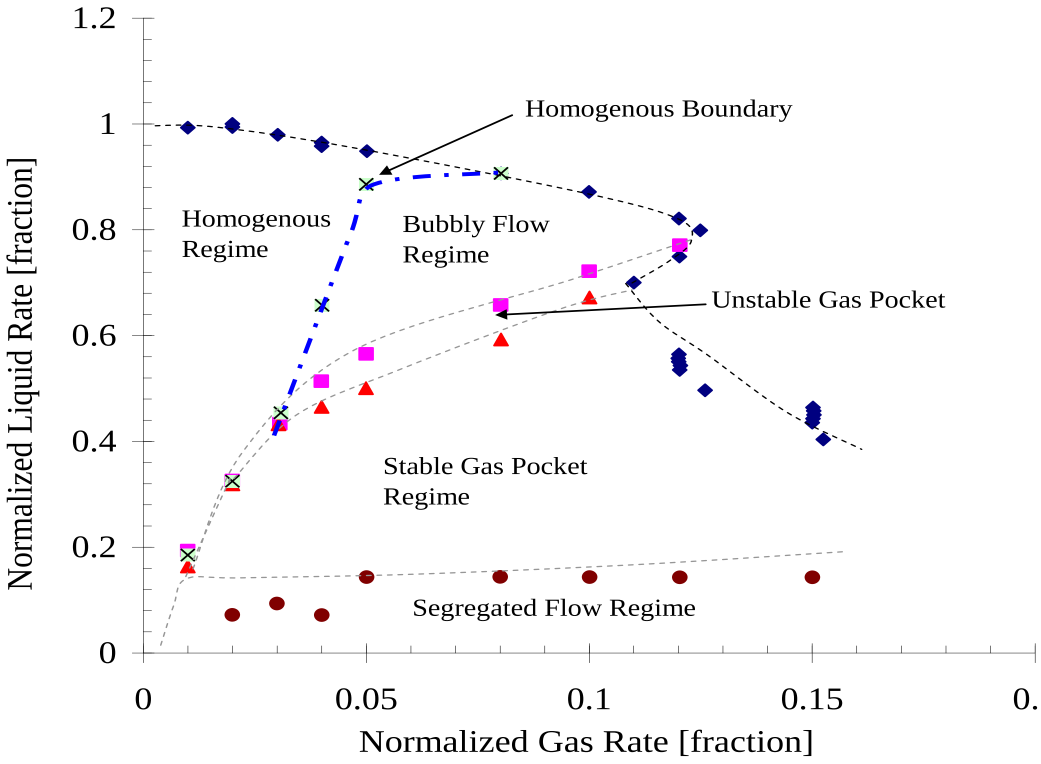

Figure 1.7 Flow pattern map for GC-6100 at 2400 rpm and 150 psig (Gamboa, 2007)

Verde et al. (2017) conducted visualization experiments on flow pattern recognition inside a rotating ESP impeller using high speed and resolution imaging technique. As shown in Figure 1.8, four different flow patterns were classified, including bubble flow (Figure 1.8a), agglomerated bubble flow (Figure 1.8b), gas pocket flow (Figure 1.8c) and segregated flow (Figure 1.8d). They observed that the intensity of pump performance degradation is directly influenced by the flow pattern within the impeller. The occurrence of the gas pocket flow pattern is linked to the intensification of the deterioration of pump performance and the appearance of operation instabilities. Moreover, the segregated flow patterns corresponded to the severe performance degradation which makes the pump incapable of generating pressure.

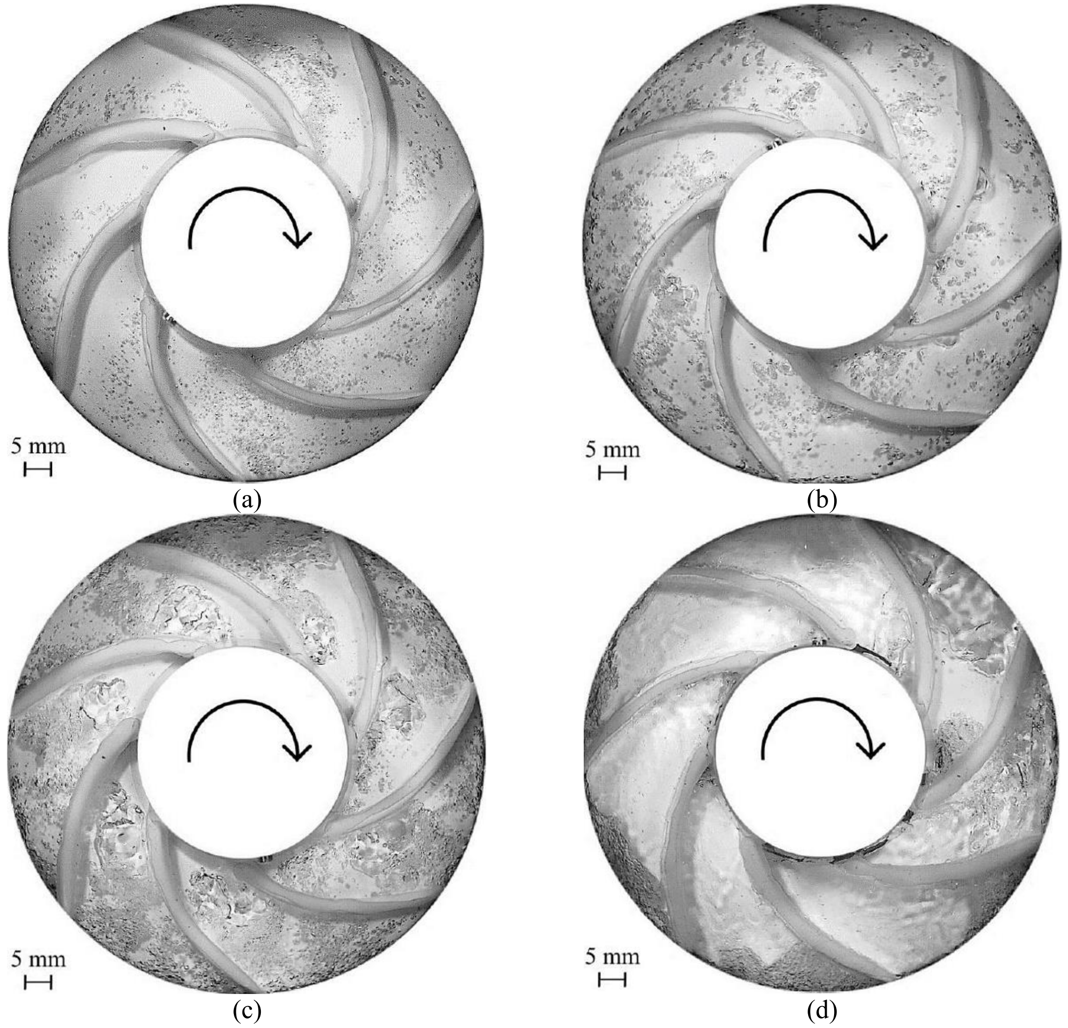

Figure 1.8 Visualized flow patterns in a rotating ESP impeller (Verde et al. 2017), (a) bubble flow pattern, (b) agglomerated bubble flow pattern, (c) gas-pocket flow pattern, (d) segregated flow pattern

Summarized by Verde et al., the schematic representations of each flow pattern are shown in Figure 1.9 with intake GVF increasing from left to right. Due to the relatively small intake GVF, the homogenous flow regime is featured by tiny and evenly-dispersed bubbles inside impeller channels, as shown in Figure 1.9(a). Under this regime, the bubbles are deemed to move together with liquid phase. Slippage between gas and liquid is small, meaning the in-situ α_G is almost the same as λ_G.

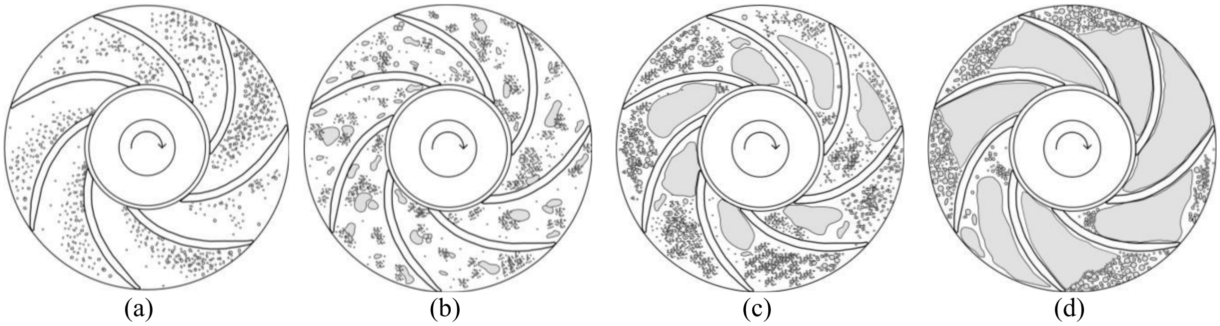

Figure 1.9 Schematic representations of flow patterns inside a rotating ESP impeller (Verde et al. 2017), (a) bubble flow, (b) agglomerated bubble flow, (c) gas-pocket flow, (d) segregated flow

As the intake GVF increases, the tiny bubbles are prone to collide and aggregate to form bigger ones, resulting in bubbly flow regime. In contrast to homogenous flow regime, the phase slippage between gas and liquid, shown by Figure 1.9(b) can no longer be neglected. Thus, depending on the intake GVF, the in-situ α_G under bubbly flow becomes higher than λ_G. A further increase of GVF induces more severe collision and aggregation of bubbles so that the large gas pocket forms. This flow pattern is similar as slug/churn flow patterns in pipelines, which are featured by a gas core/pocket followed by a liquid slug. As shown in Figure 1.9(c), the Taylor-bubble-like gas pocket forms near the suction side of ESP impeller, which occupies a significant portion of the impeller channel.

A relatively high gas flow rate and low liquid flow rate lead to the segregated flow pattern, similar to the annular/stratified flows in pipeline. As it can be seen in Figure 1.9(d), the elongated bubble expands and occupies the entire impeller length. For practical applications, the segregated flow pattern corresponds to gas-locking, an operational problem influenced not only by the pump itself but also by the whole pumping system, which gives null pump head and null flow rate (Verde et al., 2017).

Being a direct observation of flow patterns inside the ESP impeller, visualization experiments can help reveal gas-liquid flow behaviors intuitively. However, the experimental facility needs special designs associated with necessary modifications on pump geometries, such as the removal of impeller hub and attaching the Pyrex glass on its top for visualized observation. Barrios (2007) pointed out that the visualization of two-phase flow structures in a multistage ESP assembled in series was much more difficult. Thus, how to characterize the multiphase flow in ESPs has become a challenging topic. Although several technologies (Schäfer et al., 2015; Neumann et al., 2016) to visualize the internal flows inside a centrifugal pump were discussed, they required some modifications on pump geometry and the implementation was difficult to carry out. It required mounting HireCT (High-Resolution gamma-ray Computed Tomography) into the apparatus so that the internal flow structures could be visualized regardless of the opaque pump casing or volute. In addition, the data processing involved time-averaged rotation-synchronized CT scanning techniques, adding further complexity in analyzing the obtained experimental results.

Figure 1.10 shows the measurements using HireCT technique by Schäfer et al. (2015). The horizontal axis denotes the inlet GVF and the vertical axis is the volumetric averaged in-situ α_G in the rotating pump impeller. Clearly, there is a sharp α_G increase at a GVF corresponding to the severe gas-pocket formation and pumping head degradation. The step change is between inlet GVF = 2.5% and 3.0%. As confirmed by Schäfer et al. observation, such change is due to the rapid flow pattern change from bubbly flow to intermittent flow.

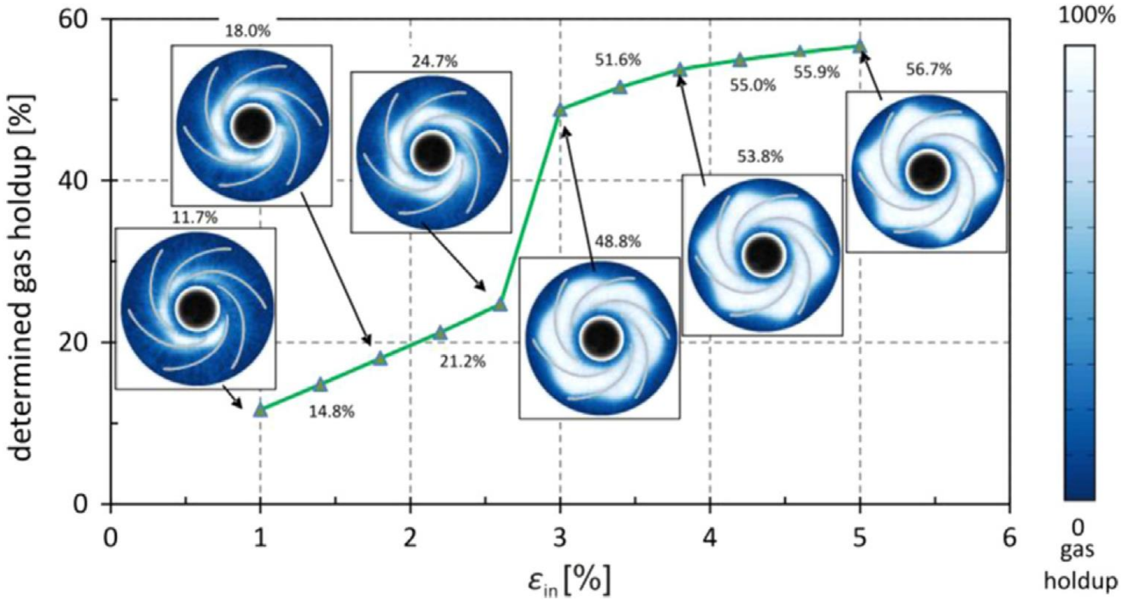

Figure 1.10 In-situ gas void fractions at $N = 1480$ rpm and various intake GVFs measured by HireCT (Schäfer et al., 2015)

The aforementioned experimental studies on ESP gas-liquid performance used tap water as the working fluid, while the gas phase was compressed air or nitrogen. Several recent experimental studies focusing on ESP gas-handling ability under viscous fluid flow were conducted by Trevisan (2009), Trevisan and Prado (2011), Banjar et al. (2013), and Paternost et al. (2015).

Using a visualization prototype built from original ESP components and with minimal geometrical modifications, Trevisan (2009), Trevisan and Prado (2011) conducted experiments to investigate the viscosity effect on liquid/gas two-phase flow through ESP. The authors identified four liquid/air flow patterns inside the impeller channels: agglomerated bubble, gas pocket, segregated gas and intermittent gas flows. It was concluded that the agglomerated bubble flow is responsible for pressure surging phenomenon, which is the initiation of pump head deterioration due to gas entrainment. The authors also observed that the increase in viscosity caused surging to occur at relatively lower inlet GVFs. Similar experimental observations were made by Banjar et al. (2013).

Paternost et al. (2015) further investigated the performance of a centrifugal pump handling single-phase viscous liquids and analyzed the impact of free gas entrainment. They concluded that the degradation of pump head was due to the stagnation of large gas-pocket formation, which became worse with the increase of liquid viscosity. An empirical correlation similar to the dimensionless analysis procedure in Solano (2009) was proposed to correlate ESP pressure increment under two-phase flow conditions accounting the inlet GVF and fluid viscosity.

Surfactants are molecules with a hydrophobic and a hydrophilic part, and therefore they preferentially adsorb at the interface of continuous/dispersed phases. In the process, they reduce the surface tension of the continuous phase (DeGennes et al. 2004). Studies of surfactant effect on bubble/droplet formation in air/water or water/oil binary immiscible two-phase flows were carried out by Eastoe and Dalton (2000), Hu et al. (2006), Omer and Pal (2013) among others. Surfactant effect on liquid loading in gas well was studied by van Nimwegen et al. (2016), Ajani et al. (2016a and 2016b). The flow pattern morphology and air-water two-phase flow characteristics due to the addition of surfactants were investigated by van Nimwegen (2015a, 2015b, 2016 and 2017).

However, studies on the surfactant effects on centrifugal pump performance under two-phase flow conditions were very few. Ogata et al. (2006) studied the effect of surfactant additives on centrifugal pump single-phase performance by experimental measurement of pump head and hydraulic efficiency curves. They observed that both total pump head and pump efficiency increased with increase of surfactant concentration. Chandel et al. (2011) conducted an experimental study on the drag reducing additive effect on the performance of centrifugal slurry pump. The obtained results show that at a rotational speed, the pump head and efficiency improve with the addition of drag reducing additive.

1.3 Numerical Simulations

With the advances of computer technology, computational fluid dynamics (CFD) becomes a more and more powerful tool to study centrifugal-pump performance under single-phase and multiphase flow conditions. Due to complicated ESP geometries, it is difficult to investigate the internal velocity and pressure fields experimentally. However, CFD offers an alternative way to simulate the complex internal flow structures. A centrifugal pump consists of an impeller rotating at a set angular velocity and a volute which is stationary. For an ESP, the rotating and stationary parts are the impeller and diffuser, which are accommodated in the rotating and stationary computational domains in CFD, respectively.

Using a 3D CFD code with the frozen-rotor interface model, the internal flow inside centrifugal pumps can be simulated, including velocity and pressure fields (Asuaje et al., 2005; Maitelli et al., 2010; Rajendran et al., 2012) as well as flow recirculation and separation (Cheah et al. 2007; Zhu et al. 2016). The frozen-rotor model is considered as steady-state simulation because it holds the rotating and stationary parts in two separate reference frames. Some transient simulations were conducted using the sliding-mesh technique to investigate the dynamic flow structures in centrifugal pumps (Gonzalez et al., 2002; Gonzalez and Santolaria, 2006; Huang et al., 2010, 2014). Gonzalez et al. performed numerical simulations of unsteady flow in a single-phase centrifugal pump, considering impeller-volute interaction. By solving viscous, incompressible Navier-Stokes (N-S) equations with the sliding mesh technique, the unsteady flow behavior inside a centrifugal pump due to impeller-volute interaction was captured. A relationship between the global variables, such as torque, as a function of impeller relative position, secondary flow in volute, etc., was obtained numerically. This approach was successful in predicting the dynamic interaction between impeller and volute. Huang et al. (2010) studied unsteady flow and pressure fluctuations due to interaction between impeller and diffuser vanes by the sliding mesh technique. His study confirmed that the global variables are primarily affected by impeller blade passing frequency.

In addition to designing turbomachinery, CFD can help engineers study the viscosity effects on centrifugal pump performance. Shojaeefard et al. (2006, 2012) conducted both experimental study and numerical simulation of a centrifugal pump handling viscous fluids. The authors stated that a good agreement between simulation and experimental data was obtained by solving the steady state RANS equations with SST k-ω turbulence model. Using the same pump geometry, Sirino et al. (2013) and Stel et al. (2014) performed numerical investigations of viscosity effects on single-stage and three-stage ESPs, respectively. Similar numerical methodologies were used in their work including SST turbulence model with transient rotor-stator techniques. Both simulation results matched experiments well under a wide range of fluid viscosity. Stel et al. (2014, 2015) pointed out that CFD simulated boosting pressure with multistage ESP geometry agreed with experimental results better than that with a single-stage geometry. The phenomenon of rising head with moderate increase of fluid viscosity was studied by Li (2014). By implementing the standard k-ε turbulence model and non-equilibrium wall function into RANS equations, the author confirmed that the rising pump head was due to the transition from hydraulically rough regime to hydraulically smooth regime. Zhu et al. (2016) solved a set of 3D, steady-state RANS equations with standard SST turbulence model using ANSYS CFX by employing the frozen-rotor technique. Their results matched correspondent experimental data well.

CFD has also been used to simulate pump performance with gas involvement, such as cavitation phenomenon (Flores et al. 2008, Jeanty et al. 2009), and free-gas entrainment flow (Barrios et al., 2009; Zhu and Zhang, 2014, 2017). Unlike single-phase simulations, the two-phase simulation requires the solution of conservation equations of mass, momentum and energy for the continuous and dispersed phases. Meanwhile, another set of constitutive equations, for describing the interphase interactions between phases, such as interfacial momentum/heat transfer, need to be solved simultaneously.

Minemura and Uchiyama (1993) solved 3D momentum equations by a finite-element method to predict gas/liquid flow behavior in a rotating centrifugal pump impeller. Tremante et al. (2002) numerically studied gas/liquid flow through a cascade axial pump by CFD simulation. Coupled with a modified k-ε turbulence model by considering the viscosity of the liquid phase and the compressibility of the gas phase, the gas/liquid distributions versus different attack angles were obtained. Caridad et al. (2004, 2008) studied ESP impeller performance handling water/air mixtures using CFD simulation. Applying two fluid models in 3D CFD simulations, the pressure and velocity fields, as well as the gas phase distributions were obtained. The gas pocket near the impeller blade was also identified and compared with experimental observations. The sensitivity analysis on GVF and bubble diameter indicated that ESP performance deteriorated with GVF or bubble diameter increase. Barrios (2007), Barrios et al. (2009) conducted multiphase CFD simulations on a single-stage ESP impeller with the new models of bubble size and drag coefficient predictions. Their simulations agreed with laboratory visualization images of streamlines and gas-accumulation zones. Qi et al. (2012) designed ESPs for geothermal application with high-temperature gas-liquid two-phase flow. Using CFD simulations, the designed mix-type centrifugal impeller and diffuser were optimized for better gas-handling and higher efficiency within a wide range of production rate. Zhu and Zhang (2014) conducted multiphase CFD simulations on a three-stage ESP with each stage comprising of an impeller and a diffuser. Comparing to experimental measurements, their work revealed that bubble size was a critical factor affecting ESP performance under gassy conditions. A new bubble size prediction model was later proposed in Zhu and Zhang (2017) based on CFD simulations. They also predicted the in-situ gas void fraction (α_G) with a mechanistic model and validated the results with numerically simulated values (Zhu and Zhang, 2016).

Multiphase flow phenomena in ESP are transient in nature, such as fluctuations of local pressure, gas void fractions, and breakup or coalescence of bubbles. To better simulate the hydrodynamics of gas-liquid two-phase flow in a rotating centrifugal pump, the unsteady CFD simulation code coupled with multiphase flow model and transient rotor-stator algorithm to account for the interactions between impeller and diffuser should be adopted. However, the computational cost for transient CFD simulations is far more than that for steady-state simulations.

Marsis et al. (2013) performed transient two-phase CFD simulations on eight multi-vane ESP designs. The predicted pump performance was confirmed by experimental results. The final design was achieved with the stage pressure increased by 4% for single-phase flow and 23% for two-phase flow at inlet GVF = 20% by optimizing the meridional profile and number of blades. Yu et al. (2013, 2015) conducted unsteady numerical simulation on gas-liquid flow in a multiphase centrifugal pump. Considering multiple interfacial momentum transfer components, such as drag force, lift force, virtual mass force and turbulent dispersion force, they concluded that the two-fluid multiphase model was able to capture the transport process more accurately than the homogeneous model. Compared to turbulent dispersion force, the drag force plays a more dominant role. Huang et al. (2014) investigated the transient inhaling process of gas initially filling a section of pipe into centrifugal pump impeller by sliding mesh and transient-frozen-rotor methods. The phase distribution, pressure and velocity versus time were computed and analyzed. Pineda et al. (2016) presented an alternative approach to obtain the distribution and concentration of the dispersed phase in a rotating centrifugal pump by solving the realizable k–ε turbulence model coupled with the volume of fluid (VOF) multiphase model. They observed that the numerically simulated results of in-situ α_G could be correlated by the Lockhart-Martinelli parameter. Zhang et al. (2016) compared the unsteady CFD simulation results of multiphase flow patterns in a three-stage centrifugal pump with the corresponding visualization experiments. Good agreement on the positions and shapes of the gas pocket was observed. Ye et al. (2016) combined the advanced transient CFD multiphase simulation with finite-element-analysis (FEA) to optimize the 3D metal printing process of hybrid stage prototype and ESPs for high-gas wells. A design-validation tool was developed and a prototype ESP was manufactured which can pump up to 75% GVF gas/liquid mixture without gas locking.

1.4 Mechanistic Modeling

1.4.1 Liquid Performance Modeling

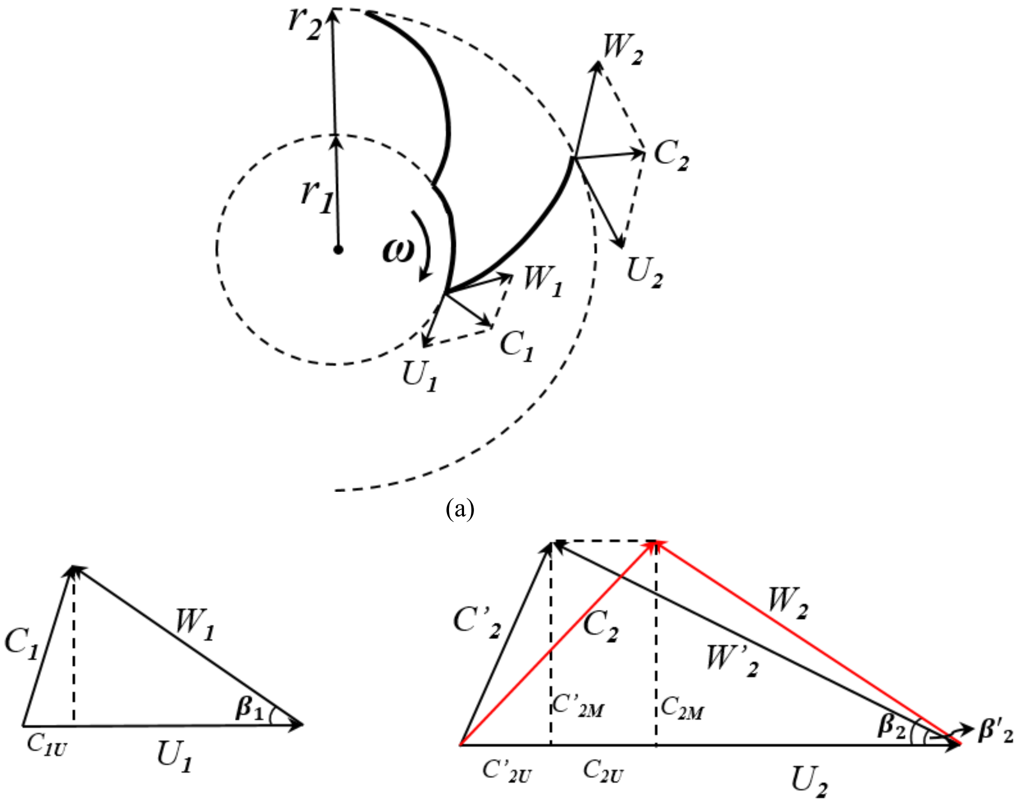

(a)

(b)

(c)

Figure 1.11 Velocity triangles, (a) schematic of impeller flow channel, (b) inlet velocity triangle, (c) outlet velocity triangle

For an ESP impeller, the velocity triangles at the intake and discharge are shown in Figure 1.11. All the variables are in SI units. The absolute velocity *C* can be decoupled into two components: relatively velocity *W* and peripheral velocity *U*, which is calculated by $\vec{U} = \vec{\Omega} \times \vec{r}$. The subscripts 1 and 2 denote the inlet and outlet of impeller, respectively. Here, *W* is relative to the impeller and *C* is relative to the global coordinate and is equal to the vector summation of *U* and *W*, e.g. $\vec{C} = \vec{W} + \vec{U}$. In Figure 1.11(c), C'_2 is an ideal absolute velocity assuming infinite number of impeller blades, while C_2 is the real absolute velocity at the impeller outlet.

According to the ideal conservation law of angular momentum in rotating centrifugal pump, the Euler head can be expressed as (Stepanoff, 1957):

$$H_E = \frac{\vec{C}_2 \cdot \vec{U}_2 - \vec{C}_1 \cdot \vec{U}_1}{g} = \frac{U_2 C_{2U} - U_1 C_{1U}}{g}, \tag{1.10}$$

where C_{1U} and C_{2U} are the projection of absolute velocities at the impeller inlet and outlet to the direction of peripheral velocities. Applying the velocity triangle relationship in Figure 1.11, one can obtain

$$H_E = \frac{U_2^2 - U_1^2}{2g} + \frac{W_1^2 - W_2^2}{2g} + \frac{C_2^2 - C_1^2}{2g}, \tag{1.11}$$

and

$$H_E = \frac{\Omega^2 \left(r_2^2 - r_1^2\right)}{g} - \frac{Q\Omega}{2\pi g h}\left(\frac{1}{\tan\beta_2} - \frac{1}{\tan\beta_1}\right), \tag{1.12}$$

where r is the radius of impeller, h is the channel height, β is the blade angle. If the fluids enter the impeller without pre-rotation, Eq. (1.12) can be written as

$$H_E = \frac{\Omega^2 r_2^2}{g} - \frac{Q\Omega}{2\pi g h \tan\beta_2}. \tag{1.13}$$

As can be seen from Eq. (1.13), the ideal Euler head H_E is in linear relationship with liquid flow rate. In reality, pressure losses in the rotor, the diffuser, and losses from the interaction between them must be deducted from the ideal Euler head, including friction, shock and recirculation losses. Therefore, the actual pump head can be calculated by

$$H = H_E - H_{frition} - H_{shock} - H_{leakage} - H_{recirculation} - H_{diffuser} - H_{disk}. \tag{1.14}$$

Figure 1.12(a) shows the change of the ideal Euler head with the outlet blade angle *β*. Figure 1.12(b) schematically shows the losses to the ideal head and the final *H*-*Q* curve of a centrifugal pump according to Eq. (1.14). Friction loss becomes prominent at high flow rates. In contrast, leakage loss is more at relatively low flow rates. Shock loss takes place when the liquid flow rate differs from the designed flow rate.

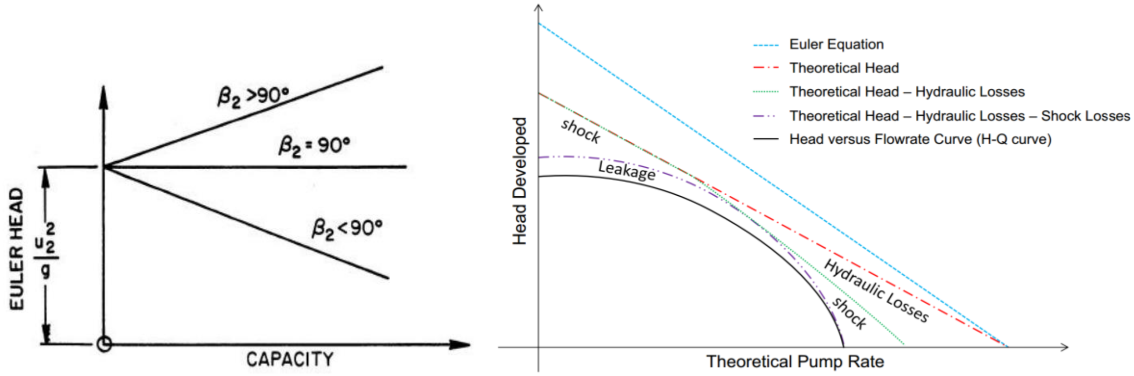

Figure 1.12 Schematic of head curves, (a) Euler heads with different outlet blade angles, (b) actual head after deducting losses

Table 1.1 summarizes studies on the friction losses inside a centrifugal pump impeller. Takacs (2009) pointed out that friction losses progressively increase with liquid rate and are due to fluid friction in the impeller.

Table 1.1: Friction loss models in literature

Reference	**Model**	
Ito (1959), Jones (1976), Churchill (1977), Shah (1978), Sun (2003)	$h_{friction} = \frac{f_{\gamma\beta\omega}Q^2}{8gD_H\pi^2 b_m^2 sin^3\beta_m}\frac{r_2 - r_1}{r_1 r_2}$	$f_{\gamma\beta\omega} = F_\gamma F_\beta F_\omega f$
Wiesner (1967), Sun and Prado (2006), Thin et al. (2008)	$h_{friction} = b_2\frac{(D_2 - D_1)(W_1 + W_2)^2}{8gsin\beta_2 r_H}$	b_2 – constant
Ito and Nanbu (1971), Bing et al. (2012)	$h_{friction} = N_a f_{\gamma\beta\omega}\frac{s}{D_H}\frac{(W_1^2 + W_2^2)^2}{4g}$	

The mechanism of shock losses in centrifugal pump is still not well studied. Thus, only empirical correlations are available in the literature. Table 1.2 lists the existing prediction models of shock loss as implemented in the prediction models. Shock losses are negligible at the best efficiency point (BEP) of the pump, but increase at lower and higher liquid flow rates. They occur at the entrance and the exit of the impeller and are caused by sudden changes in the direction of flow (Takacs, 2009).

Table 1.2: Shock loss models in literature

Reference	Model	
Stepanoff (1957) Amaral (2007) Thin et al. (2008)	$h_{shock} = k_{shock}(Q - Q_{BEP})^2$	k_s – empirical constant
Wiesner (1967) Sun and Prado (2006) Thin et al. (2008))	$h_{shock} = \frac{k_{shock}}{2g}\left(\frac{Q - Q_{BEP}}{Q_{BEP}} U_1\right)^2$	

As suggested by Tackas (2009) leakage losses, which represent the losses through the clearances between the rotating and stationary parts of the pump stage (at the impeller eye, through balancing holes, etc.), decrease with increase of liquid rates. Aungier (1995) and Bing et al. (2012) proposed similar empirical equation to calculate the leakage loss:

$$h_{leakage} = \frac{Q_{c1} U_{c1} U_2}{2Q^* g}, \tag{1.15}$$

where Q_{c1} is the volume of leakage fluid, U_{c1} is the velocity of leakage fluid, and Q^* is the ideal flow rate of the pump.

Table 1.3: Diffuser loss models in literature

Reference	Model	
Ito (1959), Jones (1976) Churchill (1977) Shah (1978), Sun (2003)	$h_{diffuser} = -\frac{F_\gamma F_\beta f Q^2}{8gD_H \pi^2 b_m^2 sin^3 \beta_m} \frac{r_{3dif} - r_{2dif}}{r_{3dif} r_{2dif}}$	
Sun and Prado (2002) Bing et al. (2012)	$h_{diffuser} = N_a(F_\gamma F_\beta f)\frac{S}{D_H}\frac{(V_{2d}^2 + V_3^2)}{4g}$	
Amaral (2007)	$h_{diffuser} = \frac{(V_{2d}^2 - V_3^2)}{2g} - C_p \frac{V_3^2}{2g}$ $V_{2d} = \frac{Q}{\pi(r_{2diff}^2 - r_{1diff}^2)}$	$C_p = \frac{(p_3 - p_2)}{0.5\rho V_3^2}$ $V_3 = V_1$

Sun and Prado (2003, 2005, and 2006) claimed that the diffuser loss is caused mainly by the friction on the diffuser walls. Table 1.3 presents the calculation formulas of diffuser losses that were implemented in the prediction models. Most equations are the same as friction loss formulas in Table 1.1.

Disk friction losses, as Stepanoff (1957) defined, are due to the contact between a rotating disk and fluid. Thus, additional power is consumed to keep the disk rotating since the viscous shear forces act on the disk surfaces (Vieira et al., 2015).

Table 1.4: Disk loss models in literature

Reference	**Model**	
Sun and Prado (2006) Amaral (2007)	$h_{disk} = \frac{\left(V'^2_2 - V^2_{2d}\right)_{BEP}}{2g}$	
Thin et al. (2008))	$h_{disk} = \frac{f_{disk} \rho \omega^3 r_2^5}{10^9 Q}$	
Van Esch (1997) Kruyt (2003)	$h_{disk} = \frac{c_m \omega^3 r_2^5}{2gQ}$	c_m is an empirical constant
Gulich (1999) Ladouani (2009)	$h_{disk} = \frac{k_{RR} f_{th} \omega^3 r_2^5}{gQ} \left(1 - \left(\frac{D_1}{D_2}\right)^5\right)$ $k_{RR} = \frac{\pi r_2}{2 R_e h} + \frac{0.02}{R_e^{0.2}} \frac{1 + h/r_2}{1 + h/(2r_2)}$ $f_{th} = exp\left(-2 \times 10^{-5} \left(\frac{v}{10^{-6}}\right)\right)^{1.34}$	$h = 0.05 r_2$

1.4.2 Gas-liquid Performance Modeling

Zakem (1980) first developed a mathematical model using a one-dimensional control volume method to analyze gas bubbles and liquid interaction for straight blade impellers. Furuya (1985) developed a similar analytical model by incorporating the pump geometry, void fraction, flow slippage, and the flow regime but neglecting the compressibility and condensation effects. The basic formula in Furuya study is given by:

$$\frac{\dot{m}_l^2}{\rho_l(dn)^2}\frac{1}{1-\alpha}\left(\frac{1}{1-\alpha}\frac{d\alpha}{ds}-\frac{1}{dn}\frac{d(dn)}{ds}\right)+\frac{\dot{m}_g^2}{\rho_g(dn)^2}\frac{1-\alpha}{\alpha^2}\left(\frac{1}{\alpha}\frac{d\alpha}{ds}+\frac{1}{dn}\frac{d(dn)}{ds}\right)$$
$$+\frac{\rho_l}{2}\left[\left(\frac{\dot{m}_g}{\rho_g\alpha dn}\right)^2\left(\frac{1}{\alpha}\frac{d\alpha}{ds}+\frac{1}{dn}\frac{d(dn)}{ds}\right)+\left(\frac{\dot{m}_l}{\rho_l(1-\alpha)dn}\right)^2\left(\frac{1}{1-\alpha}\frac{d\alpha}{ds}-\frac{1}{dn}\frac{d(dn)}{ds}\right)\right] \quad (1.16)$$
$$=(\rho_l-\rho_g)(1-\alpha)r\omega^2\sin\beta\cos\gamma-\frac{3}{8}\frac{C_d}{r_b}\rho_l\left(\frac{\dot{m}_l}{\rho_l(1-\alpha)dn}-\frac{\dot{m}_g}{\rho_g\alpha dn}\right)^2.$$

$\dot{m}_l$ and $\dot{m}_g$ are the mass flow rates of liquid and gas. s is the streamline coordinate. n is the coordinate normal to the streamline coordinate s. β is the angle between relative flow velocity and circumferential direction. γ is the angle between the radial direction and the stream surface. C_d is the drag coefficient. r_b is the bubble radius. Comparing with experimental data in literature, the model predictions were within the relative average error band of ±30% for GVF < 20%, and ±50% for GVF > 30%.

Sachdeva et al. (1988, 1994) conducted a comprehensive investigation of two-phase flow in ESPs with air/water and diesel/CO_2 mixtures. A dynamic five-equation, one-dimensional, two-fluid model accounting for pump geometry, intake pressure and GVF, fluid properties, was developed and verified to predict ESP boosting pressure. The basic equations of Sachdeva model are presented below.

The mass balance equations are

$$\frac{d(\alpha_G\rho_G W_G r\sin\beta)}{ds}=0 \quad (1.17)$$

and

$$\frac{d((1-\alpha_G)\rho_L W_L r\sin\beta)}{ds}=0, \quad (1.18)$$

where W_G and W_L are the mass flow rates of gas and liquid, respectively.

The momentum balance equations are

$$\alpha_G \rho_G V_{R,G} \frac{\partial V_{R,G}}{\partial s} = -\alpha_G \frac{\partial P}{\partial s} + \alpha_G \rho_G r \omega^2 \frac{\partial r}{\partial s} - F_{W,G} + F_i + F_v \tag{1.19}$$

and

$$(1-\alpha_G)\rho_L V_{R,L} \frac{\partial V_{R,L}}{\partial s} = -(1-\alpha_G)\frac{\partial P}{\partial s} + (1-\alpha_G)\rho_L r \omega^2 \frac{\partial r}{\partial s} - F_{W,L} - F_i - F_v\,, \tag{1.20}$$

where $V_{R,G}$ and $V_{R,L}$ are the radial components of gas and liquid absolute velocities, respectively. $F_{W,G}$ and $F_{W,L}$ are the friction forces of gas and liquid against the channel walls per unit volume of fluids. F_i is the interfacial friction force between gas and liquid per unit volume. F_v is the virtual mass force per unit volume.

Minemura et al. (1998) also studied the performance of centrifugal pumps in the nuclear industry under air-water two phase flow conditions with a low inlet GVF (< 10%). Based on energy change in the flow from the rotating impeller to the stationary volute, a 1D, two-fluid model considering fluid viscosity and air-phase compressibility in a rotating impeller was proposed. This model can be solved numerically with a prediction error of ±20% of the related flow capacity. However, both Sachdeva et al. and Minemura et al. models are valid only under a narrow application range or specific experimental conditions. Compared to Sachdeva model, the major difference in Minemura et al. model is that the momentum balance equations are based on the relative velocities of gas/liquid rather than the radial components of the absolute velocities, which are given as

$$\alpha_G \rho_G W_G \frac{\partial W_G}{\partial s} = -\alpha_G \frac{\partial P}{\partial s} + \alpha_G \rho_G r \omega^2 \frac{\partial r}{\partial s} - F_{W,G} + F_i + F_v \tag{1.21}$$

and

$$(1-\alpha_G)\rho_L W_L \frac{\partial W_L}{\partial s} = -(1-\alpha_G)\frac{\partial P}{\partial s} + (1-\alpha_G)\rho_L r \omega^2 \frac{\partial r}{\partial s} - F_{W,L} - F_i - F_v\,. \tag{1.22}$$

where W_G and W_L are the relative velocities of gas and liquid, respectively.

Based on Sachdeva et al. and Minemura et al. one-dimensional two-fluid models, Sun (2003, 2005) developed a new two-phase model including a set of one-dimensional mass and momentum balance equations for predicting ESP performance. He also improved analytical models for wall frictional losses and shock loss, as well as new correlations for the drag coefficient. The general momentum balance equation along the streamlines is given by

$$\left.\frac{dp}{dr}\right|_{streamline}=\left[-\rho_p W_p \frac{dW_p}{dr}+\rho_p \Omega^2 r+\left(\frac{dp}{ds}\right)_{f,p}\frac{ds}{dr}-\frac{M_{p,s}}{\alpha_p}\frac{ds}{dr}\right]_{streamline}, \qquad (1.23)$$

where the subscript *p* is *g* or *l* for gas or liquid phase, respectively. And $M_{p,s}$ is the interfacial momentum transfer term. Eliminating the pressure increment term at the left hand side in Eq. (1.23), the combined momentum balance equation can be expressed as

$$\rho_l W_l dW_l-\rho_g W_g dW_g=\left(\rho_l-\rho_g\right)\Omega^2 r dr+\left(\left(\frac{dp}{ds}\right)_{f,l}-\left(\frac{dp}{ds}\right)_{f,g}\right)ds-M_{l,s}\frac{1}{\alpha_l\alpha_g}ds. \qquad (1.24)$$

Applying an algorithm to solve this model, a good agreement of pump performance curve, α_G distribution, surging and gas lock conditions against correspondent experimental measurements was obtained. Although many studies for modeling ESP performance under gassy conditions were conducted, mechanistic modeling is still needed due to the over-simplification and assumptions or narrow application ranges of the existing models.

1.4.3 Closure Relationship Modeling

In mechanistic models, the closure relationships are needed on top of the conservation equations. The closure relationships in modeling centrifugal pump two-phase performance include bubble size, drag force coefficient, in-situ gas void fractions, friction factors etc.

1.4.3.1 Bubble Size Prediction (d_b). The bubble size prediction is a critical closure relationship in mechanistic modeling of ESP performance under gassy conditions. However, a generally validated mechanistic model for predicting bubble size in centrifugal pumps is not available. Several proposed bubble size models for centrifugal pump are either empirical or semi-empirical. They were verified with specific pumps and air/water as working fluids (Murakami and Minemura 1974; Barrios 2007; Gamboa 2008). The generality of these models is questionable. The bubble characteristics inside the rotating impeller are affected by many factors, including fluid properties (density, viscosity, surface tension), pump geometry and operating parameters (rotational speed, flow rates).

By photographing the bubble dispersion in a pump with a transparent Plexiglas casing, Murakami and Minemura (1974a and 1974b) correlated the observed bubble sizes with a linear relationship of Sauter Mean Diameter (d_{32}) versus GVF (Eq. 1.25):

$$d_m = 21.82\left(\frac{N}{6.862}\right)^{-\frac{3}{4}}\left(0.618+4.273\lambda\right). \tag{1.25}$$

Although Eq. (1.25) is based on rotational speed (N) and inlet GVF, the empirical nature limited its applicability. Another model of bubble size in a centrifugal pump was proposed by Estevam (2002) based on analogy to gas-liquid two-phase pipe flow. Applying Hinze (1955) theory for droplet breakup mechanism in turbulent flow to bubble size prediction in centrifugal pump, Estevam obtained the following equation to calculate the maximum dispersed bubble size:

$$d_{\max} = 1.17\left(\frac{\sigma}{\rho_l}\right)^{\frac{3}{5}}\left(\frac{2f_{\beta,\omega}}{D_H}\right)^{-\frac{2}{5}}, \tag{1.26}$$

where the constant of 1.17 is a parameter accounting for the curvature of impeller flow passages; σ, ρ_l and D_H are interfacial tension, liquid density and hydraulic diameter, respectively; the friction factor ($f_{\beta,\omega}$) is determined by analogy to fluid flow in pipeline and considering rotational speed effect.

Following a similar methodology of modeling bubble size inside a centrifugal pump, Barrios (2007) proposed a bubble size prediction model based on the visualization experimental data inside ESP taken by high-speed CCD camera. Barrios pointed out that the experimental results were necessary to determine the relationship of the maximum bubble size, the critical bubble size and inlet GVF. The critical Weber number (We_{crit}) is a parameter dominating gas bubble breakup. Hence, Eq. (1.27) explicitly relates the bubble size with the rotational speed and liquid properties:

$$d_{b\_surg} = 0.0348 N^{0.8809} \lambda^{1/4} \left(\frac{\sigma}{\rho_l} \right)^{3/5} \frac{1}{\left(N^3 r_1^2 \right)^{2/5}}, \tag{1.27}$$

where r_1 is the impeller radius. Gamboa (2008) employed the Levich (1962) model for maximum stable bubble size in pipe flow and proposed an alternative way of modeling bubble size inside an ESP. Gamboa improved the bubble size model by introducing dispersed gas phase density and We_{crit} based on Kouba (2003) droplet breakup studies:

$$d_{\max} = 14.27 \left(\frac{\sigma}{\rho_l} \right)^{3/5} \left(\frac{(\Omega D)^4}{\nu} \right)^{-2/5} \left(\frac{\rho_l}{\rho_g} \right)^{1/5} \left(1 + 191.7 \lambda^{0.2} \right), \tag{1.28}$$

where ρ_g is in-situ gas density, v is liquid kinetic viscosity and Ω, D are impeller rotational speed and diameter, respectively.

Although several models are available in literature for bubble size prediction in a centrifugal pump with rotating turbulent flow, their empirical/semi-empirical natures limited the range of applications. As discussed by Gamboa (2009), the challenge in modeling bubble size inside a rotating ESP is the mechanism that dominates bubble formation, including coalescence and breakup. Therefore, investigation is needed to better understand the bubble dispersion mechanism and develop better model for bubble size prediction.

1.4.3.2 Drag Coefficient (C_D). In gas-liquid two-phase flow, the drag force is the interfacial momentum transfer due to velocity difference between gas and liquid phases (Ziegenhein et al. 2015):

$$F_D = -C_D A_p \frac{\rho_f (U - v)|U - v|}{2}, \tag{1.29}$$

where U and v are velocities of liquid and gas phases, respectively. The drag coefficient (C_D) for bubbles in no-rotating flow fields without shearing was studied by Schiller and Naumann (1933), Clift et al. (1978), Ishii and Zuber (1979), Mei et al. (1994) among others. Schiller and Naumann proposed an empirical correlation of C_D for $0.1 < Re < 800$. Clift et al. developed a more accurate expression which is valid for higher Re up to 3×10^5 (Tran-Cong et al. 2004):

$$C_D = \frac{24}{\mathrm{Re}}\left(1 + 0.15\,\mathrm{Re}^{0.687}\right) + \frac{0.42}{1 + 4.25\times10^4\,\mathrm{Re}^{-1.16}}. \tag{1.30}$$

Ishii and Zuber incorporated a correlation term $(1+\alpha_\mathrm{d})^{-\gamma}$ to account for effects of bubble volumetric fraction and flow regime, where γ is an empirical constant determined by fluid properties and particle shapes. Mei et al. studied the behavior of clean bubbles (no contaminations or surfactants involved) in a uniform flow and proposed an empirical drag C_D for a wide range of Re:

$$C_D = \frac{16}{\mathrm{Re}}\left(1+\left(\frac{8}{\mathrm{Re}}+\frac{1}{2}\left(1+3.315\,\mathrm{Re}^{-\frac{1}{2}}\right)\right)^{-1}\right). \tag{1.31}$$

For shear-induced flow, the viscous drag force exerted on bubbles is increased by broadening the near wake (van Nierop et al., 2007). Thus, the dimensionless shear rate, Strouhal number (Sr) as an indicator of shear strength, was employed by Legendre and Magnaudet (1998) to calculate C_D in shear flow for moderate-to-large Re (≥ 50):

$$Sr = \frac{d_b \omega}{|U - v|} \tag{1.32}$$

and

$$C_{D,sr} = C_{D,0}\left(1+\frac{0.55}{Sr^2}\right), \tag{1.33}$$

where $C_{D,0}$ is the drag coefficient calculated without shear effect (van Nierop et al., 2007). Rastello et al. (2009, 2011) revised Eq. (1.33) to get a better fitting of their experimental data for low, moderate and high Reynolds numbers with a broad range of Sr:

$$C_{D,sr} = C_{D,0}\left(1+\frac{0.3}{Sr^{2.5}}\right). \tag{1.34}$$

Barrios (2007) measured bubble sizes inside a single-stage ESP with a visualization experimental system and calculated the drag coefficients on stagnant bubbles in rotating flow field. Then, the drag coefficients were correlated by:

$$C_D = \frac{24}{\mathrm{Re}\cdot Y}\left(1+f\left(\mathrm{Re},Y\right)\right), \tag{1.35}$$

where Y and $f\,(\mathrm{Re},Y)$ are given by

$$f\left(\mathrm{Re},Y\right) = \frac{5.48}{24}\left(\mathrm{Re}\cdot Y\right)^{0.427}+\frac{0.36}{24}\left(\mathrm{Re}\cdot Y\right) \tag{1.36}$$

and

$$Y = 0.00983+389.9\frac{\mathrm{Re}}{N^2}. \tag{1.37}$$

1.4.3.3 Gas Void Fraction (α_G). The in-situ gas void fraction (α_G) is an important variable in two-phase flow related to the velocity slippage between two immiscible phases and the gas accumulation. However, due to the complicated pump geometries and fluid flow dynamics in the ESP impeller, it is challenging to develop a mechanistic model to predict α_G with general validity. Very few studies on mechanistic modeling of local gas void fraction in ESPs can be found in literature so far.

The simplest model for predicting α_G in multiphase centrifugal pump flows is the homogeneous model, which assumes no slippage between gas and liquid phases,

$$\alpha_G = \lambda_G = \frac{Q_G}{Q_G + Q_L} . \tag{1.38}$$

The homogenous model is valid for very low inlet GVFs when the slippage between gas and liquid is minimal. Errors will result from applying the homogeneous model to flow conditions with high inlet GVFs when the slippage is not negligible. Accounting for the phase slippage, several empirical correlations were proposed by Chisely (1997), Estevam (2002), Zapata (2003) and Pineda et al. (2016), among others.

Chisely studied loss of coolant accident with a volute-type centrifugal pump in the nuclear industry. The pressure distribution and flow regimes were determined with the experimental measurement and high-speed photographing. A model for predicting the centrifugal pump pressure increment under two-phase flow conditions was proposed. To make this model solvable, the in-situ α_G was correlated as:

$$\alpha_G = \left[1 + 0.28 \left(\frac{1 - x}{x} \right)^{0.64} \left(\frac{\rho_G}{\rho_L} \right)^{0.36} \left(\frac{\mu_L}{\mu_G} \right)^{0.07} \right]^{-1} , \tag{1.39}$$

where χ is the gas quality, μ_G and μ_L are the gas and liquid viscosities.

Estevam conducted visualization experiments on a radial type ESP to investigate its ability of handling gas-liquid mixtures. By analyzing the obtained photographs of flow structures inside the ESP impeller, an empirical model for calculating α_G was proposed:

$$\alpha_G = \frac{\lambda_G}{1-\left[\lambda_G\left(1-\lambda_G\right)\right]^{0.5}} . \tag{1.40}$$

Zapata experimentally studied the rotational speed effect on ESP two-phase performance. Using least-square regression, a new correlation of α_G was presented to predict the pump boosting pressure. The empirical correlation as function of gas and liquid flow rates and the rotational speed is given as:

$$\alpha_G = \left[\left(\frac{q_G}{q_{\max}}\right)\frac{\left(q_L/q_{\max}\right)^{-1.277-0.034{N_d}^{N_d}}}{0.598+0.223{N_d}^{N_d}}\right]^{\frac{1}{0.921+0.068{N_d}^{N_d}}} , \tag{1.41}$$

where q_G and q_L are the gas and liquid flow rates, ${N_d}^{N_d}$ is normalized rotational speed, and $q_{\max}$ is the maximum single-phase liquid flow rate.

Pineda et al. (2016) proposed an empirical correlation based on the Lockhart-Martinelli type parameter X_{tt} by non-linear regression of CFD simulated values of in-situ α_G:

$$\alpha_G = 7.119X_{tt}^{-0.8778} - 0.002138 , \tag{1.41}$$

where

$$X_{tt} = \left(\frac{\mu_L}{\mu_G}\right)^{0.1}\left(\frac{1-x}{x}\right)^{0.9}\left(\frac{\rho_G}{\rho_L}\right)^{0.5} . \tag{1.42}$$

In addition to correlations, several numerical models for prediction of multiphase flow hydrodynamics in rotating centrifugal pumps have been developed by Sachdeva (1988), Minemura et al. (1998), and Sun (2003), among others. However, these models were formulated based on 1D two-fluid conservations of mass and momentum along streamlines. Discretization of the computational domain and numerical iterations are required to obtain the solutions. Compared with empirical correlations and mechanistic models, the numerical approach is more complicated and difficult to implement.

Although many studies on predicting the in-situ liquid or gas holdup are available for multiphase pipe flow (Taitel and Dukler, 1976; Zhang et al., 2003), the mechanistic models to calculate α_G in rotating centrifugal pumps, especially ESPs, are very few. The aforementioned correlations are empirical and big errors will happen if they are applied to a wider range of flow conditions. The difficulty of measuring the in-situ α_G inside an ESP impeller hinders the development of mechanistic prediction models.

1.4.3.4 Initiation of Pressure Surging. Pressure surging, named by Lea and Bearden (1982), is a significant phenomenon that affects ESP pressure-boosting ability under gassy flow conditions, which coincides the instability of ESP operation (Gamboa, 2011). To maintain stable ESP operation and extend its field service life, it is necessary to accurately predict the critical GVF (λ_C) at which the pressure surging initiates. Due to complexity of ESP geometry and internal flow structures, the prediction of surging initiation is very difficult. Most of the existing prediction correlations and models in literature are empirical. The lack of a theoretical basis in these correlations restricts their field applications to wider range of flow conditions. Therefore, a more generic and reliable mechanistic model for predicting ESP pressure surging is needed, so that necessary precautions or measures can be taken before the inlet GVF approaches the value that initializes the drastic performance drop and further unstable flow in ESP.

Experimental studies on surging phenomenon and drastic deterioration of pressure increment in ESP under gassy flow conditions have been conducted by Turpin et al. (1986), Cirilo (1998), Pessoa (2001), Estevam (2002), Beltur (2003), Duran (2003), Zapata (2003), Barrios (2007), Gamboa (2008), and Salehi (2012), among others. Based on the experimental measurement from two testing facilities with different working fluids, Turpin et al. (1986) correlated ESP pressure surging with respect to pump intake pressure and gas/liquid flow rates as below:

$$\phi = \left(\frac{2000}{3P_i} \right) \frac{Q_G}{Q_L}, \tag{1.43}$$

where ϕ is a factor interpreted as the limit between the stable and unstable operating regimes in ESP. P_i is the intake pressure. Q_G and Q_L are gas and liquid flow rates, respectively. The authors claimed that the proposed correlation could predict the transition boundary of pump's unacceptable performance region with a wide range of inlet GVFs.

Pessoa (2001) conducted the stage-by-stage measurement of ESP two-phase pressure increment with a 22-stage GC-6100 pump. An empirical correlation to predict the initiation of apparent head degradation inside ESP with gas presence was given as:

$$\lambda_C = 0.0187 P_i^{0.4342}, \tag{1.44}$$

where λ_C is the critical GVF corresponding to the surging initiation in ESPs. Estevam (2002) performed visualization experiments and analyses of gas-liquid flow in an ESP impeller. Similar flow regimes as multiphase pipe flow were observed and categorized as bubbly flow, transition flow, and elongated-bubble flow. The linear correlation to predict ESP pressure surging was proposed as

$$\lambda_C = 31.92 - 32.15(1 - \lambda_G). \tag{1.45}$$

Duran (2003) and Zapata (2003) studied the effects of multistage and rotational speed on ESP pressure increment under two-phase flow conditions, respectively. They both developed empirical correlations for predicting pressure increment across ESP stages and flow regime boundaries. As an important closure relationship, the surging initiation corresponds to the transition boundary of dispersed bubble flow to bubbly flow in ESPs. An empirical correlation was proposed by Duran as

$$\frac{Q_G}{Q_{\max}} = \left(5.58\frac{\rho_G}{\rho_L} + 0.098\right)\left(\frac{Q_L}{Q_{\max}}\right)^{1.421}, \tag{1.46}$$

where ρ_G and ρ_L are gas and liquid densities, respectively. Q_{max} is the single-phase open flow rate, corresponding to the pump nil performance. A similar correlation for predicting surging initiation was given by Zapata (2003) as

$$\frac{Q_G}{Q_{\max}} = \frac{0.027\dfrac{Q_L}{Q_{\max}}}{0.9001 - \dfrac{Q_L}{Q_{\max}}}. \tag{1.47}$$

A recent semi-empirical correlation to predict pressure surging in rotating ESPs was proposed by Gamboa and Prado (2011). Starting from the ESP two-phase performance map, the first transition boundary for mild deterioration of pump boosting pressure and *H*-*Q* performance curves with the reverse slope was identified. The authors pointed out that the first transition boundary, coinciding with the initiation of pressure surging, could be used as an indicator for flow pattern transition from dispersed bubble flow to bubbly flow. By analyzing the relevant factors affecting ESP’s pressure increment, the new correlation based on dimensionless Π theory was given as:

$$\frac{Q_G}{Q_{\max}} = \left(\frac{\rho_G}{\rho_L}\right)^{0.2}\left(\frac{\Omega D^2}{\nu}\right)^{0.4}\left(0.102\exp\left(\frac{Q_L}{Q_{\max}}\right)\right)^{4.4682}, \tag{1.48}$$

where Ω is the pump rotational speed, *D* is the representative impeller diameter, and *v* is the liquid kinetic viscosity. The constants were obtained by nonlinear regression with experimental data. Eq. (1.48) may not give accurate predictions of pressure surging initiation for different type of ESPs.

Accurate prediction of ESP pressure surging initiation under varying flow conditions is important to maintain pump stable operations and extend pump field service life. It is also critical for the design of an ESP-based production system as well as the downhole separator selection. Due to the incomplete physics considered in the existing models or correlations, the direct applications of these formulas to different pumps or flow conditions are questionable (Gamboa and Prado, 2011).

1.5 Literature Review Summary

Although studies on centrifugal pump performance under gassy flow are available in literature, the gas bubble behavior and its effects on two-phase flow hydrodynamics in rotating ESPs are still not well understood. Natural surfactants may exist in crude oil production system. Their effects on multiphase pipe flow and the drag reduction mechanisms due to chemical additives are of great interest to researchers and applications (Ajani et al., 2016; van Nimwegen et al., 2015, 2016 and 2017). However, most experimental studies on ESP boosting pressure with gas presence were conducted without consideration of surfactant effect. Comprehensive experimental tests of ESP stage pressure increment under gassy flow with varying concentrations of surfactants should be conducted.

Due to the compact and complicated geometry, it is very difficult to visualize ESP internal flow structures and bubble movement when the impeller is rotating. Significant simplifications were made in Barrios (2007) and Gamboa (2008) preliminary visualization studies. CFD simulations can provide detailed information of flow structures inside the impeller. Previous numerical simulations paid more attention to predicting pump's overall two-phase performance rather than flow structures inside ESPs.

Mechanistic modeling of ESP two-phase performance is still preliminary in the literature. Experimental investigations are insufficient on ESP two-phase flow behaviors including flow patterns and transition boundaries. The development and validations are also critical for the accuracy of mechanistic model predictions.

CHAPTER 2

EXPERIMENTAL SETUP AND RESULTS

This chapter presents experimental details for testing ESP performance under both liquid and gas-liquid flow conditions, including experimental facility, data acquisition system (DAQ), the experimental procedure as well as experimental results. Multiple hydraulic variables and their effects on ESP stage pressure increment are demonstrated and analyzed in this chapter.

2.1 Experimental Facility

The experimental facility was rebuilt from a previous two-phase flow loop used by Salehi (2012) to conduct performance tests of TE-2700 ESP under gassy conditions. The old ESP was replaced by a brand new one. The original two-phase flow loop at TUALP was built by Cirilo (1998) and upgraded later by Romero (1999), Pessoa (2001), Beltur (2003), Duran (2003), Zapata (2003) and Gamboa (2009). The experimental facility consists of a fully-closed water flow loop and an open loop for compressed air circulation. The schematic of the facility layout is shown in Figure 2.1. The flow loop overall capacity is about 5,000 bpd of water flow rate and 186 cfm of air flow rate at 217 psig. The detailed specifications and configurations of the major components in this loop are listed in Appendix A.

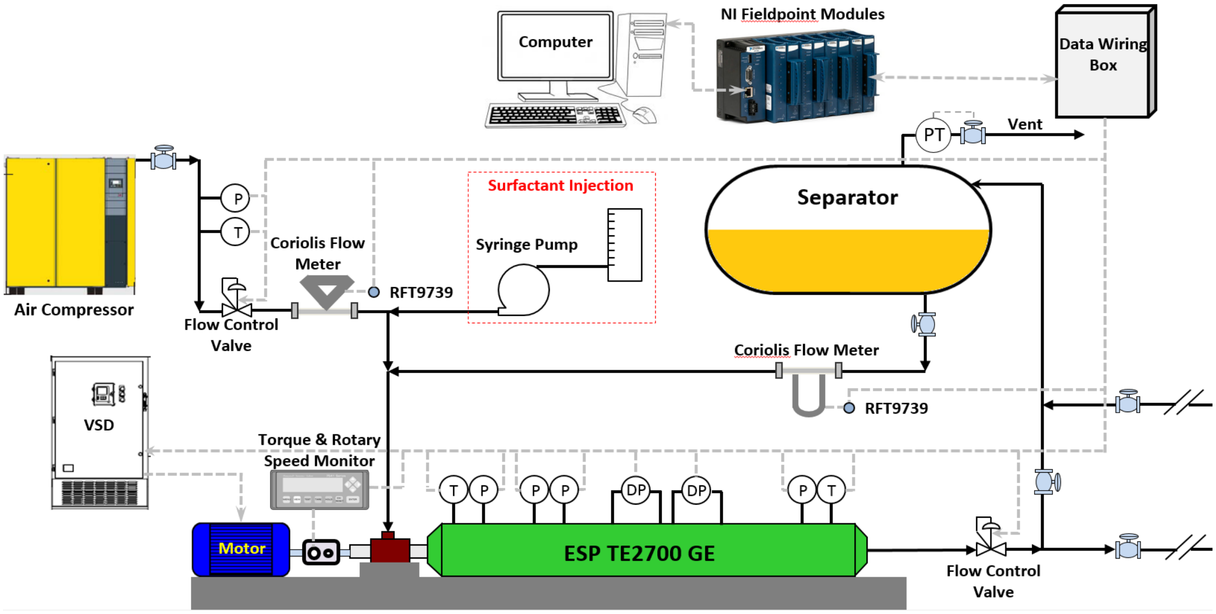

Figure 2.1 Schematic of TUALP two-phase ESP loop

2.1.1 Gas-liquid Flow Loops

As shown in Figure 2.1, the water loop with 3” stainless steel pipe is connected to a 150-barrel two-phase separator, which also serves as the water storage tank. The maximum pressure of this separator was rated at 200 psig. In this study, the separator pressure was set at 50, 100 and 150 psig so that the effects of intake pressure on ESP gas-liquid performance is shown in experiments. Another function of the two-phase separator is to ensure sufficient intake pressure (> 30 psig) so that cavitation can be avoided. A Coriolis flowmeter (Micro Motion CMF200) mounted at upstream of the ESP is used to measure the water flow rate and density. At downstream of the ESP, a flow control valve is installed to regulate the liquid flow rate.

Pressurized by a compressor (Kaeser CSD60), air flow is regulated by a gas control valve in the gas flow loop. The mass flow rate of air is measured by a Coriolis flowmeter (Micro Motion CMF025). The air density can also be measured by the same flowmeter, but the in-situ air density at ESP intake is calculated using correlations for wet air properties based on the local pressure and temperature. Air compressibility causes the difference of in-situ gas densities at the flowmeter and ESP intake. Air is mixed with water inside a T-junction prior to the inlet of the ESP. Before mixing, the chemical surfactants (e.g. alcohol) can be injected by a metering pump (Iwaki EWN-R B11) so that the fluid interfacial tension can be altered. After the fluid flows through the ESP testing section and downstream control valve, the gas/liquid mixture is discharged into the horizontal two-phase separator, where the excessive air is vented to the atmosphere and the liquid continues circulation.

2.1.2 ESP Test Bench

The ESP test bench consists of the ESP, motor, thrust chamber and other equipment that are needed for ESP operation. The studied ESP is a 14-stage TE-2700 series 538 (GE ESP). The best efficiency point (BEP) is 2700 bpd at 3500 rpm with a stage pressure increment of 22.5 psi, based on which the estimated N_S is 1638. The water performance curves at different rotational speeds are shown below, including head curves (Figure 2.2) and efficiency curves (Figure 2.3). The pump head curve moves toward the left-bottom corner when the pump rotational speed is reduced. The efficiency curve moves to the left-side on the chart. The maximum open flow rate at N = 3500 rpm is 4900 bpd, while the maximum shut-in pump head is 30 psi. In Figure 2.3, the asymptotic value of the hydraulic efficiency for TE-2700 ESP under varying rotational speeds is below 70%.

For a centrifugal pump the affinity law can be used to predict the pump head, efficiency and brake-horse-power at different rotational speeds for water flow if the performance curve at a fixed rotational speed is known.

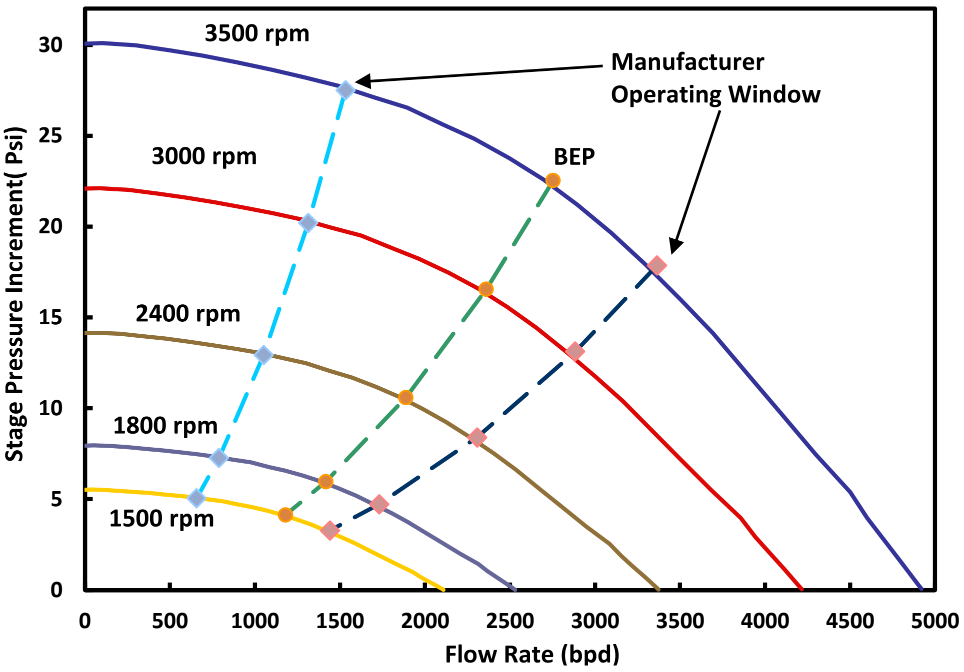

Figure 2.2 TE-2700 ESP water performance curves

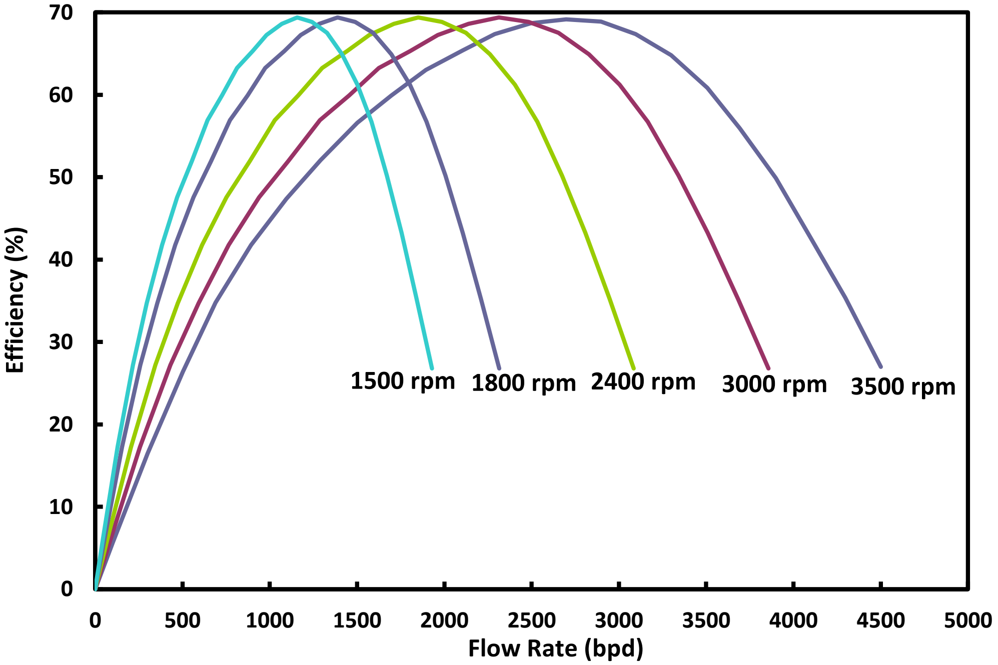

Figure 2.3 TE-2700 ESP efficiency curves

Stepanoff (1957) derived the affinity laws as below:

$$\frac{Q_1}{Q_2} = \frac{N_1}{N_2}, \tag{2.1}$$

$$\frac{H_1}{H_2} = \left(\frac{N_1}{N_2} \right)^2 , \tag{2.2}$$

$$\frac{BHP_1}{BHP_2} = \left(\frac{N_1}{N_2} \right)^3 , \tag{2.3}$$

where Q, H, BHP are flow rate, hydraulic head and brake-horse-power, respectively.

A series of quarter-inch (¼”) holes are drilled on the pump housing at stages 2, 3, 4, 5, 6, 7, 8, 9, 10, 11, 12 and 13 to allow the communication between the pressure transmitters and the working fluids. Additional holes are drilled 90° from the previous holes at the same stages. Figure 2.4(a) draws a sectional front view of the detailed positions of the threaded pressure measurement ports for installing quick connectors (Swagelok QTM2). Figure 2.4(b) shows the actual view of the ESP testing bench. Figure 2.4(c) shows a schematic of the quick connector and its mounting position at the inter-stage location. The pressure port is located between the upstream diffuser and downstream impeller. Similar inter-stage connection is made for all the other pressure ports. On the internal housing surface of each diffuser, peripheral notch is grooved so that Teflon O-rings can be installed to block fluid communication between stages.

The absolute pressure at pump inlet and stage 2 to 14 are measured by absolute pressure transducers (Rosemount 2051S). The pressure differences of stage 0~2, 3, 4, 5, 6, 7 and stage 0~14 are measured using the differential pressure transducers (Rosemount 3051S). The temperatures at the inlet of ESP and stage 14 are measured with four-wire platinum RTDs (resistance temperature detector, Rosemount 3144).

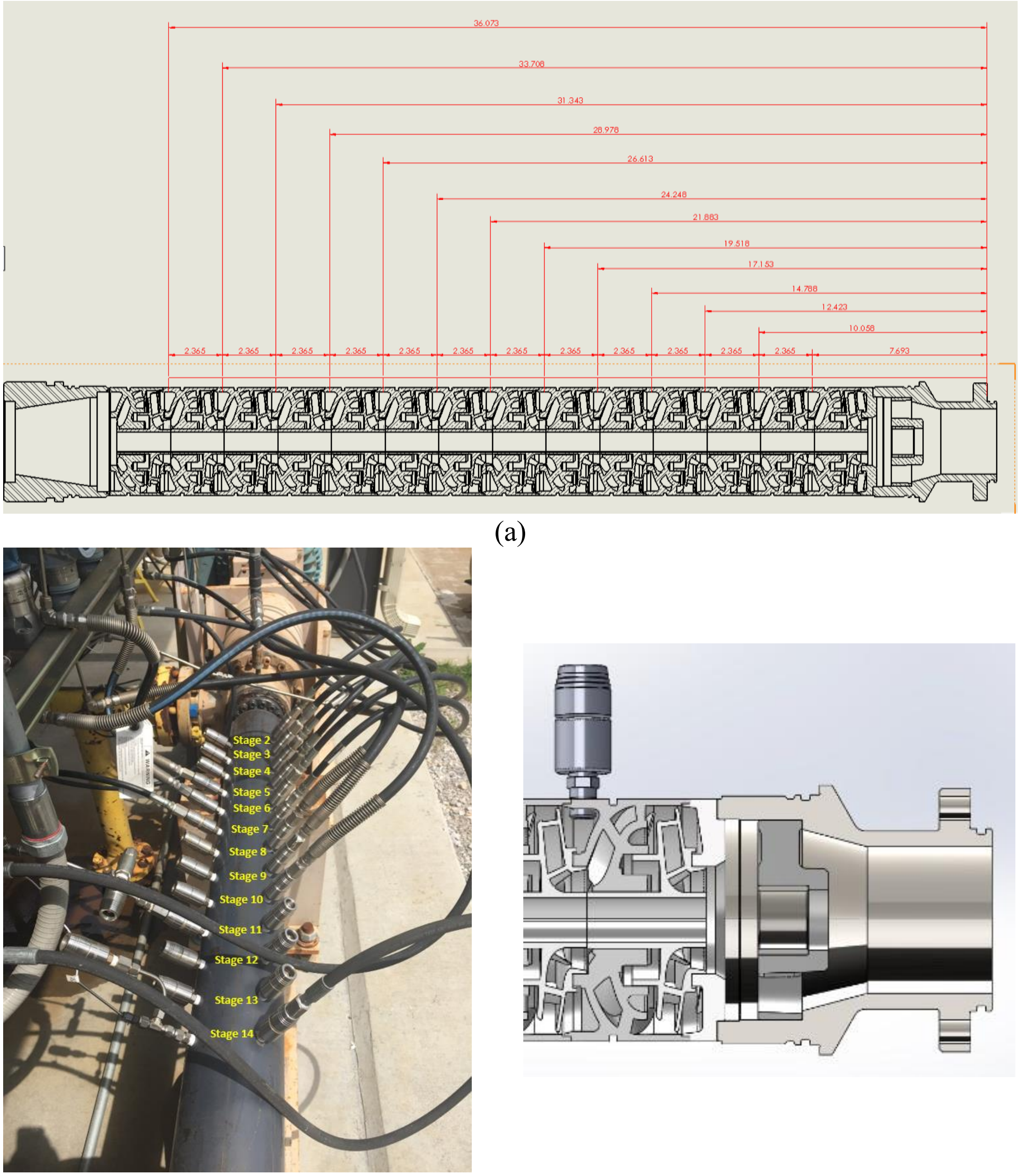

(a)

(b) (c)

Figure 2.4 ESP pressure measurement ports, (a) sectional front view of TE-2700 ESP, (b) top view of pressure measurement ports, (c) schematic of quick connector and mounting location

The ESP testing bench consists of the multistage ESP, motor, variable speed drive (VSD), thrust chamber and auxiliary electrical equipment for pump operations. ESP is driven by a four-pole 50 hp electric motor (North American H3650) via VSD (Hitachi

L300P). At the pump discharge, a 3-inch pneumatic control valve is installed to control the liquid flow rate. ESP and electric motor are connected through the thrust chamber which holds thrust force and allows the shaft rotating. The rotational speed and shaft torque are measured by the torque cell, including a sensor (Lebow 1805K) and a monitor (Lebow 7540).

2.1.3 Data Acquisition System

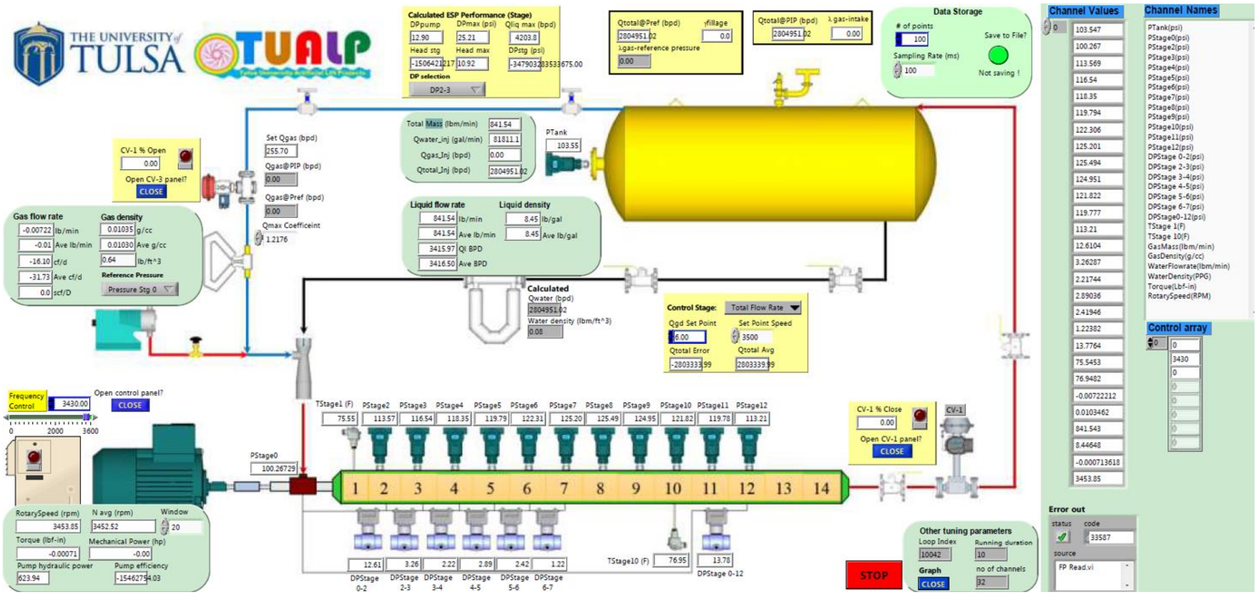

Calculated ESP Performance (Stage)
DPpump 12.90
DPmax (psi) 25.21
Qliq max (bpd) 4203.8
Head stg -1506421217
Head max 10.92
DPstg (psi) -347903283533675.00
DP selection DP2-3

Qtotal@Pref (bpd) 2804951.02
γfillage 0.0
λgas-reference pressure 0.00

Qtotal@PIP (bpd) 2804951.02
λ gas-intake 0.00

Data Storage
# of points 100
Sampling Rate (ms) 100
Save to File?
Not saving !

CV-1 % Open 0.00
Open CV-3 panel?

Set Qgas (bpd) 255.70
Qgas@PIP (bpd) 0.00
Qgas@Pref (bpd) 0.00
Qmax Coefficeint 1.2176

Total Mass (lbm/min) 841.54
Qwater_inj (gal/min) 81811.1
Qgas_Inj (bpd) 0.00
Qtotal_Inj (bpd) 2804951.02

PTank 103.55

Gas flow rate
-0.00722 lb/min
-0.01 Ave lb/min
-16.10 cf/d
-31.73 Ave cf/d
0.0 scf/D

Gas density
0.01035 g/cc
0.01030 Ave g/cc
0.64 lb/ft^3
Reference Pressure Pressure Stg 0

Liquid flow rate
841.54 lb/min
841.54 Ave lb/min
3415.97 Ql BPD
3416.50 Ave BPD

Liquid density
8.45 lb/gal
8.45 Ave lb/gal

Calculated
Qwater (bpd) 2804951.02
Water density (lbm/ft^3) 0.08

Control Stage: Total Flow Rate
Qgd Set Point 6.00
Set Point Speed 3500
Qtotal Error -2803333.99
Qtotal Avg 2803339.99

Frequency Control 3430.00
Open control panel?

PStage0 100.26729

TStage1 (F)	PStage2	PStage3	PStage4	PStage5	PStage6	PStage7	PStage8	PStage9	PStage10	PStage11	PStage12
75.55	113.57	116.54	118.35	119.79	122.31	125.20	125.49	124.95	121.82	119.78	113.21

DPStage 0-2	DPStage 2-3	DPStage 3-4	DPStage 4-5	DPStage 5-6	DPStage 6-7
12.61	3.26	2.22	2.89	2.42	1.22

TStage10 (F) 76.95
DPStage 0-12 13.78

CV-1 % Close 0.00
Open CV-1 panel?

RotarySpeed (rpm) 3453.85
N avg (rpm) 3452.52
Window 20
Torque (lbf-in) -0.00071
Mechanical Power (hp) -0.00
Pump hydraulic power 623.94
Pump efficiency -15462754.03

Other tuning parameters
Loop Index 10042
Running duration 10
Graph
no of channels 32

Channel Values	Channel Names
103.547	PTank(psi)
100.267	PStage0(psi)
113.569	PStage2(psi)
116.54	PStage3(psi)
118.35	PStage4(psi)
119.794	PStage5(psi)
122.306	PStage6(psi)
125.201	PStage7(psi)
125.494	PStage8(psi)
124.951	PStage9(psi)
121.822	PStage10(psi)
119.777	PStage11(psi)
113.21	PStage12(psi)
12.6104	DPStage 0-2(psi)
3.26287	DPStage 2-3(psi)
2.21744	DPStage 3-4(psi)
2.89036	DPStage 4-5(psi)
2.41946	DPStage 5-6(psi)
1.22382	DPStage 6-7(psi)
13.7764	DPStage0-12(psi)
75.5453	TStage 1(F)
76.9482	TStage 10(F)
-0.00722212	GasMass(lbm/min)
0.0103462	GasDensity(g/cc)
841.543	WaterFlowrate(lbm/min)
8.44648	WaterDensity(PPG)
-0.000713618	Torque(Lbf-in)
3453.85	RotarySpeed(RPM)

Control array 0
0
3430
0
0
0
0
0
0

Error out
status ✓
code 33587
source FP Read.vi

Figure 2.5 Data acquisition system of TUALP two-phase ESP loop

The data acquisition system is based on compact FieldPoint module from National Instrument (NI), which is an expandable and programmable automation controller consisting of a series of analog signal input/output modules and intelligent communication interfaces. All analog signals (4~20 mA) from field terminals (pressure transducers, temperature transmitters, flowmeters, etc.) are connected to the NI input modules (cFP-AI-111), where the sensor electric current signals are scaled up into engineering units. Similarly, the internal control signals (4~20 mA) from NI output module (cFP-AO-200) are sent to field terminals (control valves, VSD) for the control purpose. The NI modules transmit all signals and communicates to the data processing computer through RS-485 interface and Ethernet cable. A Dell computer (Optiplex 9020) equipped with Intel® duo-core processor (3.4 GHz), 16GB RAM and 1 TB hard disk serves as the data processing center.

As shown in Figure 2.5, the DAQ program is written in a graphic-programing language Labview V2014 for the data acquisition and control of flow loop. Meanwhile, the Labview-based DAQ program is able to monitor and plot real-time data, and execute control schemes as needed in the experiments. A classical proportional-integrative derivative (PID) controller is used to regulate water and air flow rates, and rotational speed. The raw data recorded by DAQ are exported into text file for further processing.

2.2 Experimental Program

2.2.1 Test Fluids

Tap water and compressed air are used in this study as the working fluids. The surfactant of isopropyl alcohol (IPA) is injected into the flow loop to reduce the interfacial tension between water and air. The liquid density is measured by Coriolis flowmeter (Micro Motion CMF200). The in-situ properties of compressed air are calculated based on the equations of states (EOS) for moist air, which are unofficially referred to as CPM-81 (Davis, 1992). The detailed equations are included in Appendix B.

The selected surfactant IPA is a harmless and environment-friendly chemical in the alcohol family (Gamboa, 2008). With injection of surfactant into the system, the surface tension between air and water is reduced significantly before a critical point called CMC (critical micelle concentration) is reached.

Meissner and Michael (1949) proposed a correlation to reflect the dependence of surface tension on the volumetric concentration of surfactants:

$$\sigma = \sigma_w \left(1 - 0.4 \log \left(1 + \frac{x_o}{a_{MM}} \right) \right), \tag{2.4}$$

where σ is the surface tension after adding the surfactant (*N/m*), σ_w is the surface tension of pure water (*N/m*), $\sigma_w = 0.0728$ *N/m* at 20 °C. a_{MM} is an empirical constant determined from experimental measurement. x_o is the solute concentration (gram mole per liter of solution). As shown in Figure 2.6, two sets of experimental data are compared with Meissner and Michael correlation: the measurements in Hu et al. (2006) and the data obtained in this study using a digital tensiometer (Attension Sigma-700). Good agreement is found between the empirical correlation and Hu et al. data. The deviation of the measurements from Meissner and Michael correlation is probably due to the contamination in the tap water used in this study compared to the distilled water used in Hu et al.

Figure 2.7 presents the solution density as function of the volumetric concentration of IPA. A linear regression with good agreement with the experimental measurements can be obtained. Compared to the literature data (Chu and Thompson, 1962), the measured solution density is slightly higher.

The working fluid is sampled and measured by digital tensiometer to get its surface tension. The volumetric concentration of surfactant in the flow loop can be obtained by interpolating the measured points in Figure 2.6. Another approach for estimating the surfactant volumetric concentration is to drain all the liquid from the loop and measure the total volume. Then, the surfactant concentration by volume is obtained by dividing the injected IPA volume with the total working fluid volume. In this study, the second method is used.

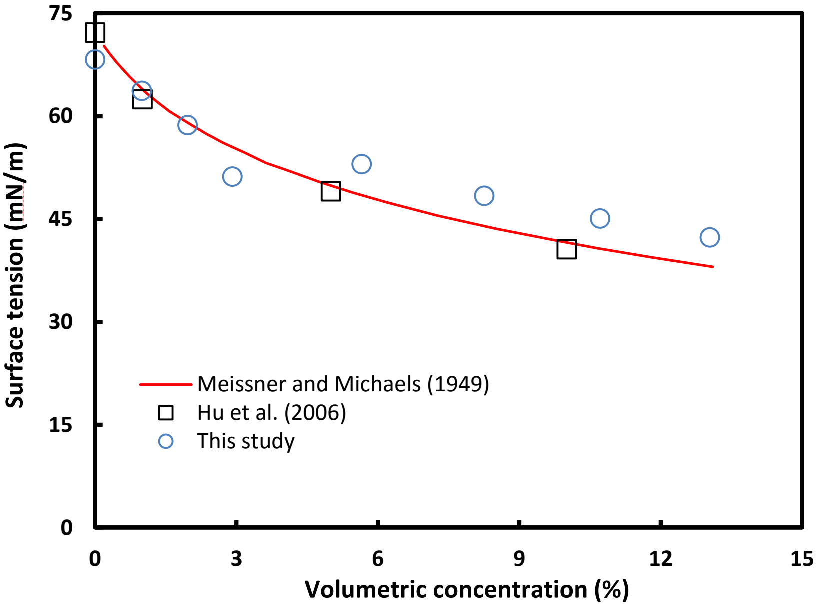

Figure 2.6 Surface tension of air/water versus IPA volumetric concentration

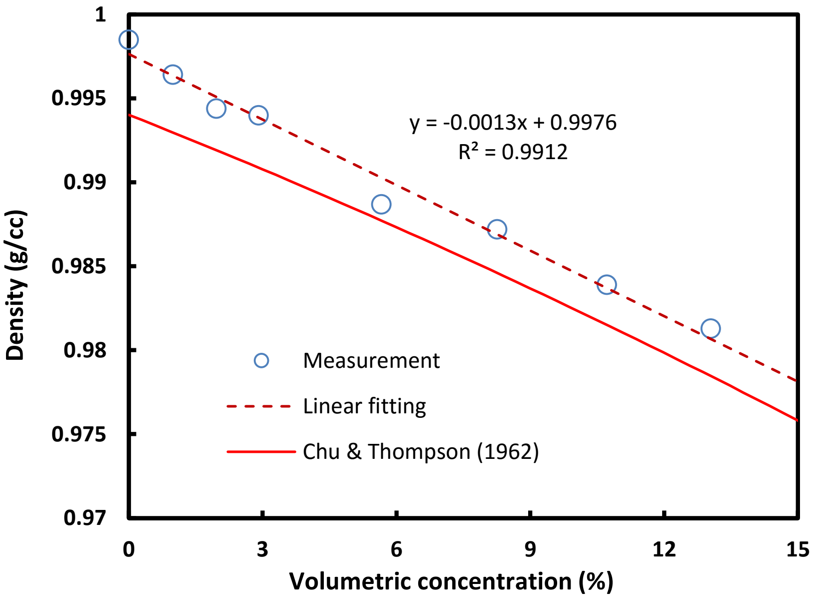

Figure 2.7 Solution density versus IPA volumetric concentration

2.2.2 Experiment Procedure

The experimental procedure adopted in this study is similar to Gamboa (2009), Salehi (2012). To better process experimental data, several dimensionless variables are introduced below.

Intake gas volumetric fraction (GVF):

$$GVF = \frac{Q_g}{Q_g + Q_l}. \tag{2.5}$$

Normalized liquid flow rate (q_{ld}):

$$Q_{ld} = \frac{Q_l}{Q_{\max}}. \tag{2.6}$$

Normalized gas flow rate (q_{gd}):

$$Q_{gd} = \frac{Q_g}{Q_{\max}}, \tag{2.7}$$

where the Q_g, Q_l are volumetric flow rates of gas and liquid at ESP inlet. Q_{max} is the maximum liquid flow rate, usually referred to as open flow capacity.

2.2.2.1 Liquid Testing Procedure. Each performance curve is obtained under constant separator pressure and rotational speed. By changing the downstream control valve opening, the liquid flow rate is regulated. The pressure at each stage is then recorded and exported to data files. Experimental measurements are carried out either continuously or stepwise. The continuous measurements require that the choke valve changes its opening continuously while the data recording is conducted simultaneously. According to Gamboa (2009) and Salehi (2012) studies, the continuous data acquisition can resemble the performance curve from the stepwise measurements. The stepwise measurements require that the experimental system reaches a stable working condition, at which the intake pressure, flow rate, and rotational speed are kept constant. Then, the hydraulic data including stage pressure increment and flowrates are recorded for a certain period of time. An arithmetic averaging is applied to each dataset so that the average value for each flow condition is obtained. In this study, the second data acquisition method is mostly employed.

2.2.2.2 Gas-liquid Testing Procedure. In this study, both surging tests and mapping tests are employed to measure ESP boosting pressure under gassy flow. For surging tests, the liquid flow rate is constant, and the gas flow rate is increased from 0 to the maximum gas flow capacity, during which the separator pressure and rotational speed are constant. The mapping test is achieved by controlling the choke valve in the circulation so that the gas flow rate is kept constant. The liquid flow rate is changed from minimum to maximum value by adjusting the opening of the downstream control valve.

2.2.2.3 Surfactant Injection. The tests with surfactant are conducted after the water flow tests are completed. The surfactant is injected continuously at a flow rate of 0.4 GPH (gallon per hour) for two cases. The first case corresponds to a total injection time of 8 hrs, and the second one corresponds to 16 hrs. Similar experimental procedures as water-air tests are repeated.

The total volume of working fluid V_{tot} in the flow loop measured by drainage is about 37 barrels, i.e. $V_{tot} \approx 1540$ gals. For case 1, the injected volume of IPA is 3.2 gal, corresponding to a surfactant volumetric concentration about 0.2%. For case 2, the volumetric concentration of IPA is about 0.41%.

2.2.3 Test Matrix

The test matrices are listed in Table 2.1 for liquid tests and Table 2.2 for gas-liquid tests.

Table 2.1: Experimental matrix for liquid tests

Pump Rotational Speed (rpm)	**Liquid Flow Rate (bpd)**
3500, 3000, 2400, 1800	100, 200, 300…

Table 2.2: Experimental matrix for gas-liquid tests

Surfactant Concentration	**Rotational Speed (rpm)**	**Intake Pressure (psig)**	**Liquid Flow Rate (bpd)**	**Gas Flow Rate (lb/m)**
0%	3500, 1800	50, 100, 150	100, 200, …	0.01, 0.02, …, 0.5
0.2%	3500, 1800	50, 100, 150	100, 200, …	0.01, 0.02, …, 0.5
0.41%	3500,1800	50, 100, 150	100, 200, …	0.01, 0.02, …, 0.5

For liquid tests, the pump performance curves are independent on the loop pressure. Four rotational speeds are used: 3500, 3000, 2400 and 1800 rpm.

For gas-liquid tests, two rotational speeds (3500 and 1800 rpm) are used. The separator pressure is regulated to control the gas properties. Three separator pressures are used: 50, 100, and 150 psig.

2.3 Experimental Results

This section presents the experimental testing results under both liquid and gas-liquid flow conditions with/without surfactant injections.

2.3.1 Liquid Performance Curves

The measured head curves with water flow at 5 different stages are shown in Figure 2.8. The horizontal and vertical coordinates are Q (in bpd) and H (in psi), respectively. Each color corresponds to a different pump rotational speed. The black solid curve at N = 3500 rpm is obtained directly from catalog, and the other catalog curves are calculated with the affinity law. Data points are experimental measurements. As can be seen, the experimental measurements of water head are close to catalog curves, which verifies the testing loop used in this study.

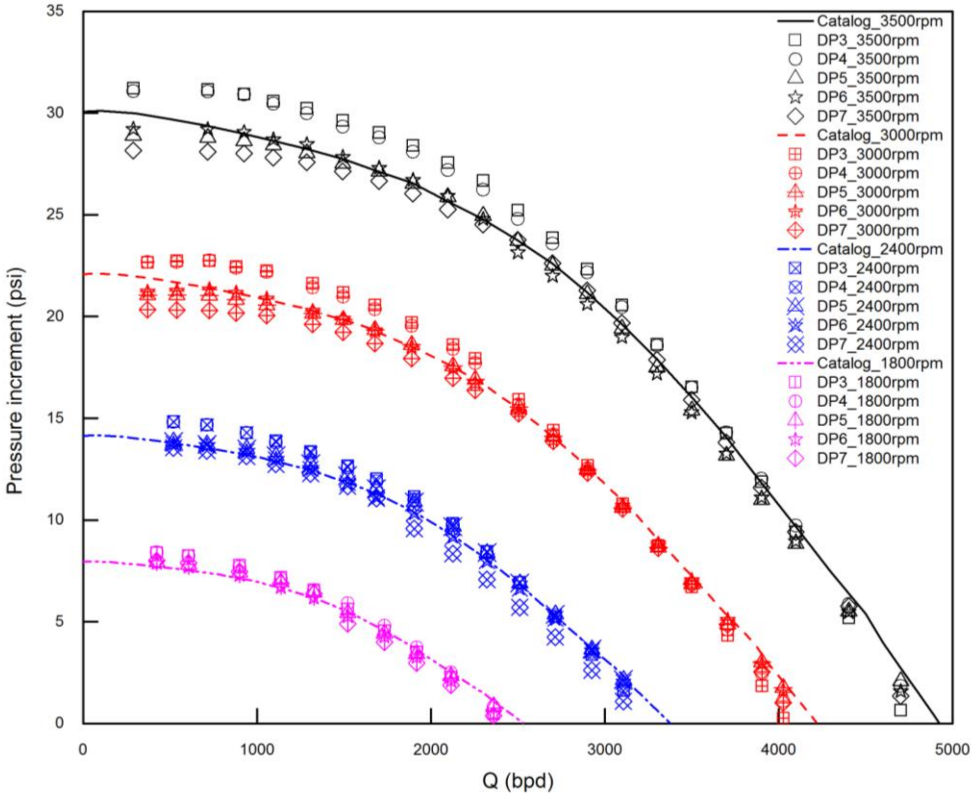

Figure 2.8 Experimental performance curves compared with catalog curves

2.3.2 Gas-liquid Performance Curves of Surging Tests

The surging tests are conducted at different separator pressures, 50, 100, and 150 psig. The effects of stage position, rotational speed, intake pressure as well as surfactant concentration are investigated. Since the first pressure port is located at the 2nd stage diffuser, the pressure measurement at stage 1 and 2 is not available. The experimental data presented in this chapter are part of the complete experimental dataset. More data representations can be found in Appendix D.

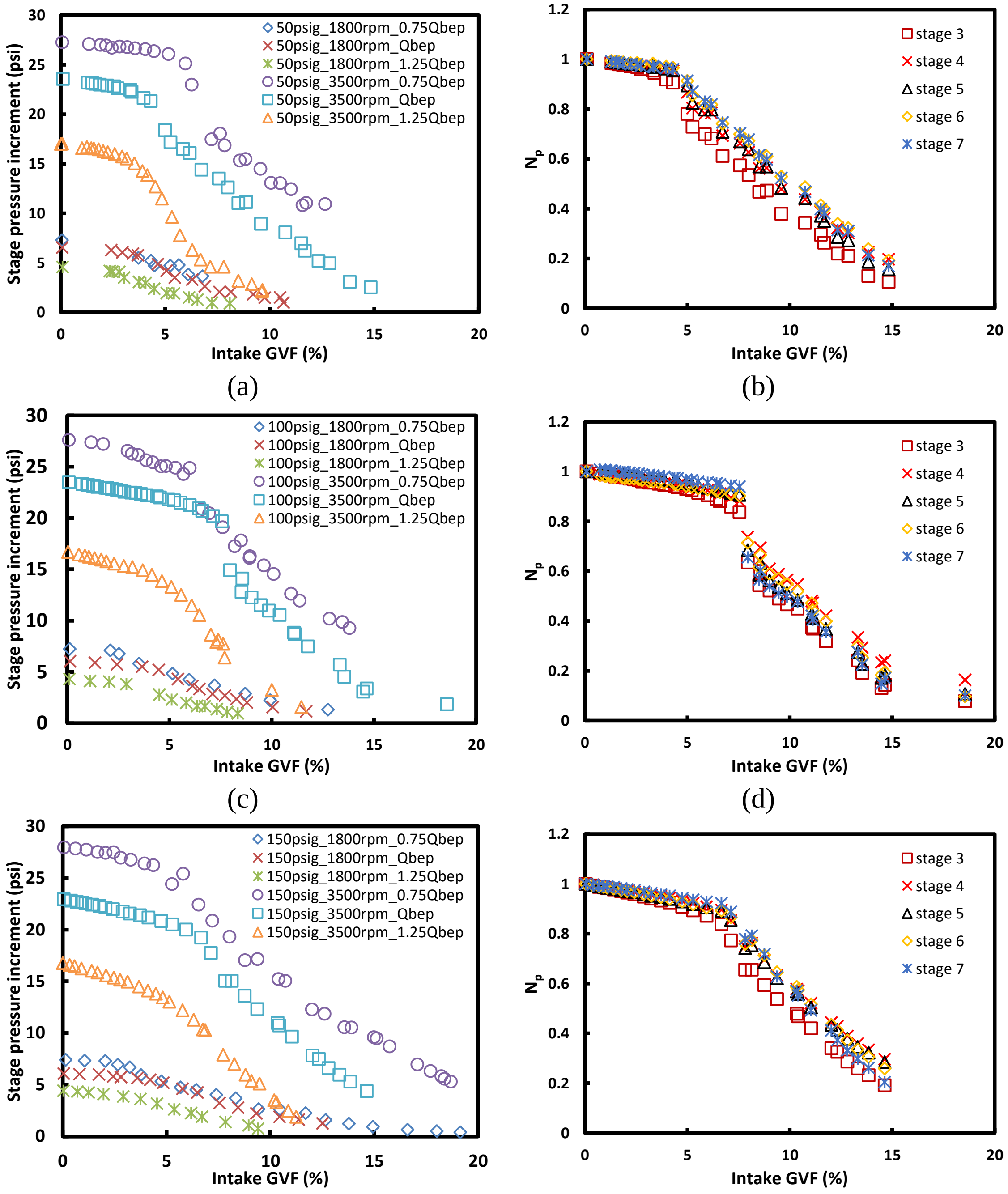

(a) (b)

(c) (d)

(e) (f)

Figure 2.9 Surging tests with water and air, (a) stage 3 at P_{sep} = 50 psig, (b) N = 3500 rpm, Q_{BEP} at P_{sep} = 50 psig, (c) stage 3 at P_{sep} = 100 psig, (d) N = 3500 rpm, Q_{BEP} at P_{sep} = 100 psig, (e) stage 3 at P_{sep} = 150 psig, (f) N = 3500 rpm, Q_{BEP} at P_{sep} = 150 psig

Figures 2.9(a), (c) and (e) illustrate the surging test results at stage 3 at different liquid flow rates (0.75Q_{BEP}, Q_{BEP}, 1.25Q_{BEP}), rotational speeds (1800, 3500 rpm), and separator pressure (P_{sep}, 50, 100, 150 psig). The separator pressure is adjusted by a pre-rated release valve installed on the separator. The vertical axis N_p stands for the normalized pressure increment, which is defined as the ratio of stage pressure increment under gas-liquid flow to the maximum pressure increment under water flow. As shown, the pump stage pressure increment decreases with the intake GVF increase, even to zero head.

The stage pressure increment in ESP is improved at higher P_{sep} with pressure surging initiates at larger GVFs. As observed in Figure 2.9, the head curve slopes dramatically change at a certain GVF, before which the ESP stage pressure increment has mild deterioration. Figures 2.9(b), (d) and (f) present the surging test results for different stages under constant water flow conditions: N = 3500 rpm, Q_L = 2700 bpd. It shows that the upstream stages have an earlier surging initiation corresponding to lower GVFs. On the contrary, surging initiation at downstream stages is delayed to higher GVFs.

Figures 2.10 and 2.11 show the viscosities of tap water, IPA and IPA solutions with different concentrations. It can be seen in Figure 2.10 that the 99.999 vol% IPA is more viscous than tap water, which results in a higher viscosity of 0.41 vol% IPA solution compared to that of 0.2 vol% IPA, as shown in Figure 2.11.

Figures 2.12 and 2.13 show the surging test results at different stages with 0.2 vol% IPA and 0.41 vol% IPA in water, respectively. Similar to surging tests with tap water in Figure 2.9, various flow conditions are included in the experimental testing. As it can be seen, the surfactant injection improves ESP ability of handling gas significantly by postponing the surging initiation to higher GVFs (Figures 2.12a and b, Figures 2.13a and b). Compared to Figure 2.9, the measurement ranges of intake GVF in Figure 2.12 and 2.13 are broadened with surfactant injections.

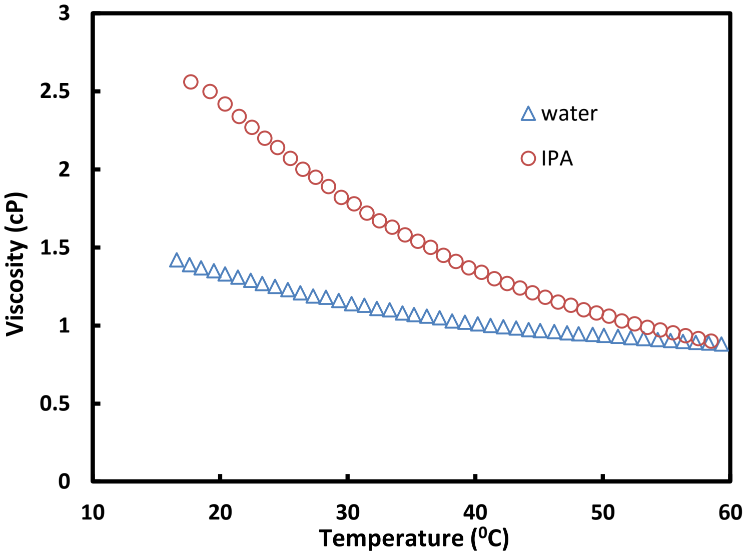

Figure 2.10 Viscosities of tap water and pure IPA versus temperature

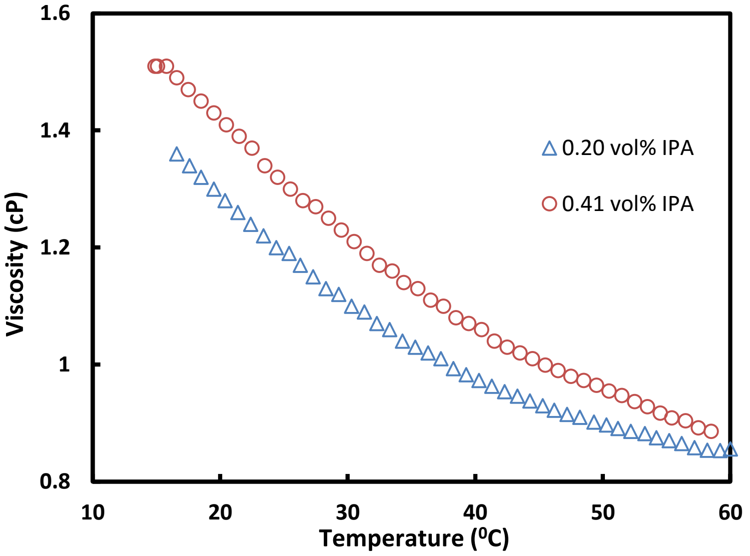

Figure 2.11 Viscosities of 0.20 vol% IPA and 0.41 vol% IPA versus temperature

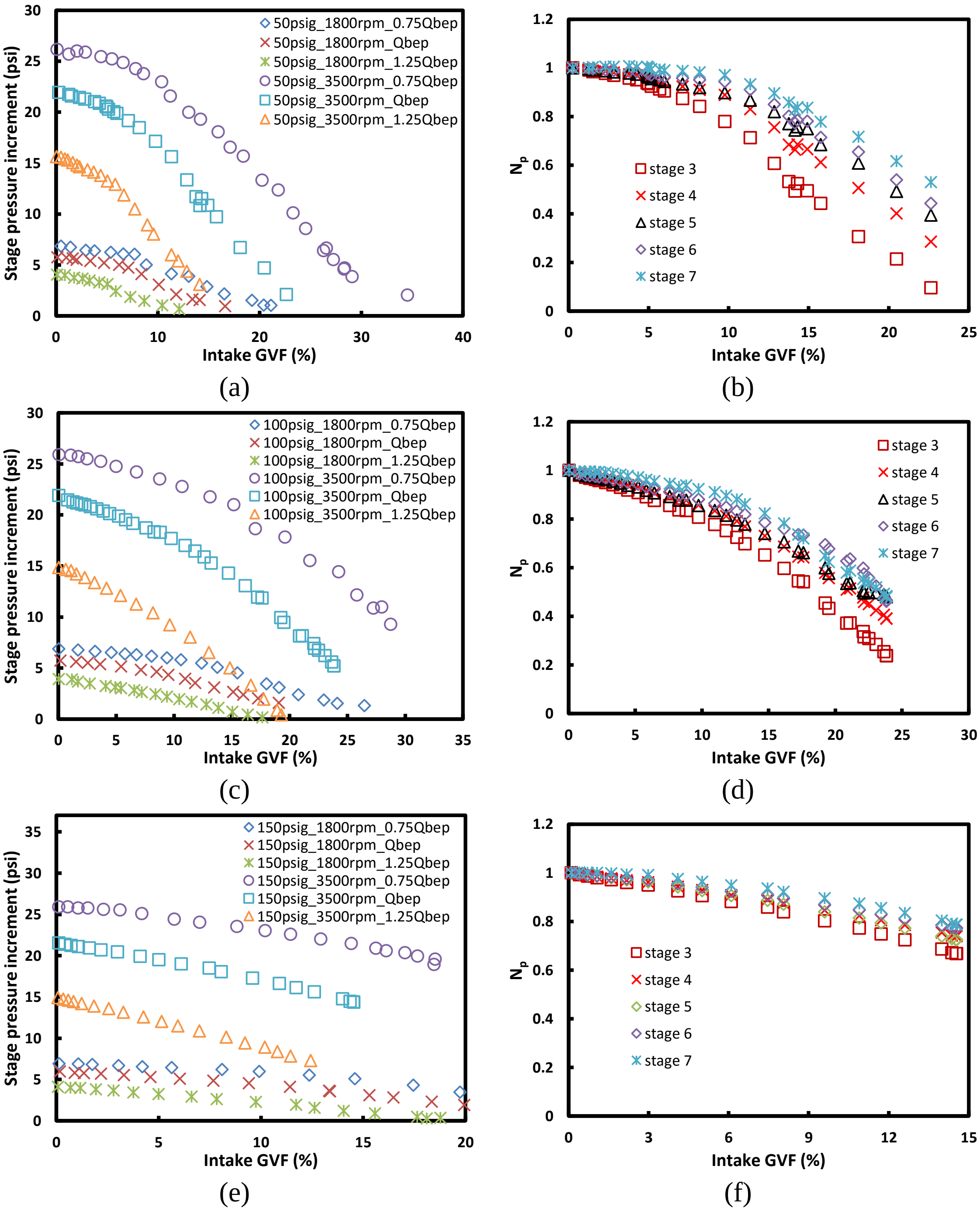

Figure 2.12 Surging tests with 0.20 vol% IPA water and air, (a) stage 3 at P_{sep} = 50 psig, (b) N = 3500 rpm, Q_{BEP} at P_{sep} = 50 psig, (c) stage 3 at P_{sep} = 100 psig, (d) N = 3500 rpm, Q_{BEP} at P_{sep} = 100 psig, (e) stage 3 at P_{sep} = 150 psig, (f) N = 3500 rpm, Q_{BEP} at P_{sep} = 150 psig

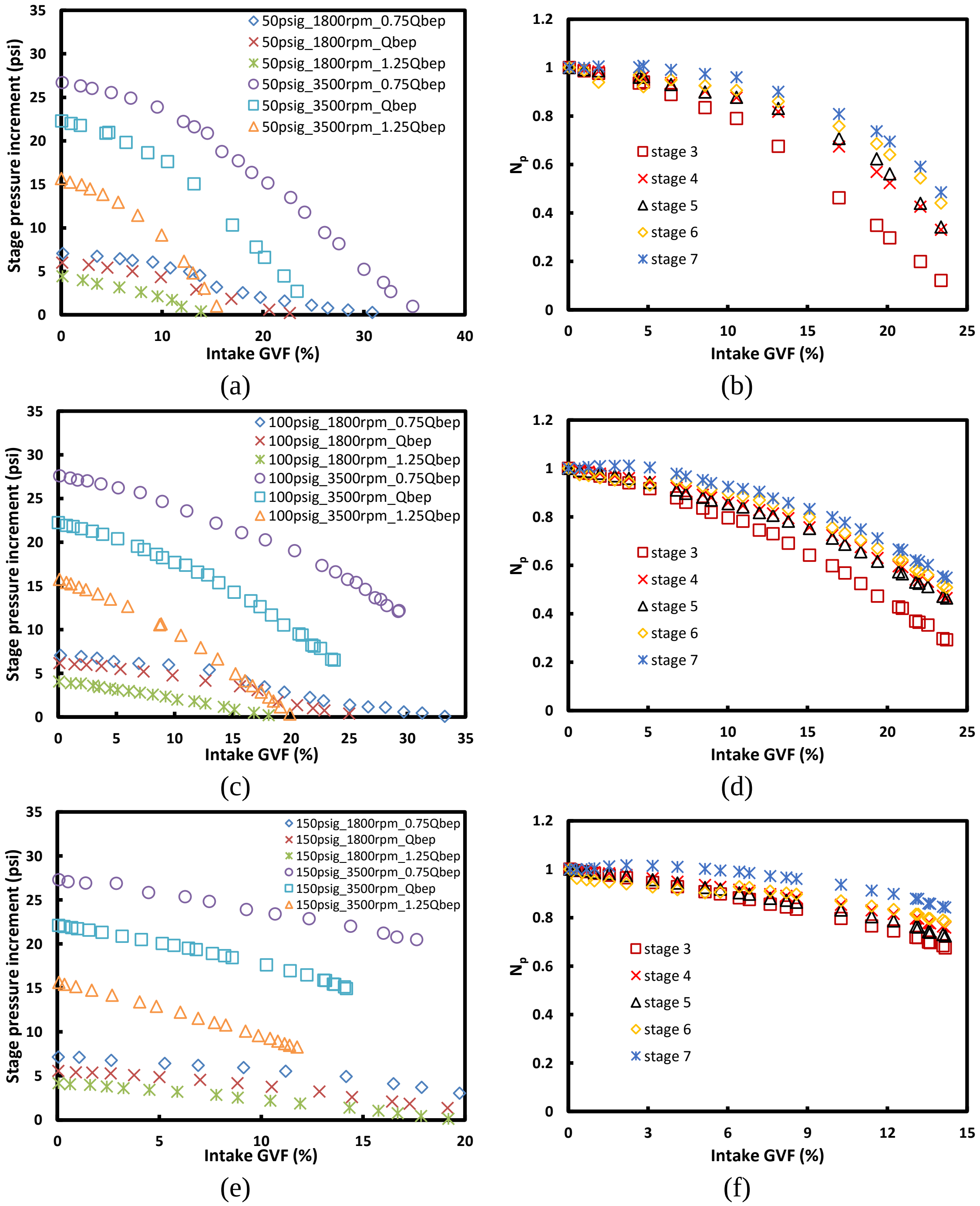

Figure 2.13 Surging tests with 0.41 vol% IPA water and air, (a) stage 3 at P_{sep} = 50 psig, (b) N = 3500 rpm, Q_{BEP} at P_{sep} = 50 psig, (c) stage 3 at P_{sep} = 100 psig, (d) N = 3500 rpm, Q_{BEP} at P_{sep} = 100 psig, (e) stage 3 at P_{sep} = 150 psig, (f) N = 3500 rpm, Q_{BEP} at P_{sep} = 150 psig

Within the experimental measurement range, the pressure surging disappears at relatively higher P_{sep} (Figures 2.12c~f; Figures 2.13c~f). The head curves decline less compared to that without surfactant injection (Figure 2.9c~f). The effects of stage number and P_{sep} also become more evident in gas-liquid flow with surfactant presence. As it can be seen in Figures 2.9(c), (e) and (f), the head curves for different stages are close to each other. In contrast, with surfactant presence, they are apart from each other especially when P_{sep} is low as shown in Figures 2.12(b), Figure 2.13(b).

Gamoba (2008) ascribed the delay of ESP pressure surging with addition of IPA to two main reasons. First, IPA reduces the surface tension between water and air. Second, which is more important, IPA alters the polarity of the bubble interface and promotes foam flow. In this study, it is shown by Figure 2.12 that the foam flow due to surfactant injection plays a dominant role in affecting ESP gas-handling ability since the reduction of surface tension with 0.2 vol% IPA is rather small (see Figure 2.6), and not sufficient to cause such improvement of ESP two-phase performance.

Due to pressure increase, the downstream stage gas density is higher. For the same mass flow rate of gas, the higher gas density leads to smaller gas bubbles and lower local GVF. Therefore, the pressure increment at downstream stages becomes higher.

2.3.3 Gas-liquid Performance Curves from Mapping Tests

Figures 2.14, 2.15 and 2.16 show the mapping test results with tap water, 0.2 vol% IPA solution, and 0.41 vol% IPA solution, respectively. The horizontal axis denotes Q_L, and the vertical axis is the stage pressure increment. Experimental results at two different rotational speeds (3500 and 1800 rpm) are presented. For N = 3500 rpm, five Q_{gd} are tested: 0.01, 0.02, 0.03, 0.04 and 0.05; for N = 1800 rpm, three Q_{gd} are tested: 0.005, 0.01, 0.015.

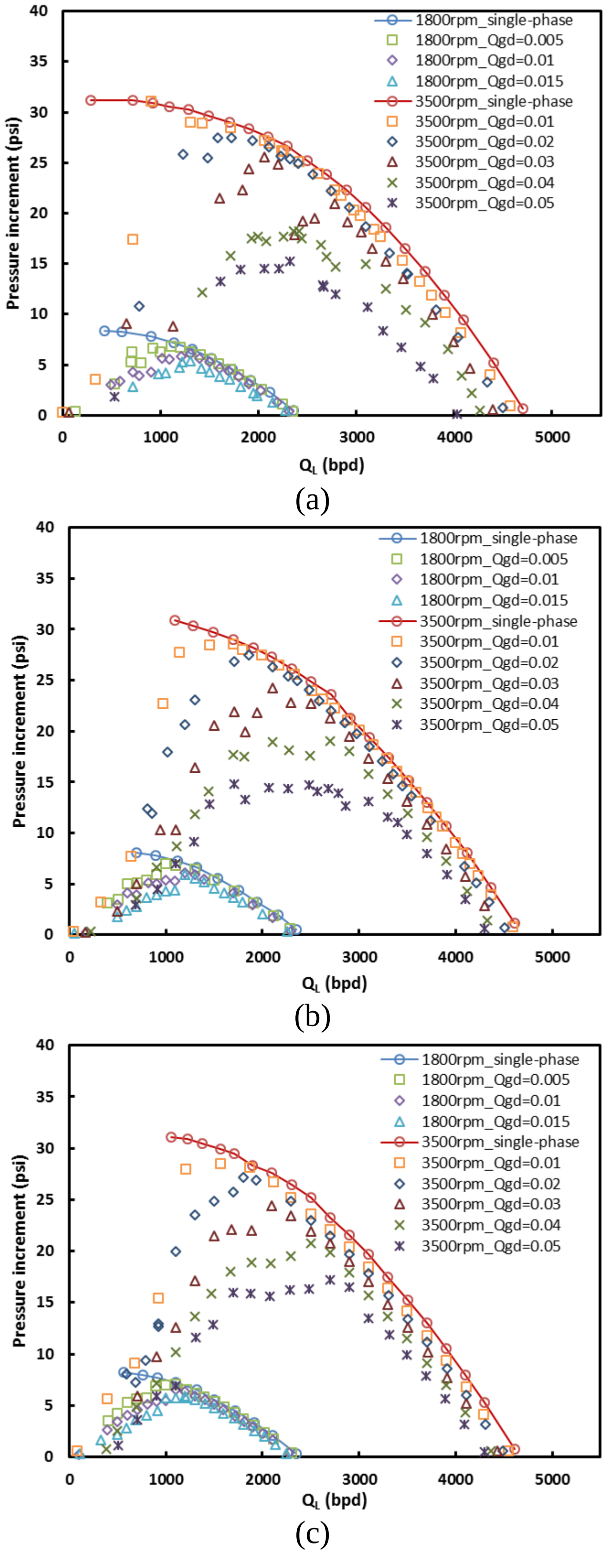

(a)

(b)

(c)

Figure 2.14 Mapping tests with tap water at stage 3, (a) P_{sep} = 50 psig, (b) P_{sep} = 100 psig, (c) P_{sep} = 150 psig

As can be seen in Figure 2.14, the mapping curves for water flow is affected by gas and liquid flow rates significantly. For small Q_{gd}, the H-Q curve is similar as water head curve. The boosting pressure increases as the liquid flow rate is reduced from the open flow rate to above 1000 bpd, at which the tests were stopped because the intake pressure was hard to control.

Compare $Q_{gd} = 0.01$ and 0.02 at $N = 3500$ rpm, $P_{sep} = 150$ psig, it is found that the gas-liquid stage pressure increment is consistent with the water head curve until a sudden drop at 1200 and 1900 bpd, respectively. At low liquid flow rates, the ESP performance of boosting pressure suffers from deteriorations more severely due to relatively higher intake GVFs. A higher Q_{gd} results in an earlier drop corresponding to a higher liquid flow rate. Similar observations can be seen from the results of $N = 1800$ rpm. P_{sep} also affects ESP boosting pressure under gas-liquid flow greatly. As P_{sep} increases, the ESP pressure increment drops at a lower Q_L. For instance, at $Q_{gd} = 0.01$ and $N = 3500$ rpm, the sudden drops occur at $Q_L = 1400$, 1300, 1200 bpd at $P_{sep} = 50$, 100, 150 psig, respectively.

For $Q_{gd} = 0.03$, 0.04, and 0.05, the breakdown of gas-liquid H-Q curves occurs at higher Q_L compared to that for $Q_{gd} = 0.01$. The pressure increment after performance breakdown approaches nil quickly with Q_L decrease, which is characterized by a steep decline slop on the H-Q curves. Gamboa (2008) concluded that the performance breakdown was due to flow pattern transition from dispersed bubble flow to bubbly flow. With a further reduction of Q_L, the intermittent flow pattern takes place, which corresponds to the second turning point in the H-Q curve. The pressure, temperature, flow rate fluctuates significantly for Q_{gd} above 0.015 at $N = 1800$ rpm, and above 0.05 at $N = 3500$ rpm. At higher P_{sep}, the pressure increment improves as can be seen in Figure 2.14(a) and (c).

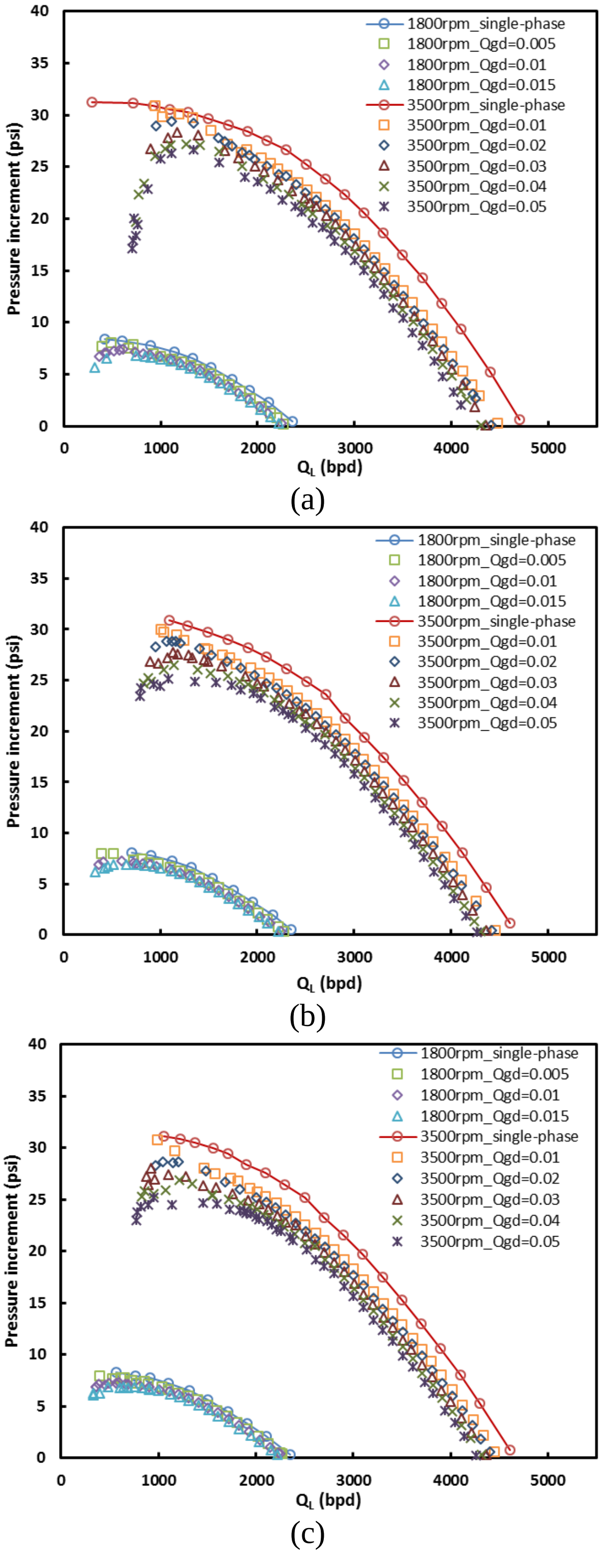

Figure 2.15 Mapping tests by 0.20 vol% IPA at stage 3, (a) P_{sep} = 50 psig, (b) P_{sep} = 100 psig, (c) P_{sep} = 150 psig

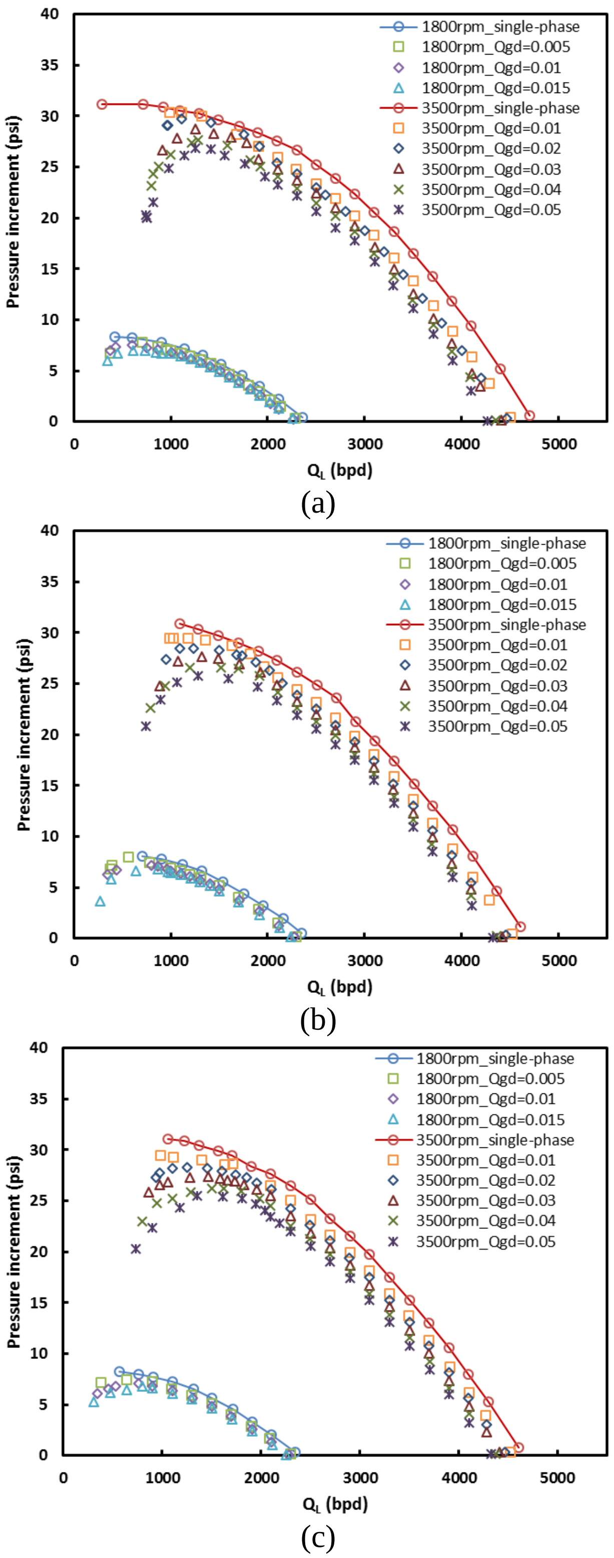

(a)

(b)

(c)

Figure 2.16 Mapping tests with 0.41 vol% IPA at stage 3, (a) P_{sep} = 50 psig, (b) P_{sep} = 100 psig, (c) P_{sep} = 150 psig

With the injection of surfactant, the two-phase *H*-*Q* curves exhibit a distinct behavior compared to that without surfactant presence. Figure 2.15 shows the mapping test results at stage 3 with 0.2 vol% IPA and different P_{sep}. As can be seen, the drops of two-phase *H*-*Q* curves are all close to Q_L = 1100 bpd at different P_{sep}. Meanwhile, the *H*-*Q* curves at different Q_{gd} are closer to the water curve, indicating significant improvements of ESP gas-handling ability. Comparing Figure 2.15 and 2.14, the injection of surfactant not only improves ESP stage pressure increment under gas-liquid flow but also stabilizes the ESP operations.

Figure 2.16 presents the mapping tests with a higher volumetric concentration of IPA (0.41 vol%). The improvement is similar as that of the 0.2 vol% IPA case. Thus, the improvement of ESP stage pressure increment under gas-liquid flow with surfactant injections may not be merely due to the reduction of surface tension. van Nimwegen et al. (2015) also pointed out that the reduction of the surface tension might not be sufficient to explain the flow behavior change with the addition of surfactants.

2.3.4 Comparison of Gas-liquid Tests

Figure 2.17 presents the effect of intake pressure on surging test results, where (a) and (b) show the head changes with GVF at *N* = 3500 and 1800 rpm. Figures 2.17(c) and (d) show the head changes with GVF for 0.2 vol% IPA solution at *N* = 3500 and 1800 rpm. As can be seen, a higher intake pressure leads to a better pump performance. The pressure surging also initiates at a higher intake GVF with the increase of P_{sep}. For no IPA flow at *N* = 3500 rpm (Figure 2.17a), pressure surging initiates at intake GVF = 4.7%, 5.9%, 7.5% for P_{sep} = 50, 100, 150 psig, respectively, while at *N* = 1800 rpm (Figure 2.17b), pressure surging initiates at GVF = 3.6%, 4.2% and 4.8%. With surfactant injection, pressure surging exhibits different behaviors (Figure 2.17c and d). At a given P_{sep}, N_p is a smooth function of intake GVF at N = 3500 rpm. At a given rotational speed, N_p at a higher P_{sep} decreases more linearly with the increase of intake GVF.

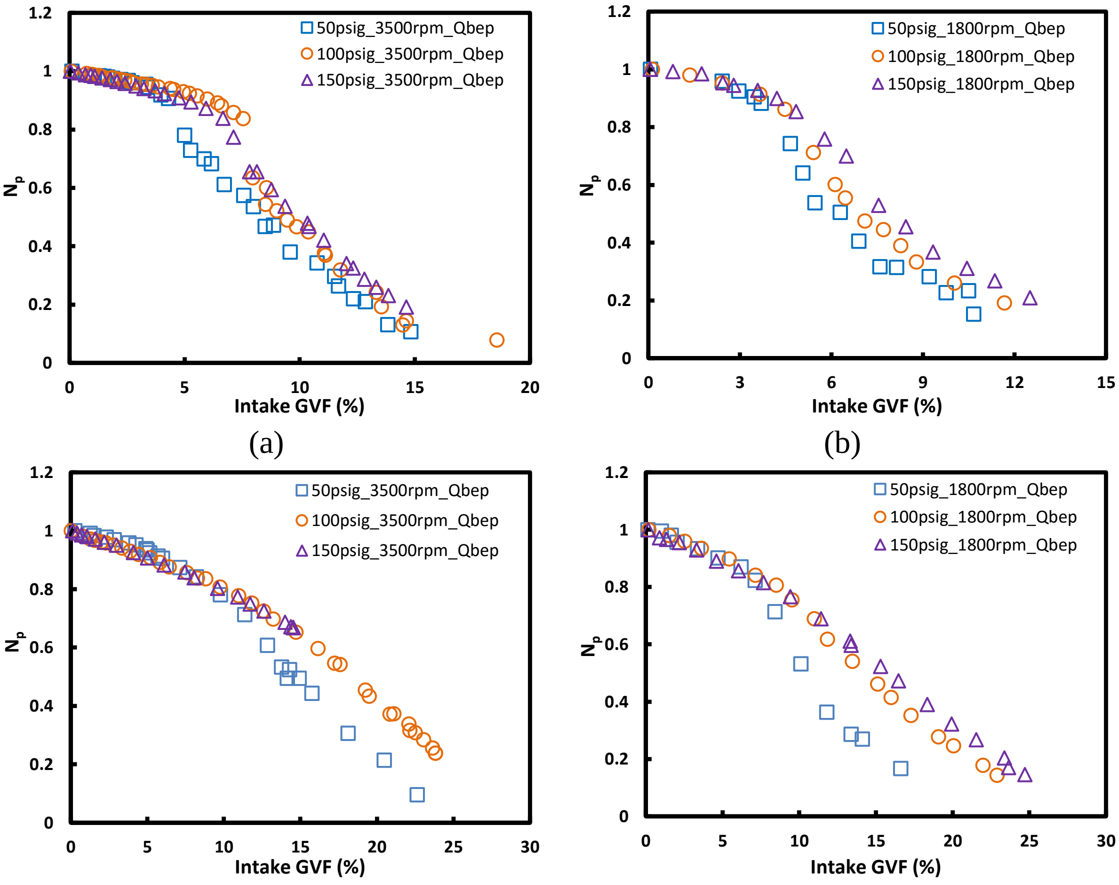

(a) (b)

(c) (d)

Figure 2.17 Effect of intake pressure on surging, (a) no IPA, N = 3500 rpm, (b) no IPA, N = 1800 rpm, (c) 0.2 vol% IPA, N = 3500 rpm, (d) 0.2 vol% IPA, N = 1800 rpm

The effect of surfactant concentrations on surging experimental results are shown in Figure 2.18, where (a) and (b) correspond to P_{sep} = 50, 150 psig at N = 3500 rpm, (c) and (d) correspond to P_{sep} = 50, 150 psig at N = 1800 rpm. Comparing Figure 2.18(a) and (b), it can be seen that the surfactant injection not only improves N_p, but also postpones the sudden drop of ESP two-phase performance to higher GVFs. Similar observations can also be found in Figures 2.18(c) and (d) corresponding to N = 1800 rpm.

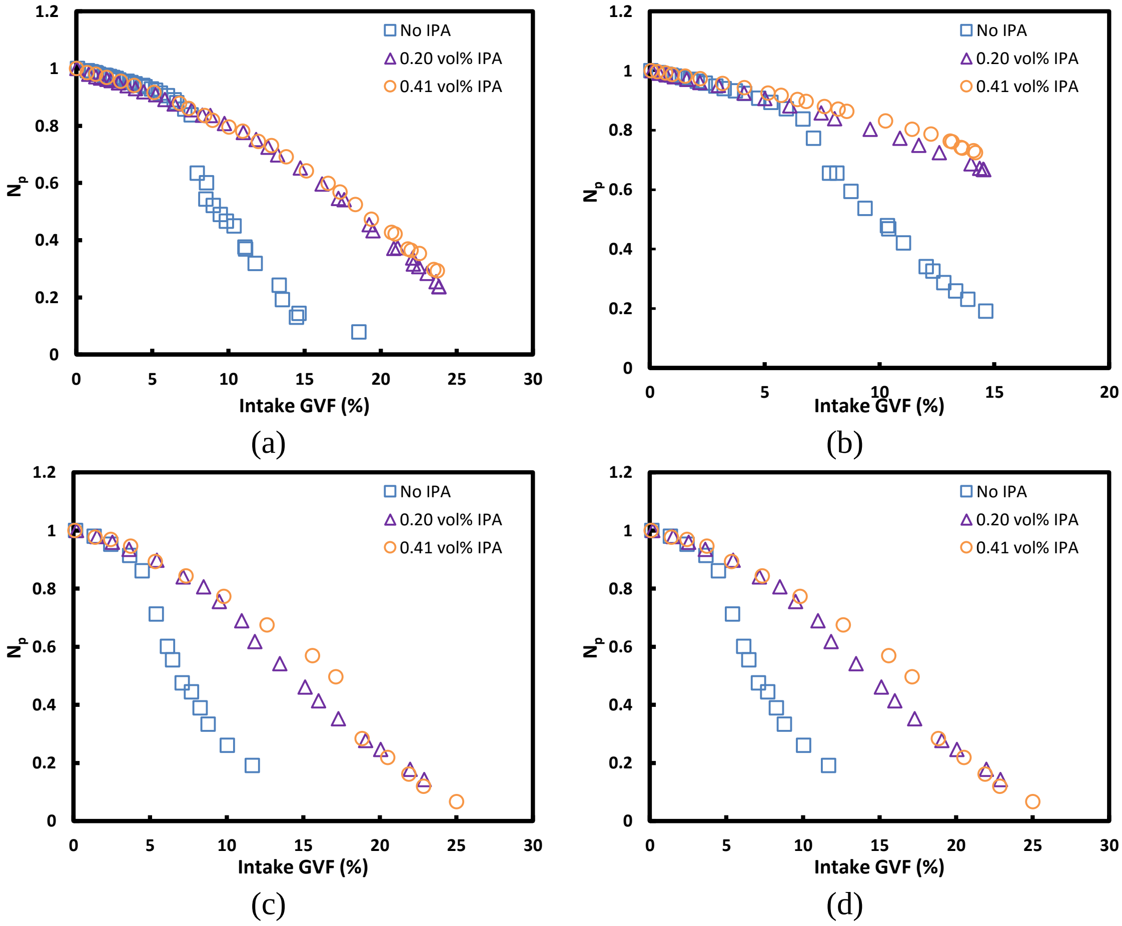

(a) (b) (c) (d)

Figure 2.18 Effect of surfactant concentration on surging, (a) P_{sep} = 100 psig, N = 3500 rpm, (b) P_{sep} = 150 psig, N = 3500 rpm, (c) P_{sep} = 100 psig, N = 1800 rpm, (d) P_{sep} = 150 psig, N = 1800 rpm

As Figure 2.19 shows, P_{sep} increase postpones the drop of gas-liquid *H*-*Q* curve to lower Q_L. At higher Q_L before the *H*-*Q* drop, the influence of P_{sep} on ESP stage pressure increment is small. As shown in Figures 2.19(c) and (d), the stage pressure increment with 0.2 vol% IPA is unaffected by the intake pressure.

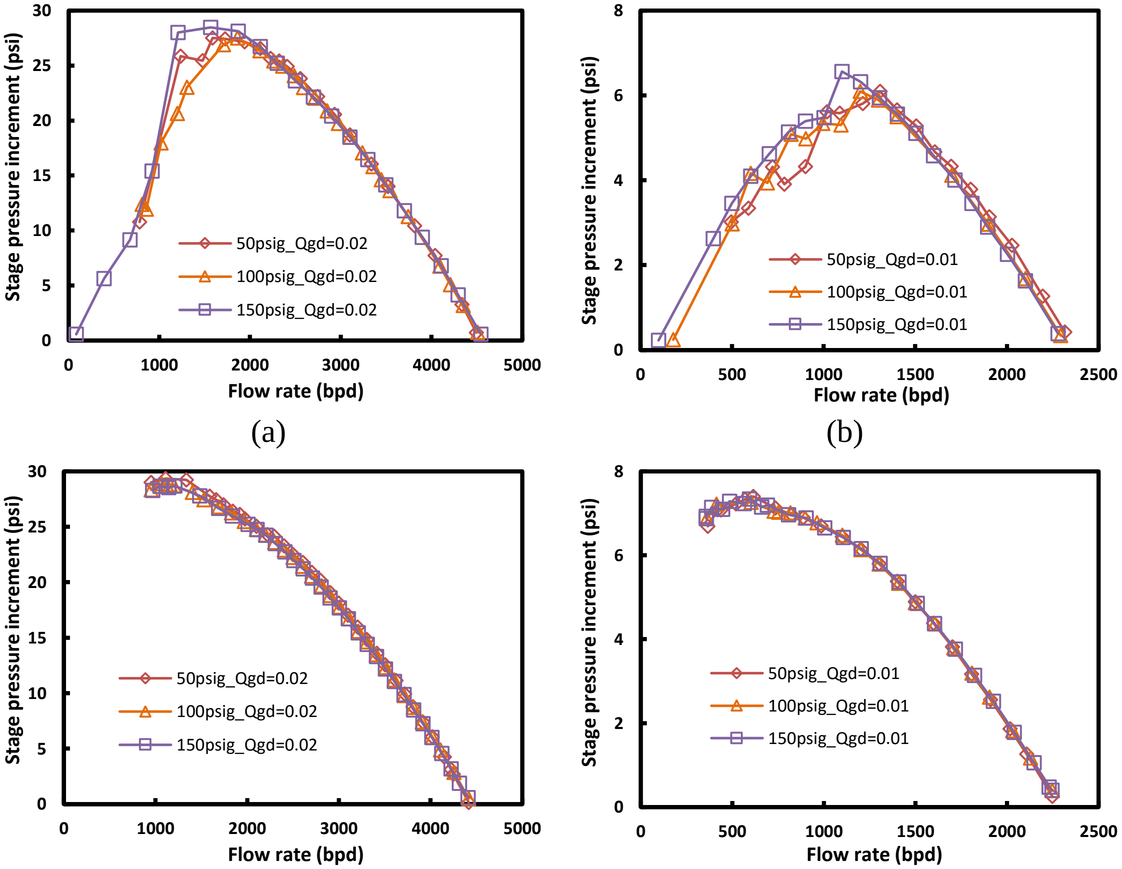

(a) (b)

(c) (d)

Figure 2.19 Effect of intake pressure on ESP performance, (a) water, N = 3500 rpm, (b) water, N = 1800 rpm, (c) 0.2 vol% IPA, N = 3500 rpm, (d) 0.2 vol% IPA, N = 1800 rpm

Figure 2.20 presents the effects of surfactant concentration on ESP mapping test results. Figures 2.20(a) and (b) correspond to P_{sep} = 50, 150 psig at N = 3500 rpm, while (c) and (d) correspond to P_{sep} = 50, 150 psig at N =1800 rpm. A clear difference can be seen at low Q_L in terms of the stage pressure increment between surfactant injection and no injection cases. Without IPA injection, the pressure increment drops to zero if liquid flow rate becomes very low. However, degradations improve significantly with surfactant presence.

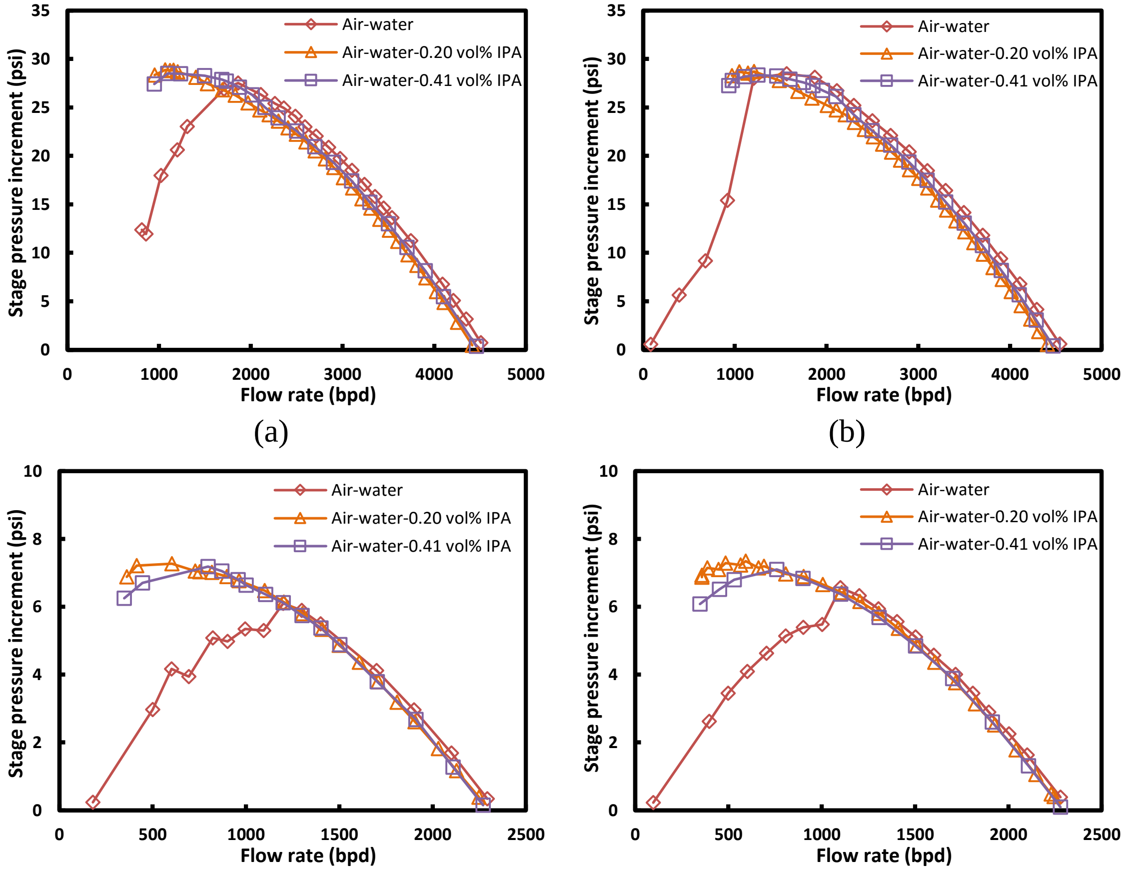

(a) (b)

(c) (d)

Figure 2.20 Effect of surfactant concentration on ESP performance, (a) P_{sep} = 100 psig, N = 3500 rpm, Q_{gd} = 0.02, (b) P_{sep} = 150 psig, N = 3500 rpm, Q_{gd} = 0.02, (c) P_{sep} = 100 psig, N = 1800 rpm, Q_{gd} = 0.01, (d) P_{sep} = 150 psig, N = 1800 rpm, Q_{gd} = 0.01

Within the measurement range, the ESP two-phase *H*-*Q* curves with different IPA concentrations are very close to each other. This verifies van Nimwegen et al. studies on the surfactant effects on gas-liquid two-phase flow characteristics. The dynamic surface tension, coupled with Marangoni flow effects, is more related to the formation and stability of foam (Rosen et al., 1991; Pugh, 1996), which reduces gas-liquid slippage (van Nimwegen et al., 2016) and changes the morphology of the gas-liquid interface (Khosla, 2012). Therefore, the ESP air-water two-phase flow behaviors are altered significantly with surfactant injection.

2.4 Experiment Summary

A thorough experimental investigation of TE-2700 ESP performance under both liquid and gas-liquid flows has been conducted. Effects on ESP boosting pressure with gas involvement are studied, including intake pressure, GVF, rotational speed, surfactant concentration. Two experimental schemes, namely surging test and mapping test, are carried out. Experimental results of ESP stage pressure increment under tap water flow match catalog head curves well, which validated the experimental setup used in this study.

For surging tests, experiments are repeated using three working fluids with different surfactant concentrations. As GVF increases, the stage pressure increment experiences mild degradation until a sudden drop of pump head, termed as pressure surging. Compared to no surfactant air-water flow, surfactant injection reduces pressure surging significantly.

In mapping tests, a clear breakdown on the gas-liquid H-Q curve is observed with liquid flow rate decrease. The surfactant presence improves the ESP two-phase boosting pressure by postponing the breakdown to lower Q_L.

The similar stage pressure increment at different surfactant concentrations indicate that the improvement of ESP performance is not only due to the surface tension reduction, but also a result of the formation of foam flow, which changes the morphology of the gas-liquid interface significantly.

CHAPTER 3

THREE-DIMENSIONAL CFD SIMULATION

In this study, the 3D numerical simulations are conducted for single-phase water or viscous oils, and air-water two-phase flows through a rotating ESP. The commercial software package ANSYS CFX 15 is used to perform the CFD simulations. The numerical configurations including computational domain, grids, mathematical models and boundary conditions are set in CFX-pre. The Navier-Stokes (N-S) equations are solved iteratively by CFX-solver until the convergence is achieved. Finally, the simulation results are presented in CFX-post, including fields of velocity and pressure, distributions of gas void fraction.

3.1 CFD Simulation of Viscous Fluid Flow

For 3D numerical simulations of viscosity effects on ESP boosting pressure, the steady-state Reynolds-Averaged-Navier-Stokes (RANS) equations with standard SST (shear stress transport) turbulence models are solved by employing the frozen-rotor technique. The simulated geometry includes 7 stages, exactly the same configuration used in Banjar (2013) experiments. Each stage comprises of a channelwise-sliced impeller and diffuser, on which the structured hexahedral grids are generated with Turbogrid 15.

3.1.1 DN-1750 ESP Geometry and Mesh

DN-1750 is a mixed-type ESP with N_S = 2900. There are 6 blades and 8 vanes in impeller and diffuser, respectively. The geometrical specifications are listed in Table 3.1. At the best efficiency point (BEP), the operation parameters are as follows: rotational speed N = 3500 rpm, mass flow rate Q = 3.3 *kg/s* (1795 bpd), hydraulic head H = 5.7 *m* (8.11 psi), and efficiency η = 68.5 %.

Table 3.1: Geometrical specifications of DN-1750 ESP

Component	**Description**	**Parameter**	**Values**
Impeller	Blade number	Z_i	6
	Tangential blade angle at inlet (deg)	β_1	19.9
	Tangential blade angle at outlet (deg)	β_2	35.6
	Blade thickness (mm)	b_i	39
	Channel length (mm)	l_i	1.7
	Inlet channel height (mm)	h_1	20.3
	Outlet channel height (mm)	h_2	36.2
	Inner radius (mm)	r_1	13.5
	Outer radius (mm)	r_2	7.1
Diffuser	Vane number	Z_d	8
	Channel length (mm)	l_d	51.9
	Partition wall thickness (mm)	b_d	3.1

Figure 3.1 displays the DN-1750 ESP 3D model, including impeller blades (Figure 3.1a), diffuser vanes (Figure 3.1b), and the entire single-stage assembly (Figure 3.1c). Since the flow fields inside centrifugal pump are axisymmetric (Zhu and Zhang, 2014), a single channel is used to save computational cost (Caridad et al., 2008). Thus, the computational domains of impeller and diffuser can be streamwisely sliced into 1/6 and 1/8 as shown in Figure 3.2(b) and (c). Similar configurations were numerically implemented on a three stage radial-type ESP to study pump two-phase performance under gas-liquid flow conditions (Zhu and Zhang, 2014 and 2017). In this study, the ESP flow domain comprises of 7 stages which are assembled in series (see Figure 3.2a). The single-stage pressure increment is obtained by calculating the pressure difference between the inlet and outlet of stage 3, while the simulated overall boosting pressure of the ESP is

obtained by subtracting total pressure at the inlet of stage 1 from total pressure at the outlet of stage 7.

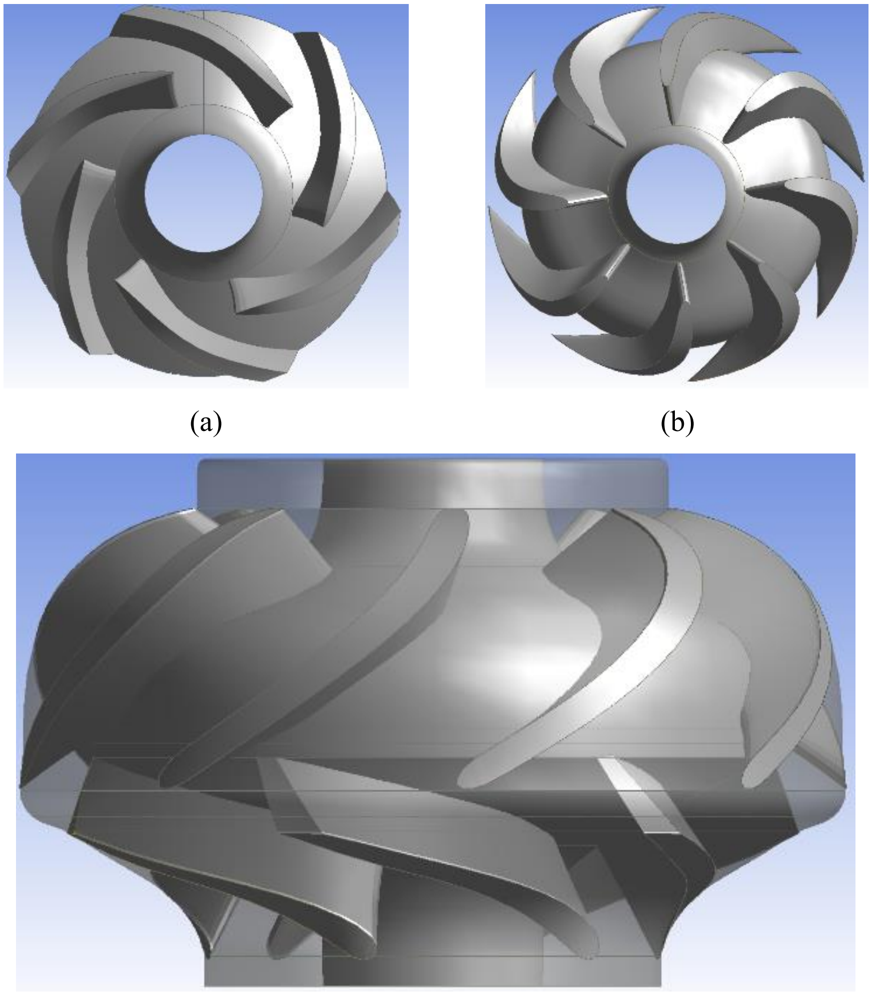
(a) (b)

(c)

Figure 3.1 Geometries of a single stage DN-1750, (a) impeller blades, (b) diffuser partitions, (c) entire 3D assembly

Due to complex pump geometry, the generation of 3D unstructured mesh of tetrahedrons is easier compared to structured mesh comprising of hexahedrons. It is a trade-off when selecting the proper mesh type to conduct CFD simulations. The unstructured mesh mostly composed of non-orthogonal grids jeopardizes the regularity of data structure, which in turn compromises algorithmic accuracy and reliability. Therefore, the high-quality structured mesh generated with ANSYS Turbogrid 15 is adopted in this study. The structured hexahedral grids for simplified multistage geometry are shown in Figure 3.2, including a single flow passage of impeller (Figure 3.2b) and diffuser (Figure 3.2c). Each domain is meshed with hexahedrons with the refinement near blade surfaces. The frozen-rotor technique is used to calculate interactions between impeller and diffuser within each stage. Impeller domains are set on a rotating frame of reference, and diffuser domains are set on a stationary one. This approach is categorized as steady state simulation, which does not account for instantaneous effects in the flow field such as pump start up.

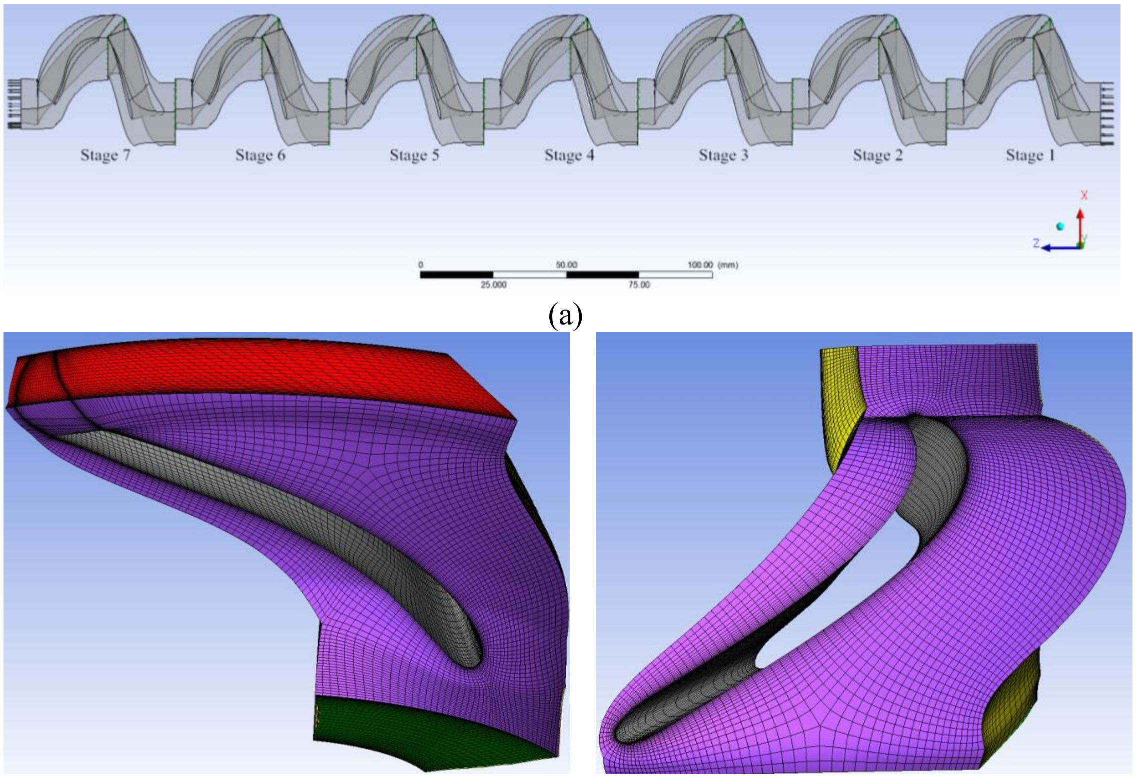

(a)

(b) (c)

Figure 3.2 Grid generation, (a) entire seven-stage assembly, (b) impeller channel mesh, (c) diffuser channel mesh

3.1.2 Governing Equations and Turbulence Model

In CFD simulation, a set of conservation equations are solved based on the continuous medium assumption, a fundamental hypothesis that treats fluid medium and motion infinitely differentiable in both time and space domains. In this study, the isothermal condition is applied to the fluid flow domain. Therefore, the conservation equation of energy can be omitted. The mass conservation equation is given by:

$$\frac{\partial \rho}{\partial t} + \nabla \cdot \left(\rho \vec{u} \right) = 0 , \tag{3.1}$$

where ρ, $\vec{u}$ are the liquid density and velocity vector. The sink/source in mass conservation equation is not taken into account in this study. The momentum conservation equation, known as N-S equation, is written as:

$$\frac{\partial \left(\rho \vec{u} \right)}{\partial t} + \nabla \cdot \left(\rho \vec{u} \vec{u} \right) = -\nabla P + \nabla \cdot \left(\bar{\bar{\tau}} \right) + \rho \vec{g} + S , \tag{3.2}$$

where $\bar{\bar{\tau}}$ is the stress-strain tensor given in Eq. (3.3), $\vec{g}$ is the gravity acceleration vector, S is external forces. For fluid flow in centrifugal pump, $S = S_{Cor} + S_{cfg}$. S_{Cor} and S_{cfg} represent the Coriolis force and centrifugal force effects. In stationary reference frame, $S_{Cor} = S_{cfg} = 0$. In a reference frame rotating with constant angular velocity (Ω), $S_{Cor} = -2\rho\vec{\Omega} \times \vec{V}$ and $S_{cfg} = -\rho\vec{\Omega} \times \left(\vec{\Omega} \times \vec{r} \right)$, where $\vec{\Omega}$ and $\vec{r}$ are angular velocity vector and position vector, respectively.

$$\bar{\bar{\tau}} = \mu \left(\nabla \vec{u} + \left(\nabla \vec{u} \right)^T \right) + \left(\lambda - \frac{2}{3} \mu \right) \nabla \cdot \vec{u} \bar{\bar{I}} . \tag{3.3}$$

Equation (3.3) describes the shear stress tensor for Newtonian fluids. In this study, the working fluid is mineral oil, which is a Newtonian fluid. μ is fluid viscosity, λ is a second coefficient of viscosity, $\bar{\bar{I}}$ is the identity matrix. For turbulent flow, the instantaneous fluid velocity $\vec{u}$ can be decoupled as:

$$\vec{u} = \bar{u} + u' \tag{3.4}$$

where $\bar{u}$ and u' are time-averaged velocity and time-varying velocity fluctuation. Substituting Eq. (3.4) into Eqs. (3.1) and (3.2) and rewriting them with indicial notation manner, one can obtain the so-called Reynolds-averaged Navier-Stokes (RANS) equations as

$$\frac{\partial \rho}{\partial t} + \frac{\partial}{\partial x_i}\left(\rho \overline{u_i}\right) = 0\,, \tag{3.5}$$

and

$$\frac{\partial\left(\rho \overline{u_i}\right)}{\partial t} + \frac{\partial}{\partial x_j}\left(\rho \overline{u_i}\,\overline{u_j}\right) = -\frac{\partial P}{\partial x_i} + \frac{\partial}{\partial x_j}\left(\bar{\bar{\tau}}_{ij} - \rho \overline{u_i' u_j'}\right) + \rho g_i + S_i\,. \tag{3.6}$$

Compared with Eq. (3.2), there is one additional term $-\rho\overline{u_i'u_j'}$ added to the momentum conservation equation, which is known as Reynolds stress tensor. Reynolds stresses reflect the instantaneous convective transport due to turbulent velocity fluctuations which act to enhance mixing additional to that caused by thermal interactions at the molecular level. Several turbulence models are available in literature to model Reynolds stresses, including standard *k-ε* (Launder and Spalding, 1974), RNG (renormalization group) *k-ε* (Yakhot et al., 1992), standard *k-ω* (Wilcox, 1998), BSL (baseline) *k-ω* (Menter, 1994) and SST *k-ω* (Menter, 1994), among others. As recommended by ANSYS (2015), the SST *k-ω* two-equation turbulence model is applied here due to its ability of handling separation flow and resolving flow very close to walls. The Reynolds stress term $-\rho\overline{u_i'u_j'}$ is related to the mean velocity gradients based on the Boussinesq hypothesis,

$$-\rho \overline{u_i' u_j'} = \mu_t\left(\frac{\partial u_i}{\partial x_j} + \frac{\partial u_j}{\partial x_i}\right) - \frac{2}{3}\delta_{ij}\left(\rho k + \mu_t \frac{\partial u_k}{\partial x_k}\right), \tag{3.7}$$

where μ_t is eddy viscosity or turbulent viscosity, which needs to be modeled further as function of k (turbulence kinetic energy) and ε (turbulence dissipation rate) or k and ω (specific dissipation rate). In this study, the SST turbulence model based on standard two-equation k-ω model is used since it incorporates the modifications for low Reynolds number effects, compressibility, and shear flow spreading. Meanwhile, it also accounts for the transport of the turbulent shear stress and gives highly accurate predictions of the onset and the amount of flow separation under adverse pressure gradients (ANSYS, 2015). Thus, the turbulent viscosity μ_t can be modeled as

$$\mu_t = \alpha^* \frac{\rho k}{\omega}. \tag{3.8}$$

Here, α^* is an empirical coefficient to account for low Reynolds number effect, while it should be equal to unity in high Reynolds number flow. To solve Eq. (3.8) and compute μ_t, two additional transport equations for turbulence kinetic energy k, and the specific dissipation rate ω, are presented as

$$\frac{\partial(\rho k)}{\partial t} + \frac{\partial}{\partial x_j}\left(\rho k \overline{u_j}\right) = \frac{\partial}{\partial x_j}\left(\left(\mu + \frac{\mu_t}{\sigma_t}\right)\frac{\partial k}{\partial x_j}\right) + G_k - Y_k + S_k \tag{3.9}$$

and

$$\frac{\partial(\rho \omega)}{\partial t} + \frac{\partial}{\partial x_j}\left(\rho \omega \overline{u_j}\right) = \frac{\partial}{\partial x_j}\left(\left(\mu + \frac{\mu_t}{\sigma_\omega}\right)\frac{\partial \omega}{\partial x_j}\right) + G_\omega - Y_\omega + D_\omega + S_\omega, \tag{3.10}$$

where σ_t and σ_ω are turbulent Prandtl numbers for k and ω, respectively. G_k and G_ω are turbulence production terms. Y_k and Y_ω represent turbulence dissipation terms. D_ω represents the cross-diffusion term. S_k and S_ω are user defined source terms. Eqs. (5) ~ (10) constitutes the general form of SST k-ω turbulence model. More details regarding empirical correlations and coefficients in SST model can be found in ANSYS CFX-solver Theory Guide (2015).

3.1.3 Numerical Schemes and Boundary Conditions

Two types of interfaces are used in CFD simulation. First, the general connection interface model is employed in each pair of impeller and diffuser interfaces, which is able to apply a frame change and connect non-matching grids. Totally, 13 pairs of general connection interfaces are generated. 7 of them are within stages, and the remaining 6 pairs are located at inter-stages. Second, periodic interfaces based on circumferential periodicity are set within each domain of impeller or diffuser, resulting in 14 pairs of periodic interfaces.

The frozen-rotor algorithm is used to simulate interactions across the interfaces of impellers and diffusers. This model treats each component of computational domain with an individual frame of reference, while it keeps the relative orientation of these components across the interface fixed. It requires the least amount of computational effort compared to other interface models. However, the frozen-rotor model is unable to capture transient effects at the frame change interface due to its steady state nature. In our simulation, the axisymmetric property of ESP geometries is used by assuming periodic flow characteristics if pump working condition is stable. The streamwise-designed blades and vanes inside ESP provide additional compensation that further weakens interactions across impeller-diffuser interfaces. Thus, the frozen-rotor algorithm is used as it offers an acceptable compromise between computational effort and numerical efficiency.

Due to the simplified geometries of impeller and diffuser, the grids at interface are non-conformal and mismatching with different pitch angles. In consideration of this, the GGI (general grid interface) mesh connections are employed, which permit non-matching of grids on either side of the two connected surfaces (ANSYS, 2015).

Boundary conditions are specified according to the corresponding experimental configurations from ESP inlet to outlet. For wetted walls, the no-slip velocity condition is imposed. As pointed out by Li (2014), the wall roughness is estimated by equivalent sand-grain roughness h_S. The dimensionless number h_S^+ is defined as

$$h_S^+ = h_S \frac{\sqrt{\tau_W / \rho}}{\nu}. \tag{3.11}$$

The range $h_S^+ \leq 5$ corresponds to hydraulically smooth regime, $5 < h_S^+ \leq 70$ corresponds to transition regime, and $h_S^+ > 70$ for hydraulically rough regime. The standard wall function holds only within hydraulically smooth regime. Thus, special attention needs to be paid to near wall treatment in turbulence model with low-*Re* flow and rough walls. In this study, the near-wall treatment is automatic wall functions for omega-based turbulence models. It automatically switches from standard wall-functions to a low-*Re* near wall formulation as the mesh is refined. We apply a simple correlation of h_S with arithmetic average of absolute values of real roughness Ra by h_S = 6 Ra (Li, 2014). For a cast wall, Ra = 12.5 ~ 50 μm. Using Ra = 50 μm, one can obtain h_S = 300 μm, which is close to 250 μm, a sand equivalent roughness of the natural surface of cast iron recommended by Patankar et al. (1972).

The total pressure with zero gradient flow direction and turbulence intensity is set at 1st stage inlet. A mass flowrate scaling down to 1/8 of inner cross-sectional area is imposed at 7th stage outlet. This is a more robust configuration of boundary conditions for numerical convergence as recommended in ANSYS (2015), especially for part-load CFD simulation (Stel et al., 2015).

All simulation cases are conducted with the same numerical schemes. For discretization of advection terms and turbulence equations in space, the high resolution scheme is used, which is a second order algorithm in ANSYS CFX-solver. For steady-state simulation, a false time step as a means of under-relaxing governing equations is applied, which requires a relatively large time scale due to robust and fully implicit CFX-solver. A fixed physical timescale of $1/(2\Omega)$ is used with maximum 500 outer loop iterations to achieve convergence. The convergence criterion is satisfied if RMS (root mean square) residual drops below 10^{-4}.

3.1.4 Results and Discussions

In this part, the numerically simulated ESP boosting pressures are presented and compared with experiment results under different flow conditions. At first, CFD simulations is compared with experimental results for water flow to validate numerical methodology. Then, experimental conditions of viscous oil flows are incorporated into numerical simulations as inputs. The outputs from CFD-post include pump pressure increment, streamline, pressure and velocity fields etc. Four rotational speeds and four oil viscosities are used to conduct experiments and numerical simulations, namely, 3500, 3000, 2500, 2000 rpm and 56, 98, 180, 220 cP.

3.1.4.1 Mesh Independence check and Turbulence Model Validation. The mesh quality depends on the dimensionless distance (y^+) at the first grid point near the wall. According to boundary layer theory, the viscous sublayer exists in the near-wall region. Within viscous sublayer, the dimensionless velocity (u^+) is a logarithmic function of y^+ away from the wall. This is also referred to as standard wall-function, which holds for $y^+ < 100$. Thus, the first grid layer should be sufficiently fine to meet wall function requirement.

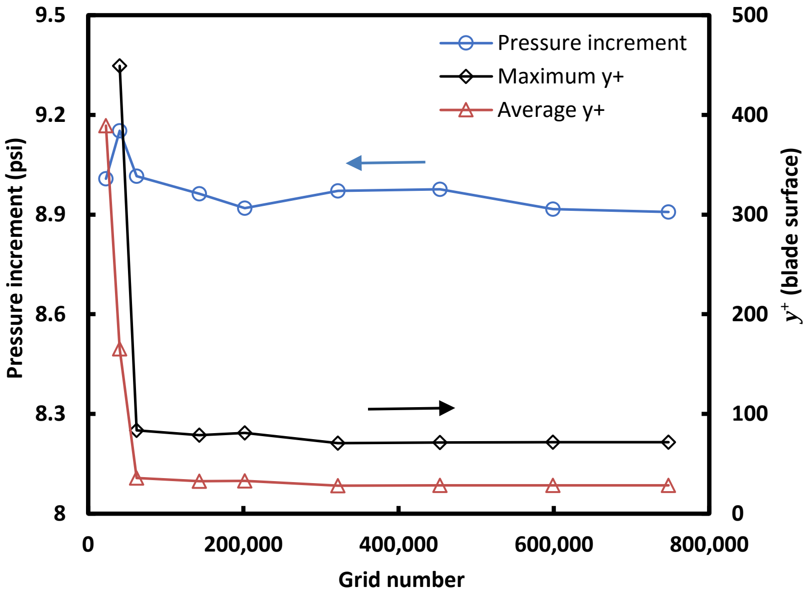

Figure 3.3 Mesh validation and wall function check for single-phase CFD simulation on DN-1750 ESP

The mesh number is counted on single-stage simplified fluid domains of impeller and diffuser. As shown in Figure 3.3, the simulated stage pressure increment becomes constant when the grid number reaches about 0.2 million, where the average value of y^+ on blade surface is below 30. Therefore, the grids used for simplified impeller and diffuser sections consist of 158,976 and 124,296 elements, respectively. Total grids for the complete seven-stage computational domain contain 1,982,904 elements, which are sufficient to guarantee grid independence.

Figure 3.4 shows the effect of turbulence models on simulated stage pressure increment and comparison with corresponding experimental results under water flow. The selection of turbulence model is a delicate task for CFD simulation, which is also a compromise of computational effort and numerical accuracy. As it can be seen in Figure 5, there is no prominent variance among different turbulence model predictions. However, the aforementioned SST turbulence model is used due to its advantages in capturing shear flow spreading and separation at low Reynolds number flow.

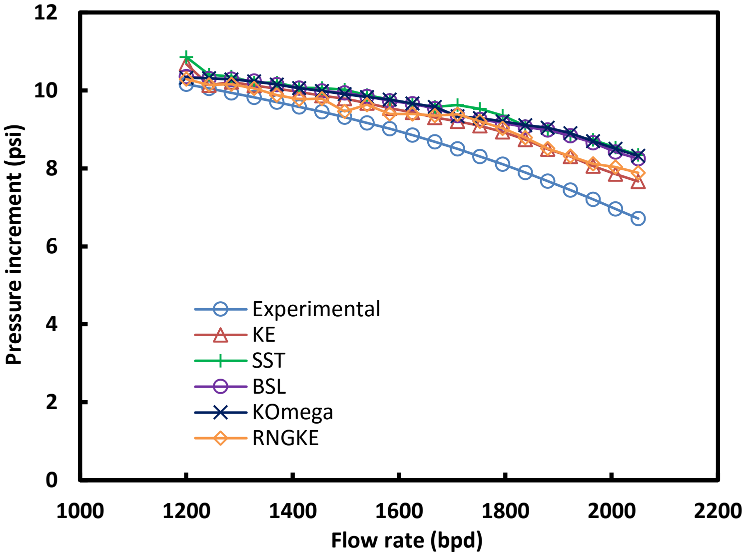

Figure 3.4 Influence of turbulence models on single-phase CFD simulation of DN-1750 ESP under water flow

3.1.4.2 Comparison with Catalog Curves. For comparison of simulated ESP boosting pressure with experimental data, the dimensionless variables: flow coefficient, head coefficient, and hydraulic efficiency are defined by Eqs. (3.12) ~ (3.14):

Flow coefficient:

$$\varphi = \frac{Q}{\Omega D_i^3} . \tag{3.12}$$

Head coefficient:

$$\psi = \frac{gH}{\Omega^2 D_i^2} . \tag{3.13}$$

Hydraulic coefficient:

$$\eta = \frac{Q\Delta P}{T\Omega} . \tag{3.14}$$

where T is shaft torque, and Ω is ESP rotational speed.

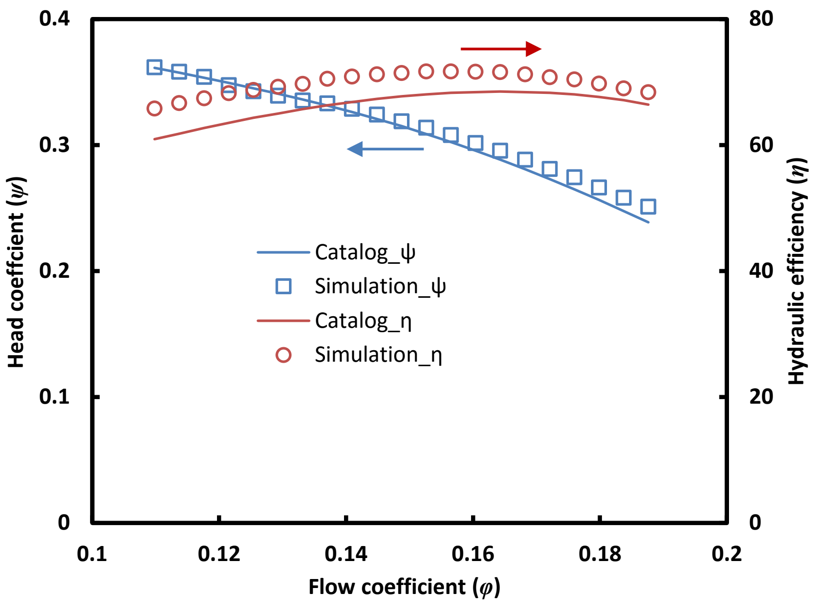

Figure 3.5 Comparison of numerical results with catalog curves
for DN-1750 ESP

Figure 3.5 above shows the comparisons of single-phase simulation results of head coefficient (*ψ*), pump efficiency (*η*) as function of flow coefficients (*φ*) with the catalog curves within the pump operation range. A good agreement can be seen for *ψ* versus *φ*. However, the simulation results for *η* are slightly higher than the catalog curve, indicating that CFD simulation over predicts ESP single-phase efficiency. This may be due to the neglect of leakage flow through the radial clearance between impeller and diffuser, which causes additional boosting pressure loss in reality. Meanwhile, the smooth wall assumption also contributes to the deviation by underestimating wall shear stresses.

3.1.4.3 Comparison with Experimental Data. Figure 3.6 shows the comparison between experimental results and numerical simulations for ESP overall pressure increment over 7 stages. The experimental tests were conducted by Banjar (2013) and Zhu et al. (2016). The measurements were taken with the differential pressure transducer spanning from the inlet of the 1st impeller to the outlet of the 7th diffuser. The corresponding numerically simulated pressure increment is calculated as

$$\Delta P = P_{stat,2} - P_{stat,1} + \frac{1}{2}\rho\left(\vec{C}_2^2 - \vec{C}_1^2\right). \tag{3.15}$$

where P_{stat} is static pressure, $\vec{C}$ is absolute velocity given by $\vec{C} = \vec{W} + \vec{U}$ according to velocity triangle. $\vec{W}$ and $\vec{U}$ are relative and peripheral velocities, respectively. Subscripts 1, 2 are for inlet and outlet.

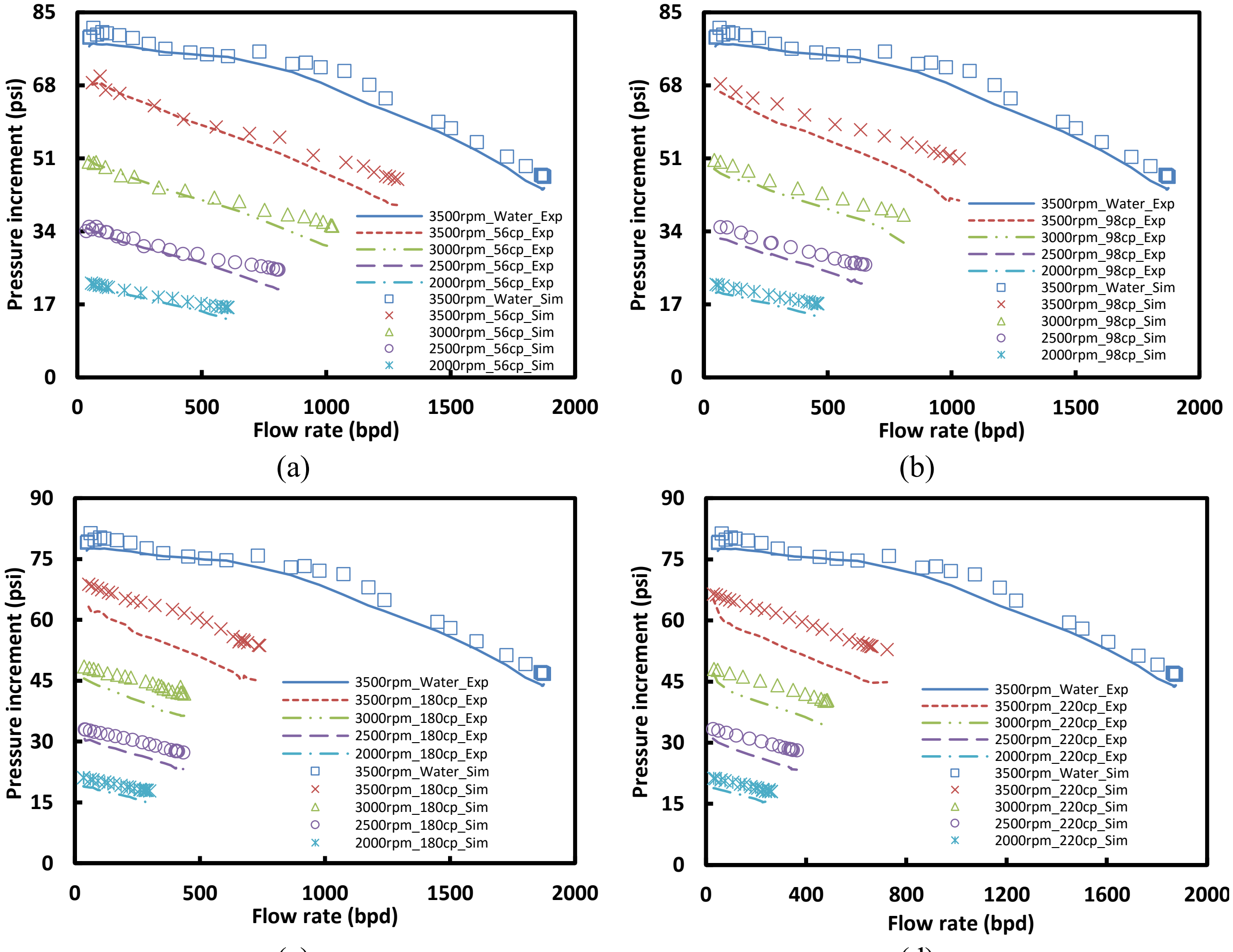

(a) (b)

(c) (d)

Figure 3.6 Comparison of CFD simulated overall performance of DN-1750 ESP with experimental results for different liquid viscosities, (a) 56 cP, (b) 98 cP, (c) 180 cP, (d) 220 cP

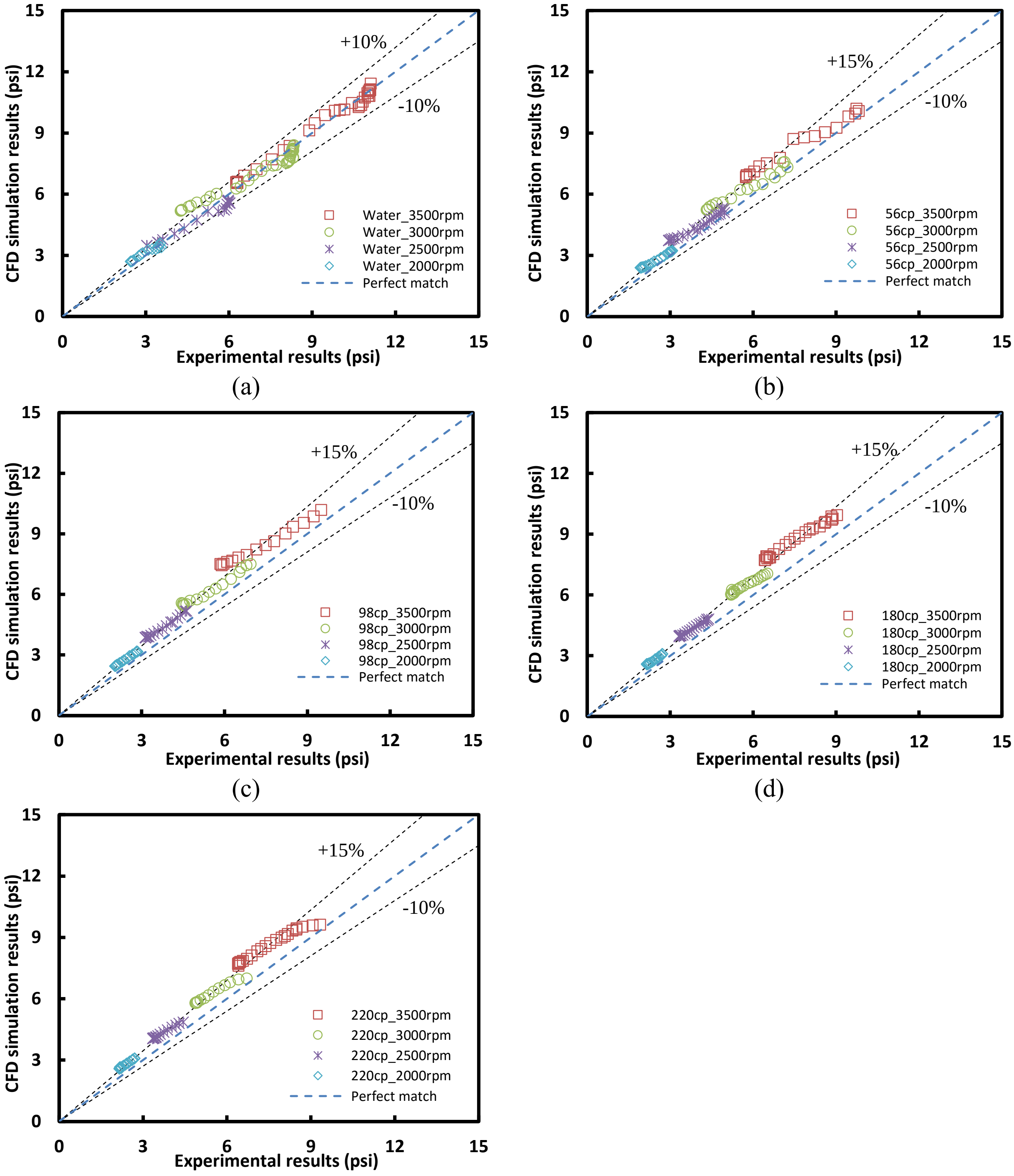

(a)

(b)

(c)

(d)

(e)

Figure 3.7 Comparison of CFD simulated ESP performances at stage 3 of DN-1750 ESP with experimental results for different liquid viscosities, (a) water, (b) 56 cP, (c) 98 cP, (d) 180 cP, (e) 220 cP

In Figure 3.6, the solid curves are experimental measurements of ESP overall pressure increment, while the symbols are CFD simulation results. A good agreement can be found in the comparison for water case. However, numerical simulation over predicts ESP boosting pressure of viscous oils with an error about 15%. With viscosity increase, the pressure increment decreases. At higher viscosity and lower flow rate, the trend becomes more linear, indicating that the flow regime changes from turbulent flow to laminar flow.

Figure 3.7 illustrates another comparison of CFD simulated ESP performance of stage 3 with corresponding experimental results for different liquid viscosities. The horizontal and vertical coordinates stand for the experimental and CFD simulation results of stage pressure increment, respectively. As can be seen, the numerical simulation predicts ESP single-stage pressure increment with an error below 15% compared with experimental results. The deviation may be partially due to pump rusty and worn conditions after years of experimental tests.

3.1.4.4 Analysis of Flow and Pressure Fields. Figure 3.8 shows the streamline plots under different flow conditions in the 3rd stage. The recirculation flow that contributes to the pump hydraulic loss is observed near the trailing edges of impeller blades. Two hydraulic factors affect the recirculation flow from the comparison in Figure 3.8. First, due to high viscosity, the flow regime shifts from turbulent flow to laminar flow, causing changes of flow recirculation inside impeller (Figures 3.8b, d, f). Second, under off-design operation conditions, the fluid velocities at the outlet of impeller deviate from blade angle increasingly. This in turn leads to additional departure of streamlines from the designed flow path. Therefore, further recirculation and pressure potential dissipation is induced (Figures 3.8(a) vs. (b), (c) vs. (d)).

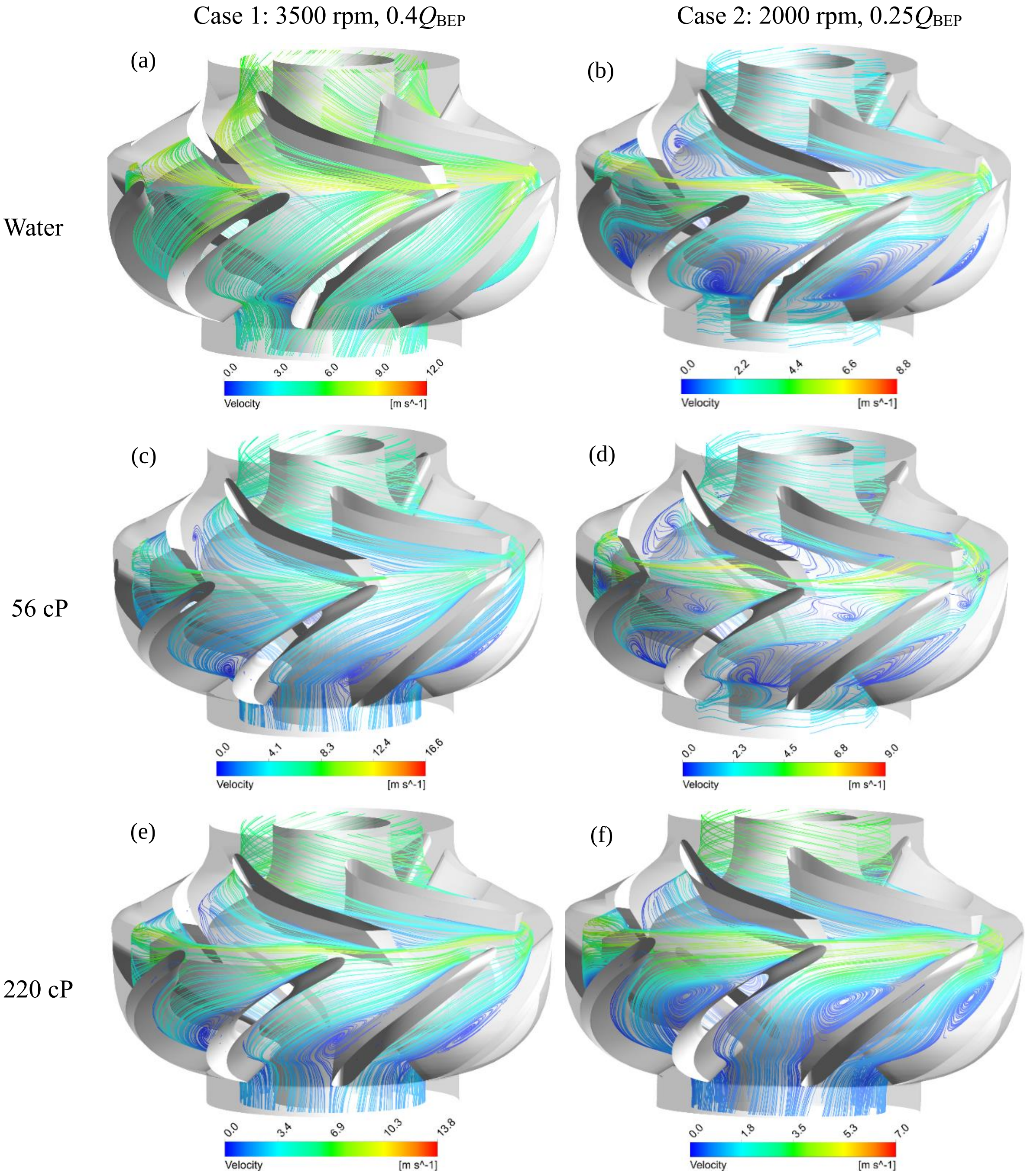

Figure 3.8 Streamline comparison under different flow conditions at half span of stage 3 in DN-1750 ESP

For the simulated cases shown in Figure 3.8, the vortices exist near the pressure sides of diffuser vane due to highly curved vane geometry. The vortex shape inside diffuser channel is affected by several factors, including viscosities, rotational speeds and liquid flow rates. However, this vortex and recirculation contribute little to ESP pressure increment.

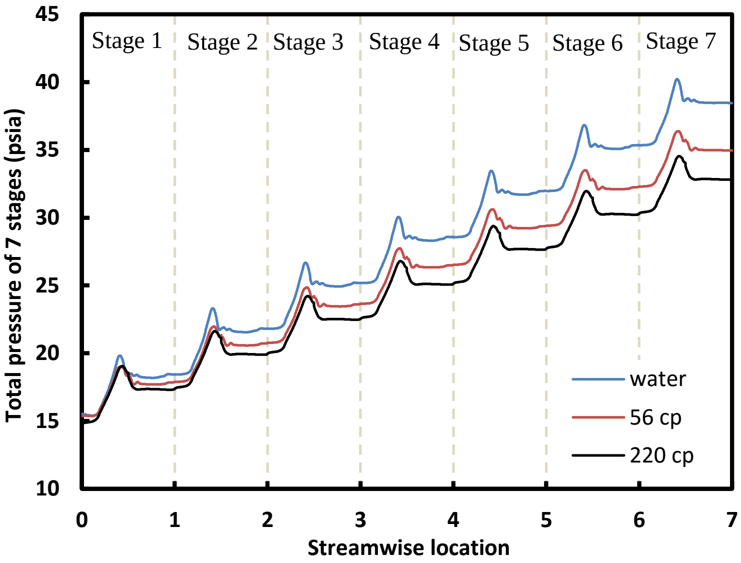

Figure 3.9 Total pressure averaged along streamwise location for DN-1750 ESP with $N = 3500$ rpm, $Q = 0.4Q_{BEP}$

ESP boosts pressure by converting kinetic energy to pressure potential. The impeller-diffuser interaction guides fluid away from impeller, which causes additional energy dissipation and local hydraulic pressure loss, resulting in abrupt pressure reduction. Figure 3.9 shows the averaged total pressure along streamwise location for the entire 7 stages at 3500 rpm and $0.4Q_{BEP}$. The streamwise location is the dimensionless distance from the inlet to the outlet. It ranges from 0 to 1 for the first stage, 1 to 2 for the second one, and so on. It can be seen in Figure 3.9 that ESP overall boosting pressure decrease with fluid viscosity increase. From inlet of stage 1 to the outlet of stage 7, the fluid pressure is boosted within the impeller of each stage. However, the pressure does not change much in diffusers. A pressure drop is observed at inter-stage due to the interaction of ESP rotating impeller and stationary diffuser. In order to improve pump hydraulic efficiency, the blade angles at impeller outlet and diffuser inlet need to be at around operation flow rate so that the pressure drop due to impeller-diffuser interaction can be minimized (Wu et al., 2015).

3.2 CFD Simulation of Gas-liquid Flow

3.2.1 TE-2700 ESP Geometry and Mesh

The studied geometry is TE-2700, a radial type ESP with Ns = 1638 based on the specific speed definition in Eq. (1.2). Its main geometrical specifications are listed in Table 3.2. At BEP, the operation parameters are as follows: rotational speed N = 3500 rpm, mass flow rate Q = 4.953 *kg/s*, hydraulic head H = 16.1 *m*, and efficiency η = 69.2%. Figure 3.1 shows pump 3D model, including impeller (Figure 3.10a) and diffuser blades (Figure 3.10b) as well as the entire computational domain for single stage (Figure 3.10c).

Table 3.2: Geometrical specifications of TE-2700 ESP

Component	**Description**	**Parameter**	**Values**
Impeller	Blade number	Z_i	5
	Tangential blade angle at inlet (deg)	β_1	19.5
	Tangential blade angle at outlet (deg)	β_2	24.7
	Blade thickness (mm)	b_i	2.72
	Channel length (mm)	l_i	76.0
	Inlet channel height (mm)	h_1	12.2
	Outlet channel height (mm)	h_2	7.84
	Inner radius (mm)	r_1	17.5
	Outer radius (mm)	r_2	56.1
Diffuser	Vane number	Z_d	9
	Channel length (mm)	l_d	87.1
	Partition wall thickness (mm)	b_d	4.48

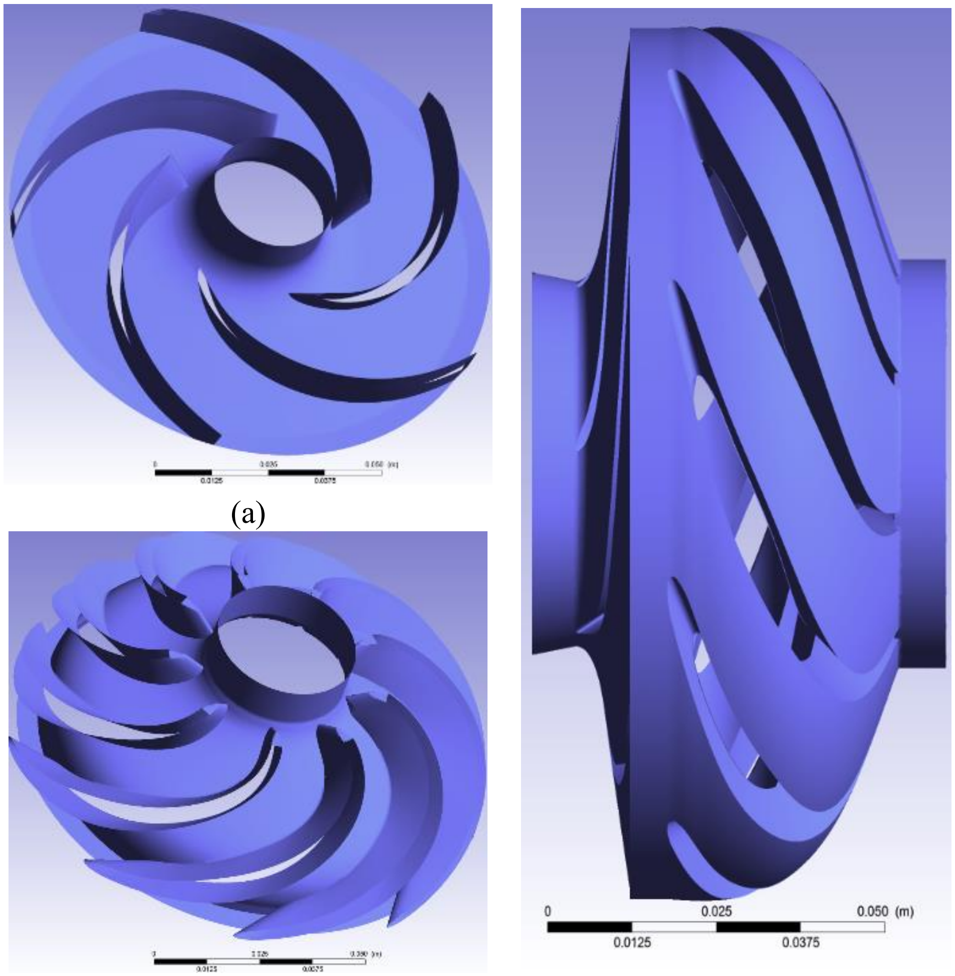

(a)

(b)

(c)

Figure 3.10 Computational domains of TE-2700 ESP, (a) impeller blade, (b) diffuser vane and (c) entire fluid domain for single stage

Numerical studies regarding comparison and selection of grid has been conducted by researchers (Becker et al., 2010; Tomita et al., 2012). The structured grids made up of hexahedrons are generated with ANSYS Turbogrid 15.0. The structured hexahedral grids based on simplified multistage geometry are shown in Figure 3.11. As mentioned above, the complete fluid domain comprises of three simplified domains of impeller Figure 3.11(b) and diffuser Figure 3.11(c). Each domain is meshed with structural hexahedrons with the refinement near blade surfaces. The frozen-rotor technique is used to calculate interactions between rotor and stator of each stage. All impeller domains are set to rotational reference frame while diffuser domains are set to stationary reference frame.

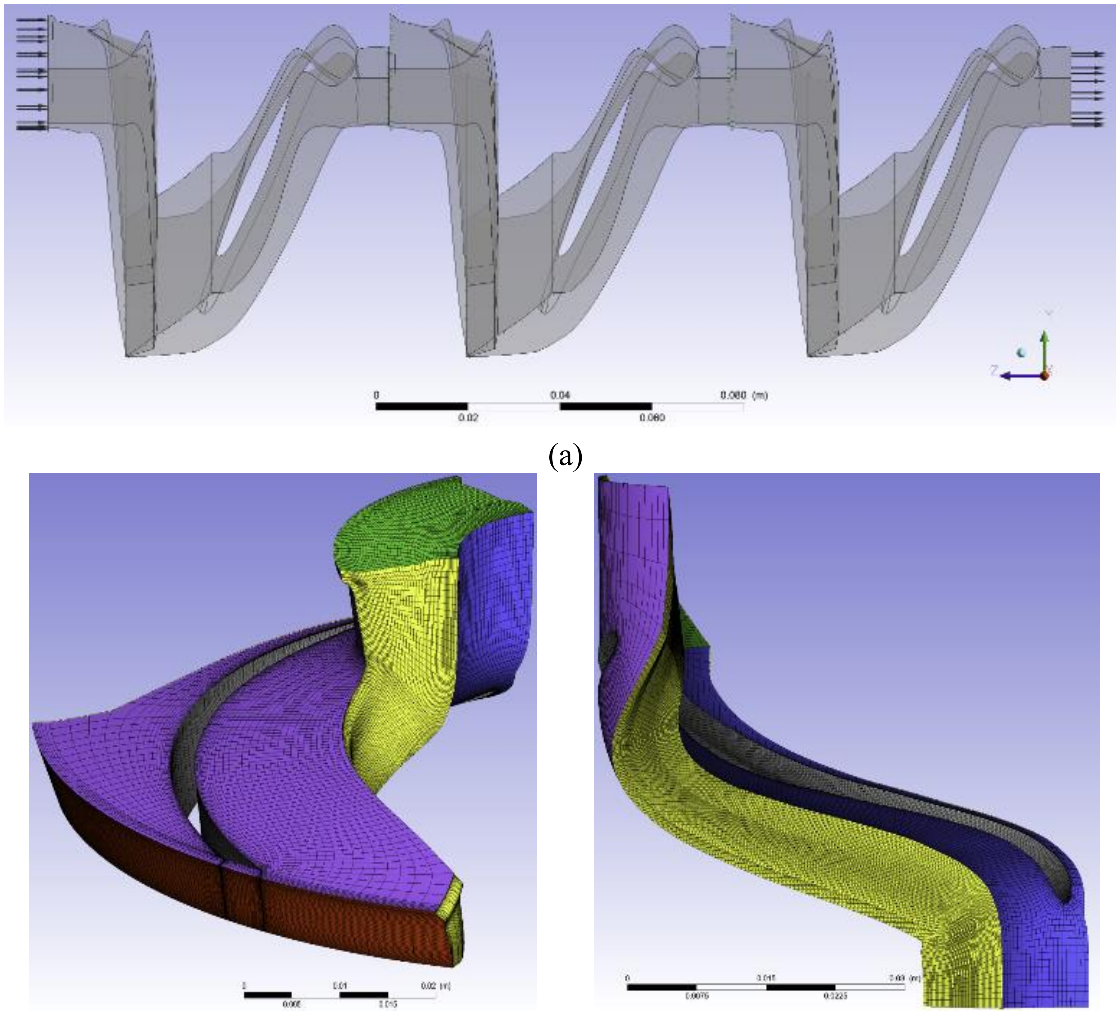

(a)

(b) (c)

Figure 3.11 Grid generation on TE-2700 ESP, (a) multistage pump assembly, (b) grid for single impeller blade and (c) grid for single diffuser channel

3.2.2 Eulerian-Eulerian Multiphase Model

This study employs Eulerian-Eulerian approach incorporated with standard k-ε turbulence model for solving the fully transient three-dimensional incompressible N-S equations as well as continuity equations for each phase. Interactions between phases can be modeled by interfacial momentum transfer terms. Assuming isothermal binary immiscible gas-liquid flow, the interfacial mass and energy transfer are not taken into account.

3.2.2.1 Eulerian-Eulerian Multiphase Model. For CFD simulation of multiphase flow, the Eulerian-Eulerian model may be more complex since it introduces additional phases together with *n* sets of conservation equations (Achouri et al., 2012), where *n* depends on phase number. But it is still recommended due to its general applicability for a wide range of volume fraction (Huang et al., 2014). Using this approach, the fields of velocity and volumetric fraction are calculated individually, while the pressure field is shared among phases (Zhu and Zhang, 2014). Assuming no mass source or interfacial mass transfer, the continuity equation of gas-liquid two phase flow can be written as

$$\frac{\partial(\rho_i \alpha_i)}{\partial t} + \nabla \cdot (\rho_i \alpha_i \vec{u}_i) = 0, \tag{3.16}$$

where ρ_i, α_i, $\vec{u}_i$ are density, volumetric fraction, velocity vector of i^{th} phase, respectively. Subscript $i = l$ or g denotes liquid or gas phase. A simple constraint that volumetric fractions sum up to unity is expressed as

$$\sum_{i=1}^{n} \alpha_i = 1. \tag{3.17}$$

The momentum balance of phase *i* yields

$$\frac{\partial(\rho_i \alpha_i \vec{u}_i)}{\partial t} + \nabla \cdot (\rho_i \alpha_i \vec{u}_i \vec{u}_i) = -\alpha_i \nabla P + \alpha_i \nabla \cdot (\bar{\bar{\tau}}_i) + \alpha_i \rho_i \vec{g} + \vec{F}_i + \vec{F}_{lift,i} + \vec{F}_{vm,i}, \tag{3.18}$$

where $\bar{\bar{\tau}}_i$ is the i^{th} phase stress-strain tensor given by Eq. (3.19), $\vec{g}$ is the gravity acceleration vector. $\vec{F}_i$, $\vec{F}_{lift,i}$, and $\vec{F}_{vm,i}$ represent interfacial forces for the interfacial momentum transfer, including external body forces (e.g. buoyancy and centrifugal forces), lift force and virtual mass force, respectively.

$$\bar{\bar{\tau}}_i = \alpha_i \mu_i \left(\nabla \vec{u}_i + \left(\nabla \vec{u}_i \right)^T \right) + \alpha_i \left(\lambda_i - \frac{2}{3} \mu_i \right) \nabla \cdot \vec{u}_i \bar{\bar{I}} \ . \tag{3.19}$$

The Eqs. (3.16) ~ (3.19) above constitute the general form of Eulerian-Eulerian inhomogeneous multiphase model. In order to solve this model, the RANS equations are adopted, which statistically average turbulence fluctuations in above transport equations. The additional Reynolds stress term in RANS equations is modeled by the two-equation turbulence model.

3.2.2.2 Standard *k*-*ε* Turbulence Model. Due to the empirical nature of most turbulence models (Gulich, 2008; Zhou et al., 2012) which quantify Reynolds stress by correlations, a universally validated turbulence model yielding optimal results for all simulation seems to be unlikely (Zhu and Zhang, 2014). The standard *k*-*ε* two equation model offers a good compromise between numerical effort and computational accuracy (ANSYS, 2015), which is widely used in industry (Maitelli et al., 2010; Qi et al., 2012). This model incorporates two transport equations for the turbulent kinetic energy (*k*) and energy dissipation rate (*ε*). Under multiphase flow condition, the standard *k*-*ε* model needs to be modified to consider turbulence within different phases. Therefore, the hypothesis of eddy viscosity is assumed to hold for each turbulent phase, which is given by

$$\mu_{eff,i} = \mu_i + \mu_{t,i} \, , \tag{3.20}$$

where $\mu_{eff,i}$ is the effective viscosity, μ_i and $\mu_{t,i}$ are molecular viscosity and turbulent viscosity of i^{th} phase, respectively. For *k*-*ε* model, the turbulent viscosity is modeled as

$$\mu_{t,i} = \rho_i C_\mu \frac{k_i^2}{\varepsilon_i} . \tag{3.21}$$

In Eq. (3.21), turbulent kinetic energy (*k*) of *i*th phase can be obtained by deriving exact transport equations (Xiang et al., 2011), while its dissipation rate (*ε*) is correlated by physical reasoning (Achouri et al., 2012). Similar to single-phase turbulent flow, the transport equations for *k* and *ε* in multiphase flow are

$$\frac{\partial(\rho_i \alpha_i k_i)}{\partial t} + \nabla \cdot \left(\rho_i \alpha_i \vec{u}_i k_i\right) = \nabla \cdot \left(\left(\mu_i + \frac{\mu_{t,i}}{\sigma_k}\right)\nabla k_i\right) + \alpha_i\left(P_i - \rho_i \varepsilon_i\right) + T_{i,j}^{(k)} \tag{3.22}$$

and

$$\frac{\partial(\rho_i \alpha_i \varepsilon_i)}{\partial t} + \nabla \cdot \left(\rho_i \alpha_i \vec{u}_i \varepsilon_i\right) = \nabla \cdot \left(\left(\mu_i + \frac{\mu_{t,i}}{\sigma_\varepsilon}\right)\nabla \varepsilon_i\right) + \alpha_i \frac{\varepsilon_i}{k_i}\left(C_{\varepsilon,1} P_i - C_{\varepsilon,2} P_i \rho_i \varepsilon_i\right) + T_{i,j}^{(\varepsilon)} , \tag{3.23}$$

where $C_{\varepsilon,1}$ and $C_{\varepsilon,2}$ are constants, σ_k and σ_ε are turbulent Prandtl numbers for *k* and *ε*, respectively. P_i is the turbulence production term due to viscous forces in phase *i*. The additional terms $T_{i,j}^{(k)}$ and $T_{i,j}^{(\epsilon)}$ represent interphase transfer of *k* and *ε*, which usually are omitted but can be added by user sources.

3.2.3 Closure Relationships

For Eulerian-Eulerian multiphase model, the interactions between phases are effected via interfacial momentum transfer terms. Thus, additional models regarding interfacial forces are needed so as to make two-fluid multiphase model closed and solvable. As shown in Eq. (3.18), the interfacial forces can be categorized into drag, lift and virtual mass forces, etc.

3.2.3.1 Drag Force. In gas-liquid two-phase flow, the drag force represents interfacial momentum transfer due to velocity difference between gas and liquid phases (Ziegenhein et al., 2015), which can be modeled by adding a source term in N-S equations:

$$F_{\mathrm{lg}}^{drag} = \frac{3}{4} C_D \frac{\rho_l \alpha_g}{d_b} \left| \vec{u}_g - \vec{u}_l \right| \left(\vec{u}_g - \vec{u}_l \right), \tag{3.24}$$

where C_D is drag coefficient. In this study, due to high shear effect inside impeller, the gas phase is treated as bubbly flow with all bubbles of the same spherical shape and size. A drag force was suggested by Grace et al. (1978):

$$C_{D_{sphere}} = \begin{cases} \dfrac{24}{\mathrm{Re}} & \mathrm{Re} < 0.01 \\ \dfrac{24\left(1 + 0.15\,\mathrm{Re}^{0.687}\right)}{\mathrm{Re}} & \mathrm{Re} > 0.01 \end{cases}. \tag{3.25}$$

In Eq. (3.25), the Reynolds number Re is defined by

$$\mathrm{Re} = \frac{\rho_l \left| \vec{u}_g - \vec{u}_l \right| d_b}{\mu_l}. \tag{3.26}$$

The Grace et al. drag model takes into account both sparsely and densely distributed fluid particles, which is suitable for gas-liquid flow with high inlet gas volume fraction.

3.2.3.2 Lift Force. In a multiphase shear flow, due to velocity gradients in the primary phase flow field, lift force exerts on dispersed particles, which is perpendicular to the direction of relative motion between phases. The force can be correlated to the relative velocity and the local liquid vorticity from Drew and Lahey (1979) as

$$F_{\mathrm{lg}}^{lift} = C_L \rho_l \left(\vec{u}_g - \vec{u}_l \right) \times \left(\nabla \times \vec{u}_l \right), \tag{3.27}$$

where C_L is lift coefficient. A lift force model proposed by Legendre and Magnaudet (1998) is adopted in this study, which is applicable mainly to the lift force of small diameter spherical fluid particles. The lift coefficient can then be estimated as

$$C_L = \sqrt{C_{L,low\mathrm{Re}}^2 + C_{L,high\mathrm{Re}}^2}\ , \tag{3.28}$$

where $C_{L,low\mathrm{Re}}$ and $C_{L,high\mathrm{Re}}$ are given by:

$$C_{L,low\mathrm{Re}} = \frac{15.3}{\pi^2}\mathrm{Re}_\omega^{-0.5}\left(1 + 0.2\frac{\mathrm{Re}_p^2}{\mathrm{Re}_\omega}\right)^{-1.5}, \tag{3.29}$$

and

$$C_{L,high\mathrm{Re}} = \frac{1}{2}\frac{1 + 16\,\mathrm{Re}_p^{-1}}{1 + 29\,\mathrm{Re}_p^{-1}}\,. \tag{3.30}$$

Here, the particle Reynolds number Re_p and vorticity Reynolds number Re_ω are defined as

$$\mathrm{Re}_p = \frac{\rho_l \left|\vec{u}_g - \vec{u}_l\right| d_p}{\mu_l}, \tag{3.31}$$

and

$$\mathrm{Re}_\omega = \frac{\rho_l \left|\nabla \times \vec{u}_l\right| d_p^2}{\mu_l}\,. \tag{3.32}$$

As suggested by Legendre and Magnaudet (1998), the validity range of the above lift force model is $0.1 < \mathrm{Re}_p < 500$, $\mathrm{Re}_\omega \leq 1$.

3.2.3.3 Virtual Mass Force. This force is due to inertia of surrounding fluid as the dispersed phase accelerates relative to the continuous phase (ANSYS, 2015). Steady-state simulation is a common practice for rotating machine, assuming flow behavior does not change with time after initial unsteady flow development. The virtual mass force is neglected since transient terms in governing equations will become zero or have negligible influence when simulation achieves steady state (Xiang, 2011).

3.2.4 Boundary Conditions and Numerical Scheme

In this study, the complete computational domain comprises of three congruent stages, each of which contains a single-channeled impeller and diffuser. Two types of interfaces are prescribed to conduct successful simulation. Firstly, the GGI was used for each pair of rotor and stator interfaces to maintain strict conservation of fluxes across these interfaces. Thus, total five GGI pairs are generated, where three of them are within stages, and the other two pairs are at inter-stages. Secondly, periodic interfaces based on rotational periodicity are set up within each computational domain of impeller or diffuser, which requires six periodic pairs.

From inlet to outlet, the boundary conditions are specified according to corresponding experimental configurations. As recommended by Caridad et al. (2008), the total pressure (170 psig) in the rotation axis direction with medium (5%) turbulence intensity is applied at the inlet, while a mass flowrate scaling down to 1/9 of diffuser domain is imposed at the outlet. For two-phase flow, the GVF is also specified at the inlet. In this study, the gas bubbles are assumed incompressible since the single-stage pressure increment with moderate or high gas void fraction is small compared to the given inlet total pressure. For walls inside impellers, the rotating frame type is adopted. Correspondingly, all diffuser walls are set to stationary frame type. In addition, the no-slip condition for liquid phase and free slip condition for gas phase at walls are used with volume fraction wall contact model. The near-wall treatment is based on the scalable wall functions.

All simulation cases under both single-phase and gas-liquid two-phase flow conditions are conducted with the same numerical schemes. For spacial discretization of advection terms and turbulence equations, the high resolution scheme is used, which is a second order algorithm in CFX-solver. For steady-state simulation, a false time step as a means of under-relaxing governing equations has been applied which requires a relatively large time scale with the robust and fully implicit CFX-solver. A fixed physical timescale of $1/(2\Omega)$ is used with the maximum 300 outer loop iterations to achieve convergence. For multiphase simulation with higher inlet GVF, the timescale is reduced to 1/4 of the physical timescale with maximum 600 iterations to promise adequate convergence. The convergence criterion is satisfied when RMS residual drops below 10^{-5}. In this study, multiphase simulations are found difficult to converge at RMS residual of 10^{-5} for some cases. However, a RMS residual below 10^{-4} is achieved for all simulation cases

3.2.5 Results and Discussions

3.2.5.1 Validations of Mesh Independence and Turbulence Model. Figure 3.12 shows the mesh validation and wall function check using single stage simplified geometry. In this study, the thickness of the first grid layer on blade surfaces is 6×10^{-5} *m*, based on which the average value of y^+ is below 60. The simulated pump head with grid number around 0.3 million deviates less than 3% from that obtained with finer meshes. Therefore, the final grids generated in simplified impeller and diffuser contain 326,910 and 267,760 elements. Total grids for the complete three-stage computational domain contain 1,784,010 elements, which are sufficient to guarantee grid independence.

The selection of turbulence model is a delicate task for CFD simulation as discussed by (Bradshaw, 1996; Asuaje et al., 2005), which is also a compromise of numerical effort and accuracy. Figure 3.13 compares simulation results using different turbulence models. The details of each turbulence model are available in CFX-solver Modeling Guide (ANSYS, 2015). As Figure 3.13 shows, there is no prominent variance among different turbulence model predictions. Due to relative less computational effort while providing high numerical accuracy, the *k*-*ε* two-equation turbulence model is used in this study.

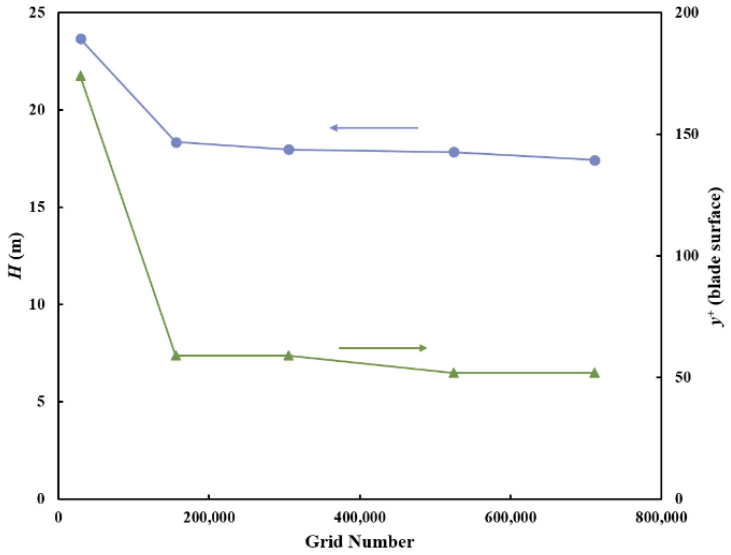

Figure 3.12 Mesh validation and wall function check for TE-2700 ESP

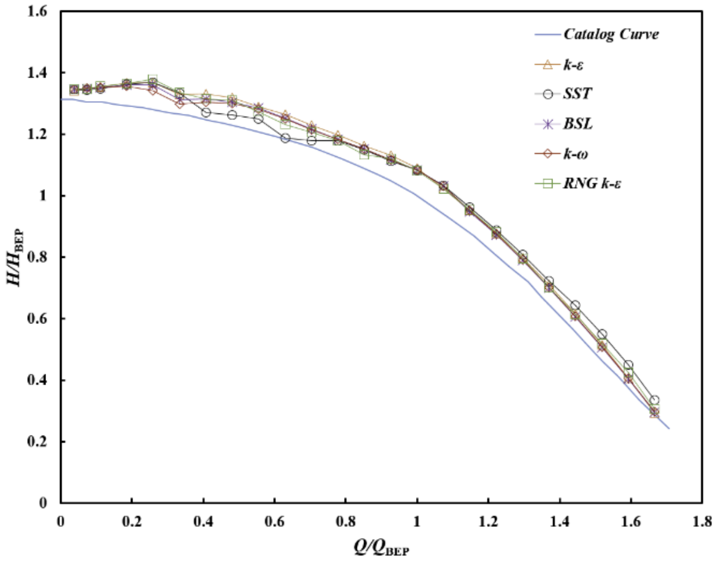

Figure 3.13 Influence of turbulence models on simulation of TE-2700 ESP water flow

3.2.5.2 Single-Phase Water Simulation. The non-dimensional variables: flow coefficient, head coefficient and power coefficient, defined by Eqs. (3.12) ~ (3.14), are used in processing experimental and numerical simulation data.

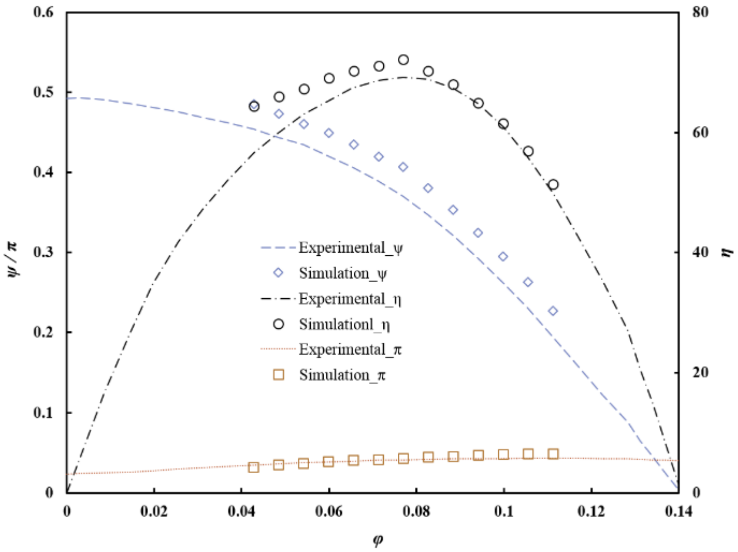

Figure 3.14 Performance curves of TE-2700 ESP under single-phase flow condition

Figure 3.14 above summarizes single-phase simulation results of head (ψ) and power (π) coefficients as well as the pump efficiency (η) as functions of flow coefficients (φ) within the pump operation range. It is noted that simulation results for head coefficient and pump efficiency are slightly higher than the experimental values, indicating that CFD simulations over predict ESP single-phase performance. As qualitatively analyzed by Zhou et al. (2012) and Jeanty et al. (2009), the overestimation could be ascribed to the neglect of leakage flow through the radial clearance between impeller and diffuser. Moreover, the smooth wall assumption adopted in this study would further contribute to the deviation of simulation results from experimental data by underestimating viscous friction losses due to wall roughness in reality.

The numerical results are consistent with the changing trends of experimental data. The power coefficient simulation results are within 3% deviation from the corresponding experimental values. The calculated pump efficiency and head coefficient seem to agree with experimental data better at relatively higher flow coefficients. This may be related to leakage flow increase at lower flow coefficients due to higher back pressure.

3.2.5.3 Two-Phase Simulation Results. Salehi (2012) experimental data are compared with CFD simulations. In Salehi experimental study, the gas injection position changed stage by stage, and the downstream stage pressure increment was measured accordingly. Considering the end-effects of centrifugal pump, the simulation results of the middle stage are used for comparison. Figure 3.15 shows the comparison of simulation results with experimental data with gas was injection at stage 4 and the differential pressure measurement at stage 5. In CFD simulation configuration, the first stage acts as the gas-injection stage, and the middle stage as the pressure-measurement stage. The normalized pressure N_p is the ratio of two-phase pressure increment to the corresponding single-phase pressure increment.

The comparison in Figure 3.15 shows that as the inlet GVF (λ_G) increases, N_p decreases. The decline trend can be captured by CFD simulations. However, the numerical results with constant bubble sizes of 0.1 mm, depart from experimental data at $\lambda_G > 10\%$. A good agreement of predicted N_p with experimental values can be obtained by using modified bubble sizes with changing GVFs. Tabib et al. (2008) also suggested to change the bubble size with change in superficial gas velocity to better represent the actual physical occurrence in multiphase CFD simulations. The departure of simulation results from experimental data using a constant bubble size is due to underestimated bubble sizes at higher GVFs. As to interphase forces, the simulated bubble sizes seem to be very close with or without considering lift force, indicating that the drag force plays a dominant role in interphase momentum transfer.

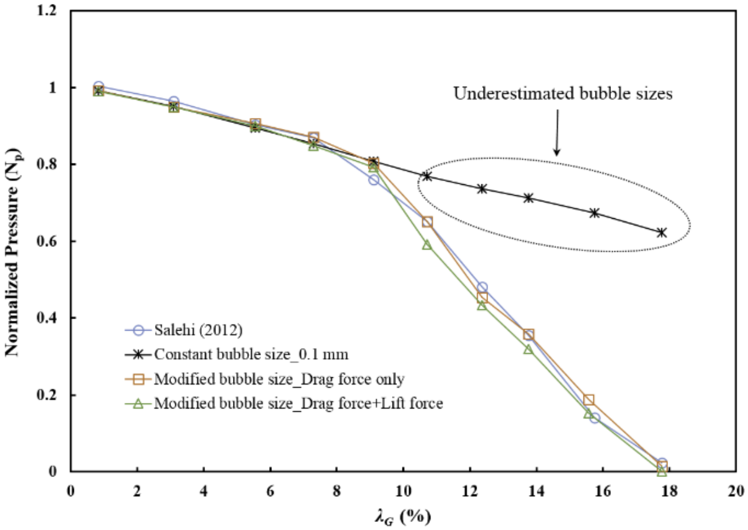

Figure 3.15 Comparison of simulated two-phase performance of TE-2700 ESP with experimental data (Salehi 2012) at BEP

Two simulation cases with different rotational speeds were performed. One case corresponds to the best efficiency point with N = 3500 rpm (Figure 3.16a). The other is at an off-design point with N = 1500 rpm (Figure 3.16b). For each case, the liquid flow rate was kept constant, namely 2700 bpd at BEP and 1153 bpd at the off-design point. The gas flow rate increased from zero until the ESP pressure increment approached nil. Figure 3.16 presents the comparisons of the predicted pump pressure increment by multiphase CFD simulations with the corresponding experimental results of Salehi. The primary vertical axis is the normalized pressure increment. The secondary vertical axis represents the bubble sizes (d_b) that were incorporated into CFD simulations.

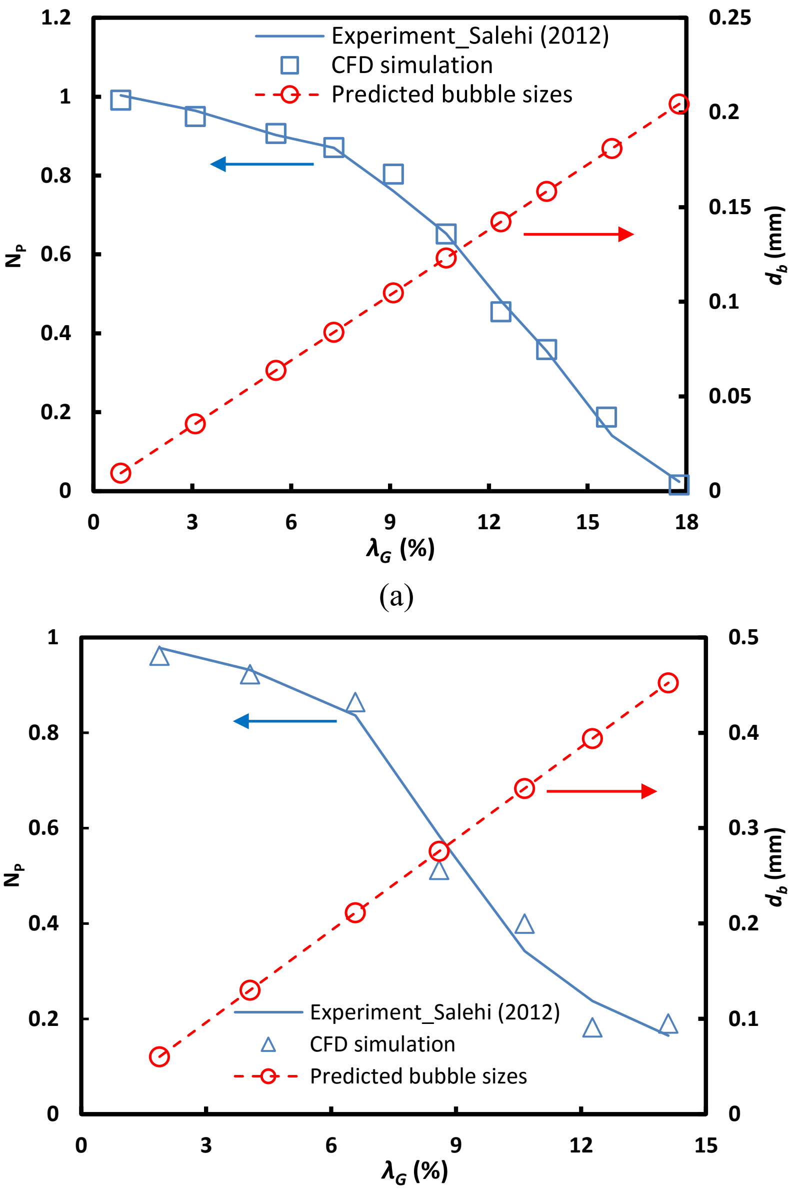

(a)

(b)

Figure 3.16 CFD simulated ESP pressure increment and the representative bubble sizes under two-phase flows, (a) $N = 3500$ rpm, (b) $N = 1500$ rpm

As Figure 3.16 shows, a drastic drop of N_p is observed if the inlet λ_G is increased to a certain value, indicating that the severe degradation of ESP pressure increment initializes due to the coalescence and accumulation of gas bubbles. In Figure 3.16(a), pressure surging occurs at λ_G around 7% for the rotational speed $N = 3500$ rpm. At $N = 1500$ rpm in Figure 3.16(b), λ_G around 6% triggers ESP pressure surging. It verifies that the surging initiation can be successfully captured by multiphase CFD simulations, which further validates the numerical methodology and the bubble size prediction model used in this study.

Case 1: $N = 3500$ rpm, $Q_L = 2700$ bpd

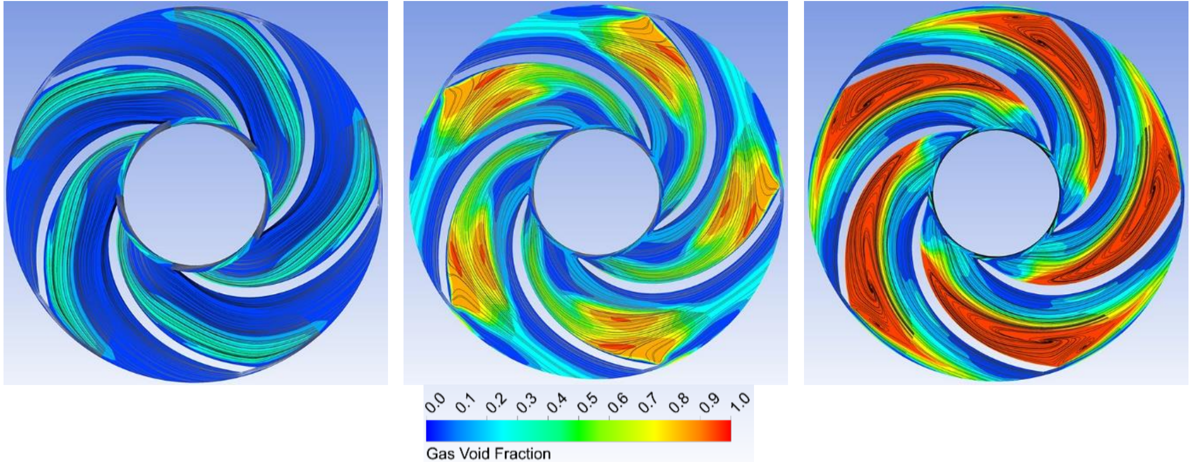

(a) $\lambda_G = 5.5\%$, $\alpha_G = 6.2\%$ (b) $\lambda_G = 12.4\%$, $\alpha_G = 26.9\%$ (c) $\lambda_G = 17.8\%$, $\alpha_G = 45.0\%$

Case 2: $N = 1500$ rpm, $Q_L = 1153$ bpd

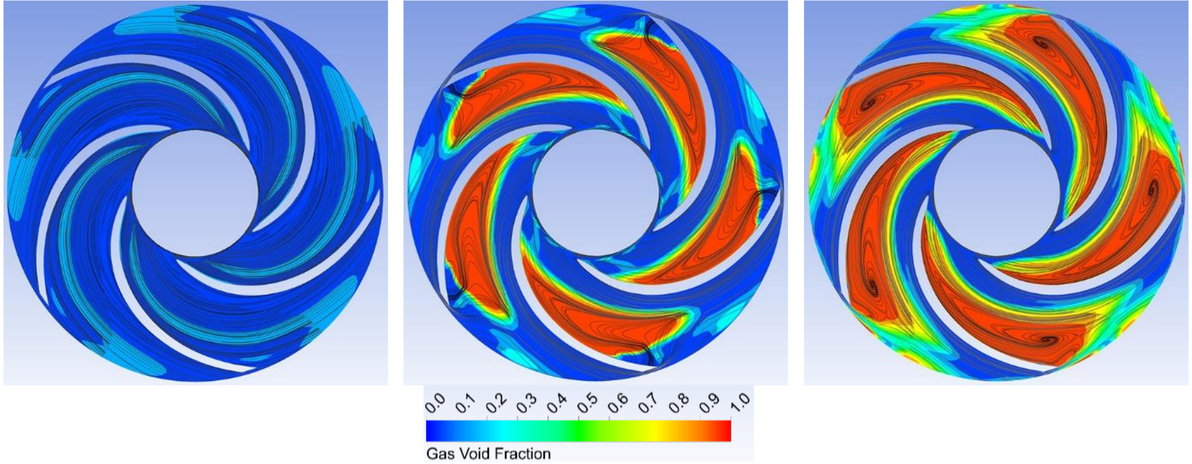

(d) $\lambda_G = 4.1\%$, $\alpha_G = 4.4\%$ (e) $\lambda_G = 8.6\%$, $\alpha_G = 28.3\%$ (f) $\lambda_G = 14.1\%$, $\alpha_G = 40.4\%$

Figure 3.17 Distribution of simulated in-situ α_G and streamlines on the half impeller span blade-to-blade surface under different flow conditions

Visualization experiments (Barrios, 2007; Murakami and Minemura, 1974; Gamboa, 2008) revealed that the reason for pump performance deterioration with gas entrainment was due to the slippage between gas and liquid, which in turn resulted in phase segregation inside flow passage. Figure 3.17 shows the simulated α_G contours and streamlines on the half impeller span blade-to-blade surface under different inlet λ_G. The average in-situ gas void fraction α_G inside the ESP impeller are given beneath each figure. Case 1 is at the BEP with N = 3500 rpm, Q_L = 2700 bpd, and case 2 is at the off-design point with N = 1500 rpm, Q_L = 1153 bpd. As demonstrated, a higher λ_G aggravates the accumulation and coalescence of gas bubbles, resulting in large gas pocket formation and thus a remarkable increase of in-situ α_G. For example, λ_G = 5.5% in case 1 leads to α_G = 6.2%. However, α_G is about 45% if λ_G is increased to 17.8%. Furthermore, gas bubbles are prone to cluster on the back side of impeller blades due to the recirculation flows depicted by the streamlines. The numerically simulated values of α_G are employed to validate our mechanistic model predictions in the next section.

The static pressure contours on the half impeller span blade-to-blade surface is shown in Figure 3.18, corresponding to the abovementioned two simulation cases. For Eulerian-Eulerian multiphase CFD simulations, an identical pressure field is shared by gas and liquid phases. As it can be seen from Figures 3.18(a) and 6(d), corresponding to the relatively low inlet λ_G and mild gas accumulations in Figures 3.17(a) and (d), the static pressure increases continuously from the impeller inlet to outlet, with the positive pressure gradient along the streamlines. However, as λ_G increases further, the pressure gradient in the ESP impeller becomes highly uneven, accompanying local zero and even the negative pressure gradient due to the large gas pocket formation. Compared to Figures 3.17(b), (c), (d) and (e), the severe gas pocket formation zones are coinciding with the constant static pressure distribution areas in Figures 3.18(b), (c), (d) and (e). Such correspondence justifies that the mechanism of ESP pressure boosting degradation under gassy flow conditions is due to the gas-liquid phase slippage, which results in accumulation and coalescence of gas bubbles.

Case 1: $N = 3500$ rpm, $Q_L = 2700$ bpd

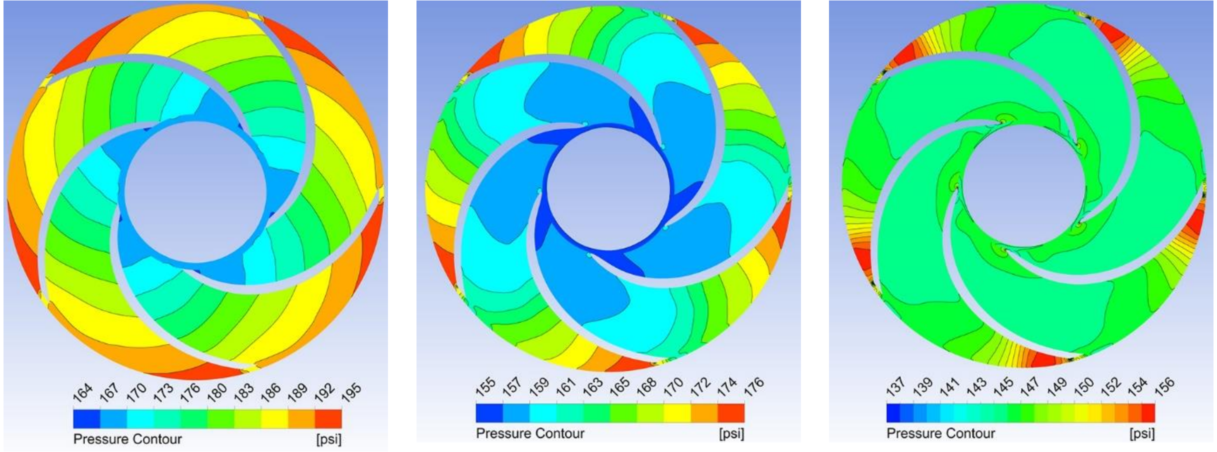

(a) $\lambda_G = 5.5\%$ (b) $\lambda_G = 12.4\%$ (c) $\lambda_G = 17.8\%$

Case 2: $N = 1500$ rpm, $Q_L = 1153$ bpd

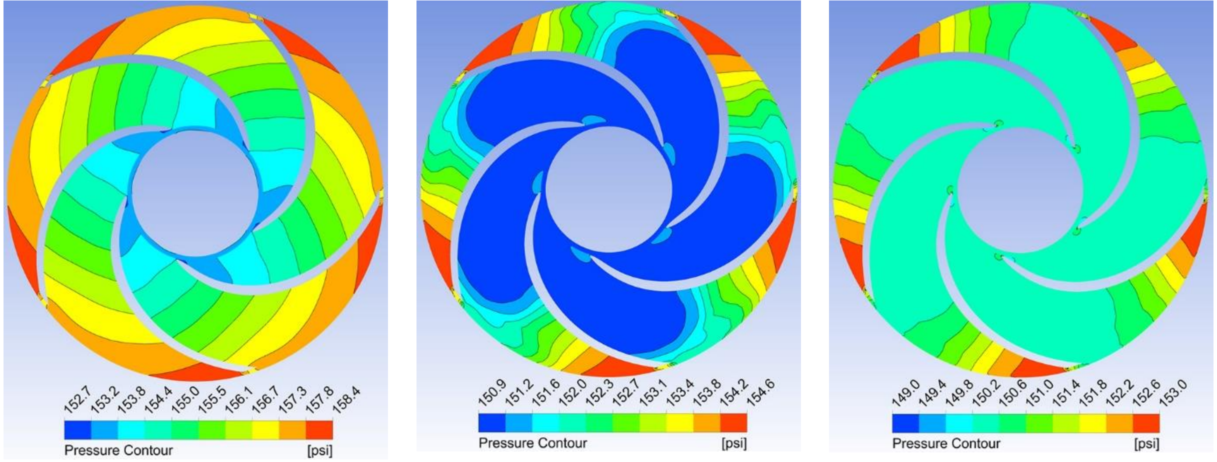

(d) $\lambda_G = 4.1\%$ (e) $\lambda_G = 8.6\%$ (f) $\lambda_G = 14.1\%$

Figure 3.18 Static pressure contours on the half impeller span blade-to-blade surface under different flow conditions

3.3 Numerical Simulation Summary

In this chapter, the numerical simulations on ESP performance under both water/viscous fluid flow and gas-liquid flow conditions are conducted. Verified by experimental data, the CFD simulation is a powerful and reliable tool to study the complex flow structures and characteristics inside a rotating ESP.

In single-phase simulations with viscous fluid flow, the simulated ESP pressure increment under water flow matches the experimental results, which validates the numerical methodology. Using SST turbulence model, the stage pressure increment under viscous fluid flow is over predicted by CFD simulation about 15%. The linear trend of *H*-*Q* curves at high liquid viscosity is captured by numerical simulations. From the numerically simulated flow structures as shown by the streamlines, the recirculation flow is observed at the trailing edges of impeller blades at high fluid viscosity or low liquid flow rate.

For two-phase simulation, a 3D CFD code is implemented to a three-stage ESP model to simulate the pump stage pressure increment with gas entrainment. Using the structured hexahedral grids and frozen-rotor techniques, the mesh independence and numerical accuracy are confirmed. The single-phase water simulation results are found to match experimental data well. For gas-liquid two-phase simulation, the Eulerian-Eulerian two-fluid model is used. The interfacial momentum transfer forces like drag and lift forces are incorporated. Compared with experimental data, two-phase simulation results with constant bubble sizes match well at low inlet gas volume fractions (GVF), but deviate at high GVFs. The simulation results are then made comparable to experimental data by adjusting the bubble size with GVF increase.

CHAPTER 4

MECHANISTIC MODELING AND RESULTS

This chapter discusses the mechanistic model of ESP performance predictions, including liquid and gas-liquid flow modeling, as well as closure relationships for bubble size prediction, in-situ gas void fraction (α_G), and flow pattern transition boundary. Meanwhile, the comparisons of mechanistic model predictions with CFD simulation results and experimental data are presented.

4.1 Mechanistic Modeling of ESP Liquid Performance

The mechanistic model of ESP boosting pressure under liquid flow is presented in this section. Different from existing models, this model predicts viscosity effects on ESP stage pressure increment. A best match flow rate (Q_{BM}) at which the flow direction at the impeller outlet matches the designed flow direction is used. When the flow rate is lower or higher than Q_{BM}, the theoretical fluid velocity at the impeller outlet needs to be projected to the flow direction corresponding to the best match flow rate.

4.1.1 Euler's Equation inside EPS Impeller

In centrifugal pump, the Euler equation is a basic and theoretical model to predict pump performance. The assumptions for Euler equation include infinite number of rotor blades, ideal fluid (no loses), steady flow and incompressible fluid (Vieira et al. 2015). Based on velocity triangles in Figure 4.1, the theoretical head for a centrifugal pump can be written as (Stepanoff 1957)

$$H_E = \frac{U_2 C_{2U} - U_1 C_{1U}}{g} . \tag{4.1}$$

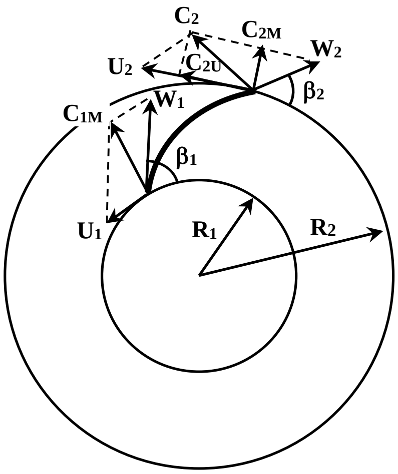

Figure 4.1 Velocity triangles at impeller inlet and outlet

Here, U is the tangential velocity, C is the absolute velocity and W is the relative velocity. The subscripts 1, 2, and U are inlet, outlet and tangential direction, respectively. g is the local gravitational acceleration. From the velocity triangles, the Euler's equation can be further expressed by velocity components as below

$$H_E = \frac{U_2^2 - U_1^2}{2g} + \frac{W_1^2 - W_2^2}{2g} + \frac{C_2^2 - C_1^2}{2g} . \tag{4.2}$$

The three terms at right hand side (RHS) of Eq. (4.2) are the hydraulic heads as a consequence of centrifugal force, velocity change through the impeller as well as dynamic effect. For each velocity component, its expression is discussed below.

The tangential velocity at impeller inlet is given by

$$U_1 = R_1 \Omega , \tag{4.3}$$

where R_1 is the radius of the impeller inlet, and Ω is the angular velocity of the impeller. Similarly, the tangential velocity at impeller outlet is expressed as:

$$U_2 = R_2 \Omega . \tag{4.4}$$

The meridional velocity at the impeller inlet can be written by

$$C_{1M} = \frac{Q + Q_{LK}}{\left(2\pi R_1 - Z_I T_B\right) y_{I1}} , \tag{4.5}$$

where Q and Q_{LK} are liquid flow rate and leakage flow rate, Z_I is the impeller blade number, T_B is the blade thickness projected to the radial direction, and y_{I1} is the impeller inlet height. Then the meridional velocity at impeller outlet is

$$C_{2M} = \frac{Q + Q_{LK}}{\left(2\pi R_2 - Z_I T_B\right) y_{I2}} . \tag{4.6}$$

Here, y_{I2} is the impeller outlet height. The relative velocities with respect to the ESP impeller inlet and outlet are

$$W_1 = \frac{C_{1M}}{\sin \beta_1} \tag{4.7}$$

and

$$W_2 = \frac{C_{2M}}{\sin \beta_2} , \tag{4.8}$$

where β_1 and β_2 are the blade angle from the tangential direction at impeller inlet and outlet, respectively.

According to the velocity triangles, the absolute velocities at impeller inlet and outlet are given below:

$$C_1 = \sqrt{C_{1M}^2 + \left(U_1 - \frac{C_{1M}}{\tan \beta_1} \right)^2} \tag{4.9}$$

and

$$C_2 = \sqrt{C_{2M}^2 + \left(U_2 - \frac{C_{2M}}{\tan \beta_2} \right)^2} . \tag{4.10}$$

From Eq. (4.1), using the velocity relationships, the theoretical pump head can also be expressed by

$$H_E = \frac{U_2\left(U_2 - W_2 \cos\beta_2\right)}{g} - \frac{U_1\left(U_1 - W_1 \cos\beta_1\right)}{g} . \tag{4.11}$$

If there is no inlet rotation, $C_{1U} = 0$ and $C_1 = C_{1M}$, then Eq. (4.12) can be reduced to

$$H_E = \frac{U_2^2}{g} - \frac{U_2 C_{2M}}{g \tan\beta_2} . \tag{4.12}$$

4.1.2 Effective Velocity at Impeller Outlet

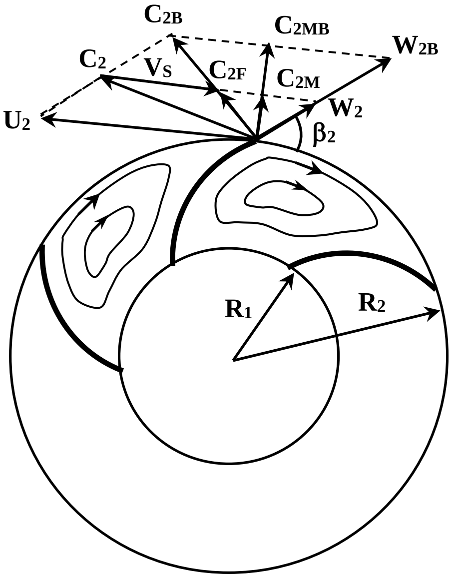

Figure 4.2 Velocity triangles at impeller outlet for $Q < Q_{BM}$

Figure 4.2 shows the velocity triangle of fluid flow and its decomposition at the outlet of impeller when $Q < Q_{BM}$. The absolute velocity of C_2 is the combined result of U_2 and W_2. V_S is the shear velocity due to the mismatch of the velocity C_2 and the fluid velocity in the designed direction corresponding to Q_{BM}. Through the trigonometry, C_{2F} and V_S are obtained as

$$C_{2F} = C_{2B} \frac{Q}{Q_{BM}} \tag{4.13}$$

and

$$V_S = U_2 \frac{Q_{BM} - Q}{Q_{BM}}, \tag{4.14}$$

where C_{2B} is the absolute fluid velocity at the impeller outlet corresponding to Q_{BM}.

The projected velocity, C_{2P}, is the projection of C_2 in the direction of C_{2B} which is the designed flow direction at Q_{BM}, which can be derived from the equation below

$$C_2^2 - C_{2P}^2 = V_S^2 - \left(C_{2P} - C_{2F}\right)^2. \tag{4.15}$$

Solving Eq. (4.15) for C_{2P}, one can obtain

$$C_{2P} = \frac{C_2^2 + C_{2F}^2 - V_S^2}{2C_{2F}}. \tag{4.16}$$

Normally, in ESP impeller channel, the recirculation that can be ascribed to velocity shear always occurs. As a result, the theoretical kinetic energy will be reduced and only partially converted to static pressure. The recirculation is dependent on the shear velocity, the channel size and the fluid viscosity. A Reynolds number can be used the estimate the recirculation effect

$$\mathrm{Re}_C = \frac{\rho V_S D_C}{\mu}, \tag{4.17}$$

where D_C is the representative impeller channel width at the outlet in flow direction,

$$D_C = \frac{2\pi R_2}{Z_I} \sin \beta_2 - T_B. \tag{4.18}$$

The shear effect is also dependent on the fluid viscosity. Therefore, the following correlation is proposed to estimate the effective velocity based on comparisons with experimental results

$$C_{2E} = C_{2F} + \sigma\left(C_{2P} - C_{2F}\right). \tag{4.19}$$

Here, σ is the slip factor, a concept proposed by Wiesner (1967) to account for the mismatch of the real outlet velocity with the ideal one, which is given by

$$\sigma = 1 - \frac{\sin^{1/2}(\beta_2)}{Z_I^{0.7}}. \tag{4.20}$$

However, Eq. (4.20) fails to account for shear velocity effect on flow recirculation in impeller, fluid velocity and channel size. A new correlation for σ is proposed as below

$$\sigma = \frac{\left(\frac{\mu_W}{\mu}\right)^{0.5}}{1 + 0.02\,\mathrm{Re}_C^{0.2}}, \tag{4.21}$$

where μ and μ_W are fluid viscosity and water viscosity, respectively.

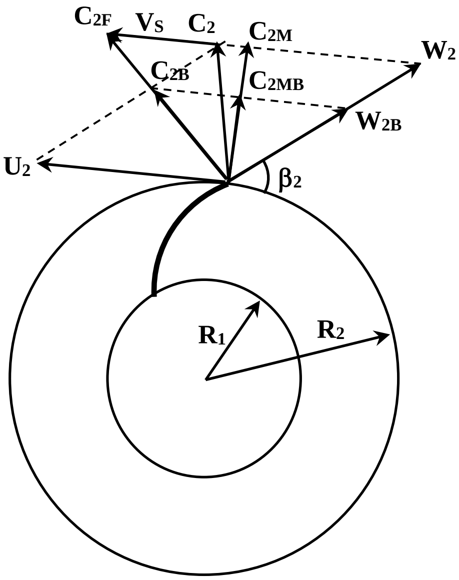

Figure 4.3 Velocity triangles at impeller outlet for $Q > Q_{BM}$

When $Q > Q_{BM}$, the expression of C_{2E} is different since there is no flow circulation at relatively higher flow rates. For this case, the velocity triangles are shown in Figure 4.3 above. Similarly, when $Q > Q_{BM}$, the C_{2F} is calculated the same as Eq. (4.13), while V_S should be written as

$$V_S = U_2 \frac{Q - Q_{BM}}{Q_{BM}}. \tag{4.22}$$

The effective velocity, C_{2E}, is the projection of C_2 in the direction of C_{2B}. Thus,

$$C_2^2 - C_{2E}^2 = V_S^2 - \left(C_{2F} - C_{2E}\right)^2. \tag{4.23}$$

Solve above equation and obtain the expression for C_{2E} when $Q > Q_{\mathrm{BM}}$ as

$$C_{2E} = \frac{C_2^2 + C_{2F}^2 - V_S^2}{2C_{2F}}. \tag{4.24}$$

For both circumstances ($Q < Q_{\mathrm{BM}}$ and $Q > Q_{\mathrm{BM}}$), the effective Euler head can be written by:

$$H_{EE} = H_E + \frac{C_{2E}^2 - C_2^2}{2g}, \tag{4.25}$$

where H_{EE} denotes the modified theoretical Euler head. H_E is given by Eq. (4.12). C_{2E} is calculated by Eq. (4.19) and Eq. (4.24) for $Q < Q_{\mathrm{BM}}$ and $Q > Q_{\mathrm{BM}}$, respectively.

4.1.3 Head Losses

Takacs (2009) listed three head loss types in centrifugal pumps, namely hydraulic losses, shock losses, and leakage losses. The actual pump head is the result after subtracting all the head losses from Euler head. The hydraulic losses caused by fluid friction and diffusion losses inside impeller channels increase steadily with the liquid flow rate. The shock losses are negligible at BEP, but increase at lower or higher liquid rate. They are due to sudden changes of flow direction at the inlet and outlet of impeller. The leakage losses always exist as long as the liquids flow through the clearances between the rotating and stationary parts of the pump stage, including impeller eye, balancing holes. However, the leakage losses diminish with the increased liquid flow rates due to lower back pressure. In this study, analysis of head losses is performed and each loss is mathematically modeled and formulated.

4.1.3.1 Friction Losses. The fluid flows inside the impeller and diffuser can be treated as channel flows. Thus, the friction losses in the impeller can be expressed as

$$H_{FI} = f_{FI} \frac{V_I^2 L_I}{2gD_I}, \tag{4.26}$$

where f_{FI} is the friction factor, V_I is the representative fluid velocity, L_I is the channel length, and D_I is the representative (hydraulic) diameter of the channel. Similarly, the friction loss in the diffuser can be estimated by

$$H_{FD} = f_{FD} \frac{V_D^2 L_D}{2gD_D}, \tag{4.27}$$

where f_{FD} is the friction factor, V_D is the representative fluid velocity, L_D is the channel length, and D_D is the representative (hydraulic) diameter of the channel. The Moody friction factors are functions of Reynolds number and relative roughness of the walls. Churchill (1977) equations are used to calculate the friction factors across the transition from laminar flow to turbulent flow. The representative Reynolds numbers in the impeller and diffuser are

$$\mathrm{Re}_I = \frac{\rho V_I D_I}{\mu} \tag{4.28}$$

and

$$\mathrm{Re}_D = \frac{\rho V_D D_D}{\mu}. \tag{4.29}$$

In this study, the representative diameter of the impeller channel is defined as

$$D_I = \frac{4Vol_I}{A_{SI}}, \tag{4.30}$$

where Vol_I is the volume of an impeller channel, and A_{SI} is the total wall area of an impeller channel. Similarly, the representative diameter of the diffuser channel is given by

$$D_D = \frac{4Vol_D}{A_{SD}}, \tag{4.31}$$

where Vol_D is the volume of a diffuser channel, and A_{SD} is the total wall area of a diffuser channel. The representative fluid velocity in the impeller channel is

$$V_I = \frac{Q + Q_{LK}}{A_I Z_I}, \tag{4.32}$$

where Q_{LK} is the leakage flow rate which circulates through the impeller in addition to the ESP throughput, A_I is the representative impeller channel cross sectional area, and Z_I is the impeller blade number. The representative fluid velocity in the diffuser channel is

$$V_D = \frac{Q}{A_D Z_D}, \tag{4.33}$$

where A_D is the representative diffuser channel cross sectional area, and Z_D is the diffuser vane number. Here, A_I and A_D are defined by

$$A_I = \frac{Vol_I}{L_I} \tag{4.34}$$

and

$$A_D = \frac{Vol_D}{L_D}. \tag{4.35}$$

4.1.3.2 Head Losses due to Turns. When fluid enters or exits ESP impeller and diffuser, pressure head losses are caused due to the changes of flow directions. The head losses for the turns in impeller and diffuser can be estimated as

$$H_{TI} = f_{TI} \frac{V_I^2}{2g} \tag{4.36}$$

and

$$H_{TD} = f_{TD} \frac{V_D^2}{2g}, \tag{4.37}$$

where f_{TI} and f_{TD} are the local drag coefficients, which are determined from experiments.

4.1.3.3 Leakage Losses. The pressure head difference across the leakage can be calculated by

$$H_{LK} = H_{IO} - \frac{U_2^2 - U_{LK}^2}{8g}, \tag{4.38}$$

where H_{IO} is the head increase across the impeller, and U_{LK} is the tangential velocity due to the impeller rotation at the leakage

$$U_{LK} = R_{LK}\Omega, \tag{4.39}$$

where R_{LK} is the radius corresponding to the leakage. Since the fluid rotation is caused by only one side, half of the tangential velocity of the impeller rotation may be counted. The head increase by the impeller can be estimated as

$$H_{IO} = H_{EE} - H_{FI} - H_{TI}. \tag{4.40}$$

The head loss across the leakage consists of contraction, expansion and friction components

$$H_{LK} = 0.5\frac{V_L^2}{2g} + 1.0\frac{V_L^2}{2g} + f_{LK}\frac{V_L^2 L_G}{2gS_L}, \tag{4.41}$$

where L_G is the leakage channel length, S_L is the width of the leakage. Therefore, the fluid velocity through the leakage can be calculated by

$$V_L = \sqrt{\frac{2gH_{LK}}{f_{LK}\frac{L_G}{S_L} + 1.5}}. \tag{4.42}$$

Assuming smooth leakage channel, the friction factor f_{LK} can be estimated based on Reynolds number and Churchill (1977) equations.

$$\mathrm{Re}_L = \frac{\rho V_L S_L}{\mu}. \tag{4.43}$$

Then, the leakage flow rate can be calculated,

$$Q_{LK} = 2\pi R_{LK} S_L V_L. \tag{4.44}$$

4.2 Mechanistic Modeling of Gas-liquid ESP Performance

This section discusses the mechanistic model development for gas-liquid flow inside a rotating ESP. Based on the slug dynamics in two-phase pipe flow, similar modeling procedure is performed, including the formulations of governing equations, closure relationships development, and computational algorithms.

4.2.1 Slug Dynamics in Rotating Centrifugal Pump

As shown in Figure 4.4, slug flow in pipe consists of a liquid slug body and a gas core region. For the slug flow in rotating ESP (see Figure 4.4b), similar structures can be observed from previous visualization experiments, although the exact shapes of the Taylor bubbles may vary. In this study, the slug flow regime in a rotating ESP under gassy conditions is assumed to associate with Taylor bubble flow, which is consistent with slug flow in pipes.

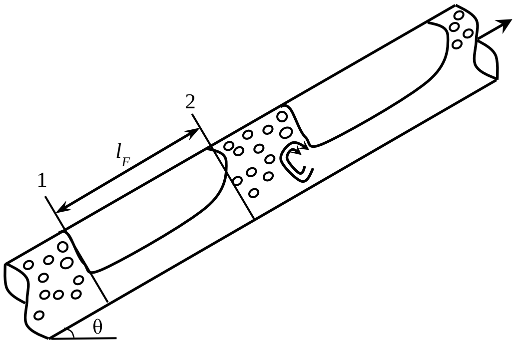

(a) control volume in unified model for two-phase pipe flow

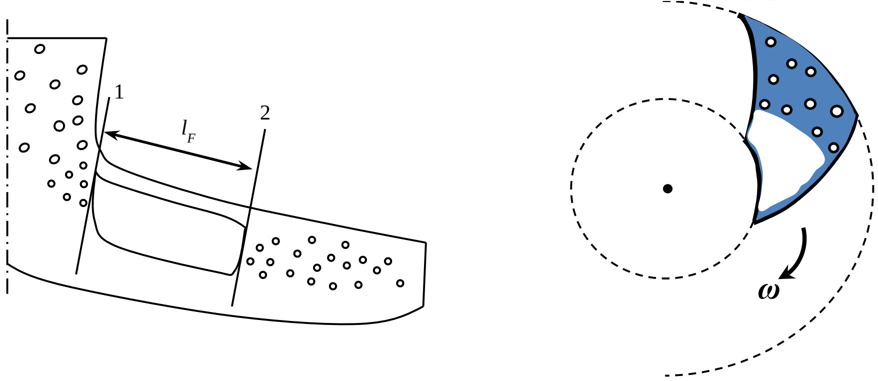

(b) slug flow in centrifugal pump

Figure 4.4 Schematic of slug flows in pipe and centrifugal pump

Proposed by Sachdeva (1998) and Sun (2003), the momentum equations along the streamline in a rotating centrifugal pump should be written as below

$$\left.\frac{dp}{dr}\right|_{streamline} = \left[-\rho_p W_p \frac{dW_p}{dr} + \rho_p \Omega^2 r + \left(\frac{dp}{ds}\right)_{f,p} \frac{ds}{dr} - \frac{M_{p,s}}{\alpha_p} \frac{ds}{dr} \right]_{streamline}, \tag{4.45}$$

where the subscript p is for phase, e.g. g for gas and l for liquid phase; *streamline* mean that the forces are projected on the streamline direction. $M_{p,s}$ is the interfacial momentum transfer between gas and liquid phases.

Multiplying Equation (4.45) by *dr/ds*:

$$\underbrace{\frac{dp}{ds}}_{a}=\underbrace{-\rho_p W_p \frac{dW_p}{ds}}_{b}+\underbrace{\left(\frac{dp}{ds}\right)_{f,p}}_{c}\underbrace{-\frac{M_{p,s}}{\alpha_p}}_{d}\underbrace{+\rho_p \Omega^2 r\Big|_{stream\,line}}_{e}, \tag{4.46}$$

where the subscript *s* is for the streamline direction. Terms (a ~ e) in the above equation correspond to pressure gradient, advection, friction, interfacial momentum transfer, and centrifugal body force, respectively. Apply Eq. (4.46) to the slug film in rotating centrifugal pump

$$\frac{(p_2-p_1)}{l_F}=\frac{\rho_L(v_T-v_F)(v_S-v_F)}{l_F}-\frac{\tau_I S_I+\tau_F S_F}{H_{LF}A}+\rho_L\Omega^2 R_I\Big|_{stream\,line} \tag{4.47}$$

and

$$\frac{(p_2-p_1)}{l_F}=\frac{\rho_C(v_T-v_C)(v_S-v_C)}{l_F}+\frac{\tau_I S_I}{(1-H_{LF})A}+\rho_C\Omega^2 R_I\Big|_{stream\,line}, \tag{4.48}$$

where Eq. (4.47) is the momentum balance of liquid phase, and Eq. (4.48) is for gas core/Taylor bubble. Then the combined momentum equation in a rotating ESP slug flow is obtained

$$\begin{aligned}&\frac{\rho_L(v_T-v_F)(v_S-v_F)-\rho_C(v_T-v_C)(v_S-v_C)}{l_F}-\frac{\tau_F S_F}{H_{LF}A}-\\&\tau_I S_I\left(\frac{1}{H_{LF}A}+\frac{1}{(1-H_{LF})A}\right)+(\rho_L-\rho_C)\Omega^2 R_I\Big|_{stream\,line}=0.\end{aligned} \tag{4.49}$$

Compared to the combined momentum equation for slug flow in pipe (Zhang et al., 2003), the difference in Eq. (4.49) is the body force term. All the velocities are the relative velocities to the ESP channel (see Figure 1.10).

4.2.2 Flow Pattern Transition

The flow pattern transition boundaries are similar to two-phase pipe flow. The flow map can be divided into four different flow regimes, namely dispersed bubble flow, bubbly flow, intermittent flow, and segregated flow. Based on the limited visualization results, the intermittent and segregated flows in a rotating ESP are slug flow and concurrent annular flow, respectively.

4.2.2.1 Dispersed Bubble to Bubbly Flow Transition. Gamboa and Prado (2011) summarized the flow pattern map in ESP based on pump's *H-Q* performance curves under two-phase flow conditions. From their study, three flow pattern regimes corresponding to different sections of *H-Q* curves can be identified, e.g.: homogeneous flow regime, bubbly flow regime, and gas pocket regime. They concluded that the pressure surging is an indicator of flow pattern transition from dispersed bubble flow to bubbly flow inside the ESP impeller. In wellbore flow, the transition boundary for these two flow patterns is modeled as (Shoham, 2006):

$$d_{\max} \leq d_{CD}\,, \tag{4.50}$$

where d_{max} is maximum bubble size in turbulent flow field, d_{CD} is the critical bubble diameter at which the bubbles start to deform and coalesce to form bigger ones. This critical diameter was first proposed by Brodkey (1967) and then modified by Barnea et al. (1982):

$$d_{CD} = 2\left[\frac{0.4\sigma}{(\rho_L - \rho_G)g}\right]^{0.5}. \tag{4.51}$$

In turbulent flow, bubbles are subjected to deformation, break-up, and coalescence by turbulence forces and interfacial tensions. According to Hinze (1955) theory, turbulence forces (τ), acting on the surface of the fluid particle tend to break up the bubbles into finer ones. On the other hand, interfacial tensions tend to coalesce small bubbles to generate bigger ones.

For the flow pattern transitions inside ESPs, similar bubble breakup and coalescence mechanism in pipe flow can be applied to rotating ESP multiphase flow. However, the calculations of $d_{\max}$ and d_{CD} in ESP impeller under two-phase flow conditions should be necessarily modified. The bubble size prediction model in centrifugal turbulent flow has been proposed in Zhu and Zhang (2017). The formula to estimate the representative bubble size in rotating ESP is given as

$$d_{\max} = 10.056\lambda_G \left(\frac{\sigma}{\rho_c}\right)^{\frac{3}{5}} \left(\frac{\Delta P Q_L}{\rho_c V}\right)^{-\frac{2}{5}} \left(\frac{\rho_c}{\rho_d}\right)^{\frac{1}{5}}, \tag{4.52}$$

where σ is the surface tension, ΔP is the pressure increment of single stage ESP, Q_L is the liquid flow rate, and V is the impeller volume. Subscripts c and d denote the continuous and dispersed phases, corresponding to water and air, respectively. Based on Barnea et al. (1982) study, the critical bubble diameter in the centrifugal multiphase flow can be modified as

$$d_{CRIT} = 2\left[\frac{0.4\sigma}{(\rho_L - \rho_G)\Omega^2 R_I}\right]^{0.5}, \tag{4.53}$$

where d_{CRIT} is the critical bubble diameter in multiphase centrifugal flow, R_I is the representative impeller diameter. The gravity acceleration g is replaced by centrifugal acceleration $\Omega^2 R_I$. In rotating ESP flow, the drag force should be balanced by centrifugal buoyancy force in radial direction due to the negligible effect of gravitational acceleration compared with centrifugal acceleration (Zhu and Zhang, 2017).

Substitute Eq. (4.61) and Eq. (4.62) into Eq. (4.59), the mechanistic model to predict the critical GVF at which ESP surging initiates can be obtained as

$$\lambda_C = \frac{2\left[\dfrac{0.4\sigma}{(\rho_L - \rho_G)\Omega^2 R_I}\right]^{\frac{1}{2}}}{10.056\left(\dfrac{\sigma}{\rho_L}\right)^{\frac{3}{5}}\left(\dfrac{\Delta P Q_L}{\rho_L V}\right)^{-\frac{2}{5}}\left(\dfrac{\rho_L}{\rho_G}\right)^{\frac{1}{5}}}. \tag{4.54}$$

4.2.2.2 Bubbly Flow to Intermittent Flow. For gas-liquid two-phase flow in pipeline, the transition boundary of bubbly flow to slug flow is predicted by bubble packing limit in 3D cubic lattice. The bubble coalescence increases sharply promoting the formation of Taylor-bubbles and slugging if the void fraction reaches 0.25, e.g. $\alpha_{Crit} = 0.25$. In rotating flow, α_{Crit} should be modified to accommodate rotational speeds associated with the mixing effect. At higher rotational speed N, bubbles are smaller with high surface energy. Turbulence energy is also high to break up bubbles. Thus, a higher α_{Crit} should be used. A correlation is proposed in this study

$$\alpha_{Crit} = \frac{\pi}{6} - \left(\frac{\pi}{6} - \frac{1}{4}\right)\exp\left(-\left(\frac{N}{N_{REF}}\right)^n\right), \tag{4.55}$$

where N_{REF} is the rotational speed at best efficient point, which is 3500 rpm for most ESPs. If $N = 0$ rpm (no-rotation), Eq. (4.55) is reduced to $\alpha_{Crit} = 0.25$, which is the value of the critical gas void fraction used in prediction of the transition boundary from bubbly flow to slug flow in two-phase well flow. If $N = +\infty$, the equation reduces to $\alpha_{Crit} = 0.52$, which corresponds to the maximum packing of bubbles. The index n is an empirical constant determined by experimental data.

4.2.2.3 Intermittent Flow to Segregated Flow. When the transition from slug flow to annular flow occurs, the momentum exchange term can be neglect. Given the superficial gas velocity v_{SG}, and making a guess for the superficial liquid velocity v_{SL}, the critical liquid holdup of the film can be obtained by following procedure.

The combined momentum balance equation can be reduced to

$$-\frac{\tau_F S_F}{H_{LF} A} - \tau_I S_I \left(\frac{1}{H_{LF} A} + \frac{1}{(1 - H_{LF})A} \right) + (\rho_L - \rho_C)\Omega^2 R_I \Big|_{stream\,line} = 0 \,. \tag{4.56}$$

The liquid holdup of the film can be calculated by

$$H_{LF} = \frac{\left(H_{LS}(v_T - v_T) + v_{SL}\right)\left(v_{SG} + v_{SL} F_E\right) - v_T v_{SL} F_E}{v_T v_{SG}} \,, \tag{4.57}$$

where v_F, H_{LC} and v_C can be expressed as:

$$v_F = \frac{v_{SL}(1 - F_E)}{H_{LF}} \,, \tag{4.58}$$

$$H_{LC} = \frac{v_{SL} F_E (1 - H_{LF})}{v_S - v_{SL}(1 - F_E)} \,, \tag{4.59}$$

$$v_C = \frac{v_S - v_{SL}(1 - F_E)}{1 - H_{LF}} \,. \tag{4.60}$$

A new value of v_F can be calculated from Eq. (4.65), and finally v_{SL} is obtained by

$$v_{SL} = \frac{v_F H_{LF}}{1 - F_E} \,. \tag{4.61}$$

Several iterations are required to converge. Thus, the transition boundary of slug flow to annular flow can be determined by the curve of v_{SL} versus v_{SG} in a flow pattern map.

4.2.3 Models for Different Flow Patterns

Once the flow pattern is determined, the combined momentum equation can be solved to obtain the in-situ gas void fraction (α_G) in a rotating ESP impeller. Then, the gas-liquid mixture density can be calculated to predict the pressure increment.

4.2.3.1 Dispersed Bubble Flow Model. For this flow regime, slippage between gas and liquid phases is neglected. Thus, the in-situ gas void fraction α_G in ESP impeller is

$$\alpha_G = \lambda_G . \tag{4.62}$$

The gas-liquid mixture density in ESP impeller and diffuser can be calculated as

$$\rho_M = (1 - \lambda_G)\rho_L + \lambda_G \rho_G \tag{4.63}$$

and

$$\rho_I = \rho_D = \rho_M . \tag{4.64}$$

where ρ_M is the density of gas-liquid mixture, ρ_I, ρ_D are the representative densities in ESP impeller and diffuser, respectively.

4.2.3.2 Bubbly Flow Model. Similar to the bubbly flow in two-phase pipe flow, the slippage between gas and liquid phases in ESP bubbly flow cannot be neglected.

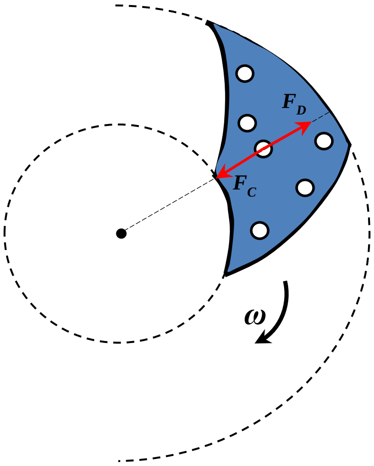

Figure 4.5 Schematic of force balance in radial direction on a gas bubble in rotating flow field

In rotating multiphase flow, the rotation generates a centrifugal force field where gas and liquid experience different body forces due to the density difference. This is similar as the buoyancy effect in a gravitational field. Consequently, the gas phase has a tendency to “float” toward the rotation center, since the gas density is much lower than liquid. Figure 4.5 shows the force balance on a gas bubble inside a rotating ESP flow field. Here, F_C and F_D represent the centrifugal buoyancy and drag force in the radial direction, respectively.

For the radial force balance, the gravity is neglected since it is much smaller than the centrifugal force (Estevam, 2002 and 2003; Barrios 2007). Due to the phase slippage, the liquid radial velocity (V_{LR}) is higher than the gas radial velocity (V_{GR}) and the drag force on the gas bubble points outward. The centrifugal buoyancy force, acting inward on the gas bubble, can be calculated as

$$F_C = \frac{\pi d_B^3}{6}\left(\rho_L - \rho_G\right) R_I \Omega^2, \tag{4.65}$$

where R_I is the representative impeller radius. The drag force on the gas bubble can be expressed as

$$F_D = C_D \rho_L \frac{V_{SR}^2}{2}\frac{\pi d_B^2}{4}. \tag{4.66}$$

V_{SR} is the relative velocity or velocity difference between liquid and gas in the radial direction. By equalizing Eq. (4.65) and (4.66), one can solve for V_{SR}

$$V_{SR} = \sqrt{\frac{4d_B}{3C_D}\frac{\left(\rho_L - \rho_G\right)}{\rho_L} R_I \Omega^2}. \tag{4.67}$$

For the gas-liquid flow inside ESP impeller, the total flow rate through the impeller is (Q+Q_{LK}), where Q_{LK} is the leakage flow rate through the stage gap between the impeller and diffuser. Then, the flow rates of gas and liquid can be calculated by: $(Q+Q_{LK})\ \lambda_G$ and $(Q+Q_{LK})(1-\lambda_G)$, respectively. The radial components of the liquid and gas velocities are:

$$V_{LR}=\frac{(Q+Q_{LK})(1-\lambda_G)}{(2\pi R_I-Z_IT_B)Y_I(1-\alpha_G)} \tag{4.68}$$

and

$$V_{GR}=\frac{(Q+Q_{LK})\lambda_G}{(2\pi R_I-Z_IT_B)Y_I\alpha_G}\,. \tag{4.69}$$

where Z_I is the impeller blade number, T_B is the blade thickness, Y_I is the representative impeller height. Thus, $V_{SR}=V_{LR}-V_{GR}$ can be expressed as

$$V_{SR}=\frac{(Q+Q_{LK})}{(2\pi R_I-Z_IT_B)Y_I}\left(\frac{1-\lambda_G}{1-\alpha_G}-\frac{\lambda_G}{\alpha_G}\right). \tag{4.70}$$

This equation can be rearranged into a quadratic relationship of λ_G and α_G as below:

$$R_S\alpha_G^2+(1-R_S)\alpha_G-\lambda_G=0\,, \tag{4.71}$$

where

$$R_S=\frac{V_{SR}(2\pi R_I-Z_IT_B)Y_I}{Q+Q_{LK}}\,. \tag{4.72}$$

Solving Eq. (4.71) and discarding the negative root, α_G can be obtained as

$$\alpha_G=\frac{R_S-1+\sqrt{(1-R_S)^2+4R_S\lambda_G}}{2R_S}\,. \tag{4.73}$$

To make Eq. (4.73) solvable, additional closure relationships for d_b and C_D are needed. In this study, the representative bubble sizes in a rotating ESP impeller can be calculated by Zhu and Zhang (2017) as

$$d_{32}=6.034\lambda_G\left(\frac{\sigma}{\rho_c}\right)^{\frac{3}{5}}\left(\frac{\Delta Pq}{\rho_cV}\right)^{-\frac{2}{5}}\left(\frac{\rho_c}{\rho_d}\right)^{\frac{1}{5}}, \tag{4.74}$$

where d_{32} is the Sauter mean diameter, ΔP is the pressure increment of single stage ESP, and V is the volume of impeller channel. Subscripts c and d denote the continuous and dispersed phases, respectively. The gas bubble size is needed to predict α_G. Previous studies (Chen and Middleman, 1967; Berkaman and Calabrese, 1988; Phongikaroon et al., 2001) suggest that a coefficient k can be used to correlate d_{32} and $d_{\max}$:

$$d_{32} = kd_{\max}. \tag{4.75}$$

The values of k may vary in different flows. Chen and Middleman (1967) proposed $k = 0.63$ for Rushton turbines in baffled tanks. Berkaman and Calabrese (1988) used $k = 0.67$ for Kenics static mixer. Phongikaroon et al. (2001) applied $k = 0.44$ to the Ross & Silverson rotor-stator mixer. Gamboa (2008) studied the bubble sizes inside a mixed-type ESP and reached $k = 0.42$ from the experimental data. In this study, the k value is obtained by comparing the model predicted α_G with the CFD simulation results so that a best-match k value can be optimized.

The drag coefficient C_D is based on the Legendre and Magnaudt (1998) approach for the viscous drag force on a spherical bubble in a rotating flow field,

$$C_D = C_{D,0}\left(1 + 0.55 Sr^2\right), \tag{4.76}$$

where Sr is the Strouhal number defined by $Sr = d_B\Omega/|u-v|$. u and v are phase velocities. $C_{D,0}$ is the drag coefficient proposed by Clift et al. (1978) without shear effect:

$$C_{D,0} = \frac{24}{\mathrm{Re}}\left(1 + 0.15\,\mathrm{Re}^{0.687}\right). \tag{4.77}$$

A recent numerical study by Rastello et al. (2011) showed that the Legendre and Magnaudt (1998) model is valid for Re > 50. At lower Reynolds number, Eq. (4.77) should be modified as:

$$C_D = C_{D,0}\left(1 + 0.3Sr^{2.5}\right). \tag{4.78}$$

Therefore, the drag coefficient C_D used in this paper combines Eq. (4.85) and Eq. (4.87) to cover a wide range of the Reynolds number. Then, Eq. (4.73) together with the closure relationships for the representative bubble size d_b and drag coefficient C_D can be solved for the in-situ α_G inside a rotating ESP impeller. An initial guess of V_{SR} and several iterations are needed to converge the solution. With the obtained α_G, the mixture density in ESP impeller and diffuser can be calculated by

$$\rho_I = \left(1 - \alpha_G\right)\rho_L + \alpha_G \rho_G \tag{4.79}$$

and

$$\rho_D = \left(1 - \lambda_G\right)\rho_L + \lambda_G \rho_G\,. \tag{4.80}$$

4.2.3.3 Intermittent Flow Model. The intermittent flow in a rotating ESP is very complicated with the transient and turbulent slug/churn flow characteristics inside highly curved channels. In this study, a co-current two-fluid slug model is applied to ESP intermittent flow. The basic assumption is that the Taylor bubbles prevail if the intake GVF increases further after the formation of gas pocket. According to Estevam (2002) and Thum et al. (2006) visualization experiments, where the elongated bubble followed by a short liquid slug was observed, such assumption is reasonable due to the neglect of gravitational force. The governing equations have been derived in previous sections. Additional closure relationships, such as friction factors at solid wall and liquid-gas interface, liquid entrainment rate, slug liquid holdup, translational velocity and slug length, are needed to make the governing equations solvable.

The shear stresses in the combined momentum equation Eq. (4.49) are given by:

$$\tau_F = f_F \frac{\rho_L |v_F| v_F}{2} \tag{4.81}$$

and

$$\tau_I = f_I \frac{\rho_C |v_C - v_F| (v_C - v_F)}{2}. \tag{4.82}$$

where the subscripts F and I are for film and interface, respectively. Based on Blasius correlation, the friction factor f_F at the solid wall can be expressed as

$$f = C\,\mathrm{Re}^{-n}, \tag{4.83}$$

where C = 16, n = 1 for laminar flow if Reynolds number is less than 2000; C = 0.0046, n = 0.2 for turbulence flow in smooth pipe if the Reynolds number is higher than 3000. The wall roughness should be accounted for in a rough channel. For Reynolds number between 2000 and 3000, the friction factor is interpolated to prevent discontinuity across the transition regime.

For the interfacial friction factor, Asali (1984) correlation, which is improved by Ambrosini et al. (1991), can be used:

$$f_I = f_G \left(1 + 13.8 We_G^{0.2} \mathrm{Re}_G^{-0.6} \left(h_F^+ - 200\sqrt{\rho_G/\rho_L}\right)\right), \tag{4.84}$$

where the dimensionless variables We_G and Re_G are given by

$$We_G = \frac{\rho_G v_C^2 d}{\sigma} \tag{4.85}$$

and

$$\mathrm{Re}_G = \frac{\rho_G v_C d}{\mu_G}. \tag{4.86}$$

h_F^+ is the dimensionless thickness of the liquid film, which is calculated as

$$h_F^+ = \frac{\rho_G h_F v_C^*}{\mu_G}, \tag{4.87}$$

where

$$v_C^* = \sqrt{\frac{\tau_I}{\rho_G}} \,. \tag{4.88}$$

Assuming uniform film thickness δ_L in ESP slug flow (Sylvester, 1987), the geometrical parameters are derived as below:

$$A_C = \pi (d_I - 2\delta_L)^2 / 4 \,, \tag{4.89}$$

$$A_F = \pi \delta_L (d_I - \delta_L), \tag{4.90}$$

$$S_I = \pi (d_I - 2\delta_L), \tag{4.91}$$

$$S_L = \pi d \,, \tag{4.92}$$

where A_C and A_F are the cross section area of gas core and liquid film. S_I and S_L are the perimeter of interface and liquid film, respectively. d_I is the equivalent hydraulic diameter in impeller. The hydraulic diameter of liquid film and gas core are given as

$$d_F = 4\delta_L (d_I - \delta_L) / d_I \tag{4.93}$$

and

$$d_C = (d_I - 2\delta_L). \tag{4.94}$$

Therefore, the Reynolds number for gas core and film can be determined by

$$\mathrm{Re}_C = \frac{\rho_C v_C d_C}{\mu_C} \tag{4.95}$$

and

$$\mathrm{Re}_F = \frac{\rho_L v_F d_F}{\mu_L} \,. \tag{4.96}$$

The liquid entrainment fraction, f_E is defined as the fraction of liquid flow rate that is entrained in the gas core as droplets. The empirical correlations proposed by Wallis (1969) and Ishii and Mishima (1989) are used in this study.

Wallis (1969) correlation:

$$F_E = 1 - \exp\left(-0.125\left(\frac{10^4 v_{SG}\mu_G}{\sigma}\left(\frac{\rho_G}{\rho_L}\right)^{0.5} - 1.5\right)\right). \tag{4.97}$$

Ishii and Mishima (1989) correlation:

$$F_E = \tanh\left(7.25\times 10^{-7}\left(\frac{\rho_G v_G^2 d_F}{\sigma}\left(\frac{\rho_L-\rho_G}{\rho_G}\right)^{1/3}\right)^{1.25}\mathrm{Re}_F^{0.25}\right). \tag{4.98}$$

The unified model proposed by Zhang et al. (2003) is employed to calculate the slug liquid holdup, a parameter to make the governing equations solvable.

$$H_{LS} = \frac{1}{1+\dfrac{T_{SM}}{3.16\left[\left(\rho_L-\rho_G\right)g\sigma\right]^{1/2}}}, \tag{4.99}$$

where T_{SM} is expressed as

$$T_{SM} = \frac{1}{C_E}\left[\begin{array}{l}\dfrac{f_S}{2}\rho_S v_M^2 + \dfrac{d}{4}\dfrac{\rho_L H_{LF}\left(v_T-v_F\right)\left(v_M-v_F\right)}{l_s} \\ +\dfrac{d}{4}\dfrac{\rho_C\left(1-H_{LF}\right)\left(v_T-v_C\right)\left(v_M-v_C\right)}{l_s}\end{array}\right]. \tag{4.100}$$

And C_E is given by:

$$C_E = \frac{2.5-\left|\sin\left(\theta\right)\right|}{2}, \tag{4.101}$$

where θ is the inclination angle of pipe. g in Eq. (4.99) can be replaced by centrifugal acceleration $\Omega^2 R_I$ in radial type ESPs,

$$H_{LS} = \frac{1}{1+\dfrac{T_{SM}}{3.16\left[\left(\rho_L-\rho_G\right)\Omega^2 R_I\sigma\right]^{1/2}}}. \tag{4.102}$$

Slug flow in a rotating ESP can be viewed as co-current downward flow and the inclination angle can be assumed to be $\theta = -\pi/2$. Thus, $C_E = 0.75$.

The mixture density in slug body is defined as

$$\rho_S = \rho_L H_{LS} + \rho_G (1 - H_{LS}). \tag{4.103}$$

The friction factor is calculated with the Reynolds number given by

$$\mathrm{Re}_S = \frac{\rho_S v_S d}{\mu_L}. \tag{4.104}$$

An initial guess using Gregory et al. (1978) correlation can be used:

$$H_{LS} = \left(1 + \left(\frac{v_S}{8.66} \right)^{1.39} \right)^{-1}. \tag{4.105}$$

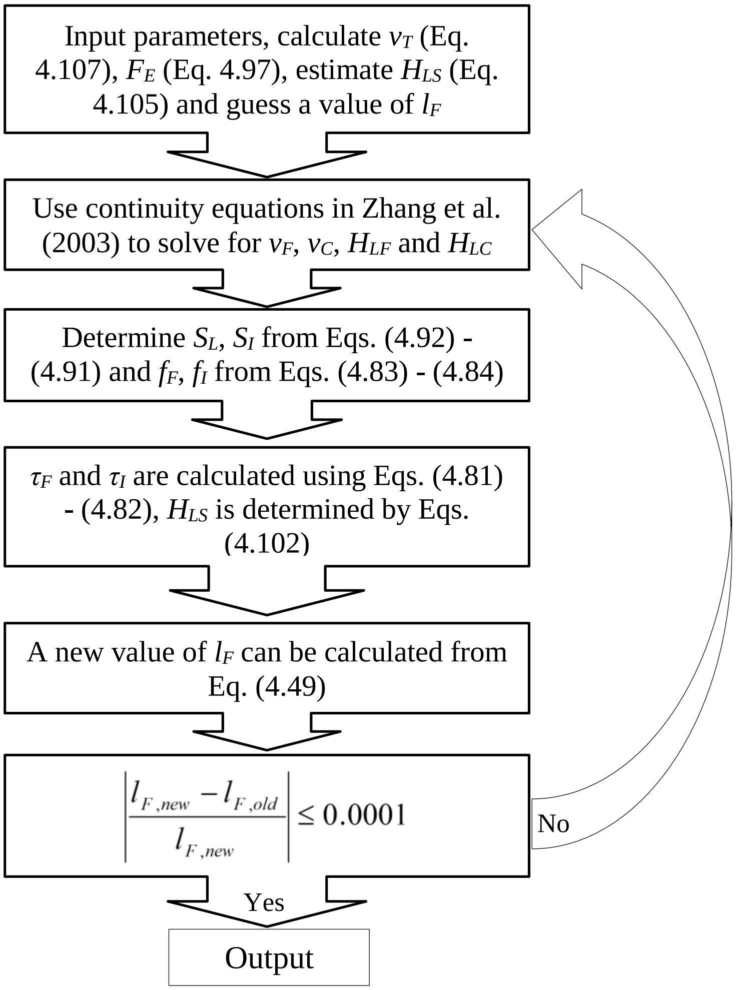

Figure 4.6 Flow chart for slug flow calculation inside a rotating ESP impeller

There is no study regarding slug or Taylor bubble length in a rotating ESP impeller under two-phase flows. Since the bubbles accumulate from the suction to discharge of ESP's impeller, which eventually occupies the whole flow passage and chokes fluid flow, the flow passage length can be deemed as portion of the slug unit length in pipe flow. The calculation flow chart for slug flow in rotating ESP impeller is presented in Figure 4.6.

4.2.3.4 Segregated Flow Model. For segregated flow pattern, the combined momentum equation of Eq. (4.58) is reduced to Eq. (4.65). A uniform liquid film thickness δ_L is assumed,

$$\delta_L = \frac{d_I}{2}\left(1 - \sqrt{1 - H_{LF}}\right) . \tag{4.106}$$

The above mentioned Eqs. (4.98) ~ Eq. (4.103) are used to describe the geometrical parameters of liquid film and gas core. Thus, the mass balance equations in the segregated flow are given by:

$$q_F = q_L = A_P v_{SL}(1 - f_E) = v_F A_F , \tag{4.107}$$

and

$$q_C = q_G + q_E f_E = A_P (v_{SG} + v_{SL} f_E) = v_C A_C . \tag{4.108}$$

where the velocities of liquid film and gas core can be calculated by:

$$v_F = v_{SL} \frac{(1 - f_E) d_I^2}{4\delta_L (d_I - \delta_L)} , \tag{4.109}$$

and

$$v_C = \frac{(v_{SG} + v_{SL} f_E) d_I^2}{(d_I - 2\delta_L)^2} . \tag{4.110}$$

Similar to the intermittent flow, the closure relationships of Eqs. (4.81) ~ (4.84) are used to calculate the shear stress τ_I and τ_F in Eq. (4.56). The Reynolds number calculation follows Eqs. (4.95) and (4.96). And the gas core properties are given by:

$$\rho_C = \rho_G \alpha_C + \rho_L (1 - \alpha_C), \tag{4.111}$$

And

$$\mu_C = \mu_G \alpha_C + \mu_L (1 - \alpha_C). \tag{4.112}$$

where the gas core void fraction α_C is calculated as:

$$\alpha_C = \frac{v_{SG}}{v_{SG} + v_{SL} f_E} \quad . \tag{4.113}$$

From Eqs. (4.97) ~ (4.98), the liquid entrainment fraction f_E can be determined. Thus, all unknowns in Eq. (4.65) can be related to the liquid holdup of film H_{LF}, which can be solved by iterations. Finally, the total gas void fraction can be calculated as:

$$\alpha_T = \alpha_C \left(1 - 2\frac{\delta_L}{d_I}\right)^2 . \tag{4.114}$$

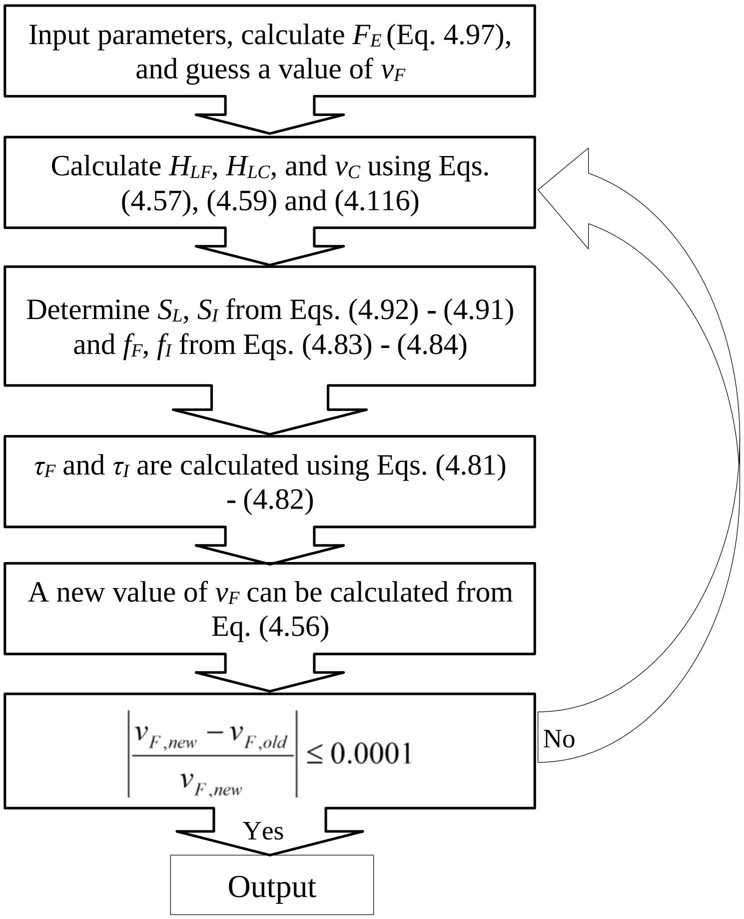

Figure 4.7 Flow chart for segregated flow calculation in rotating ESP impeller

The calculation procedure for the segregated flow is shown in Figure 4.7. Figure 4.8 summarizes the complete calculation flow chart for ESP impeller under two-phase flow conditions.

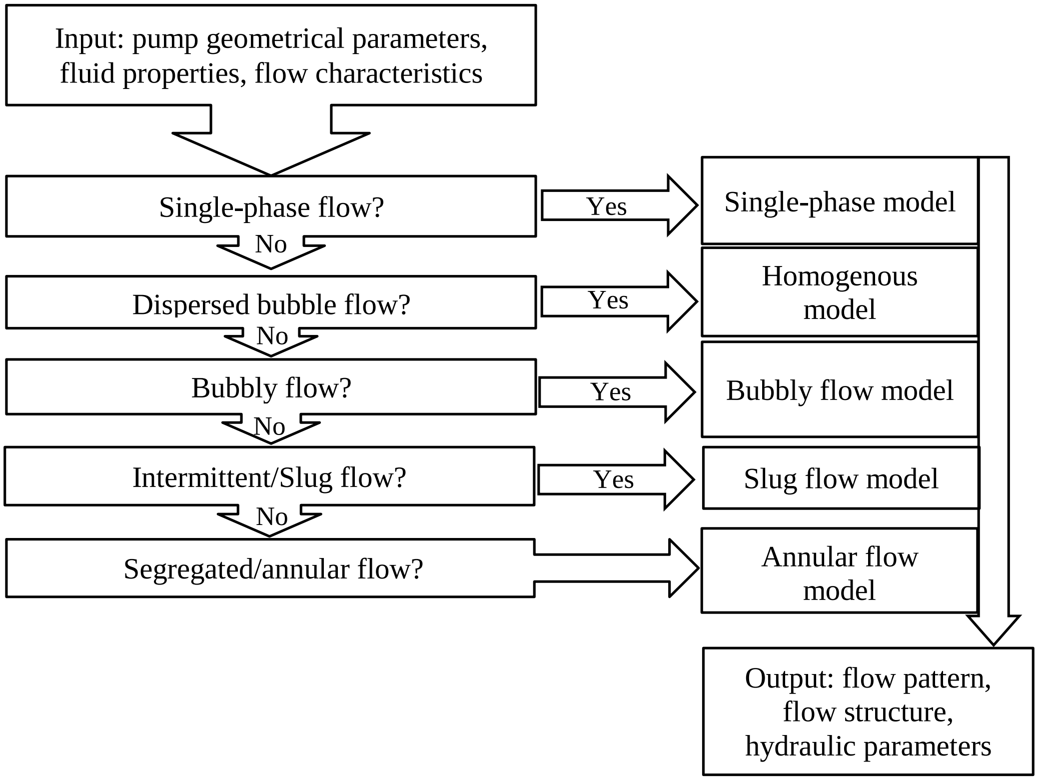

Figure 4.8 Flow chart for gas-liquid flow calculation inside a rotating ESP impeller

4.2.4 ESP Head of Gas-liquid Flow

As discussed in previous sections, the in-situ gas void fraction (α_G) can be predicted through the mechanistic models. Thus, the mixture properties of gas and liquid can be estimated based on which the ESP boosting pressure can be calculated. This mechanistic model considers effects of gas volumetric fraction, gas density (or density difference between gas and liquid, also reflecting pressure effect), bubble size (as a result of turbulence, shear, interfacial tension, etc.), liquid viscosity, rotation speed, flow rates besides the pump geometry. The volumetric average density of the gas-liquid mixture in an ESP impeller is calculated as:

$$\rho_I = (1-\alpha_G)\rho_L + \alpha_G\rho_G \, . \tag{4.115}$$

The mixture density in the ESP diffuser can be estimated based on the no-slip gas volumetric fraction λ_G,

$$\rho_D = (1-\lambda_G)\rho_L + \lambda_G\rho_G \, . \tag{4.116}$$

Based on the Euler equation, when $Q < Q_{\mathrm{BM}}$, the boost pressure in ESP can be expressed as,

$$P_{EE} = \rho_I \frac{U_2^2 - U_1^2}{2} + \rho_I \frac{W_1^2 - W_2^2}{2} + \rho_I \frac{C_{2E}^2 - C_1^2}{2} + \rho_D \frac{C_{2F}^2 - C_1^2}{2} \, . \tag{4.117}$$

When $Q > Q_{BM}$ the boost pressure in ESP can be expressed as,

$$P_{EE} = \rho_I \frac{U_2^2 - U_1^2}{2} + \rho_I \frac{W_1^2 - W_2^2}{2} + \rho_I \frac{C_{2E}^2 - C_1^2}{2} + \rho_D \frac{C_{2E}^2 - C_1^2}{2} \, . \tag{4.118}$$

4.3 Mechanistic Model Results

This section presents the prediction results by mechanistic models and the comparisons against the available experimental data, including previous studies in TUALP and the experimental measurements conducted in this study. The validations of closure relationships, including bubble size prediction, surging initiation and in-situ gas void fractions etc., against either experimental data or numerical simulation results are also presented.

4.3.1 Bubble Size Prediction Model Validation

As Figure 4.9 shows, the bubble sizes predicted by the new model match the CFD simulated values much better (Figure 4.9a). The existing bubble size models predict the representative bubble sizes in rotating ESP impeller with higher than 100% errors, some even more than 400%. In contrast, the predicted bubble sizes by the new model proposed in this study (Eq. 4.61) are mostly bounded by ±10% error lines (see Figure 4.9b).

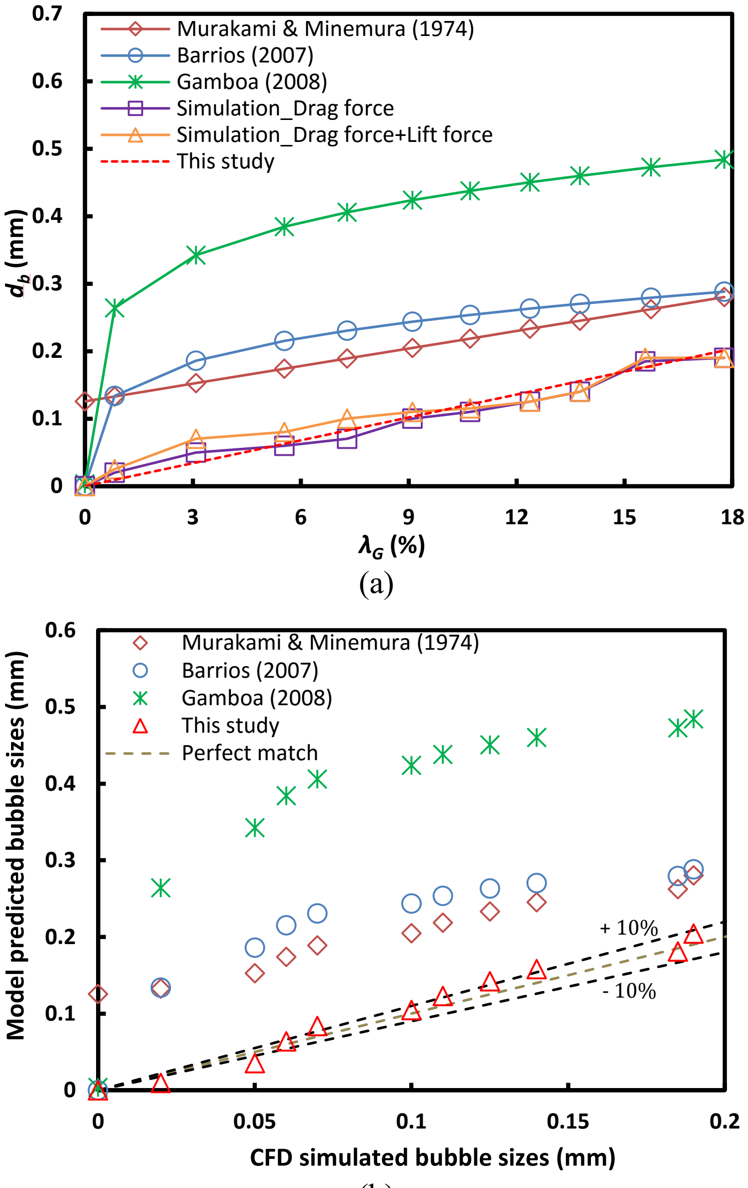

(a)

(b)

Figure 4.9 Comparison of bubble size predictions by existing models with CFD simulated results at BEP, (a) d_b versus λ_G, (b) model prediction deviations

To verify the new bubble size prediction model, an off-design point from Salehi experimental study is selected for further CFD simulations according to the affinity laws (Stepanoff, 1957). The rotational speed at the off-design point is 1500 rpm. Thus, the liquid flow rate and pumping head are calculated as 2.123 kg/s and 2.96 m. Gas is injected at stage 10, while the liquid flow rate is kept constant. The bubble sizes used to conduct CFD simulations are estimated by Eq. (4.61), as shown in Figure 4.10.

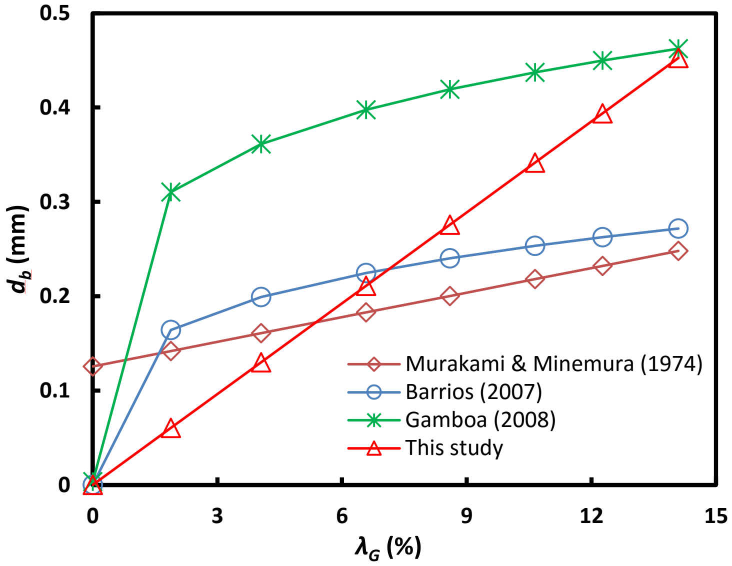

Figure 4.10 Estimated bubble sizes at the off-design point with $N = 1500$ rpm

Compared to BEP with rotational speed of 3500 rpm, the bubble sizes predicted by existing models remain almost unchanged. However, the predicted bubble sizes by the new model at lower rotational speed are considerably bigger than that at high rotational speed. This is reasonable since the turbulent kinetic energy is lower at lower pump rotational speed, which leads to bigger bubble size.

With the predicted bubble sizes by Eq. (4.61), CFD simulations are carried out at the off-design point. Figure 4.11 summarizes the error analysis of the numerically-simulated ESP two-phase performance under both BEP and the off-design point, corresponding to N = 3500 rpm and 1500 rpm. All the CFD simulation results of N_p in

Figure 4.11 are obtained with the incorporation of the new bubble size model. As can be seen, a good agreement between numerical simulation results of N_p against Salehi experimental results is obtained, which further validates the bubble size modeling methodology adopted in this study.

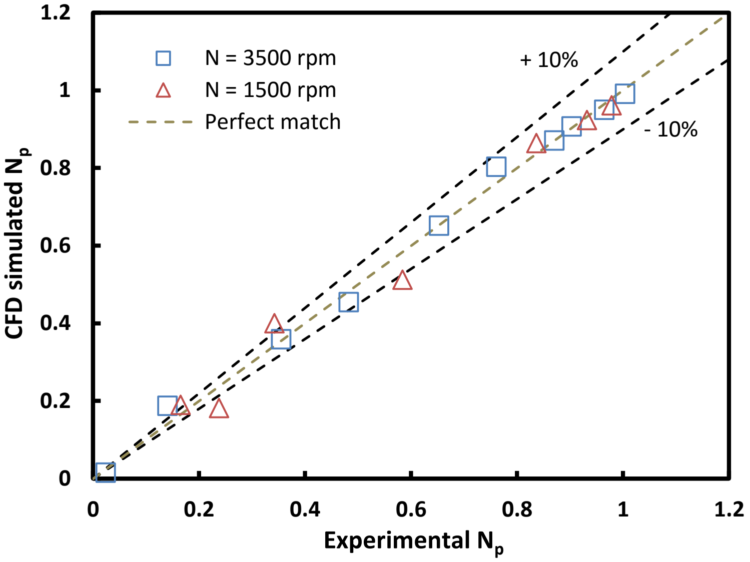

Figure 4.11 CFD simulated normalized pressures with new bubble size model compared with experimental data

4.3.2 Surging Initiation Model Validation

As discussed above, the surging initiation is of great importance to ESP operations under two-phase flow conditions since it not only corresponds to the flow pattern transition from dispersed bubble flow to bubble flow, but also coincides with the instabilities of ESP flow conditions. Here, the mechanistic model predicted ESP pressure surging initiation is compared with the experimental observation.

Figure 4.12 compares the predictions of surging initiation correlations available in the literature. The same flow conditions with rotational speed N = 3500 rpm and pump intake pressure at P_{sep} = 150 psig are used. As Figure 4.12 shows, the predictions of ESP surging initiation vary significantly among the existing correlations. Turpin et al. (1986) and Pessoa (2001) suggested that pressure surging is independent on liquid flow rates. Other studies (Duran, 2003; Zapata, 2003; Gamboa and Prado, 2011) indicate that λ_C changes with Q_L. However, these correlations exhibit very different trends. Duran and Zapata correlations predict λ_C in monotonic-increase trend with respect to Q_L. Gamboa and Prado correlated λ_C and Q_L by a concave quadratic function, and claimed that this model was validated for $Q_L/Q_{max} > 0.2$, beyond which the prediction error might occur.

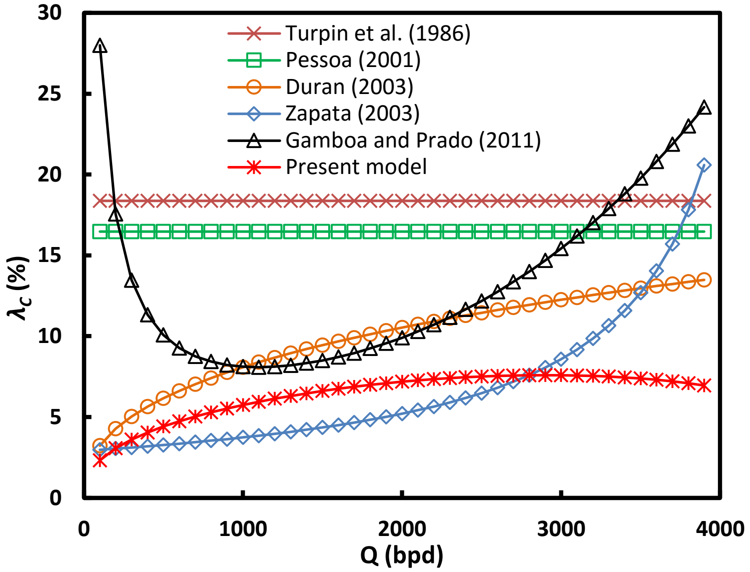

Figure 4.12 Comparison of surging initiation models at $N = 3500$ rpm and $P_{sep} = 150$ psig

The contradictions in the existing surging correlations imply that the dominant mechanism for initiating pressure surging and causing ESP boosting pressure breakdown is still not well understood. Inevitably, empirical methods were used to formulate these correlations. Thus, it is questionable to extend these correlations to different flow conditions or pumps.

The new mechanistic model of this study is also presented in Figure 4.12. Different from the empirical correlations in literature, λ_C predicted by Eq. (4.54) exhibits a dome shape with a local maximum λ_C at Q_L close to BEP. From the bubble size model (Eq. 4.52), BEP approximately corresponds to the minimum value of d_{max}. Small bubble size results in a higher λ_C.

At lower Q_L, the turbulent kinetic energy in ESP impeller is small. It is easier for bubbles to coalesce and form larger size. The flow pattern transition and pressure surging will occur earlier at lower λ_C. At higher Q_L, the hydraulic head of ESP becomes lower. Thus, the turbulent kinetic energy of fluids will decrease according to Padron (2004) study $\varepsilon = k\Delta PQ_L/(\rho V)$, where k is a constant obtained from experiments. Bubbles are more likely to coalesce and generate bigger ones, leading to quicker decrease of pump boosting pressure.

Figure 4.13 shows the validation of the new mechanistic model by comparing with the experimental results of surging test at BEP flow conditions. The separator pressure is kept at 100 psig. The stages 3, 5 and 7 are investigated. Five liquid flow rates are tested, i.e. 1868, 2335, 2700, 3035, and 3502 bpd. The experimental values of λ_C can be obtained by reading from the surging test plots, where the ESP pressure surging is considered to be triggered if the pump stage pressure increment deviates more than 5% from the linear trend of surging test plots corresponding to relatively lower GVFs.

As can be seen from Figure 4.13, the solid curves represent model predicted λ_C, while the red circles are obtained from the surging test plots. The error bar is marked on each data point to show the experimental measurement error. The detailed error analysis regarding GVF calculation is presented in Appendix F. From the comparison in Figure

4.13, a good agreement of model predicted λ_C with experimental results is found for the investigated stages. Besides, the dome-shape λ_C versus liquid flow rates Q_L is confirmed by experimental results.

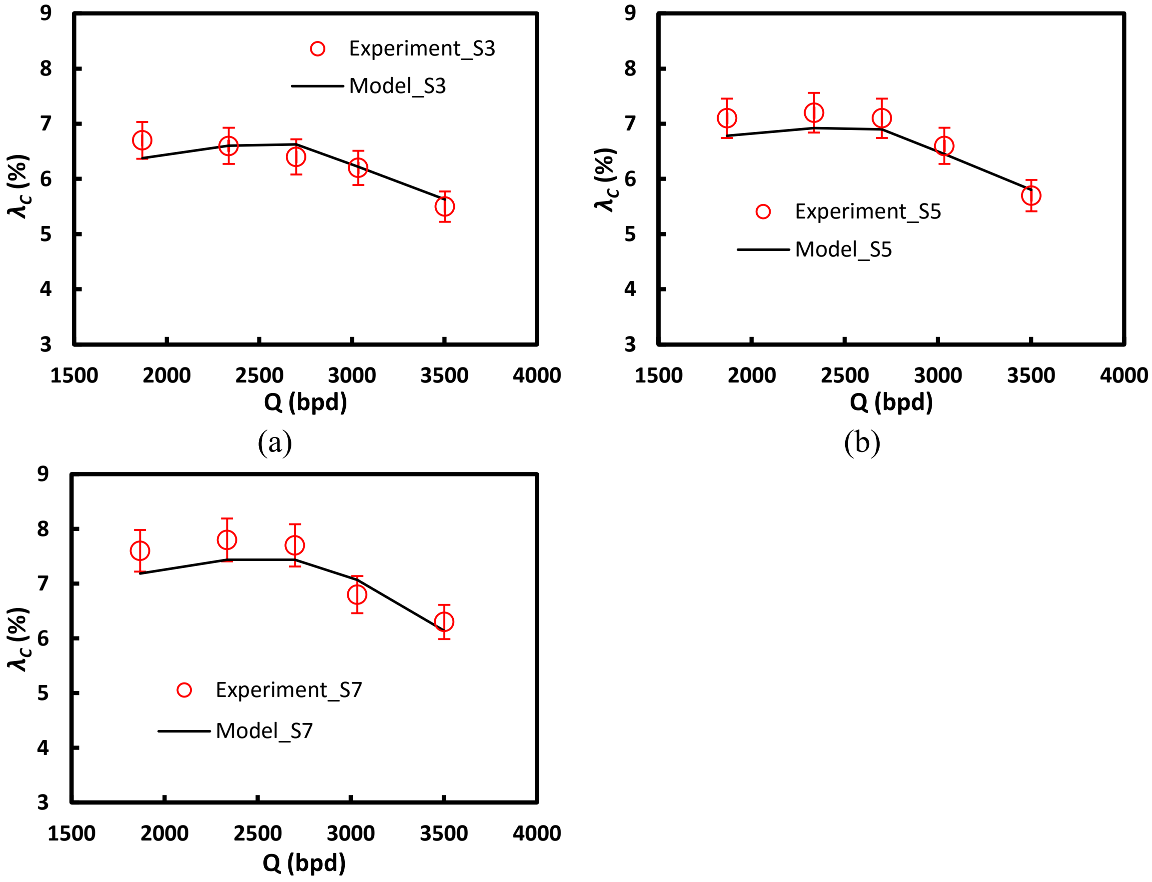

(a)

(b)

(c)

Figure 4.13 Comparison of mechanistic model predictions with surging test results at N = 3500 rpm, P_{sep} = 100 psig in different ESP stages, (a) stage 3, (b) stage 5, (c) stage 7

The comparison of mechanistic model predictions with data from Gamboa (2008) experimental study is presented in Figure 4.14. Using the single-stage mixed-type GC-6100 ESP, Gamboa conducted extensive surging tests under varying flow conditions, including different rotational speeds (1500, 1800, 2400 and 3000 rpm) and inlet pressure (100, 150, 200, and 250 psig), as well as various liquid/gas flow rates. The predicted λ_C are obtained with the same flow conditions in Gamboa experiments. The mechanistic model predicted λ_C is mostly bounded by –20% and +10% error lines. Besides the measurement error (see Appendix F), the difference between model predictions and data may be resulted from the pump type and geometrical differences.

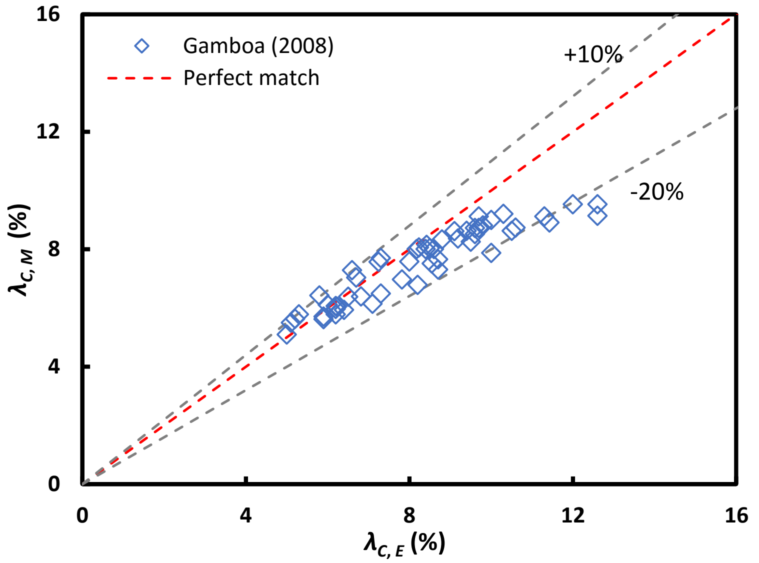

Figure 4.14 Comparison of model predicted λ_C with Gamboa (2008) experimental results

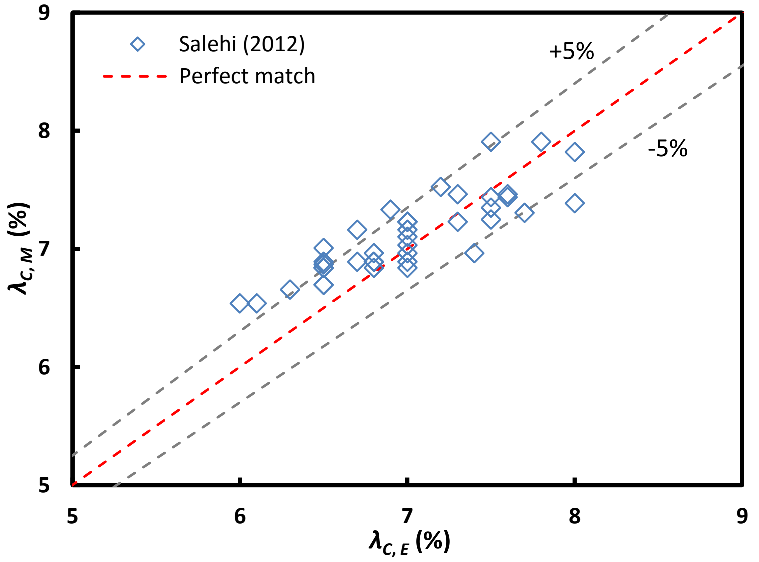

Figure 4.15 Comparison of model predicted λ_C with Salehi (2012) experimental results

A satisfactory agreement is observed between the model predictions and experimental results of Salehi (2012) for surging tests on a multistage ESP, as shown in Figure 4.15 above. With the same pump model used in this study, Salehi conducted experimental investigation of stage effect on ESP pressure increment under water-nitrogen two-phase flow conditions. The measurement covers a wide range of flow conditions, including gas/liquid flow rates, pump rotational speeds, inlet pressure and pump stages. The comparison of model predicted λ_C with Salehi experimental results shows a prediction error about ±5%, which further verifies the reliability of the proposed surging initiation model.

4.3.3 In-situ Gas Void Fraction (α_G) Validation

The direct validation of the mechanistic model for predicting α_G in a rotating ESP impeller with experimental measurements is not available. An indirect validation approach by comparing α_G predicted from the mechanistic model with CFD simulated values is used in this study. The numerically simulated ESP pressure increment under gassy flow conditions are first adjusted to the corresponding experimental results. Extracting the gas phase fraction distributions from the numerical simulation outputs, the comparison between the mechanistic model predictions and the numerical simulation results for the in-situ α_G can be carried out.

Figure 4.16 compares the in-situ α_G obtained by the mechanistic model for bubbly flow in a rotating ESP impeller with the corresponding multiphase CFD simulation results. The solid lines depict the CFD simulated α_G, while the dashed lines represent mechanistic model predictions. The homogeneous model denoted by the dot-dash line, is also included for comparison. From CFD simulation results, a non-linear increasing trend of the in-situ α_G versus λ_G can be observed. Although good agreement between α_G predicted by the homogeneous model and the CFD simulations is seen at relatively low λ_G, the numerically simulated α_G deviates from the homogeneous model prediction as λ_G increases to above 5%. As shown in Figure 4.16, the mechanistic model predictions agree well with the numerically-simulated α_G in trend. The values of in-situ α_G calculated by the mechanistic model slightly deviate from the corresponding numerical results. However, the predictions are much better if compared with the previous empirical correlations (see Figures 4.17 and 4.18 below).

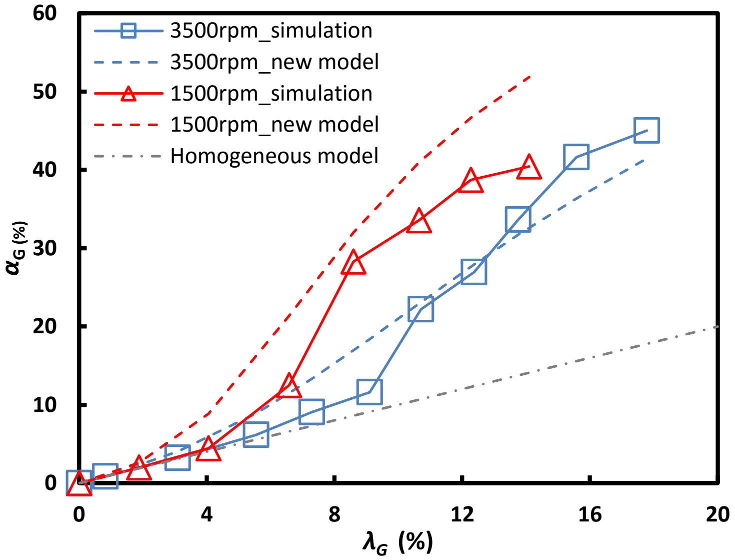

Figure 4.16 Comparison of model predicted α_G with CFD simulations

Figure 4.17 compares the new mechanistic model predictions of in-situ α_G with empirical correlations at N =3500 rpm. The new mechanistic model predicts α_G with an error less than 25%, and most values are bounded by 10% error line. In contrast, the in-situ α_G predicted by the empirical correlations deviates from numerical results significantly as

λ_G increases. Such discrepancy implies that the slippage-dominated two-phase flow mechanism in an ESP impeller is not fully captured by empirical correlations.

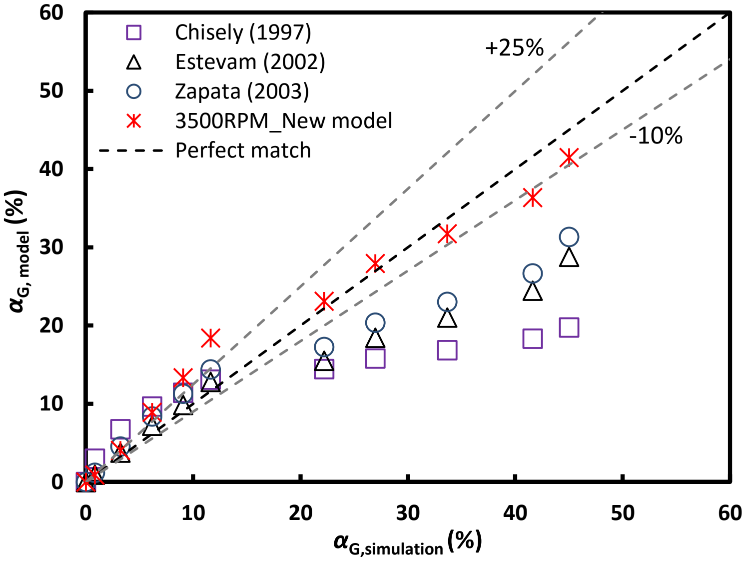

Figure 4.17 Comparison of new mechanistic model with empirical correlations at N = 3500 rpm against CFD simulated α_G

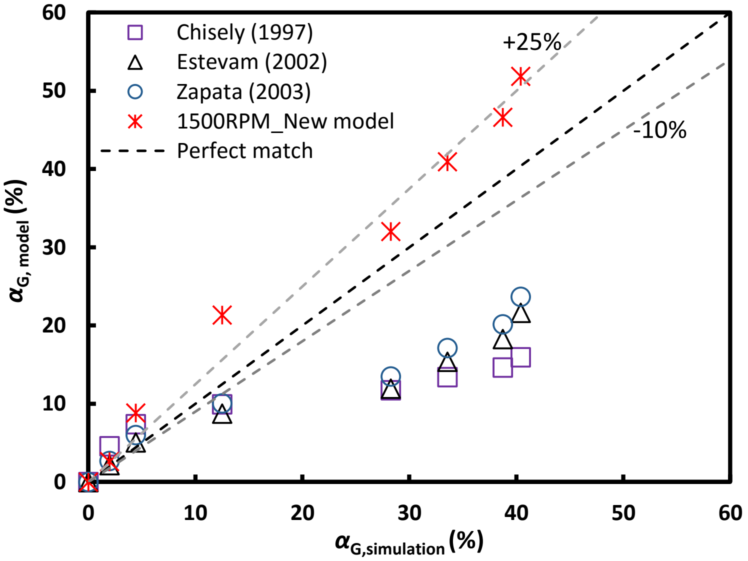

Figure 4.18 Comparison of new mechanistic model with empirical correlations at N = 1500 rpm against CFD simulated α_G

Another comparison is shown in Figure 4.18 for N = 1500 rpm. Again, the in-situ α_G predicted by the new mechanistic model, with the maximum prediction error bounded by 25% error lines, is much better than the previous empirical correlations, whose predictions exceed more than 50% error.

For mechanistic modeling, the closure relationships are needed to make models solvable, including bubble size and drag coefficient calculations, and thus it is necessary to study their effects on predicting in-situ α_G.

Figure 4.19 compares the in-situ α_G predicted by the mechanistic model with implementations of different bubble size models under BEP flow conditions. As can been seen, the considerable deviation of the obtained α_G by the mechanistic model from numerical simulation results occurs if the Gamboa bubble size model is used. By incorporating the Barrios bubble size model, the predicted in-situ α_G is closer to the CFD simulation results. However, the values depart from numerically-simulated α_G at higher λ_G. The difference is more prominent under off-design flow conditions with N = 1500 rpm, which is shown in Figure 4.20.

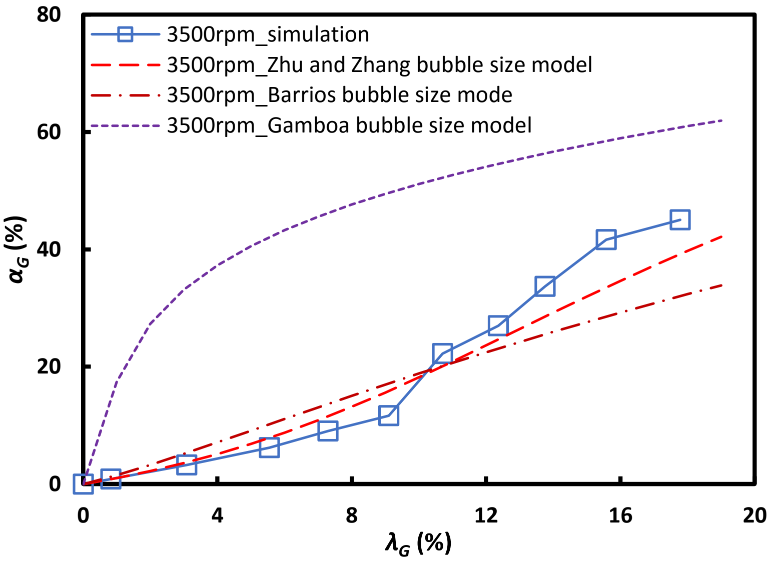

Figure 4.19 Effects of bubble size models on α_G prediction at N = 3500 rpm

As shown in Figure 4.20, the in-situ α_G is underestimated with the Barrios bubble size model at higher λ_G (> 7%). The Gamboa bubble size model results in remarkable overestimations of α_G compared with the CFD simulation results. However, by using the bubble sizes calculated from Eq. (4.83) into the mechanistic model, the in-situ α_G predictions are much better. Thus, compared with the existing bubble size models in literature, the model proposed in our previous study (Zhu and Zhang, 2015) provides the best prediction of α_G inside the rotating ESP impeller.

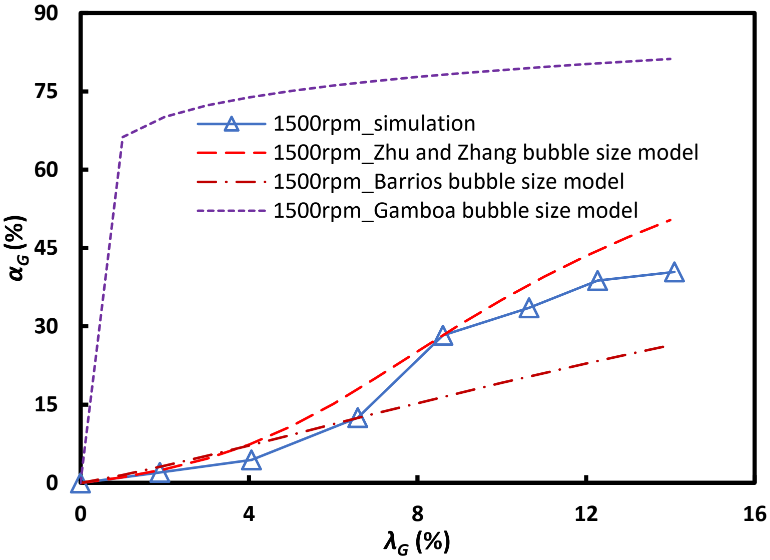

Figure 4.20 Effects of bubble size models on α_G prediction at $N = 1500$ rpm

The drag coefficient (C_D) characterizes the interfacial momentum transfer by drag forces between gas and liquid phases. The empirical correlations (Eqs. 4.85 ~ 4.87) based on the C_D in pipe flows are used in this study.

Figures 4.21 and 4.22 show the comparison of mechanistic model predicted α_G with the numerical simulation results using two different C_D calculation methods. One is based on the Barrios correlation (Eqs. 1.35 ~ 1.37). The other one is a new model for calculating C_D proposed in this study. It combines the Legendre and Magnaudt (1998) model (Eq. 4.85) and the Rastello et al. (2011) model (Eq. 4.87) to cover a wide range of Reynolds number.

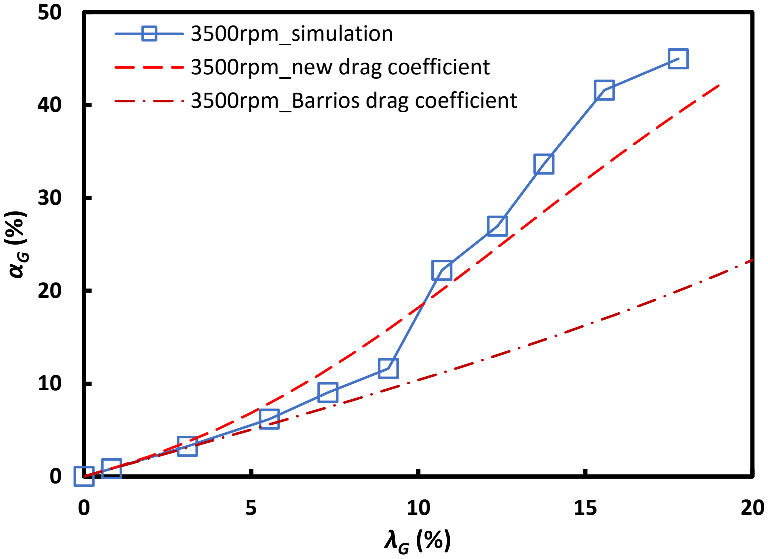

Figure 4.21 Effect of drag coefficient models on α_G prediction at $N = 3500$ rpm

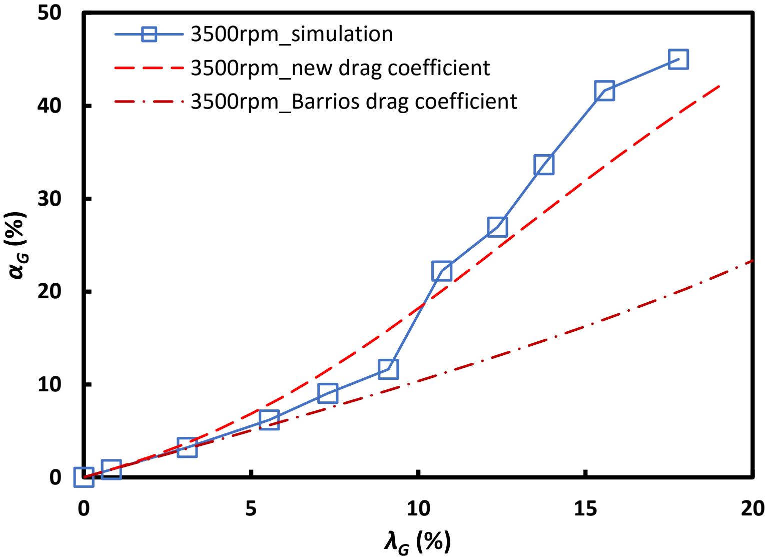

Figure 4.22 Effect of drag coefficient models on α_G prediction at $N = 1500$ rpm

Compared with the CFD simulated in-situ α_G, the mechanistic model using the new C_D calculation approach gives a better agreement at both BEP (Figure 4.21) and the off-design operation point (Figure 4.22). Applying the Barrios C_D correlation to the mechanistic model, the predictions of in-situ α_G, match the numerically-simulated values at small λ_G (< 5%). Considerable deviation is found at higher λ_G (> 7%) and lower rotational speed (N = 1500 rpm). Moreover, the non-linear trend of the in-situ α_G versus λ_G is not well captured if the Barrios C_D correlation is use in the mechanistic model. Much better predictions of in-situ α_G can be achieved using the new C_D calculation approach in the mechanistic model.

4.3.4 Single-phase ESP Performance

For single-phase water flow, experiments on ESP boosting pressure are conducted with different rotational speeds and flow rates. The mechanistic model predictions are compared with the corresponding experimental results. For viscous fluid flow, the previous experimental data from TAULP are used to compare with the mechanistic model.

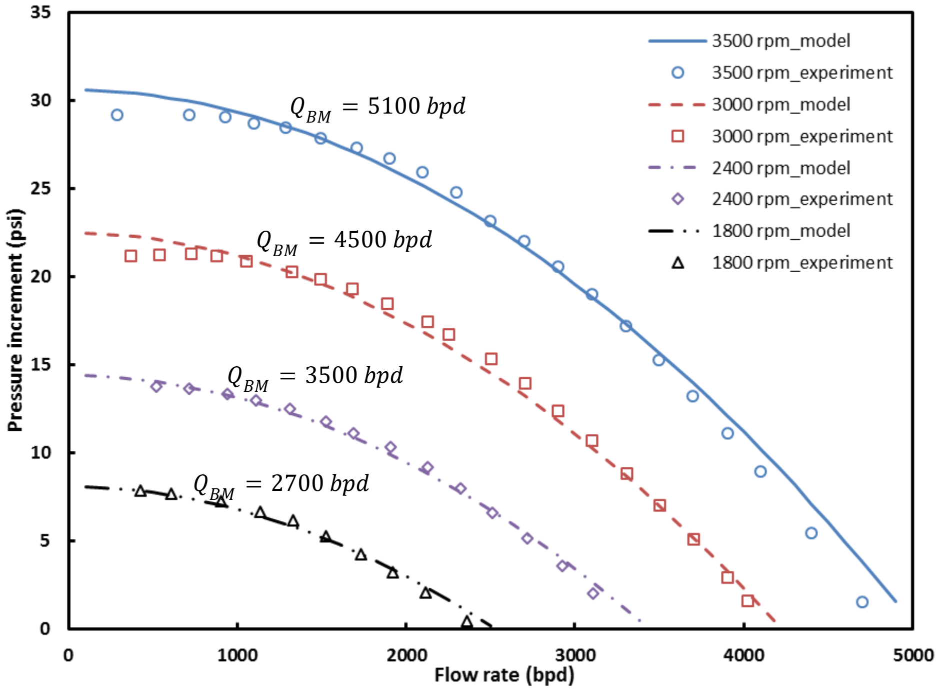

Figure 4.23 Comparison of mechanistic model, experimental data and catalog curves for predicting ESP stage pressure increment with water flow

Solano (2009) carried out an extensive experimental study on the effects of fluid viscosity on the single-phase performance of DN-1750 ESP. By changing the temperature, oil viscosity was controlled. Three flow cases corresponding to different N_S were selected, which ended up with a database containing more than 140,000 data points. In this study, we use the same flow conditions as configured by Solano in mechanistic model calculations of ESP pressure increment. A sample dataset comprising of 4,000 randomly selected data points is used to run calculations. Figure 4.24 summarizes the comparison results.

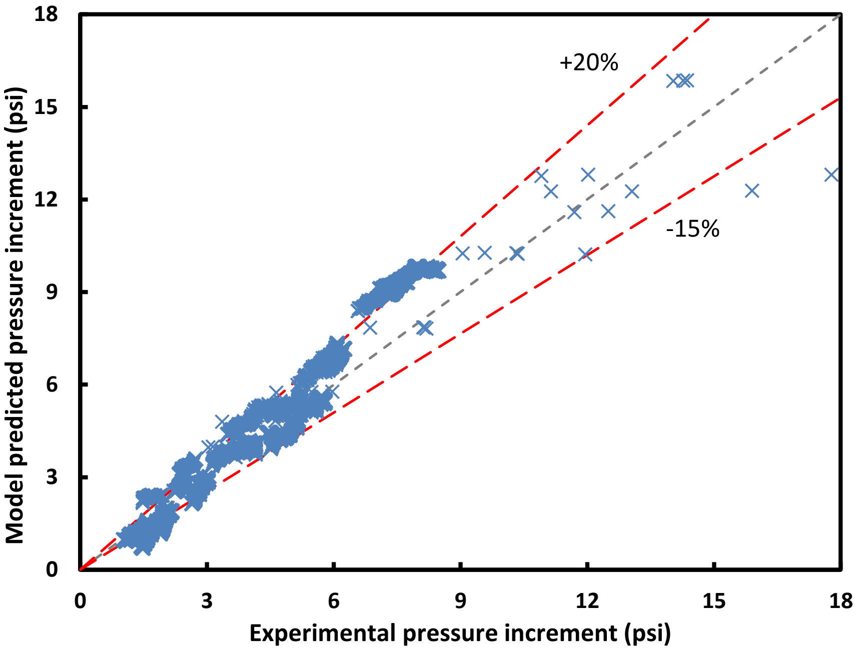

Figure 4.24 Comparison of model predictions with Salano (2009) experiments under viscous fluid flow in DN-1750 ESP

As it can be seen in Figure 4.24, the stage pressure increments predicted by the mechanistic model with different fluid viscosities are comparable to Solano (2009) experimental data. The prediction errors are mostly bounded by ±20% error lines. The mechanistic model predictions are also comparable to CFD simulated pump boosting pressure in Section 3.1. The numerical simulation has 15% error in predicting ESP pressure increment under viscous fluid flow.

Figure 4.25 shows the effect of fluid viscosity on TE-2700 ESP boosting pressure predicted by mechanistic modeling. A small rise of pump head is observed at fluid viscosities from water viscosity to about 10 cP. This can be attributed to the reduction of friction loss due to the transition of hydraulic-rough flow regime near the wall to hydraulic-smooth flow as discussed by Li (2000, 2014).

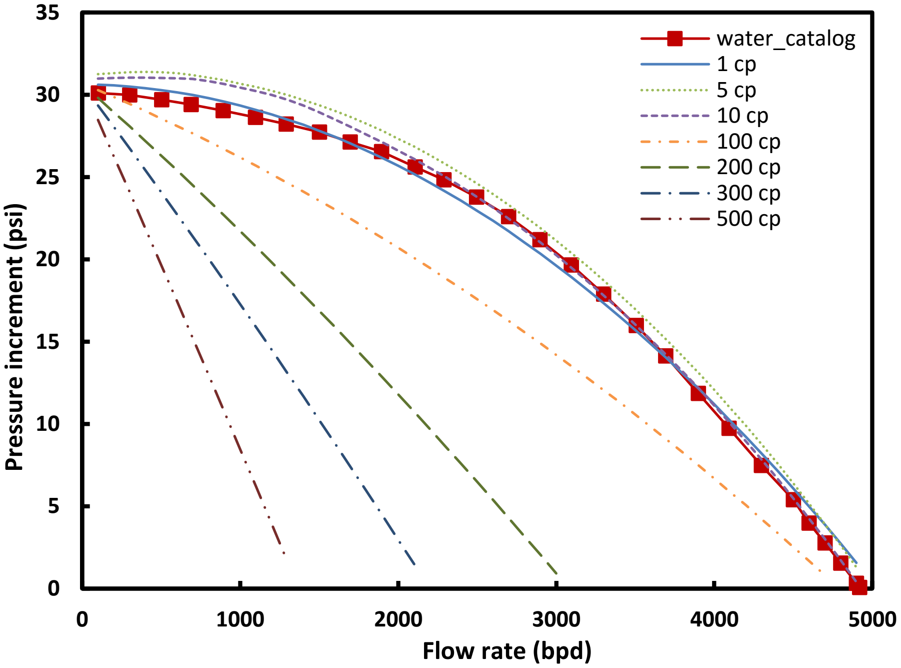

Figure 4.25 Effect of fluid viscosity on boosting pressure of TE-2700 ESP

Similar to the numerical simulations presented in Section 3.1, the mechanistic model predictions of stage pressure increment at relatively high fluid viscosities exhibit linear relationship with liquid flow rate. This is due to the flow regime transition from turbulent flow to laminar flow.

4.3.5 Gas-liquid ESP Performance

The mechanistic model of ESP two-phase flow consists of two parts. First, the flow pattern is determined with the flow conditions, including gas/liquid flow rates, pump geometries, fluid properties. Second, with the flow pattern determined, the corresponding flow model is called to calculate all the flow parameters including gas in-situ void fractions and pressure increment.

As pointed out by Gamoba (2008), flow pattern changes at the deflections on either ESP *H*-*Q* performance curves or surging testing curves. Thus, by analyzing the experimental data in Section 2.3, the flow patterns can be estimated. The comparison of model predicted flow patterns in a rotating ESP impeller against the readings from performance curves is therefore conducted. Two flow cases were selected for comparison purpose. One case corresponds to N = 3500 rpm, P_{sep} = 100 psig, and the other is at a lower rotational speed N = 1800 rpm, P_{sep} = 100 psig.

As shown in Figures 4.26 and 4.27, the flow pattern map for ESP gas-liquid flow is divided into four areas, namely dispersed bubble flow (I), bubbly flow (II), intermittent flow (III), and segregated flow (IV). The flow characteristics of each flow pattern was discussed in previous sections (Sections 1.2 and 4.2). Compared to Gamboa (2008) visualization experiments, similar flow pattern transition boundaries are predicted by the mechanistic model. At low gas flow rate (Q_G), the dispersed bubble flow encompassed by the blue line or bubbly flow bounded by the red line prevails. With increase of gas flow rate or decrease of liquid flow rate (Q_L), slug flow takes place with the boundary of the green line. The segregated flow (regime IV) corresponds to extremely low Q_L.

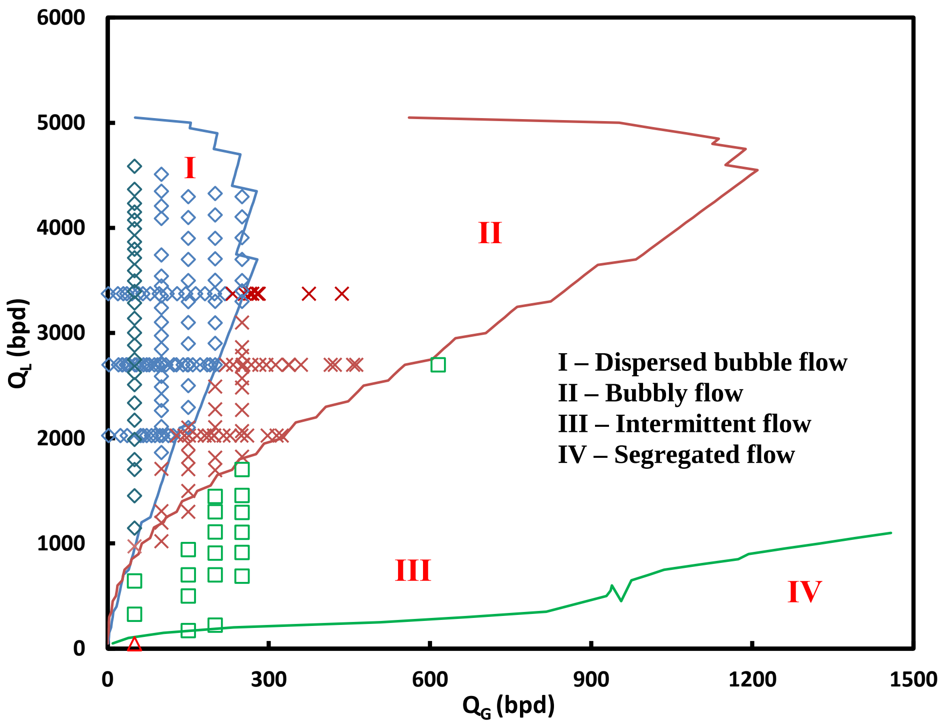

Figure 4.26 Air-water two-phase flow pattern map in TE-2700 ESP predicted by mechanistic model at $N = 3500$ rpm, $P_{sep} = 100$ psig

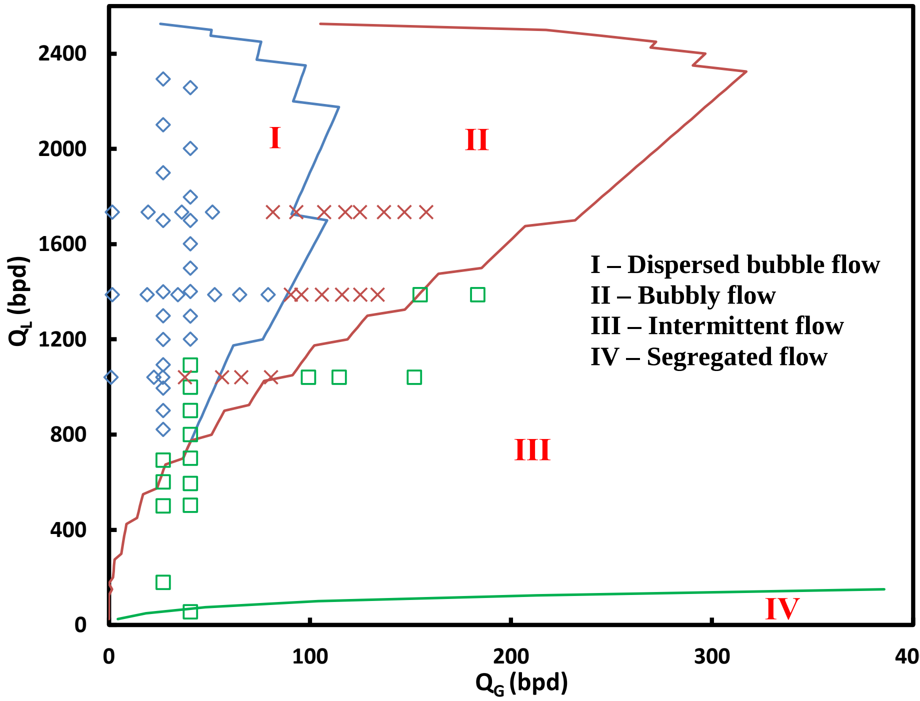

Figure 4.27 Air-water two-phase flow pattern map in TE-2700 ESP predicted by mechanistic model at $N = 1800$ rpm, $P_{sep} = 100$ psig

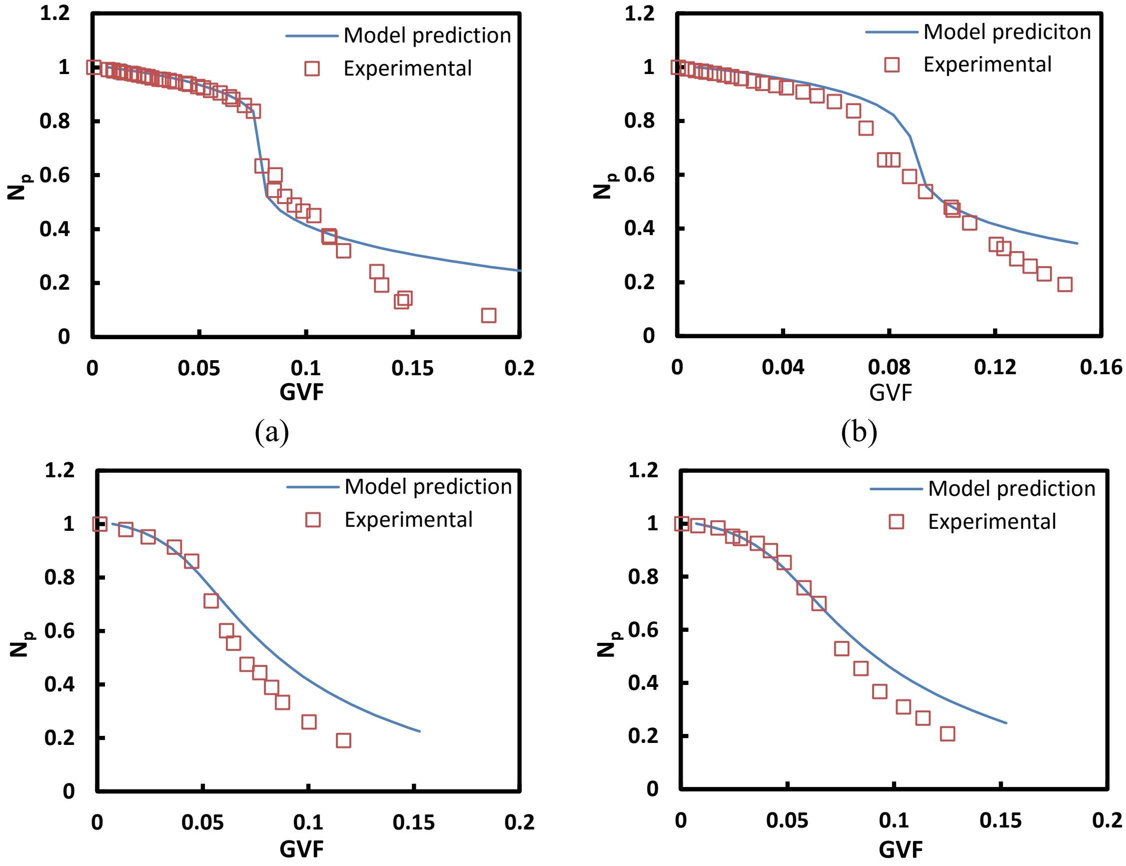

(a) (b)

(c) (d)

Figure 4.28 Comparison of predicted N_p by mechanistic model with correponding experimental measurement results under surging tests at stage 2-3, (a) N = 3500 rpm, P_{sep} = 100 psig, (b) N = 3500 rpm, P_{sep} = 150 psig, (c) N = 1800 rpm, P_{sep} = 100 psig, (d) N = 1800 rpm, P_{sep} = 150 psig

At N = 3500 rpm, P_{sep} = 100 psig (Figure 4.26), the mechanistic model predicted flow patterns are comparable to that detected from experimental performance curves. For the transition boundary from dispersed bubble to bubbly flow, corresponding to the initialization of pressure surging, the agreement is very good. Worthy to be noted is that the transition from bubbly flow to intermittent flow is predicted well by the critical gas-void fraction α_G (Eq. 4.64). Due to the limitation of experimental facility, the measurements were only conducted at relatively low Q_G, beyond which the nil pump boosting pressure accompanied by severe fluctuations of liquid flow rates was observed. For N = 1800 rpm, P_{sep} = 100 psig, the model predicted flow patterns are found to match the experimental detections at high Q_L.

Figure 4.28 shows the model predictions of normalized stage boosting pressure (N_p) versus the intake GVFs at different flow conditions. From the comparisons in Figure 4.28(a) and 4.28(b) at N = 3500 rpm, it is found that the model predictions agree well with experimental data in trends, while the values depart at high GVFs. The deviations may be due to the underestimated in-situ gas void fractions (α_G), resulting in the overestimated mixture densities in the rotating ESP impeller. In addition, the flow pattern prediction error also contributes to the deviations. Similarly, good agreement of model predicted N_p with experimental results in trends is found in Figures 4.28(c) and (d) at N = 1800 rpm.

The model comparisons with the mapping test data are presented in Figures 4.29 and 4.30, for N = 3500 rpm and N = 1800 rpm, respectively. For different gas flow rates (Q_{gd}), the model predicted ESP stage pressure increments are compared with experimental measurements. As Figure 4.29 shows, the ESP performance predicted by mechanistic model agrees well with experimental data at low liquid flow rates (Q_L). The model demonstrates a good match in predicting the *H*-*Q* curve shapes compared with the experimental measurements. However, the deviation at high Q_L, especially when $Q_L > Q_{BEP}$, indicates that the bubble sizes are under estimated.

Similar observations are found in Figure 4.30 at N = 1800 rpm, although the overall prediction error by mechanistic model the measured ESP stage pressure increment is slightly lower than that at N = 3500 rpm. More comparisons of the mechanistic model with experiments are available in Appendix E.

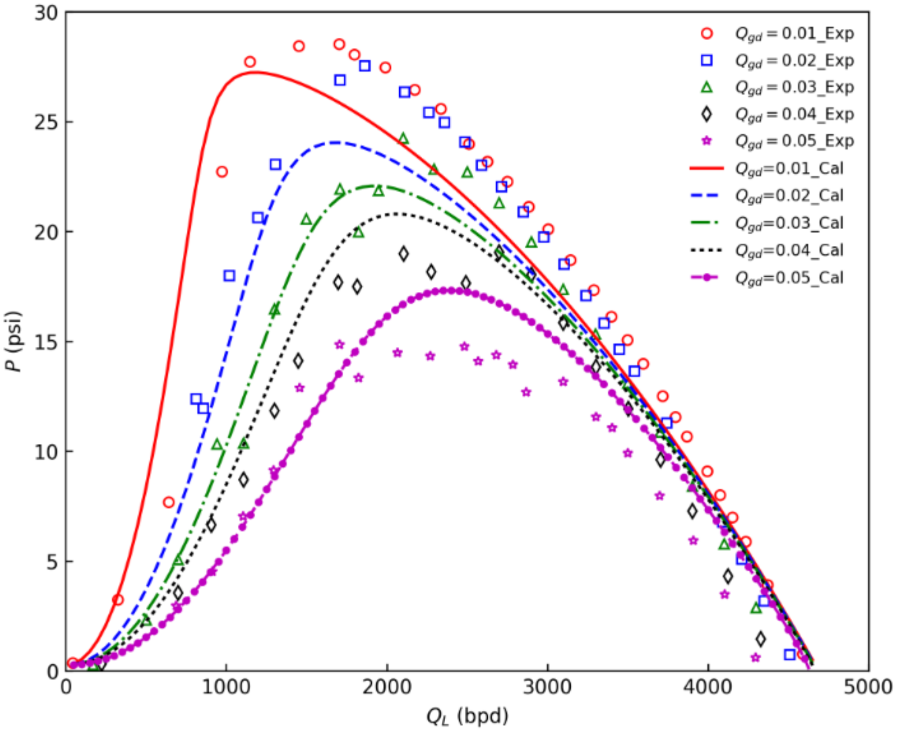

Figure 4.29 Comparison of predicted stage pressure increment by mechanistic model with experimental results at stage 3, $N = 3500$ rpm, $P_{sep} = 100$ psig

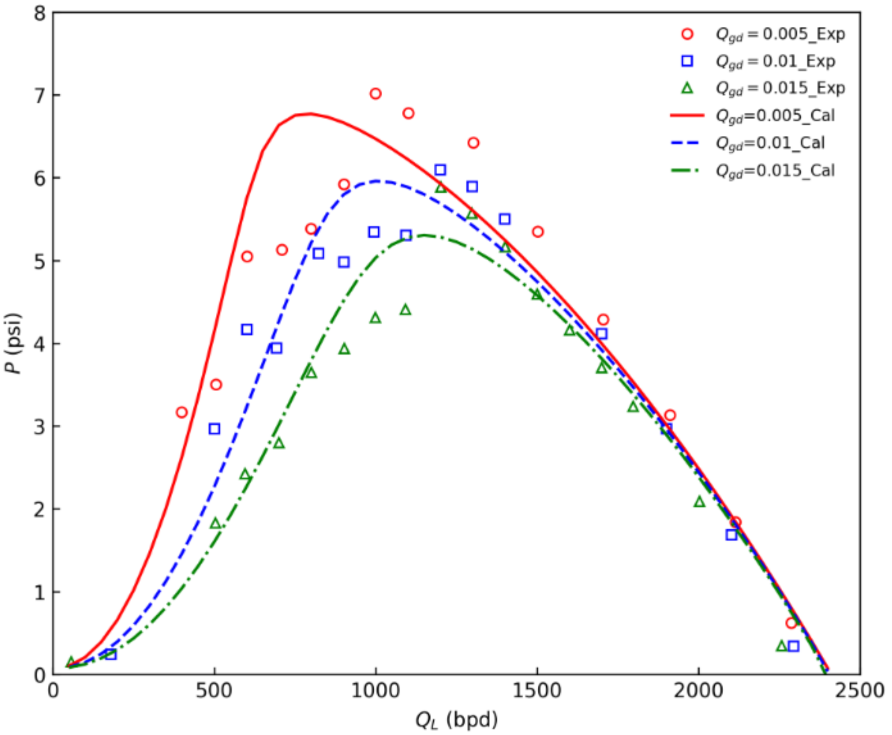

Figure 4.30 Comparison of predicted stage pressure increment by mechanistic model with experimental results tests at stage 3, $N = 1800$ rpm, $P_{sep} = 100$ psig

4.4 Mechanistic Modeling Summary

A comprehensive mechanistic model for ESP performance under liquid and gas-liquid flow is presented. This model starts with the Euler equation for centrifugal pump. A novel modification on the effective velocities at the outlet of ESP impeller is made based on a best match flow rate at which the flow direction at the impeller outlet matches the designed flow direction. Several head losses and their effects on pump performance are analyzed and modeled. Compared to previous models which are either based on empirical closure relationships to account for shear effects or based on numerical iterations to solve the partial differential equations, the new mechanistic model is much easier to use. The predicted ESP pressure increment under both single-phase water and viscous fluid flow is found to match the corresponding experimental data.

For ESP gas-liquid flow, the mechanistic model is based on the unified model in two-phase pipe flow. Starting from the basic conservations of continuity and momentum in a rotating ESP impeller, the governing equations are reformulated such that the flow pattern prediction and flow model for calculating the hydraulic parameters of each flow pattern are derived and incorporated into the comprehensive two-phase mechanistic model. To make the model solvable, the closure relationships including bubble size, drag force coefficient, in-situ gas void fraction are proposed and validated by either numerical simulations or experimental results. The new model can predict the flow pattern map inside a rotating ESP impeller and stage pressure increment. The model predictions of stage pressure increment match well with experimental measurements in trend and values. Moderate deviations are found at relatively high gas/liquid flow rates. Further improvements on flow pattern transition boundary and bubble size predictions are needed.

CHAPTER 5

CONCLUSIONS AND RECOMMENDATIONS

In this study, three research methods, including experimental measurement, numerical simulation, mechanistic modeling, are utilized to perform a comprehensive study on ESP performance under gas-liquid flow conditions.

5.1 Summary and Conclusions

5.1.1 Experimental Study

1. The measured ESP stage pressure increment with tap water flow matches catalog performance curves well. This validates the experimental setup used in this study.
2. Two testing schemes are employed to assess ESP performance under different gas-liquid flow conditions. One is surging test (constant liquid flow rate) and the second is mapping test (constant gas flow rate).
3. For surging tests, experiments are repeated using three fluids with different surfactant concentrations. With gas flow rate increase, the stage pressure increment surfers from mild degradation to a sudden drop head corresponding to pressure surging. After surfactant is added, the initiations of pressure surging are postponed to higher GVFs.
4. For mapping tests, the gas volumetric flow rates are fixed, but the liquid flow rates vary in a broad range. A sudden drop on the two-phase *H*-*Q* curve occurs when

liquid flow rate is reduced to a certain value for air-water flow without surfactant. In contrast, the surfactant presence significantly improves ESP two-phase stage pressure increment by postponing the sudden drop to lower liquid flow rate.

5. The small changes in the two-phase *H-Q* performance curves with different surfactant concentrations indicate that the improvement of ESP boosting pressure is not only due to the reduction of surface tension, but also due to the formation of foam flow, which changes the morphology of the gas-liquid interface significantly.

5.1.2 CFD Simulation

1. The CFD simulations on ESP performance under both single-phase viscous fluid flow and gas-liquid two-phase flow conditions are successfully performed and validated with experimental measurements.
2. For single-phase simulation of high-viscosity fluid flow, the 3D, steady-state RANS equations with standard SST turbulence models are solved in ANSYS CFX by employing the frozen-rotor technique. With structured hexahedral mesh, the simulated pressure increment is comparable to corresponding experimental data. Flow structures inside ESP impeller and diffuser channels are analyzed. At pump BEP, the boosting pressure decreases 30-40% when oil viscosity increases from 10 cP to 100 cP. ESP becomes ineffective when oil viscosity is higher than 200 cP. With oil viscosity increase, pump *H-Q* performance curve becomes more linear. CFD simulation reveals that the recirculation flow at impeller blade trailing edge is more prominent at lower liquid flow rates.
3. For two-phase simulations, a 3D CFD scheme is implemented on a three-stage ESP

geometry to simulate the pump-pressure increment under various flow conditions. By use of structured hexahedral grids and the frozen-rotor technique, the mesh independence and numerical accuracy are verified. At low GVFs, the numerically simulated pump pressure increment with constant bubble size agrees well with experimental measurements. At high GVFs, the simulation results deviate from experimental pump performance curves considerably. By increasing bubble size, the simulated ESP performance can be tuned to match experimental results. Through this process, a bubble-size change trend with varying GVFs is obtained. A mechanistic model for the maximum stable bubble size in a rotating turbulent flow field is developed to correlate the CFD simulated bubble sizes. Further, numerical simulation results using the new bubble size prediction model agree well with experimental data.

4. Based on the comparison of CFD simulated ESP boosting pressure with corresponding experimental measurements, a mechanistic model to predict the in-situ α_G inside a rotating ESP impeller is developed and further validated by numerical simulation results.

5.1.3 Mechanistic Modeling

1. A comprehensive mechanistic model for predicting ESP stage pressure increment under both liquid and gas-liquid flows is developed. For single-phase prediction model, the effect of fluid viscosity on ESP boosting pressure is incorporated. For two-phase ESP flow, the model can predict flow pattern transition boundaries and pressure increment.

2. Starting from the Euler equation for centrifugal pump, a novel modification on the effective velocities at the outlet of ESP impeller is made based on best match flow rate at which the flow direction at the impeller outlet matches the designed flow direction. Several head losses and their effects on pump performance are analyzed and modeled, including friction, recirculation and flow turns. Compared with the previous experimental data of ESP boosting pressure with high-viscous fluid flows, the prediction error of mechanistic model is within ±20%.
3. The mechanistic model of ESP performance under gassy conditions is developed based on the conservations of mass and momentum in the impeller. The model predicted flow patterns agree well with that detected from *H*-*Q* performance curves. The stage pressure increments calculated by mechanistic model are also consistent with experimental measurements in trends and values. Deviations are found at relatively high gas/liquid flow rates, which requires further improvements on flow pattern transition boundary and bubble size predictions. Future improvement will be made through investigations of the closure relationships and validation with experimental results.

5.2 Recommendations

The following recommendations may be considered in future studies:

1. For experimental facility, add a boosting pump in the liquid flow loop to help stabilize the liquid flow rate. Replace the current air supply with a high-capacity air compressor or gas bottles. Add a heat exchanger in the liquid flow loop to maintain

the fluid temperature, so that the viscosity of fluids, such as mineral oil can be regulated.

2. The numerical simulations can be improved by performing the transient CFD simulation of ESP dynamic phenomena, and incorporating more sophisticated closure relationships, e.g. MUSIG (multiple size group), poly-dispersed phases (oil, water and gas), multi-momentum-transfer mechanisms (virtual mass force, turbulence dispersion force, wall lubrication force etc.), so that the two-phase flow mechanisms inside the rotating ESPs can be better simulated.
3. For mechanistic modeling, the closure relationships including bubble size prediction, drag coefficient, interfacial friction factor, translational velocity and slug unit length in rotating flow fields, can be improved by examining and comparing available models.

NOMENCLATURE

A	area, L^2, m^2
b	blade thickness, L, m
BEP	best efficiency point
BHP	brake horsepower, ML^2/T^3, $kg\cdot m^2/s^3$
C	absolute velocity, L/T, m/s
C_D	drag force coefficient
C_L	lift force coefficient
d	bubble diameter, L, m
D_i	impeller diameter, L, m
f	friction factor
f_E	liquid entrainment factor
F_E	liquid entrainment factor
$\vec{F}$	interfacial force vector, $M/(LT^2)$, Pa
$\vec{g}$	gravity acceleration vector, $L/(T^2)$, m/s^2
GVF	gas volumetric fraction
h	channel height, L, m or hydraulic head, L, m
H	hydraulic head, L, m or holdup
$\bar{\bar{I}}$	identity matrix
k	turbulent kinetic energy, $L^2/(T^2)$, m^2/s^2

l	channel length, L, m
$\dot{m}$	mass flow rate, M/T, kg/s
M	momentum transfer term per unit volume, M/($^{\mathrm{L2T2}}$), Pa/m
n	phase number
N	rotational speed, 1/L, rpm
p	pressure, M/(LT^2), Pa
ΔP	stage pressure increment, M/(LT^2), Pa
P	pressure, M/(LT^2), Pa
q	flow rate, L^3/T, m^3/s
Q	mass flow rate, M/T, kg/s
r	radius, L, m
Re	Reynolds number
s	streamline, L, m
Sr	Strouhal number
t	time, T, s
T	torque, (ML^2)/T^2, kg·m^2/s^2
$\vec{u}_i$	phase velocity vector, L/T, m/s
U	peripheral velocity, L/T, m/s
v	velocity, L/T, m/s
v'	velocity fluctuation, L/T, m/s
V	velocity, L/T, m/s
Vol	volume, L^3, m^3
W	relative velocity in ESP, L/T, m/s

We	Weber number
x	mass fraction or mole fraction
Y	channel height, L, m
Z	blade number

Greek Symbols

α	gas void fraction
β	tangential blade angle, *deg*
δ	Film thickness, L, m
η	efficiency
λ_G	no-slip gas void fraction (GVF)
μ	dynamic viscosity, M/(LT), Pa·s
μ_t	turbulent viscosity, M/(LT), Pa·s
μ_{eff}	effective viscosity, M/(LT), Pa·s
ω	specific dissipation rate or turbulent frequency, 1/T, s^{-1}
Ω	angular speed, 1/T, rad/s
φ	flow coefficient
ψ	head coefficient
ρ	fluid density, M/L^3, kg/m^3
σ	surface tension, M/T^2, N/m or slip factor
σ_k, σ_ε	turbulent Prandtl number for k and ε
τ	external force exerting on bubbles, $M/(LT^2)$, Pa
$\overline{\overline{\tau}}$	stress-strain tensor, $M/(LT^2)$, Pa

ε	turbulent energy dissipation rate per unit mass, L^2/T^3, m^2/s^3

Subscripts

1	inlet
2	outlet
32	Sauter mean diameter
B	bubble or blade
b	blade
bep	best efficiency point
b_surg	bubble at pressure surging
BM	Best match
c	continuous phase
cfg	centrifugal force
C	gas core
CD	critical
Cor	Coriolis force
CRIT	critical
d	diffuser or dispersed phase
D	diffuser
eff	effective
E	Euler
EE	effective
F	film

FI	fluid in ESP impeller
FD	fluid in ESP diffuser
g	gas phase
G	gas phase
H	hydraulic parameter
i	impeller or phase i
I	Interface or impeller
l	liquid phase
lg	liquid to gas
L	liquid phase
LF	liquid film
LK	leakage
max	maximum
min	minimum
M	meridional direction or mixture
o	initial or equivalent
p	relative to project area or particle or phase (gas/liquid)
R	radius direction
$sphere$	sphere
$streamline$	projection on streamline
$stat$	static
S	specific speed or shear or slug body
SD	diffuser channel wall

SG	superficial gas
SI	impeller channel wall
SL	superficial liquid
SR	shear in the radial direction
sep	separator
TI	turn loss in impeller
TD	turn loss in diffuser
U	peripheral direction
v	virtual mass force
vm	virtual mass
w	water
W	wall

BIBLIOGRAPHY

1. Achouri, R., Mokni, I., Mhiri, H., and Bournot, P., 2012. A 3D CFD simulation of a self-inducing pitched blade turbine downflow. *Energy Conversion and Management*, 64: 633–641.
2. Ajani, A., Kelkar, M., Sarica, C. and Pereyra, E., 2016. Effect of surfactants on liquid loading in vertical wells. *International Journal of Multiphase Flow*, 83:183-201.
3. Ajani, A., Kelkar, M., Sarica, C. and Pereyra, E., 2016. Foam flow in vertical gas wells under liquid loading: Critical velocity and pressure drop prediction. *International Journal of Multiphase Flow*, 87: 124-135.
4. Amaral, G.D.L. do, 2007. Single-phase flow modeling of an ESP operating with viscous fluids. M.Sc. Thesis, State University of Campinas, Campinas, São Paulo, Brazil.
5. Amaral, G., Estevam, V., and França, F.A., 2009. On the influence of viscosity on ESP performance. SPE *Production & Operations*. 24 (2): 303-310.
6. Ambrosini, W., Andreussi, P. and Azzopardi, B.J., 1991. A physically based correlation for drop size in annular flow. *International Journal of Multiphase Flow*, 17(4): 497-507.
7. Ansys, 2015. CFX-Solver Modeling Guide, ANSYS Inc., Canonsburg, PA.
8. Asali, J.C., 1987. Entrainment in vertical gas-liquid annular Flows, PHD Dissertation, University of Illinois at Urbana-Champaign, Champaign, IL.
9. Asuaje, M., Bakir, F., Kouidri, S., Kenyery, F. and Rey, R., 2005. Numerical

modelization of the flow in centrifugal pump: volute influence in velocity and pressure fields. *International journal of rotating machinery*, 2005(3), 244-255.

10. Aungier, R.H., 1995. Mean streamline aerodynamic performance analysis of centrifugal compressors. Transactions of ASME *Journal of Turbomachinery*, 117: 360-360.
11. Banjar, H.M., Gamboa, J., Zhang, H.-Q., 2013. Experimental study of liquid viscosity effect on two-phase stage performance of electrical submersible pumps. In: SPE Annual Technical Conference and Exhibition, SPE 166374, Society of Petroleum Engineers.
12. Barnea, D., Shoham, O. and Taitel, Y., 1982. Flow pattern transition for vertical downward two phase flow. *Chemical Engineering Science*, 37(5): 741-744.
13. Barnea, D. and Brauner, N., 1985. Holdup of the liquid slug in two phase intermittent flow. *International Journal of Multiphase Flow*, 11(1): 43-49.
14. Barrios, L., 2007. Visualization and modeling of multiphase performance inside an electrical submersible pump. PhD Dissertation, the University of Tulsa, Tulsa, Oklahoma.
15. Barrios, L., Prado, M.G., and Kenyery, F., 2009. CFD modeling inside an electrical submersible pump in two-Phase flow condition. In ASME 2009 Fluids Engineering Division Summer Meeting, Vol. 1: Symposia, Parts A, B and C, Vail, Colorado USA, 2-6 August, 457-469.
16. Barrios, L., and Prado, M.G., 2011. Experimental visualization of two-phase flow inside an electrical submersible pump stage. ASME *Journal of Energy Resources Technology*, 133(4): 042901.

17. Barrios, L.J., Scott, S. L., Sheth, K.K., 2012. ESP technology maturation: subsea boosting system with high GOR and viscous fluid. In: SPE Annual Technical Conference and Exhibition, SPE 159186, Society of Petroleum Engineers.
18. Batchelor, G.K., 1953. *The Theory of Homogeneous Turbulence*. Cambridge Science Classics, Cambridge University Press.
19. Becker, K., Heitkamp, K., and Kugeler, E., 2010. Recent progress in a hybrid-grid CFD solver for turbomachinery flows. In Proceedings Fifth European Conference on Computational Fluid Dynamics ECCOMAS CFD, Vol. 2010.
20. Beltur, R., 2003. Experimental investigation of two-phase flow performance of ESP stages. Master Thesis, the University of Tulsa, Tulsa, Oklahoma.
21. Bendiksen, K.H., 1984. An experimental investigation of the motion of long bubbles in inclined tubes. *International Journal of Multiphase Flow*, 10(4): 467-483.
22. Berkman, P.D., and Calabrese, R.V., 1988. Dispersion of viscous liquids by turbulent flow in a static mixer. AIChE *Journal*, 34(4): 602-609.
23. Bing, H., Tan, L., Cao, S. and Lu, L., 2012. Prediction method of impeller performance and analysis of loss mechanism for mixed-flow pump. *Science China Technological Sciences*, 55(7): 1988-1998.
24. Bradshaw, P., 1996. Turbulence modeling with application to turbomachinery. *Progress in Aerospace Sciences*, 32(6): 575–624.
25. Brodkey, R.S., 1967. *The Phenomena of Fluid Motion*. Addison-Wesley Press, Boston, MA.
26. Calderbank, P.H. 1958. Physical rate processes in industrial fermentation. Part I: The interfacial area in gas-liquid contacting with mechanical agitation. *Transactions of the*

Institution of Chemical Engineers, 36(5): 433-440.

27. Caridad, J., and Kenyery, F., 2004. CFD analysis of electric submersible pumps (ESP) handling two-phase mixtures, ASME *Journal of Energy Resources Technology*, 126: 99-104.
28. Caridad, J., Asuaje, M., Kenyery, F., Tremante, A. and Aguillón, O., 2008. Characterization of a centrifugal pump impeller under two-phase flow conditions. *Journal of Petroleum Science and Engineering*, 63(1), 18-22.
29. Chandel, S., Singh, S.N. and Seshadri, V., 2012. Effect of additive on the performance characteristics of centrifugal and progressive cavity slurry pumps with high concentration fly ash slurries. *International Journal of Fluid Mechanics Research*, 39(3): 67-74.
30. Cheah, K.W., Lee, T.S., Winoto, S.H., and Zhao, Z.M., 2007. Numerical flow simulation in a centrifugal pump at design and off-design conditions. *International Journal of Rotating Machinery*, 2007: 83641.
31. Chen, H.T., and Middleman, S., 1967. Drop size distribution in agitated liquid-liquid systems. AIChE *Journal*, 13(5): 989-995.
32. Chisely, E.A., 1997. Two phase flow centrifugal pump performance. PhD Dissertation, Idaho State University, Pocatello, Idaho.
33. Chu, K.Y. and Thompson, A.R., 1962. Densities and refractive indices of alcohol-water solutions of n-Propyl, Isopropyl, and Methyl Alcohols. *Journal of Chemical and Engineering Data*, 7(3): 358-360.
34. Churchill, S.W., 1977. Friction-factor equation spans all fluid-flow regimes. *Chemical engineering*, 84(24): 91-92.

35. Cirilo, R., 1998. Air-water flow through electric submersible pumps. Master Thesis, the University of Tulsa, Tulsa, Oklahoma.

36. Clift, R., Grace, J., and Weber, M., 1978. *Bubbles, Drops, and Particles*, Academic Press.

37. Davies, J.T., 1972. *Turbulence Phenomena*, New York: Academic Press.

38. Davis, Richard S., 1992. Equation for the determination of the density of moist air (1981/91), *Metrologia*, 29(1): 67-70.

39. DeGennes, P-G., Brochard-Wyart, F., and Quere, D., 2004. *Capillarity and Wetting Phenomena*. New York: Springer.

40. Drew, D.A., and Lahey, R.T., 1979. Application of general constitutive principles to the derivation of multidimensional two-phase flow equations. *International Journal Multiphase Flow*, 5(4): 243–264.

41. Duran, J., 2003. Pressure effects on ESP stages' air-water performance. Master Thesis, the University of Tulsa, Tulsa, Oklahoma.

42. Eastoe, J. and Dalton, J. 2000. Dynamic surface tension and adsorption mechanisms of surfactants at the air–water interface. *Advances in Colloid and Interface Science*, 85: 103-144.

43. Estevam, V., 2002. A phenomenological analysis about centrifugal pump in two phase flow operation. PhD Dissertation, Universidade Estadual de Campinas.

44. Estevam, V., França, F.A., and Alhanati, F.J., 2003. Mapping the performance of centrifugal pumps under two-phase conditions. COBEM2003-0039, 17th International Congress of Mechanical Engineering, Sao Paulo, Brazil, November, 2003.

45. Ferziger, J.H. and Peric M., 1996. *Computational Methods for Fluid Dynamics*.

Springer, Berlin, Germany.

46. Flores, N.G., Goncalves, E., Rolland, J., and Rebattet, C., 2008. Head drop of a spatial turbopump inducer. *ASME Journal of Fluids Engineering*, 130(11): 111301.

47. Furuya, O., 1985. Analytical model for prediction of two-phase (noncondensable) flow pump performance. ASME *Journal of Fluids Engineering*, 107(1): 139-147.

48. Gamboa, J., 2008. Prediction of the transition in two-phase performance of an electrical submersible pump. PhD Dissertation, the University of Tulsa, Tulsa, Oklahoma.

49. Gamboa, J., and Prado, M., 2011. Review of electrical-submersible-pump surging correlation and models. SPE *Production & Operations*, 26(04): 314-324.

50. Godfrey, J. C., Obi, F. I. N., and Reeve, R.N., 1989. Measuring drop size in continuous liquid-liquid mixers. *Chemical engineering progress*, 85(12): 61-69.

51. Gonzalez, J., Fernandez, J., Blanco, E., and Santolaria, C., 2002. Numerical simulation of the dynamic effects due to impeller-volute interaction in a centrifugal pump. *ASME Journal of Fluids Engineering*, 124: 348-355.

52. Gonzalez, J., and Santolaria, C., 2006. Unsteady flow structure and global variables in a centrifugal pump. ASME *Journal of Fluids Engineering*, 128: 937-946.

53. Gregory, G.A., Nicholson, M.K. and Aziz, K., 1978. Correlation of the liquid volume fraction in the slug for horizontal gas-liquid slug flow. *International Journal of Multiphase Flow*, 4(1): 33-39.

54. Gülich, J.F., 1999a. Pumping highly viscous fluids with centrifugal pumps – Part 1. World Pumps 1999a (395), 30–34.

55. Gülich, J.F., 1999b. Pumping highly viscous fluids with centrifugal pumps – Part 2. World Pumps 1999b (396), 39–42.

56. Gulich, J.F., 2007. *Centrifugal Pumps*. Berlin Heidelberg, Springer, New York.

57. Hesketh, R.P., Russell, T.W.F., and Etchells, A.W., 1987. Bubble size in horizontal pipelines, AIChE *Journal*, 33(4): 663–667.

58. Hinze, J.O., 1955. Fundamentals of the hydrodynamic mechanism of splitting in dispersion processes. AIChE *Journal*, 1(3): 289-295.

59. Hu, B., Nienow, A.W., Stitt, E.H. and Pacek, A.W., 2006. Bubble sizes in agitated solvent/reactant mixtures used in heterogeneous catalytic hydrogenation of 2-butyne-1, 4-diol. *Chemical Engineering Sci*ence, 61(20): 6765-6774.

60. Huang, S., Mohamad, A.A., Nandakumar, K., Ruan, Z.Y., and Sang, D.K., 2010. Numerical simulation of unsteady flow in a multistage centrifugal pump using sliding mesh technique. *Progress in Computational Fluid Dynamics*, 10(4): 239-245.

61. Huang, S., Su, X., Guo, J., and Yue, L., 2014. Unsteady numerical simulation for gas-liquid two-phase flow in self-priming process of centrifugal pump. *Energy Conversion and Management*, 85: 694-700.

62. Hydraulic Institute, 1948. Tentative Standards of Hydraulic Institute: Charts for the Determination of Pump Performance When Handling Viscous Liquids. The Institute, OH.

63. Ippen, A.T., 1945. The Influence of Viscosity on Centrifugal Pump Performance. Issue 199 of Fritz Engineering Laboratory Report, ASME Paper No. A-45-57.

64. Ishii, M. and Zuber, N., 1979. Drag coefficient and relative velocity in nubbly, droplet or particulate Flows. AIChE *Journal*, 25(5): 843-855.

65. Ishii, M. and Mishima, K., 1989. Droplet entrainment correlation in annular two-phase flow. *International Journal of Heat and Mass Transfer*, 32(10): 1835-1846.

66. Ito, H., 1959. Friction factors for turbulent flow in curved pipes. ASME *Journal of Basic Engineering*, 81(2): 123-134.

67. Ito, H., and Nanbu, K., 1971. Flow in rotating straight pipes of circular cross section. ASME *Journal of Basic Engineering*, 93: 383-394.

68. Jeanty, F., De Andrade, J., Asuaje, M., Kenyery, F., Vásquez, A., Aguillón, O. and Tremante, A., 2009. Numerical simulation of cavitation phenomena in a centrifugal pump. In ASME 2009 Fluids Engineering Division Summer Meeting (pp. 331-338). American Society of Mechanical Engineers, Vail, Colorado USA, August, 2009.

69. Jones, O.C., 1976. An improvement in the calculation of turbulent friction in rectangular ducts. ASME *Journal of Fluids Engineering*, 98(2): 173-180.

70. Khosla, V., 2012. Visual investigation of annular flow and the effect of wall wettability. M.Sc. thesis, Delft University of Technology.

71. Kouba, G.E., 2003. Mechanistic models for droplet formation and breakup. In ASME/JSME 2003 4th Joint Fluids Summer Engineering Conference, Honolulu, Hawaii, USA, July, 2003, Vol. 1: 1607–1615.

72. Ladouani, A. and Nemdili, A., 2009. Influence of Reynolds number on net positive suction head of centrifugal pumps in relation to disc friction losses. *Forschung im Ingenieurwesen*, 73(3): 173.

73. Launder, B.E., and Spalding, D.B., 1974. The numerical computation of turbulent flows. *Computer Methods in Applied Mechanics and Engineering*, 3(2): 269-289.

74. Lea, J.F., and Bearden, J.L., 1982. Effect of gaseous fluids on submersible pump performance. *Journal of Petroleum Technology*, 34(12): 2-922.

75. Legendre, D., and Magnaudet, J., 1998. The lift force on a spherical bubble in a viscous

linear shear flow. *Journal of Fluid Mechanics*, 368: 81–126.

76. Levich, V., 1962. *Physicochemical hydrodynamics*, 1st edition. Prentice Hall.

77. Li, W.G., 2000. The "sudden-rising head" effect in centrifugal oil pumps. *World Pumps*, 2000(409): 34-36.

78. Li, W.G., 2002. Experimental investigation of performance of commercial centrifugal oil pump. World Pumps 2002 (425), 26–28.

79. Li, W.G., 2014. Mechanism for onset of sudden-rising head effect in centrifugal pump when handling viscous oils. ASME *Journal of Fluids Engineering*, 136 (7): 074501.

80. Maitelli, C., Bezerra, V., and Da Mata, W., 2010. Simulation of flow in a centrifugal pump of ESP systems using computational fluid dynamics. *Brazilian Journal of Petroleum and Gas*, 4(1): 1-9.

81. Marsis, E., Pirouzpanah, S. and Morrison, G., 2013. CFD-based design improvement for single-phase and two-phase flows inside an electrical submersible pump. In ASME 2013 Fluids Engineering Division Summer Meeting, American Society of Mechanical Engineers, Incline Village, Nevada.

82. Meissner, H.P. and Michaels, A.S., 1949. Surface tensions of pure liquids and liquid mixtures. *Industrial & Engineering Chemistry*, 41(12): 2782-2787.

83. Menter, F.R., 1994. Two-equation eddy-viscosity turbulence models for engineering applications. AIAA *Journal*, 32(8):00201598-1605.

84. Minemura, K., and Uchiyama, T., 1993. Three-dimensional calculation of air-water two-phase flow in centrifugal pump impeller based on a bubbly flow model. ASME *Journal of Fluids Engineering*, 115(4): 766-771.

85. Minemura, K., Uchiyama, T., Shoda, S., and Kazuyuki, E., 1998. Prediction of air-

water two-phase flow performance of a centrifugal pump based on one-dimensional two-fluid model. ASME *Journal of Fluids Engineering*, 120(2), 327-334.

86. Minumura, K., and Murakami, M., 1980. A theoretical study on air bubble motion in a centrifugal pump impeller. ASME *Journal of Fluids Engineering*, 102(4): 446-455.
87. Murakami, M. and K. Minemura., 1974. Effects of entrained air on the performance of a centrifugal pump (1st report, performance and flow conditions). *Bulletin of the JSME*, 17(110): 1047-1055.
88. Murakami, M. and K. Minemura., 1974. Effects of entrained air on the performance of a centrifugal pump (2nd report, effects of number of blades). *Bulletin of the JSME*, 17(112): 1286-1295.
89. Neumann, M., Schäfer, T., Bieberle, A. and Hampel, U., 2016. An experimental study on the gas entrainment in horizontally and vertically installed centrifugal pumps. ASME *Journal of Fluids Engineering*, 138(9), 091301.
90. Nicklin, D.J., 1962. Two-phase bubble flow. *Chemical Engineering Science*, 17(9): 693-702.
91. Ogata, S., Kimura, A. and Watanabe, K., 2006. Effect of surfactant additives on centrifugal pump performance. ASME *Journal of Fluids Engineering*, 128(4): 794-798.
92. Omer, A. and Pal, R., 2013. Effects of surfactant and water concentrations on pipeline flow of emulsions. *Industrial & Engineering Chemistry Research*, 52: 9099-9105.
93. Padron, G.A., 2004. Effect of surfactants on drop size distributions in a batch, rotor-stator mixer. PhD thesis, University of Maryland, College Park, MD.
94. Patankar, S.V., and Spalding, D.B., 1972. A calculation procedure for heat and mass

transfer in three dimensional parabolic flows. *International Journal of Heat and Mass Transfer*, 15(10): 1787-1806.

95. Paternost, G.M., Bannwart, A.C. and Estevam, V., 2015. Experimental study of a centrifugal pump handling viscous fluid and two-phase flow. SPE *Production & Operations*, 30(2): 146-155.

96. Pereyra, E.J., 2011. Modeling of integrated compact multiphase separation system (cmss©). PhD thesis, The University of Tulsa, Tulsa, Oklahoma.

97. Pessoa, R., 2001. Experimental investigation of two-phase flow performance of electrical submersible pump stages. Master thesis, the University of Tulsa, Tulsa, Oklahoma.

98. Phongikaroon, S., 2001. Effect of dispersed phase viscosity and interfacial tension on drop size distribution in a batch rotor-stator mixer. PhD thesis, University of Maryland, College Park, MD.

99. Pineda, H., Biazussi, J., López, F., Oliveira, B., Carvalho, R.D., Bannwart, A.C. and Ratkovich, N., 2016. Phase distribution analysis in an Electrical Submersible Pump (ESP) inlet handling water–air two-phase flow using Computational Fluid Dynamics (CFD). *Journal of Petroleum Science and Engineering*, 139: 49-61.

100. Pugh, R.J., 1996. Foaming, foam films, antifoaming and defoaming. *Advances in Colloid and Interface Science*, 64: 67-142.

101. Qi, X., Turnquist, N., and Ghasripoor, F., 2012. Advanced electric submersible pump design tool for geothermal applications. GRC *Transaction*, 36: 543-548.

102. Rajendran, S. and Purushothaman, K., 2012. Analysis of a centrifugal pump impeller using ANSYS-CFX. *International Journal of Engineering Research & Technology*,

1(3): 1-6.

103. Rastello, M., Marié, J.L., Grosjean, N. and Lance, M., 2009. Drag and lift forces on interface-contaminated bubbles spinning in a rotating flow. *Journal of Fluid Mechanics*, 624: 159-178.

104. Rastello, M., Marié, J.L., and Lance, M., 2011. Drag and lift forces on clean spherical and ellipsoidal bubbles in a solid-body rotating flow. ASME *Journal of Fluid Mechanics*, 682: 434-459.

105. Rosen, M.J., Hua, X.Y., Zhu, Z.H., 1991. Dynamic surface tension of aqueous surfactant solutions: IV relationship to foaming. Surfactants in Solution, 11: 315–327.

106. Sachdeva, R., 1988. Two-phase flow through electric submersible pumps. PhD Dissertation, the University of Tulsa, Tulsa, Oklahoma.

107. Sachdeva, R., Doty, D.R., and Schmidt, Z., 1994. Performance of electric submersible pumps in gassy wells. SPE *Production & Facilities*, 2: 55-60.

108. Salehi, E., 2012. ESP performance in two-Phase flow through mapping and surging tests at various rotational speeds and intake pressures. Master thesis, the University of Tulsa, Tulsa, OK.

109. Santos-Moreau, V., Brunet-Errard, L., and Rolland, M., 2012. Numerical CFD simulation of a batch stirred tank reactor with stationary catalytic basket. *Chemical Engineering Journal*, 207: 596-606.

110. Schäfer, T., Bieberle, A., Neumann, M., Hampel, U., 2015. Application of gamma-ray computed Tomography for the analysis of gas holdup distributions in centrifugal pumps. *Flow Measurement and Instrumentation*, 46: 262-267.

111. Schiller, L. and Naumann, A., 1933. Fundamental calculations in gravitational

processing. *Zeitschrift Des Vereines Deutscher Ingenieure*, 77: 318-320.

112. Shah, R.K., 1978. A correlation for laminar hydrodynamic entry length solutions for circular and noncircular ducts. ASME *Journal of Fluids Engineering*, 100(2): 177-179.
113. Shoham, O., 2006. *Mechanistic Modeling of Gas-liquid Two-phase Flow in Pipes*. Richardson, TX: Society of Petroleum Engineers.
114. Shojaeefard, M.H., Boyaghchi, F.A., Ehghaghi, M.B., 2006. Experimental study and three-dimensional numerical flow simulation in a centrifugal pump when handling viscous fluids. IUST *International Journal of Engineering Science*, 17 (3), 53–60.
115. Shojaeefard, M.H., Tahani, M., Ehghaghi, M.B., Fallahian, M.A., Beglari, M., 2012. Numerical study of the effects of some geometric characteristics of a centrifugal pump impeller that pumps a viscous fluid. *Computers & Fluids*, 2012 (60), 61–70.
116. Sirino, T., Stel, H., Morales, R.E., 2013. Numerical study of the influence of viscosity on the performance of an electrical submersible pump. In: ASME 2013 Fluids Engineering Division Summer Meeting, American Society of Mechanical Engineers.
117. Solano, E.A., 2009. Viscous effects on the performance of electro submersible pumps (ESP's). Master Thesis, the University of Tulsa, Tulsa, OK.
118. Stel, H., Sirino, T., Prohmann, P.R., Ponce, F., Chiva, S., Morales, R.E., 2014. CFD investigation of the effect of viscosity on a three-stage electric submersible pump. In: ASME 2014 4th Joint US-European Fluids Engineering Division Summer Meeting collocated with the ASME 2014 12th International Conference on Nanochannels, Microchannels, and Minichannels. American Society of Mechanical Engineers.
119. Stel, H., Sirino, T., Ponce, F.J., Chiva, S., Morales, R.E.M., 2015. Numerical investigation of the flow in a multistage electric submersible pump. *Journal of*

Petroleum Science and Engineering, 136: 41–54.

120. Stepanoff, A. J., 1957. *Centrifugal and Axial Flow Pumps: Theory, Design and Application, 2nd Edition*. New York, NY, USA: John Wiley & Sons.
121. Stern, F., Wilson, R.V., Coleman, H.W., and Paterson, E.G., 2001. Comprehensive approach to verification and validation of CFD simulations-Part 1: methodology and procedures. ASME *Journal of Fluids Engineering*, 123(4): 793-802.
122. Sulc, D. and Ditl, P., 2000. Energy dissipation in flocculation and dispersion tanks-study. In Proceedings of 14th International Congress of Chemical and Process Engineering CHISA, Prague, Czech Republic, August 2000.
123. Sun, D., 2003. Modeling gas-liquid head performance of electrical submersible pumps. PhD Dissertation, the University of Tulsa, Tulsa, Oklahoma.
124. Sun, D. and Prado, M.G., 2005. Modeling gas-Liquid head performance of electric submersible pumps. *Journal of Pressure Vessel Technology*, 127(1): 31-38.
125. Sun, D. and Prado, M.G., 2006. Single-phase model for electric submersible pump (ESP) head performance. SPE *Journal*, 11(01): 80-88.
126. Sylvester, N.D., 1987. A mechanistic model for two-phase vertical slug flow in pipes. ASME *Journal of Energy Resources Technology*, 109(4): 206-213.
127. Tabib, M.V., Roy, S.A., and Joshi, J.B., 2008. CFD simulation of bubble column analysis of interphase forces and turbulence models. *Chemical Engineering Journal*, 139(3): 589–614.
128. Takacs, G., 2009. *Electrical Submersible Pumps Manual: Design, Operations, and Maintenance*. Gulf Professional Publishing, Burlington, USA.
129. Taitel, Y., Dukler, A.E., 1976. A model for predicting flow regime transitions in

horizontal and near horizontal gas-liquid flow. AIChE *Journal*, 22 (1): 47-55.

130. Taitel, Y., Bornea, D. and Dukler, A.E., 1980. Modelling flow pattern transitions for steady upward gas-liquid flow in vertical tubes. AIChE *Journal*, 26(3): 345-354.
131. Thin, K.C., Khaing, M.M. and Aye, K.M., 2008. Design and performance analysis of centrifugal pump. *World Academy of Science, Engineering and Technology*, 46: 422-429.
132. Thum, D., Hellmann, D.H. and Sauer, M., 2006. Influence of the patterns of liquid-gas flows on multiphase-pumping of radial centrifugal pumps. In 5th North American Conference on Multiphase Technology (pp. 79-90).
133. Tomita, J.T., da Silva, L.M., and da Silva, D.T., 2012. Comparison between unstructured and structured meshes with different turbulence models for a high pressure turbine application. In ASME Turbo Expo: Turbine Technical Conference and Exposition, Copenhagen, Denmark, June, 2012, Vol. 8: 1633-1645.
134. Tran-Cong, S., Gay, M. and Michaelides, E.E., 2004. Drag coefficients of irregularly shaped particles. *Powder Technology*, 139(1): 21-32.
135. Tremante, A., Moreno, N., Rey, R., and Noguera, R., 2002. Numerical turbulent simulation of the two-phase flow (liquid/gas) through a cascade of an axial pump. ASME *Journal of Fluids Engineering*, 124: 371-376.
136. Trevisan, F.E., 2009. Modeling and visualization of air and viscous liquid in electrical submersible pump. PhD dissertation, the University of Tulsa, Tulsa, Oklahoma.
137. Trevisan, F., Prado, M., 2011. Experimental investigation of the viscous effect on two-phase-flow patterns and hydraulic performance of electrical submersible pumps. *Journal of Canadian Petroleum Technology*. 50 (4): 45–52.

138. Turpin, J.L., Lea, J.F., and Bearden, J.L., 1986. Gas-liquid through centrifugal pumps-correlation of Data. In Proceedings of the Third International Pump Symposium, Texas A&M University, College Station, Texas, USA.

139. Van Esch, B.P.M., 1997. Simulation of three-dimensional unsteady flow in hydraulic pumps. Master Thesis, University of Twente, Enschede, Netherlands.

140. Van Nierop, E.A., Luther, S., Bluemink, J.J., Magnaudet, J., Prosperetti, A. and Lohse, D., 2007. Drag and lift forces on bubbles in a rotating flow. ASME *Journal of Fluid Mechanics*, 571: 439-454.

141. Van Nimwegen, A.T., Portela, L.M. and Henkes, R.A., 2015. The effect of surfactants on vertical air/water flow for prevention of liquid loading. SPE *Journal*, 4: 488-500.

142. Van Nimwegen, A.T., Portela, L.M. and Henkes, R.A.W.M., 2015a. The effect of surfactants on air–water annular and churn flow in vertical pipes. Part 1: morphology of the air–water interface. *International Journal of Multiphase Flow*, 71: 133-145.

143. Van Nimwegen, A.T., Portela, L.M. and Henkes, R.A.W.M., 2015b. The effect of surfactants on air–water annular and churn flow in vertical pipes. Part 2: Liquid holdup and pressure gradient dynamics. *International Journal of Multiphase Flow*, 71: 146-158.

144. Van Nimwegen, A.T., Portela, L.M. and Henkes, R.A.W.M., 2016. The effect of surfactants on upward air–water pipe flow at various inclinations. *International Journal of Multiphase Flow*, 78: 132-147.

145. Van Nimwegen, A.T., Portela, L.M. and Henkes, R.A.W.M., 2017. The effect of the diameter on air-water annular and churn flow in vertical pipes with and without surfactants. *International Journal of Multiphase Flow*, 88: 179-190.

146. Verde, W.M., Biazussi, J.L., Sassim, N.A. and Bannwart, A.C., 2017. Experimental study of gas-liquid two-phase flow patterns within centrifugal pumps impellers. *Experimental Thermal and Fluid Science* (in press).

147. Vieira, T.S., Siqueira, J.R., Bueno, A.D., Morales, R.E.M., and Estevam, V., 2015. Analytical study of pressure losses and fluid viscosity effects on pump performance during monophase flow inside an ESP stage. *Journal of Petroleum Science and Engineering*, 127(2015): 245-258.

148. Wallis, G.B., 1969. *One-dimensional Two-phase Flow*. McGraw-Hill Book Co. Inc., New York City.

149. White, F., 2005. *Viscous Fluid Flow, 3rd edition*. McGraw-Hill Series in Mechanical Engineering, McGraw-Hill Science.

150. Wiesner, F.J., 1967. A review of slip factors for centrifugal impellers. ASME *Journal of Engineering for Power*, 89(4):558-566.

151. Wilcox, D.C., 1998. *Turbulence modeling for CFD*, 2nd edition., DCW Industries Inc., La Cañada, CA.

152. Wilson, R.V., Stern, F., Coleman, H.W., and Paterson, E.G., 2001. Comprehensive approach to verification and validation of CFD simulations-Part 2: application for RANS simulation of a cargo/container ship. ASME *Journal of Fluids Engineering*, 123(4): 803-810.

153. Wood Group ESP, 2004. *Product Catalog*. Wood Group ESP, Inc, Oklahoma City, OK.

154. Wu, D., Yan, P., Chen, X., Wu, P., and Yang, S., 2015. Effect of trailing-edge modification of a mixed-flow pump. ASME *Journal of Fluids Engineering*, 137(10):

101205.

155. Xiang, M., Cheung, S., Yeoh, G., Zhang, W., and Tu, J., 2011. On the numerical study of bubbly flow created by ventilated cavity in vertical pipe. *International Journal of Multiphase Flow*, 37(7): 756–768.

156. Yakhot, V., Orszag, S.A., Thangam, S., Gatski, T.B., Speziale, C.G., 1992. Development of turbulence models for shear flows by a double expansion technique. *Physics of Fluids A: Fluid Dynamics*, 4(7): 1510-1520.

157. Ye, Z., Rutter, R., Martinez, I. and Marsis, E., 2016. CFD and FEA-Based, 3D metal printing hybrid stage prototype on electric submersible pump ESP system for high-gas wells. In SPE North America Artificial Lift Conference and Exhibition. Society of Petroleum Engineers, Woodlands, Texas, October, 2016.

158. Yu, Z.Y., Zhu, B.S., Cao, S.L. and Wang, G.Y., 2013. Application of two-fluid model in the unsteady flow simulation for a multiphase rotodynamic pump. In *IOP Conference Series: Materials Science and Engineering*, 52(6): 062003.

159. Yu, Z., Zhu, B. and Cao, S., 2015. Interphase force analysis for air-water bubbly flow in a multiphase rotodynamic pump. *Engineering Computations*, 32(7): 2166-2180.

160. Zakem, S., 1980. Determination of gas accumulation and two-phase slip velocity ratio in a rotating impeller. *Polyphase Flow and Transportation Technology*, 12(11): 167-173.

161. Zapata, L., 2003. Rotational speed effects on ESP two-phase performance. Master thesis, the University of Tulsa, Tulsa, Oklahoma.

162. Zhang, H.-Q., Wang, Q., Sarica, C. and Brill, J.P., 2003. Unified model for gas-liquid pipe flow via slug dynamics—Part 1: model development. ASME *Journal of Energy*

Resources Technology, 125: 266-273.

163. Zhang, H.-Q., Wang, Q., Sarica, C. and Brill, J.P., 2003. Unified model for gas-liquid pipe flow via slug dynamics—Part 2: model validation. ASME *Journal of Energy Resources Technology*, 125: 274-283.
164. Zhang, H.-Q., Wang, Q., Sarica, C., Brill, J.P., 2003. A unified mechanistic model for slug liquid holdup and transition between slug and dispersed bubble flows. *International journal of multiphase flow*, 29(1): 97-107.
165. Zhang, H.-Q., Wang, Q., Sarica, C. and Brill, J.P., 2004. Unified model of heat transfer in gas-liquid pipe flow. In SPE Annual Technical Conference and Exhibition. Society of Petroleum Engineers.
166. Zhang, H.-Q. and Sarica, C., 2006. Unified modeling of gas/oil/water pipe flow-Basic approaches and preliminary validation. SPE *Projects, Facilities & Construction*, 1(02): 1-7.
167. Zhang, H.-Q., 2013. TUALP Spring Advisory Board Meeting, the University of Tulsa, Tulsa, OK.
168. Zhang, J., Li, Y., Cai, S., Zhu, H. and Zhang, Y., 2016. Investigation of gas–liquid two-phase flow in a three-stage rotodynamic multiphase pump via numerical simulation and visualization experiment. *Advances in Mechanical Engineering*, 8(4): 1-13.
169. Zhou, D., Sachdeva, R., 2010. Simple model of electric submersible pump in gassy well. *Journal of Petroleum and Engineering*, 70, 204-213.
170. Zhou, L., Shi, W., Lu, W., et al., 2012. Numerical investigations and performance experiments of a deep-well centrifugal pump with different diffusers. ASME *Journal of Fluids Engineering*, 134: 071102.

171. Zhu, J., Banjar, H., Xia, Z., and Zhang, H.-Q., 2016. CFD simulation and experimental study of oil viscosity effect on multi-stage electrical submersible pump (ESP) performance. *Journal of Petroleum Science and Engineering*, 146, 735-745.

172. Zhu, J., and Zhang, H.-Q., 2014. CFD simulation of ESP performance and bubble size estimation under gassy conditions. In SPE Annual Technical Conference and Exhibition, Society of Petroleum Engineers, Amsterdam, the Netherlands, October, 2014.

173. Zhu, J., and Zhang, H.-Q., 2016. Mechanistic modeling and numerical simulation of in-situ gas void fraction inside ESP impeller. *Journal of Natural Gas Science and Engineering*, 36, 144-154.

174. Zhu, J., and Zhang, H.-Q., 2017. Modeling of gas bubble size in electrical submersible pump (ESP) through numerical simulation. SPE *Production & Operations*, 2017.

175. Zhu, J., Guo, X., Liang, F., and Zhang, H.-Q., 2017. Experimental study and mechanistic modeling of pressure surging in electrical submersible pump. *Journal of Natural Gas Science and Engineering*, under review.

176. Ziegenhein, T., Rzehak, R., and Lucas, D., 2015. Transient Simulation for Large Scale Flow in Bubble Columns. *Chemical Engineering Science*, 122: 1-13.

APPENDIX A

EQUIPMENT AND INSTRUMENT SPECIFICATIONS

Table A.1: TUALP gas-liquid flow loop equipment specifications

Equipment	Model	Capacity	Purpose
Separator	–	150 bbl	Water storage maintain pressure
ESP pump	GE Oil & Gas Wood Group TE-2700	BEP:2700 bpd, 3500 rpm	Testing bench
Electric motor	North American H3650	50 hp	Drive motor
Air compressor	Kaeser CSD60	186 cfm, 217 psi	Gas source
Variable speed drive	Hitachi L300P	50 hp	Altering rotational speed
ESP thrust chamber	Schlumberger REDA NO.88AB1- LT	–	Thrust bearing box
Liquid control valve	Fisher Controls 657	–	Liquid flow rate control
Gas control valve	Emerson Process Management 24588SB	–	Gas flow rate control
Metering pump	Iwaki EWN-R B11	0.4 GPH, 250 psi	Surfactant injection

Table A.2: TUALP gas-liquid flow loop instrumentation specifications

Transducer	Model	Range
Temperature transmitter	Emerson Rosemount 3144	-50℃ – 85℃
Absolute pressure transmitter	Emerson Rosemount 2051S	0 to 500 psig
Differential pressure transmitter	Emerson Rosemount 3051S	-10 to 50 psig
Coriolis liquid flowmeter	Micro Motion CMF200	0 to 1600 lb/min
Coriolis gas flowmeter	Micro Motion CMF025	0 to 40 lb/min
Torque/rotary speed sensor and monitor	Sensor: Lebow model 1805 Monitor: Lebow model 7540	0 to 22000 rpm 0 to 5000 lbf-in

Table A.3: TUALP gas-liquid flow loop DAQ specifications

Device	**Features**
Data processing computer	Dell Optiplex 9020, i7-4770 CPU @ 3.4 GHz, RAM: 16GB, HD: 1TB
National Instruments cFP-AI-111	• 16 single-ended analog current input channels • Three input ranges: ±20, 0–20, and 4–20 mA • 16-bit resolution • Three filter settings: 50, 60, and 500 Hz • Hot swappable • 2300 V_{rms} transient overvoltage protection • –40 to 70 °C operation
National Instruments cFP-AO-200	• Eight 0–20 or 4–20 mA outputs • 0.5 mA over ranging • 12-bit resolution • Up to 1 kΩ load impedance (with 24 V loop supply) • Indicators for open current loops • Short-circuit protection • 2300 V_{rms} transient overvoltage protection between the inter-module communication bus and the I/O channels • –40 to 70 °C operation • Hot plug-and-play
National Instruments cFP-1804	• Network interface: 10 BaseT and 100 BaseTX Ethernet, IEEE802.3, 10/100 Mbps • One RS-232 (DCE) serial port, 300 to 115200 bps • 11 to 30 VDC, 20W • 2300 V_{rms} transient overvoltage protection •–40 to 70 °C operation

APPENDIX B

CALCULATION EQUATIONS FOR FLUID PROPERTIES

The moist air density can be calculated based on Comite International des Poid et Measures (CIPM-81) formulas (Davis 1992). The CIPM-81 correlations require air temperature, pressure, relative humidity (or dew-point temperature) and mole fraction of carbon dioxide, as well as a number of constants.

The density of moist air can be calculated by,

$$\rho = \frac{pM_a}{ZRT}\left[1 - x_v\left(1 - \frac{M_V}{M_a}\right)\right] \tag{B.1}$$

where, p is the pressure, T the temperature, x_v the mole fraction of water vapor, M_a the molar mass of dry air, M_V the molar mass of water, R the molar gas constant, and Z the compressibility factor. M_a is calculated by an auxiliary equation,

$$M_a = 28.9635 + 12.011\left(x_{CO_2} - 0.0004\right) \tag{B.2}$$

where, x_{CO_2} is the mole fraction of carbon dioxide. x_v is calculated by following steps. First the saturation vapor pressure p_{SV} is given by,

$$p_{SV} = 1 \times \exp\left(AT^2 + BT + C + \frac{D}{T}\right) \tag{B.3}$$

where, A, B, C, D are constants, as summarized in Table B.1. Next the enhancement factor f is obtained by,

$$f = \alpha + \beta p + \gamma t^2 \tag{B.4}$$

t is the temperature in degrees Celsius. The Greek letters, α, β, γ are constants as listed in Table B.1. Thus, the x_v can be calculated,

$$x_V = hf\left(p,t\right)\frac{p_{SV}\left(t\right)}{p} = f\left(p,t_r\right)\frac{p_{SV}\left(t_r\right)}{p} \tag{B.5}$$

Then the compressibility Z is obtained:

$$Z = 1 - \frac{p}{T}\left[a_0 + a_1 t + a_2 t^2 + \left(b_0 + b_1 t\right)x_V + \left(c_0 + c_1 t\right)x_V^2\right] + \frac{p^2}{T^2}\left(d + e x_V^2\right) \tag{B.6}$$

where, a_0, a_1, a_2; b_0, b_1; c_0, c_1; d and e are constants as well, which are listed in Table B.1.

Table B.1: Summary for all constants in calculating air density

Parameters	**Constants**		**Values**
Saturation vapor pressure p_{SV}	A	10^{-5} K^{-2}	1.2811805
	B	10^{-2} K^{-1}	-1.9509874
	C		34.04926034
	D	10^{3} K	-6.3536311
Enhancement factor f	α		1.00062
	β	10^{-8} Pa^{-1}	3.14
	γ	10^{-7} K^{-2}	5.6
Compressibility factor Z	a_0	10^{-6} K Pa^{-1}	1.62419
	a_1	10^{-8} Pa^{-1}	-2.8969
	a_2	10^{-10} K^{-1} Pa^{-1}	1.0880
	b_0	10^{-6} K Pa^{-1}	5.757
	b_1	10^{-8} Pa^{-1}	-2.589
	c_0	10^{-4} K Pa^{-1}	1.9297
	c_1	10^{-6} Pa^{-1}	-2.285
	d	10^{-11} K^{2} Pa^{-2}	1.73
	e	10^{-8} K^{2} Pa^{-2}	-1.034
Gas constant R	R	J mol^{-1} K^{-1}	8.31441
$M_a\,(x_{CO_2} = 0.0004)/R$	$M_a R^{-1}$	10^{-3} kg K J^{-1}	3.48353

APPENDIX C

BUBBLE SIZE MODELING

Following similar approaches adopted by Estevam (2002), Barrios (2007) and Gamboa (2008), the bubble size prediction model is proposed. A good agreement between CFD simulation results of pump performance and experimental data is achieved using the predicted bubble sizes.

Hinze (1955) proposed the mechanism for break-up and coalescence of fluid particles based on the balance between external force and surface tension force. In turbulent flow, the external force is turbulent dynamic pressure force which tends to deform and break liquid particles, while surface tension force resists such deformation. The ratio of the above two forces, known as the Weber number, is given by

$$We_{crit} = \frac{\tau}{\sigma / d_{\max}} . \tag{C.1}$$

Here, We_{crit} is the critical Webber number, τ (Pa) is turbulence pressure force, σ (N/m) is the surface tension and d_{max} (m) is the maximum diameter of a stable bubble in turbulent flow, which is comparable to the largest eddy size under Kolmogoroff scale. Levich (1962) proposed similar force balance model and considered the balance as internal pressure and capillary pressure. Thus the density is included through internal pressure force term (Hesketh et al. 1987). The modified We_{crit} formula by Levich is defined as

$$We_{crit} = \frac{\tau}{\sigma / d_{\max}} \left(\frac{\rho_d}{\rho_c} \right)^{\frac{1}{3}} , \tag{C.2}$$

where ρ_c (kg/m^3) and ρ_d (kg/m^3) are fluid densities of continuous phase and dispersed phase, respectively. The turbulence pressure force is characterized as $\tau = \rho \overline{v'^2}$. The mean-square velocity fluctuation term, $\overline{v'^2}$ is a function of the energy dissipation rate per unit mass denoted by ε (m^2/s^3), which was derived by Batchelor (1953):

$$\overline{v'^2} = 2(\varepsilon d_{\max})^{2/3}. \tag{C.3}$$

Substitute above equation into Levich's model for We_{crit}, and rearrange the obtained formula with d_{max} at the left hand side (LHS):

$$d_{\max} = \left(\frac{We_{crit}}{2}\right)^{3/5} \left(\frac{\sigma}{\rho_c}\right)^{3/5} \varepsilon^{-2/5} \left(\frac{\rho_c}{\rho_d}\right)^{1/5}. \tag{C.4}$$

To estimate maximum bubble size in turbulent flow from Eq. (4.48), ε and We_{crit} should be known. Davies (1972), Sulc and Ditl (2000) proposed approximation for ε in agitated tanks, but the equation for ε in centrifugal pumps are still not available in literature. Padron (2004) postulated ε as function of dissipated energy in a centrifugal pump by Eq. (4.49), based on which Pereyra (2011) derived size prediction model for oil droplets dispersed in water phase.

$$\varepsilon = k\left(\frac{\Delta P q}{\rho_c V}\right)^{-2/5}, \tag{C.5}$$

where ΔP (Pa) is the pressure increment of observed pump, q (m^3/s) is the volumetric liquid flow rate, V (m^3) is the single-stage pump flow volume, k is a constant. Then Eq. (4.48) can be written as

$$d_{\max} = k\left(\frac{We_{crit}}{2}\right)^{3/5} \left(\frac{\sigma}{\rho_c}\right)^{3/5} \left(\frac{\Delta P q}{\rho_c V}\right)^{-2/5} \left(\frac{\rho_c}{\rho_d}\right)^{1/5}. \tag{C.6}$$

Eq. (C.6) can be used to calculate d_{max} for single bubble in centrifugal pump with turbulent flow. To consider inlet no-slip GVF effects, Murakami and Minumura (1974) found out that d_{max} increased proportionally to the gas void fraction by a factor of λ_G. Calderbank (1958) used a factor of $4.15\sqrt{\alpha}$, while Godfrey (1989) correlated by exponential factor of $C_1(\lambda_G)^{C_2}$, where C_1 and C_2 are constants that should be determined by experiments. We can consider critical bubble sizes as linear function of λ_G. Then, the equation for calculating d_{max} is expressed as

$$d_{\max} = C^* \lambda_G \left(\frac{We'_{crit}}{2} \right)^{3/5} \left(\frac{\sigma}{\rho_c} \right)^{3/5} \left(\frac{\Delta Pq}{\rho_c V} \right)^{-2/5} \left(\frac{\rho_c}{\rho_d} \right)^{1/5}, \tag{C.7}$$

where C^* is a constant. Kouba (2003) derived We_{crit} in terms of droplet/bubble deformation. For spherical bubble dual dispersion, the We_{crit} is given by

$$We_{\max} = \frac{8n}{C_D\left(1 - 2V_r + V_r^2\right)} \frac{d_o}{d_p}, \tag{C.8}$$

where V_r is the ratio of dispersed phase velocity to continuous phase velocity, n is phase number. Assuming drag coefficient $C_D = 0.4$ in turbulent flow, the critical Weber number is calculated to be $We_{crit} = 40$. Based on experimental observations in rotor-stator system, the relation of maximum bubble diameter with Sauter mean diameter (d_{32}) can be correlated by multiplying a constant number of 0.42 (Gamboa, 2008) or 0.44 (Phongikaroon, 2001). In this study, a mean value of 0.43 was assumed to correlate d_{max} and d_{32}. Let $C^* = 1/0.43 = 2.326$, and then substitute $C^* = 2.326$ and $We_{crit} = 40$ into Eq. (C.7). The following equation is obtained:

$$d_{\max} = 14.06\lambda_G \left(\frac{\sigma}{\rho_c} \right)^{\frac{3}{5}} \left(\frac{\Delta Pq}{\rho_c V} \right)^{-\frac{2}{5}} \left(\frac{\rho_c}{\rho_d} \right)^{\frac{1}{5}}. \tag{C.9}$$

So d_{32} is calculated by multiplying the above equation with the constant number of 0.43.

That is

$$d_{32} = 6.034\lambda_G \left(\frac{\sigma}{\rho_c}\right)^{\frac{3}{5}} \left(\frac{\Delta P q}{\rho_c V}\right)^{-\frac{2}{5}} \left(\frac{\rho_c}{\rho_d}\right)^{\frac{1}{5}}. \tag{C.10}$$

APPENDIX D

ADDITIONAL EXPERIMENTAL PUMP HEAD CURVES

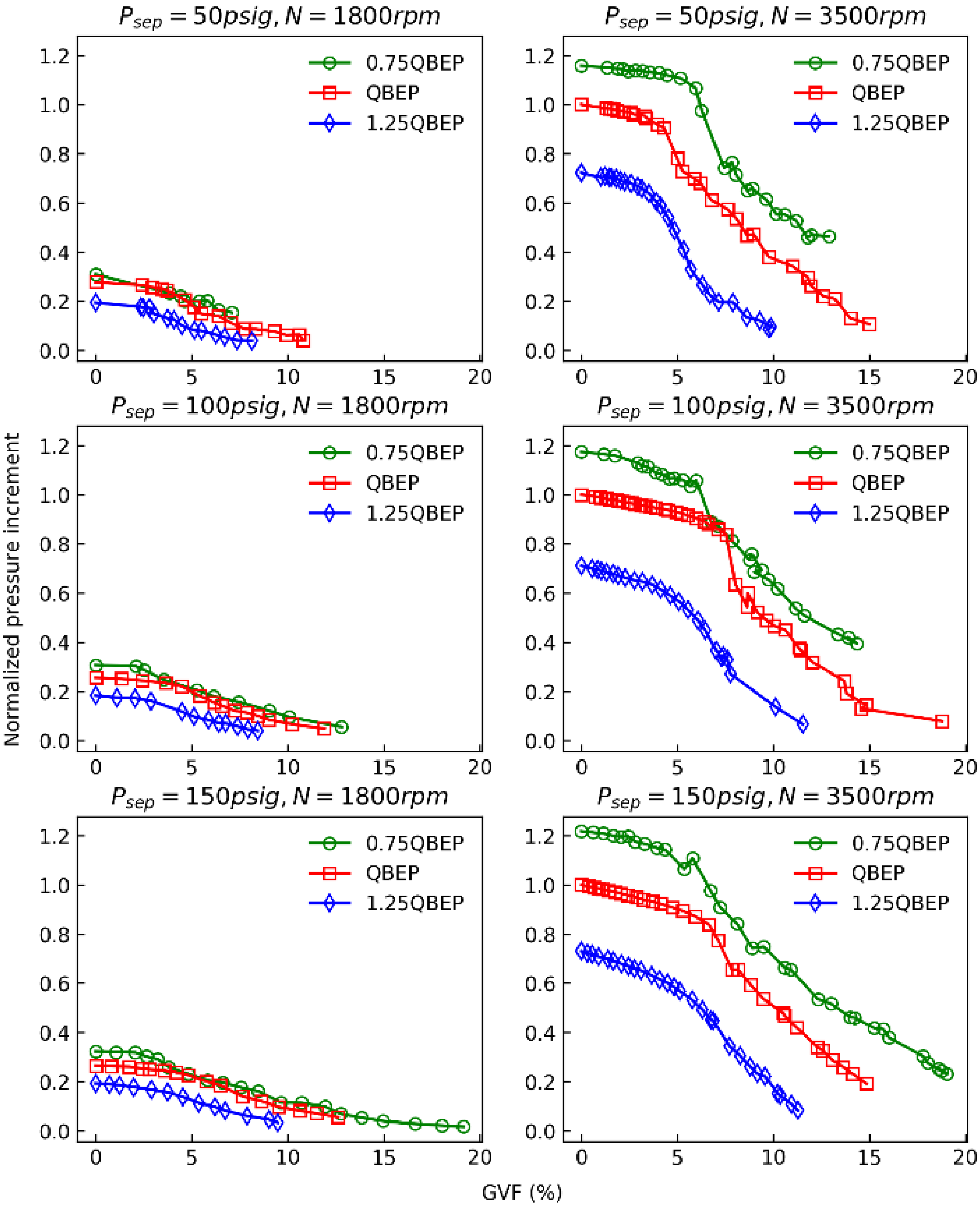

Figure D.1 Suring test results for water and air at stage 3 with different P_{sep} and N

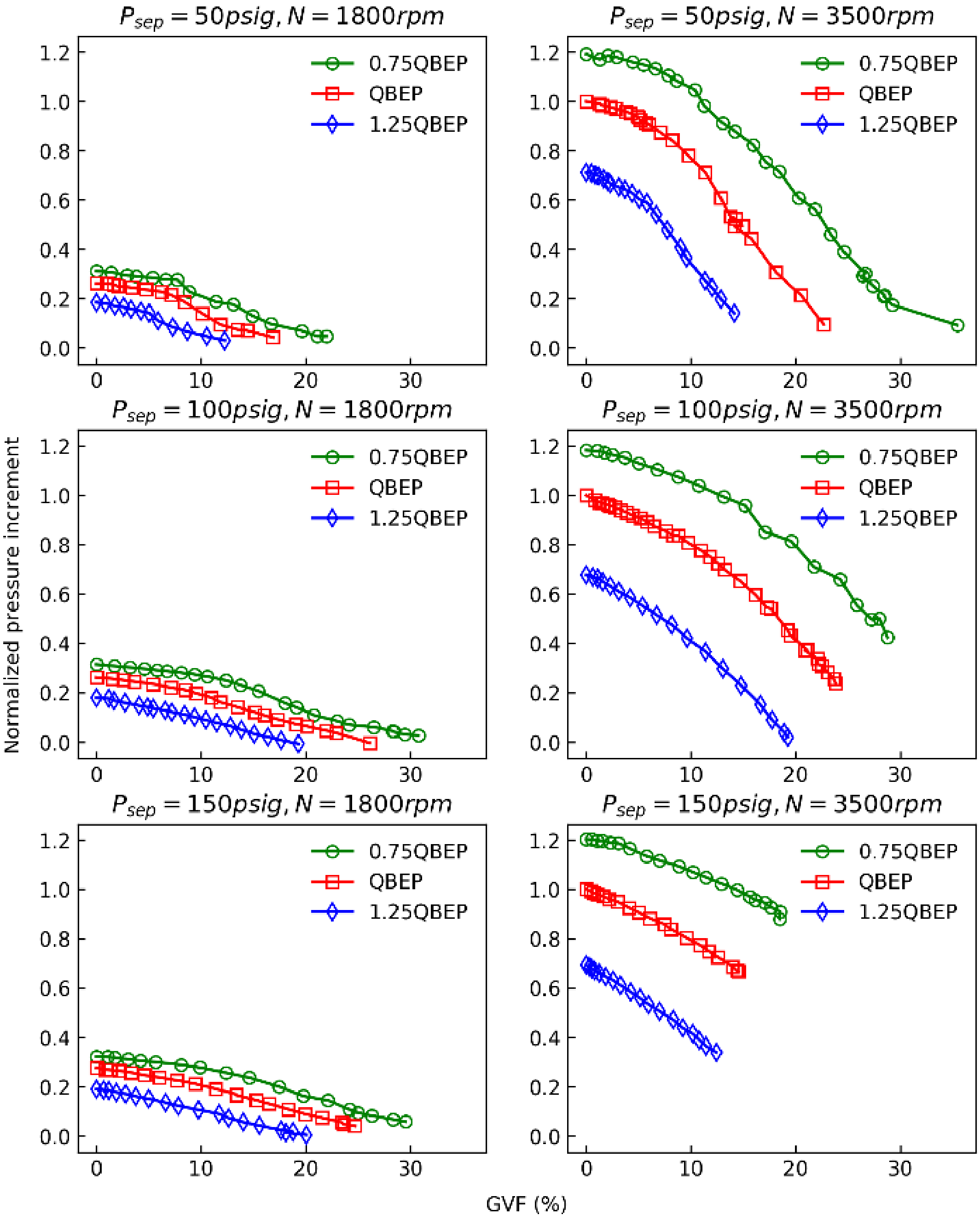

Figure D.2 Suring test results for water + 0.2vol% IPA solution and air at stage 3 with different P_{sep} and N

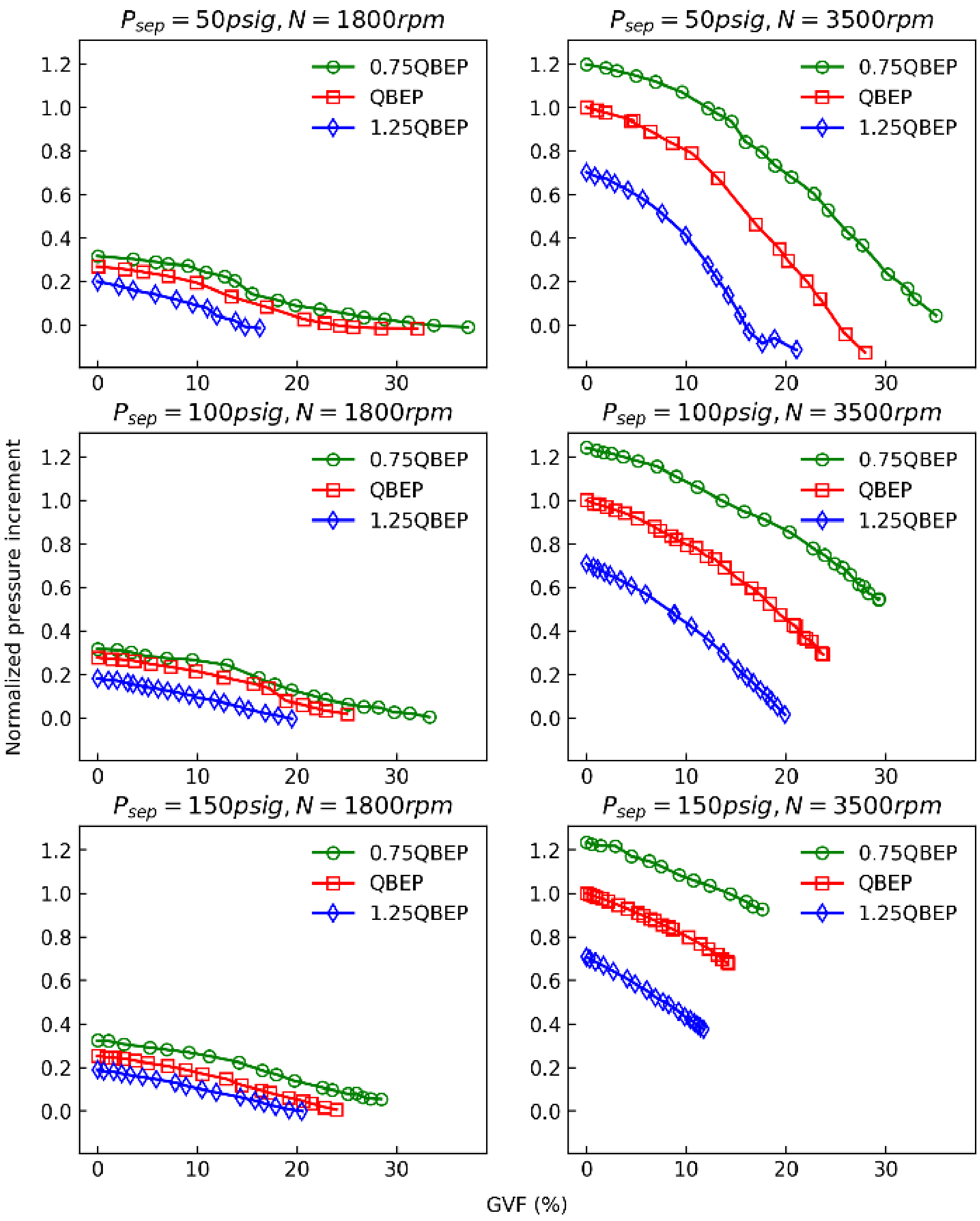

Figure D.3 Suring test results for water + 0.4vol% IPA solution and air at stage 3 with different P_{sep} and N

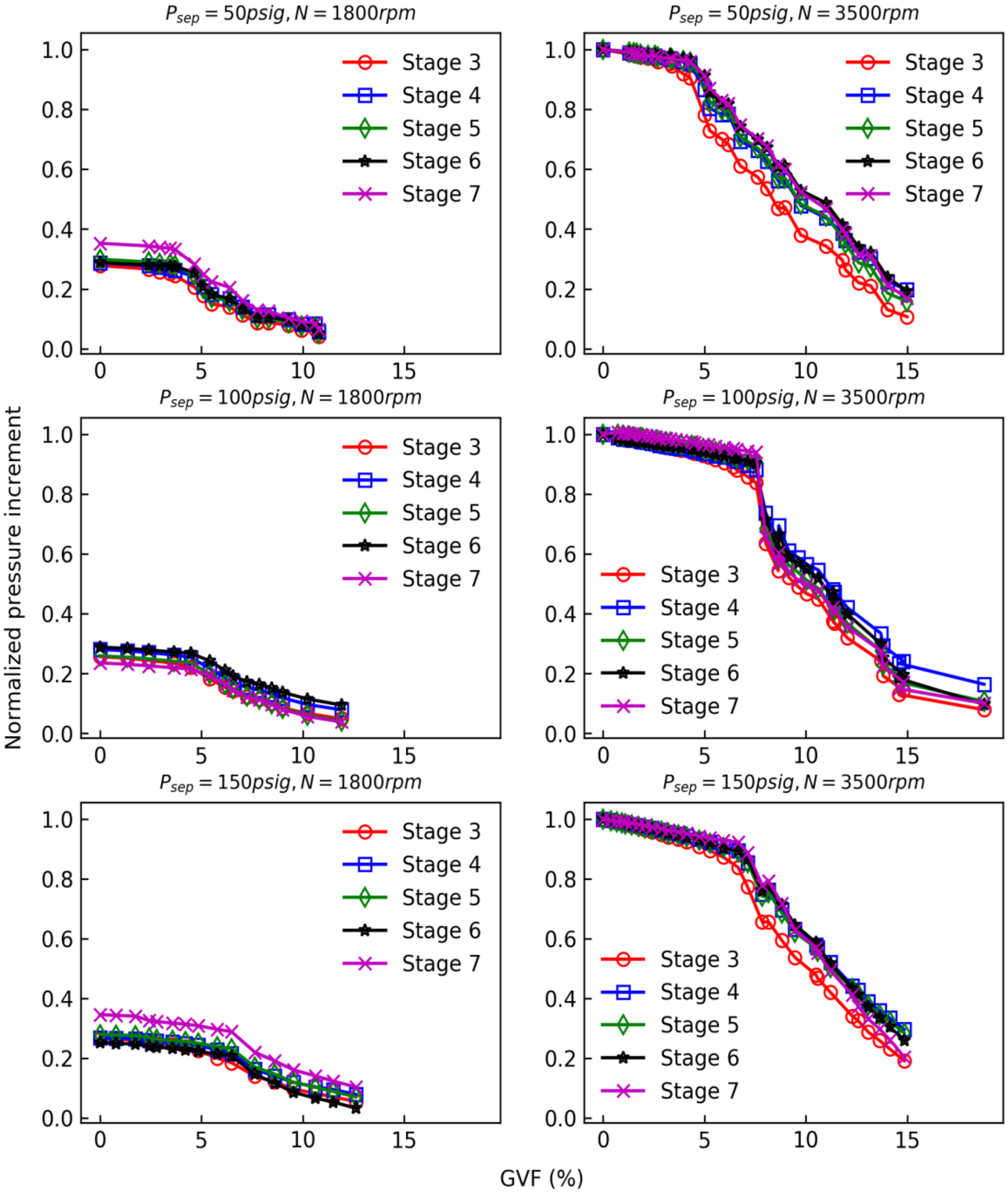

Figure D.4 Suring test results for water and air at Q_{BEP} with different P_{sep} and N

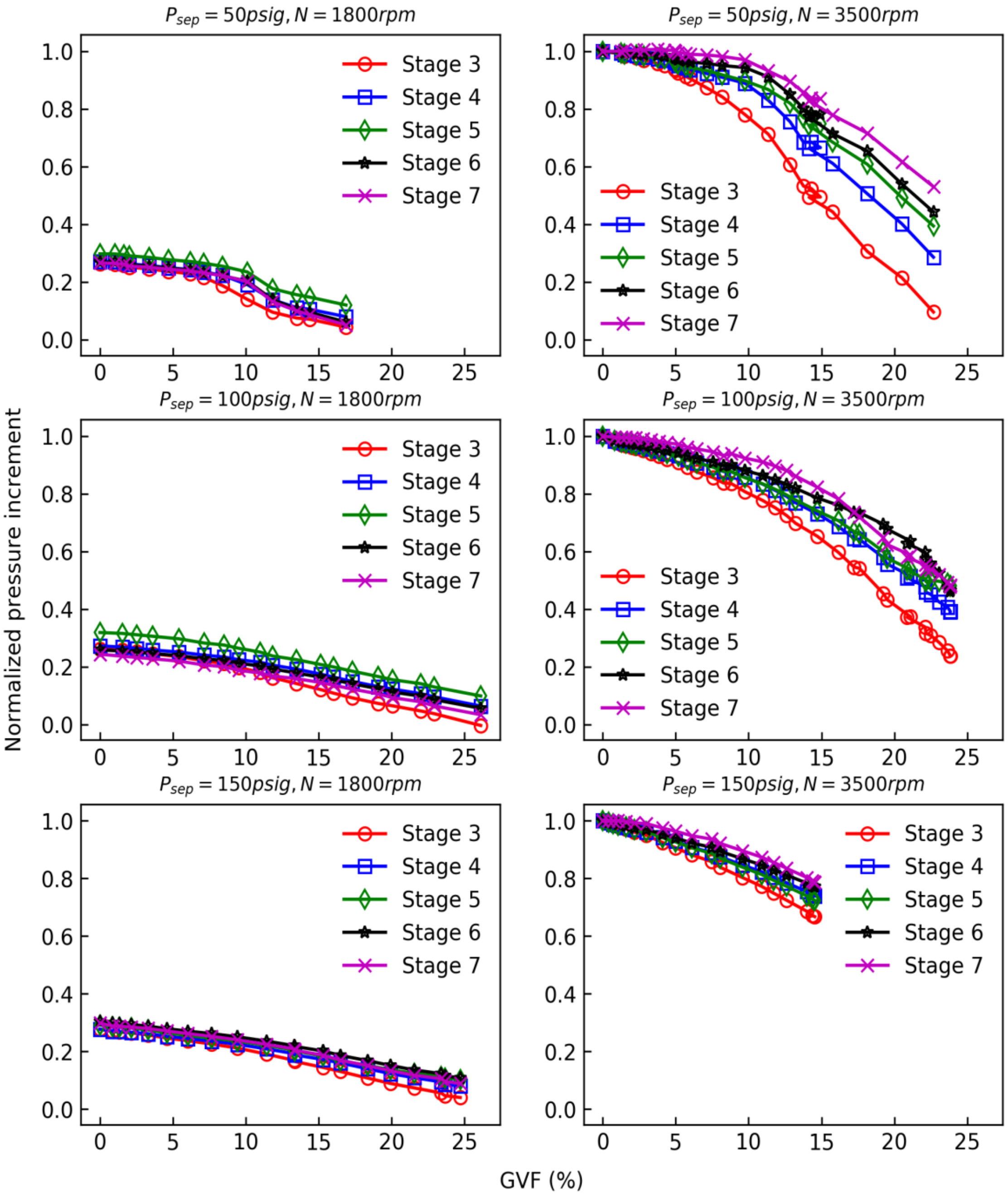

Figure D.5 Suring test results for water + 0.2vol% IPA solution and air at Q_{BEP} with different P_{sep} and N

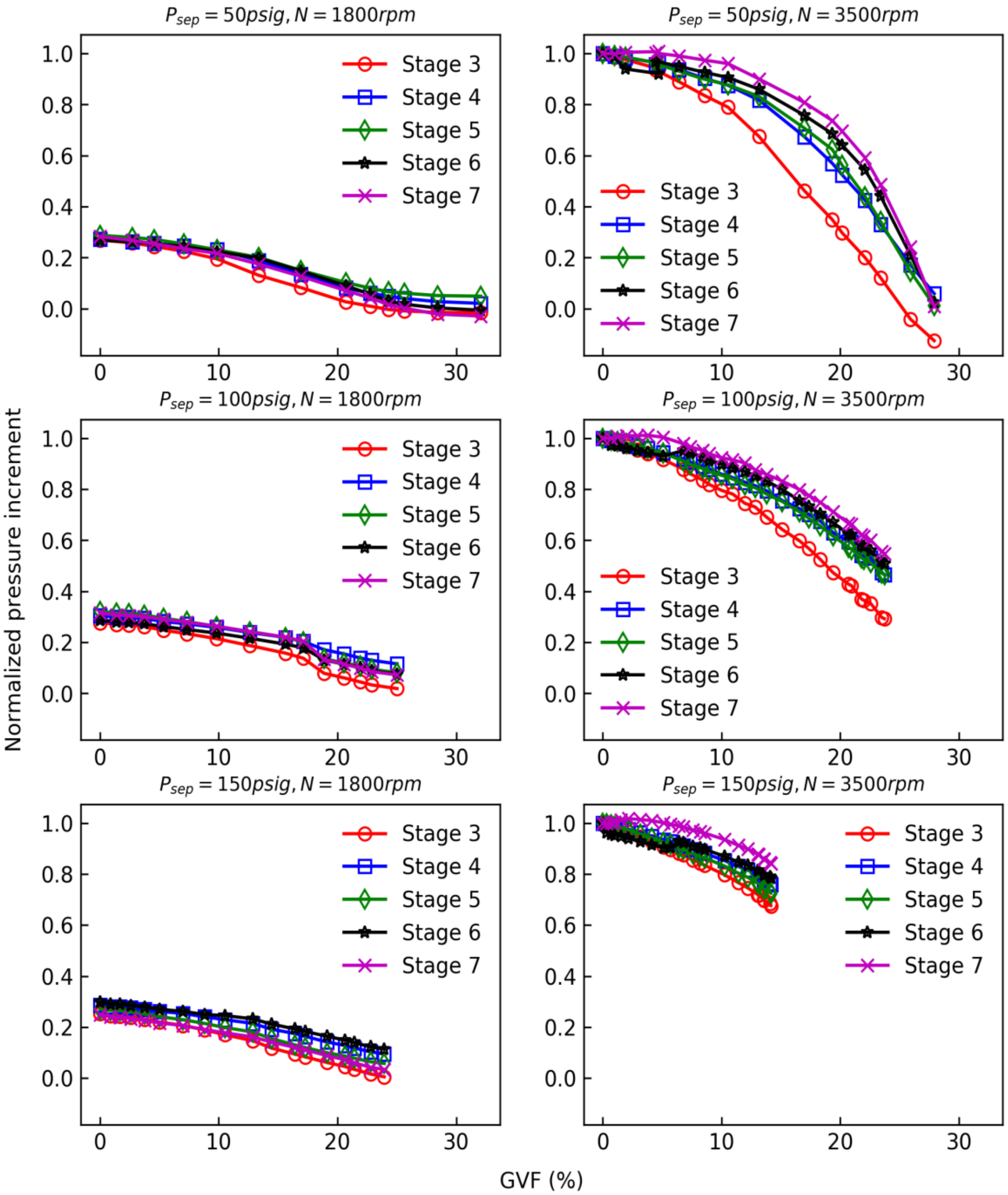

Figure D.6 Suring test results for water + 0.4vol% IPA solution and air at Q_{BEP} with different P_{sep} and N

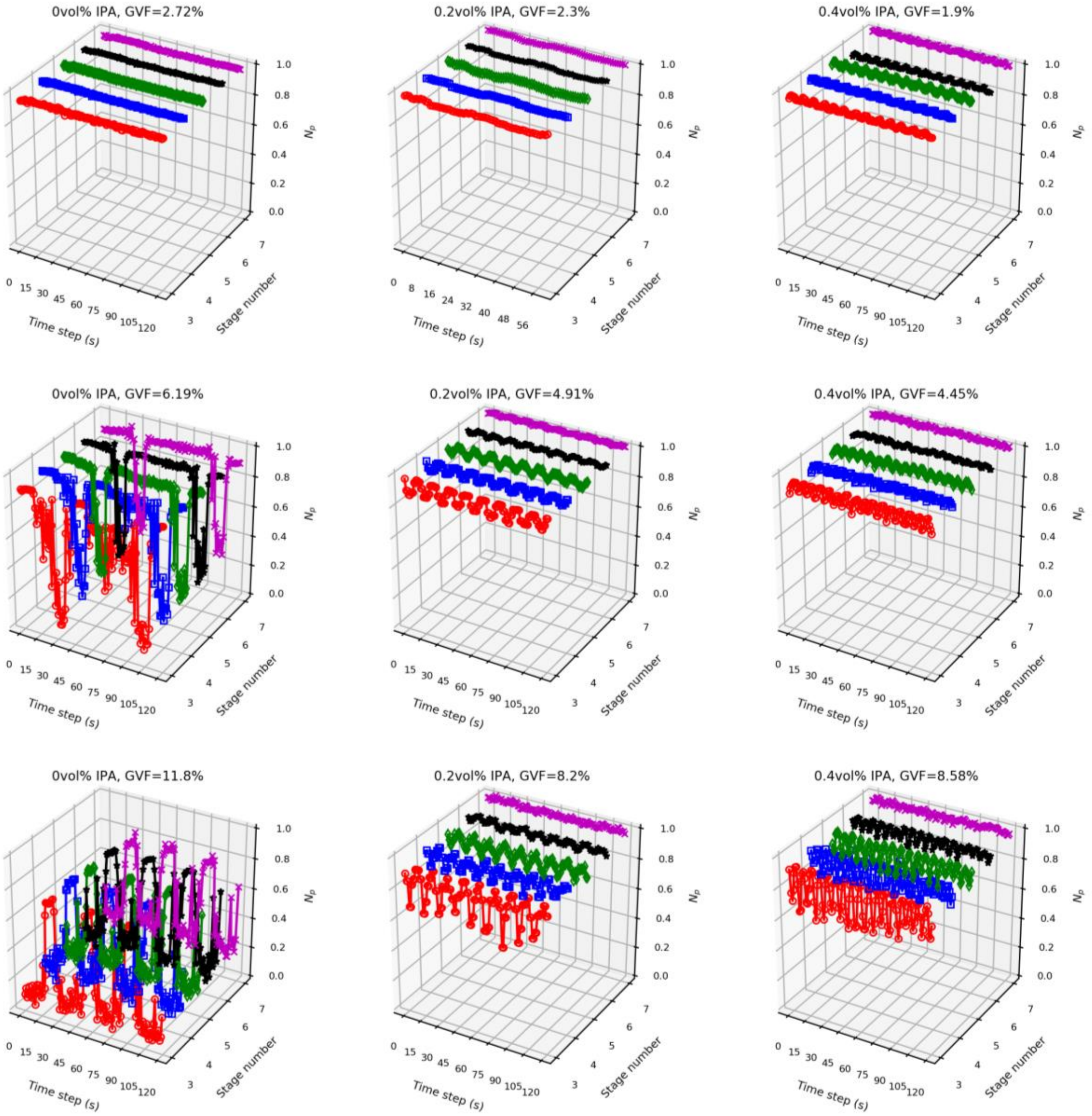

Figure D.7 Transient suring test results at Q_{BEP} with P_{sep} = 50 psig and N = 3500 rpm

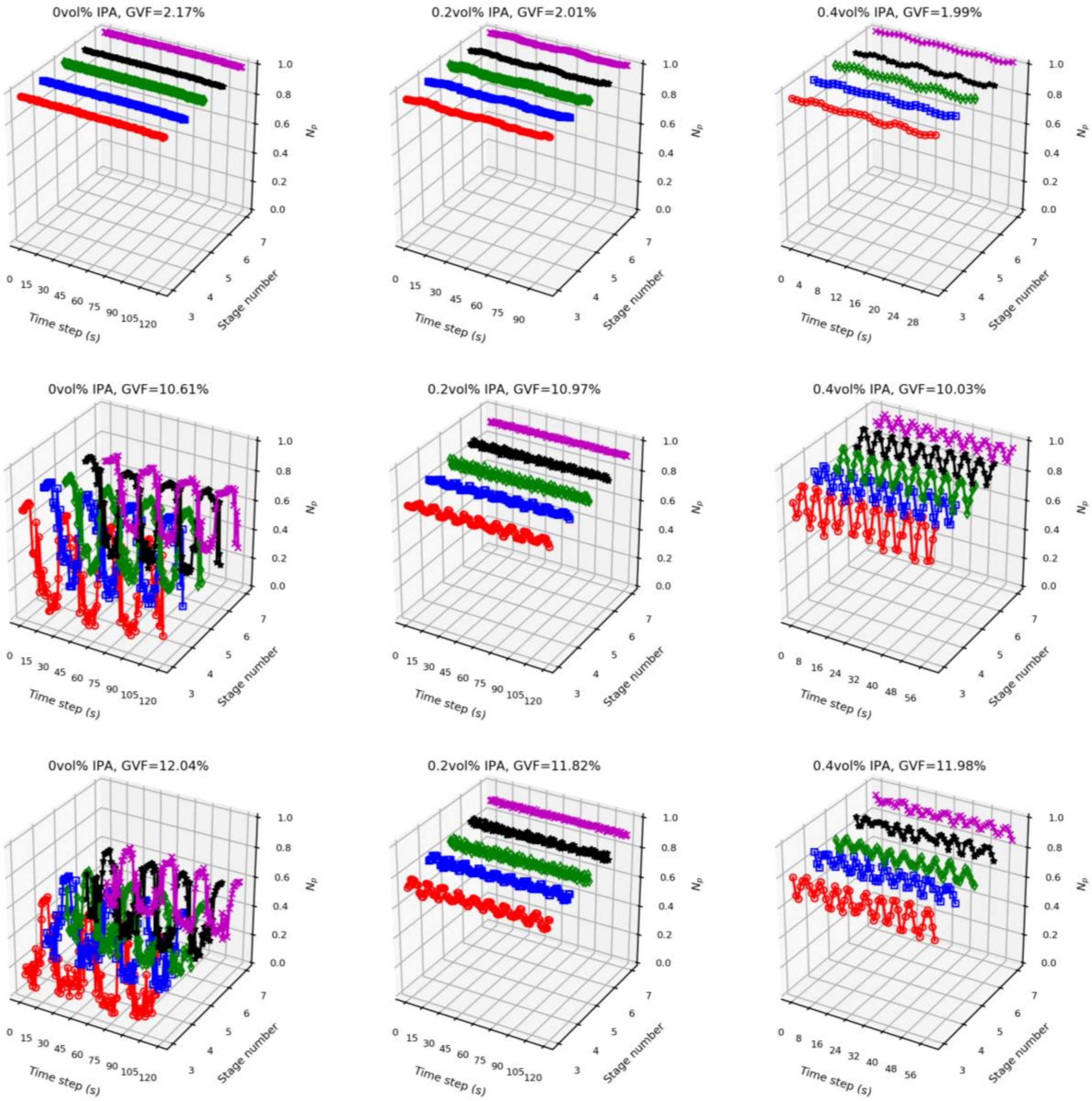

Figure D.8 Transient surging test results at Q_{BEP} with P_{sep} = 100 psig and N = 3500 rpm

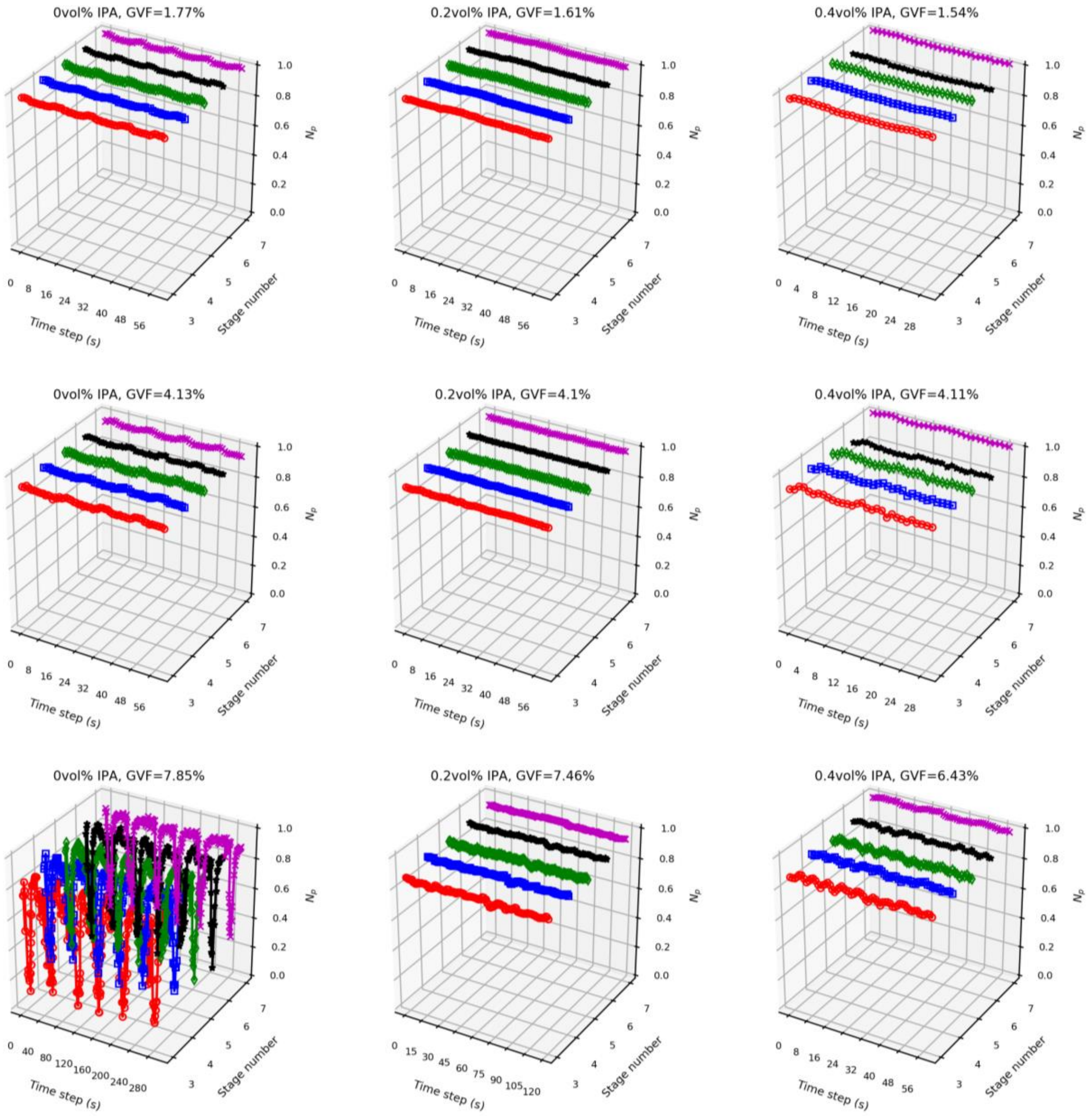

Figure D.9 Transient surging test results at Q_{BEP} with P_{sep} = 150 psig and N = 3500 rpm

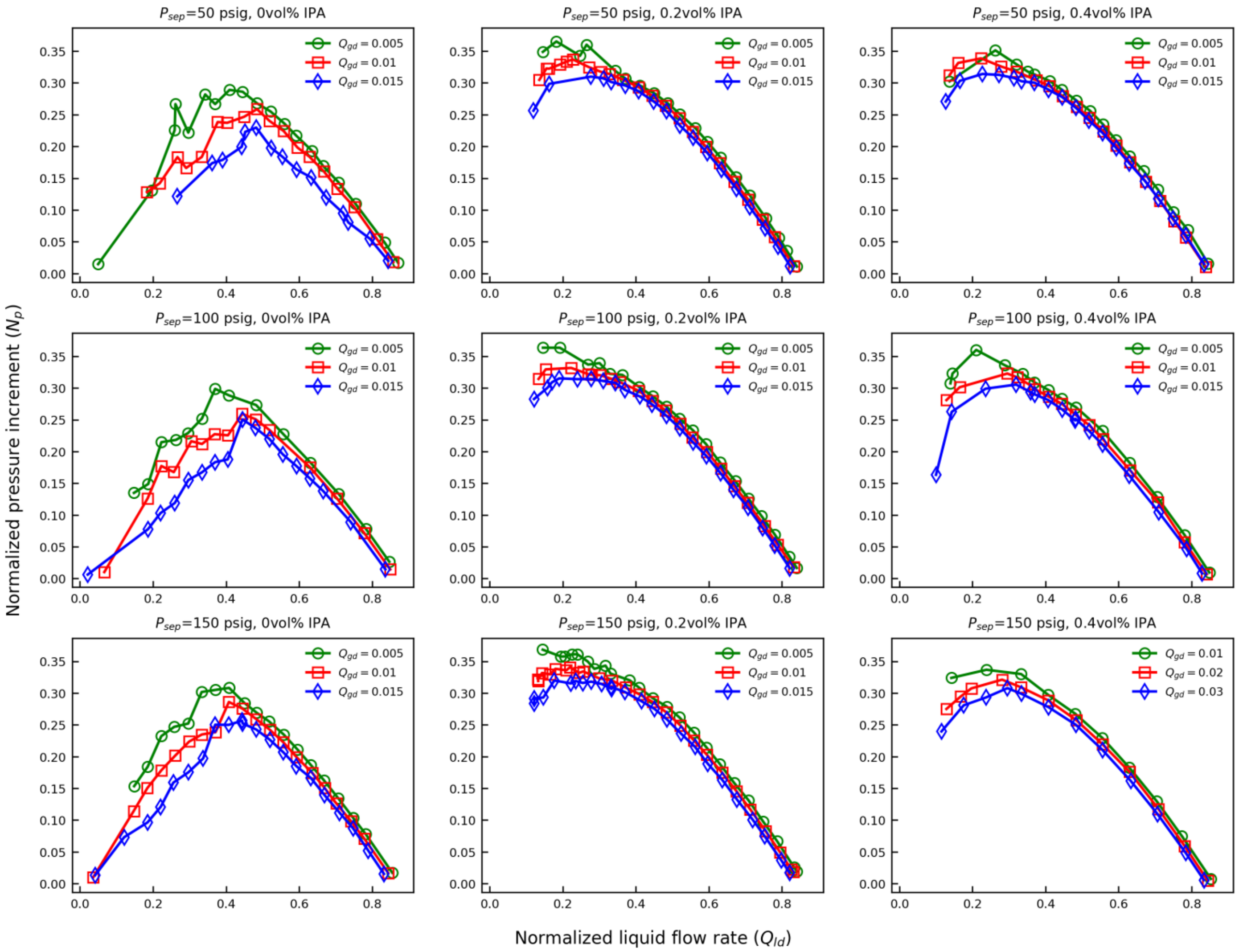

Figure D.10 Mapping test results at stage 3 with different P_{sep} and N = 1800 rpm

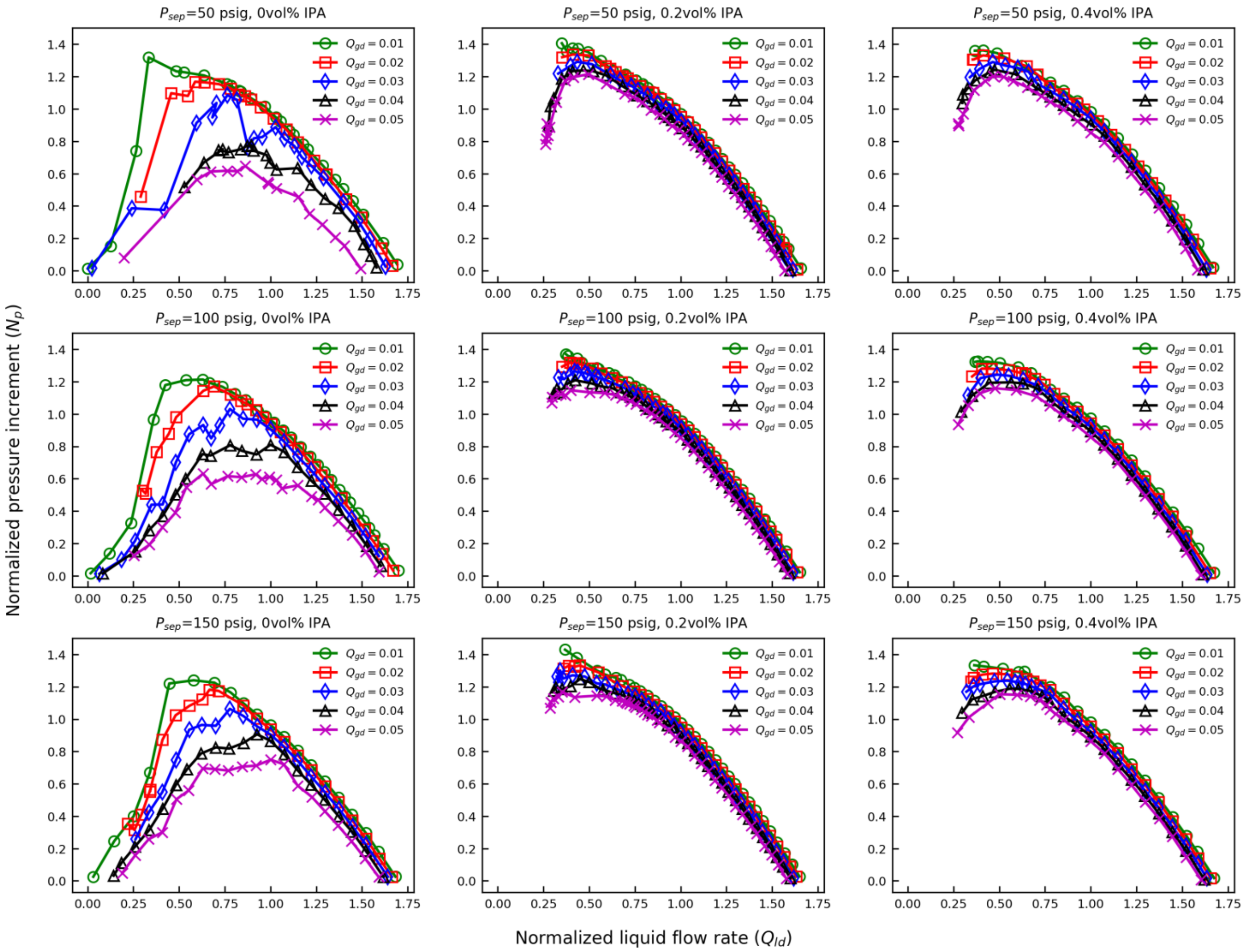

Figure D.11 Mapping test results at stage 3 with varying P_{sep} and N = 3500 rpm

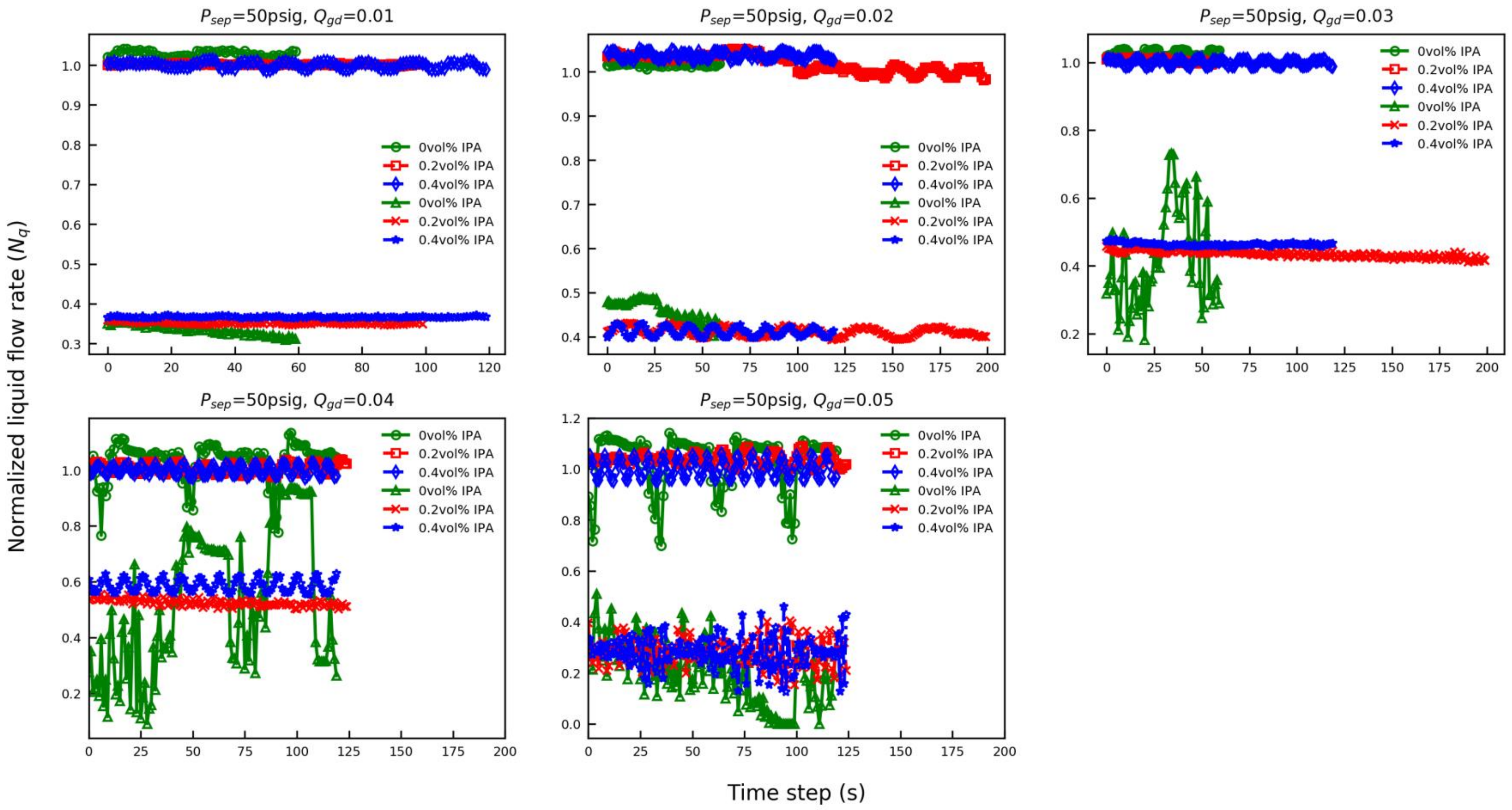

Figure D.12 Transient mapping test results at P_{sep} = 50 psig and N = 3500 rpm

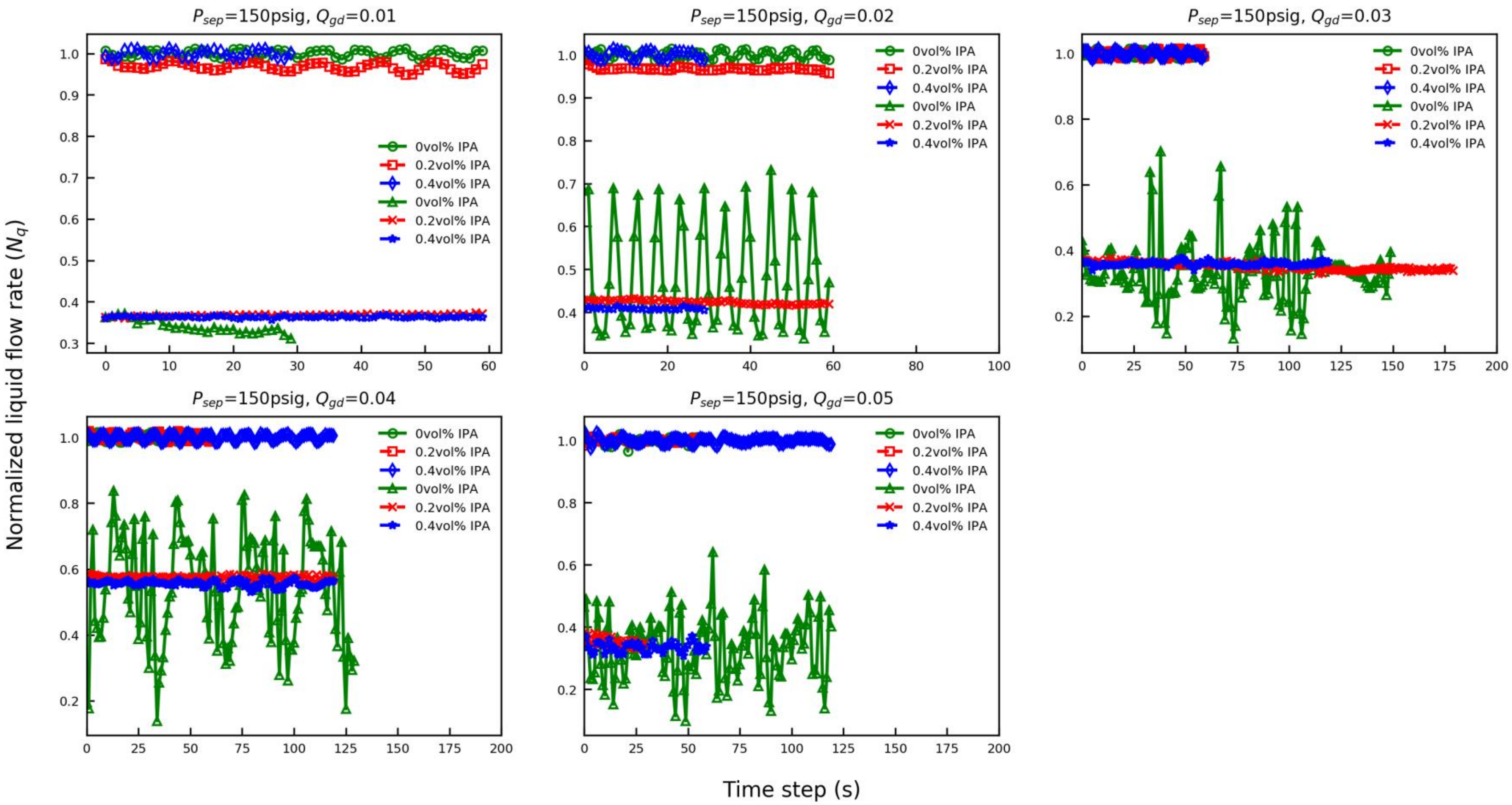

Figure D.13 Transient mapping test results at P_{sep} = 150 psig and N = 3500 rpm

APPENDIX E

MECHANISTIC MODEL VALIDATION SUPPLEMENTS

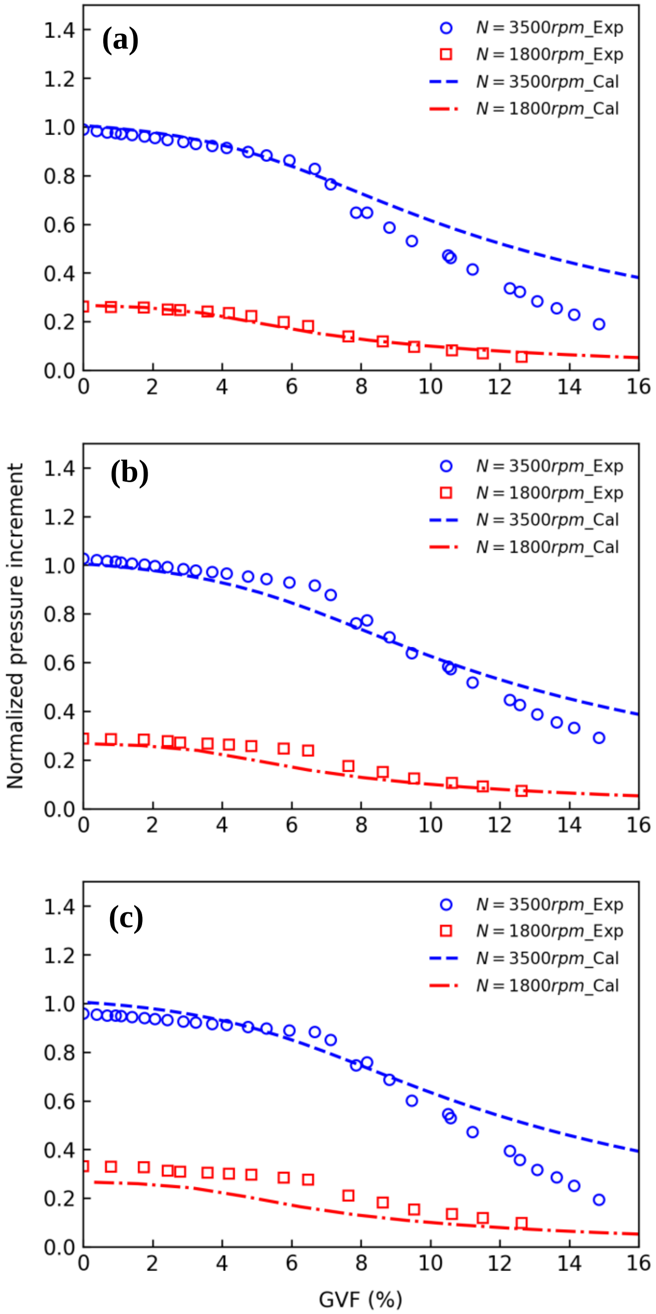

Figure E.1 Model comparison for surging tests at P_{sep} = 150 psig and $Q_L = Q_{\text{BEP}}$, (a) stage 3, (b) stage 5, (c) stage 7

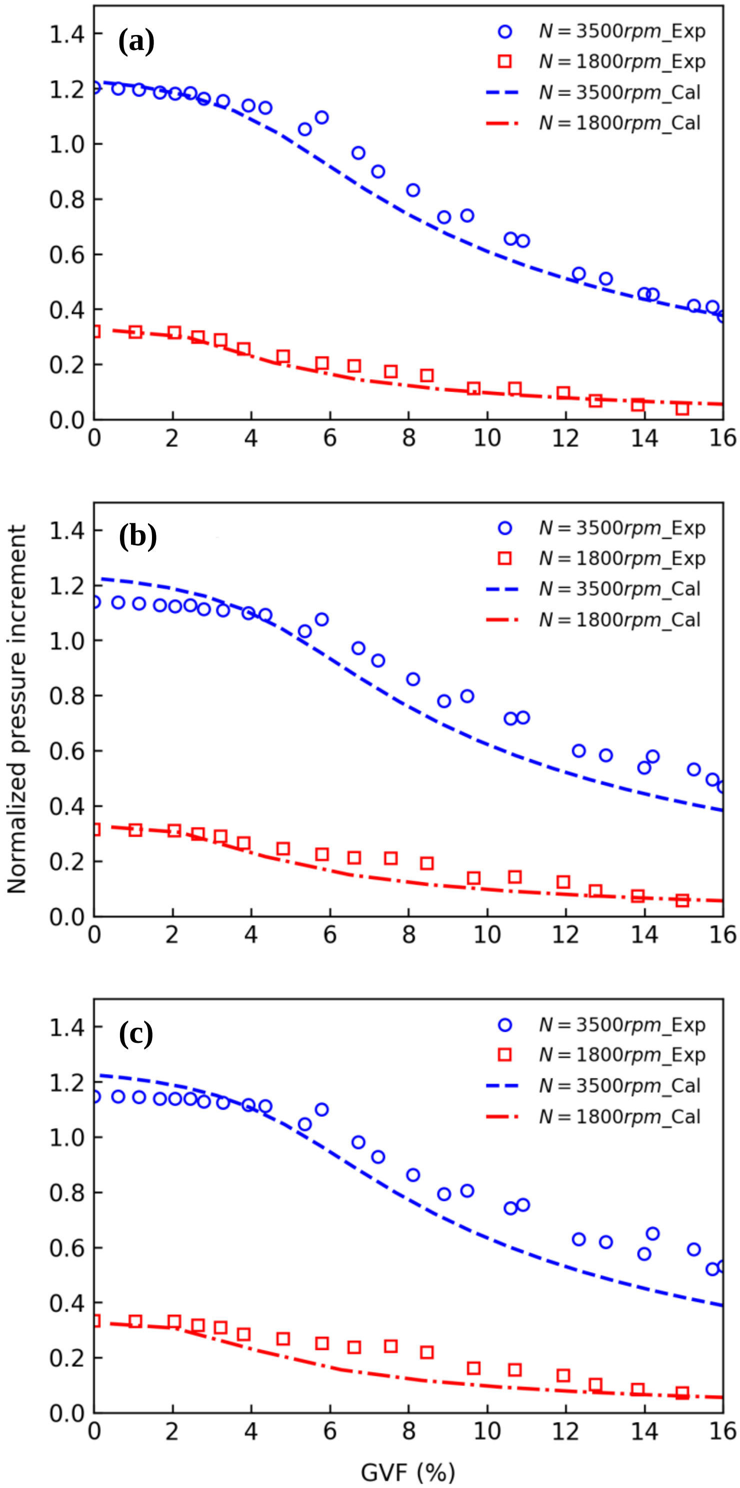

Figure E.2 Model comparison for surging tests at P_{sep} = 150 psig and $Q_L = 0.75Q_{\mathrm{BEP}}$, (a) stage 3, (b) stage 5, (c) stage 7

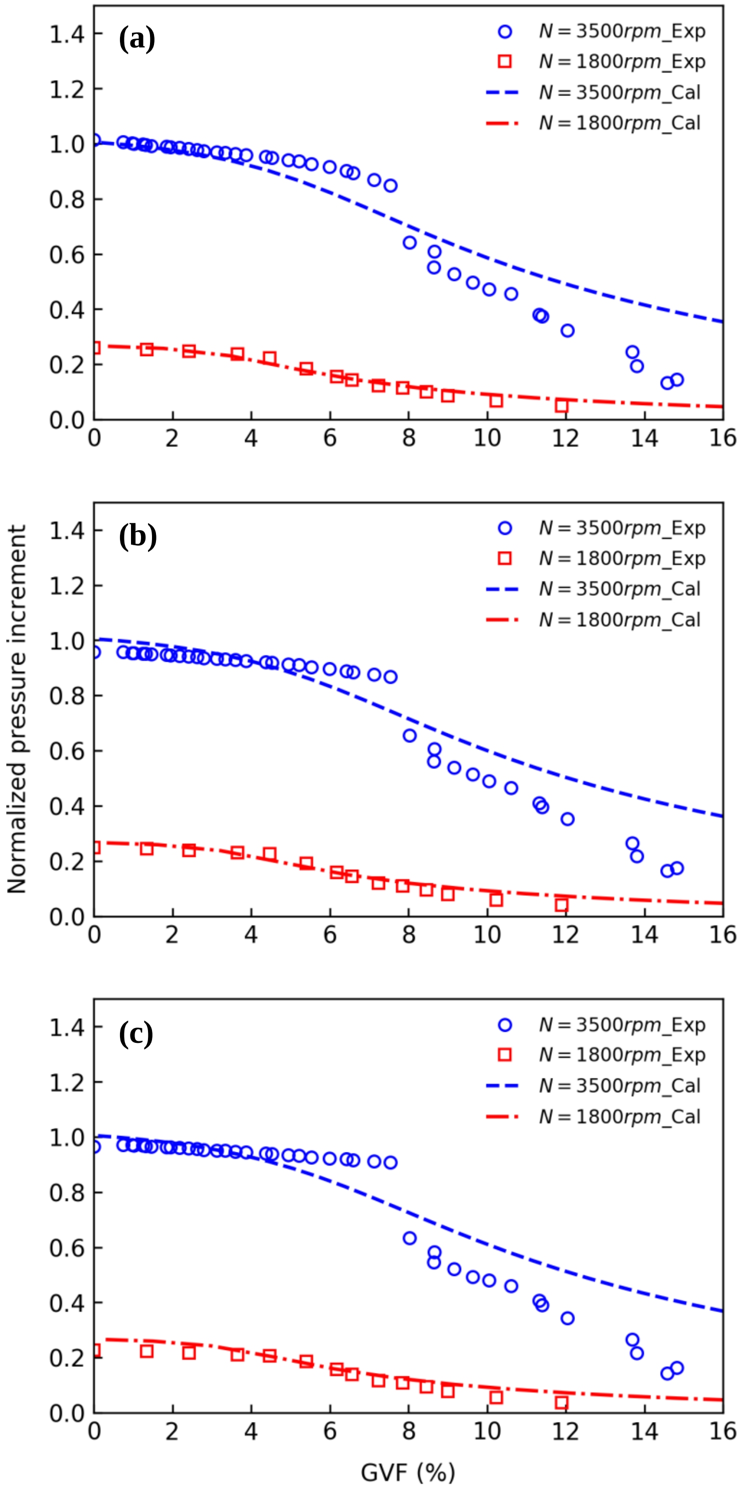

Figure E.3 Model comparison for surging tests at P_{sep} = 100 psig and $Q_L = Q_{\mathrm{BEP}}$, (a) stage 3, (b) stage 5, (c) stage 7

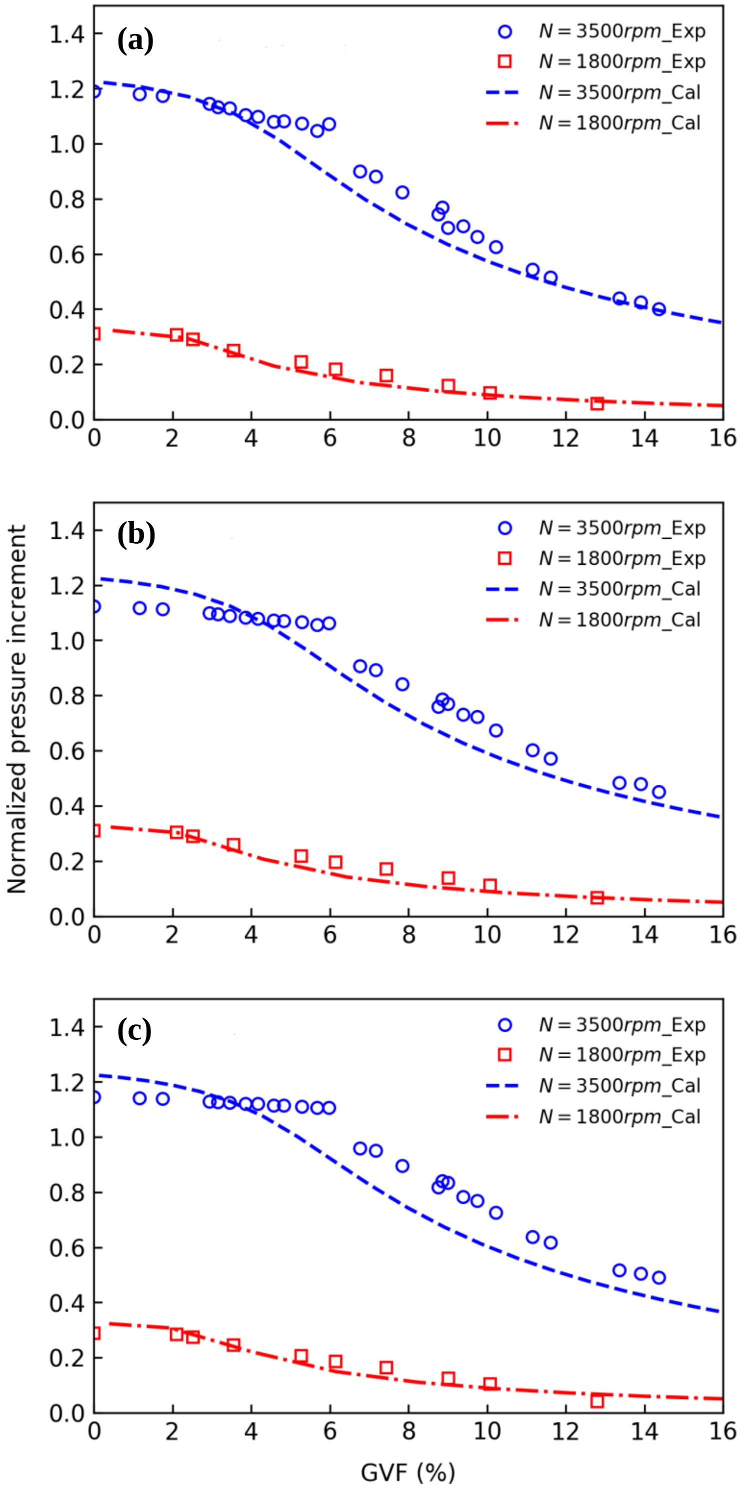

Figure E.4 Model comparison for surging tests at P_{sep} = 100 psig and $Q_L = 0.75Q_{BEP}$,
(a) stage 3, (b) stage 5, (c) stage 7

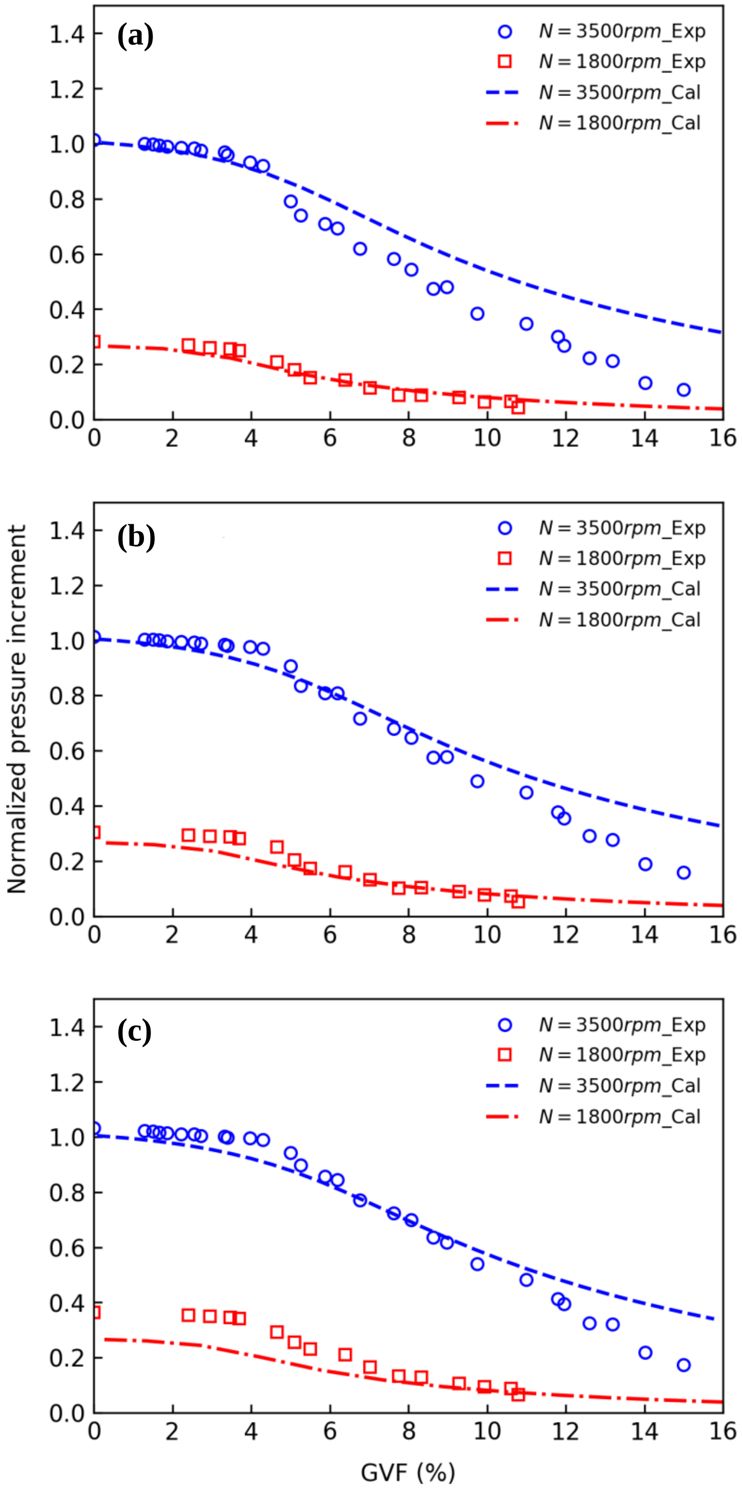

Figure E.5 Model comparison for surging tests at P_{sep} = 50 psig and $Q_L = Q_{\mathrm{BEP}}$, (a) stage 3, (b) stage 5, (c) stage 7

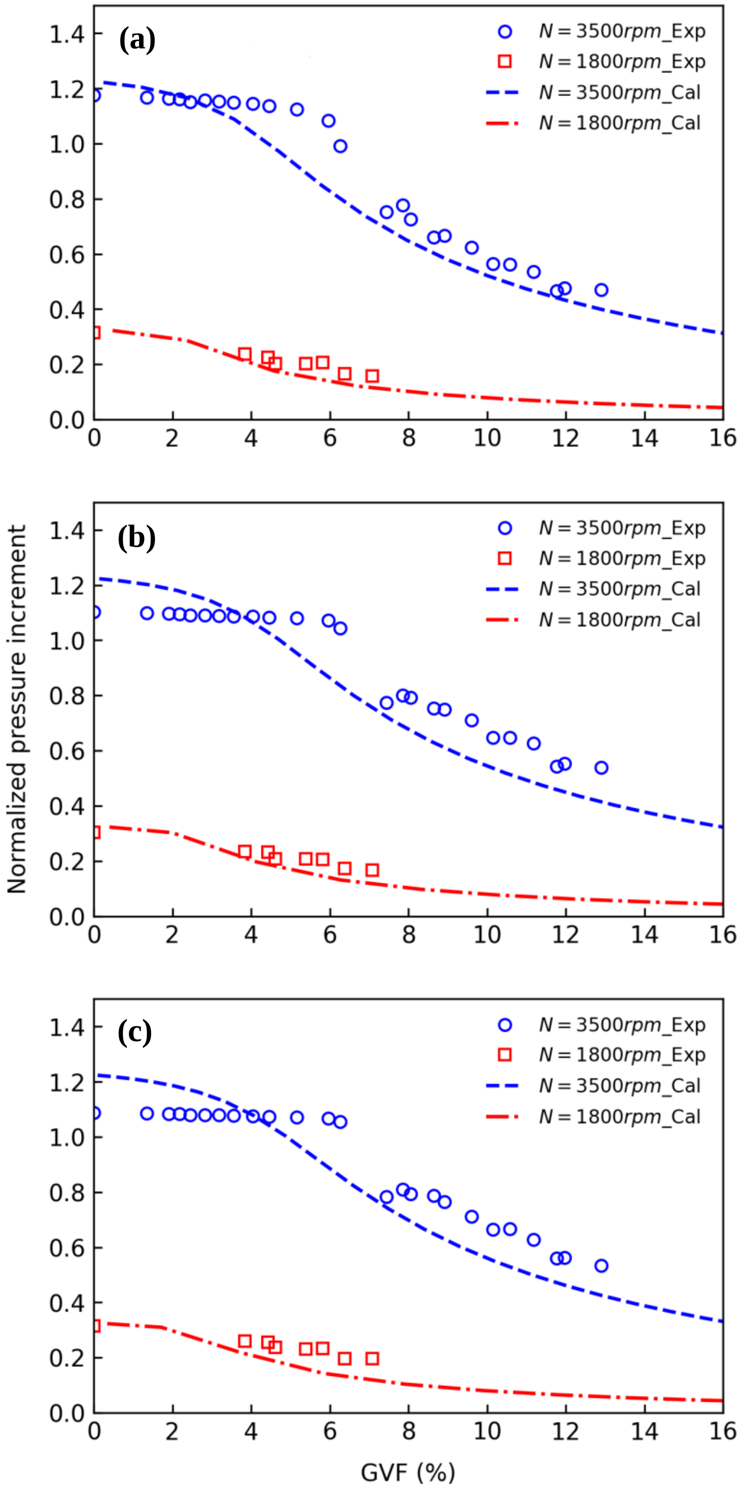

Figure E.6 Model comparison for surging tests at P_{sep} = 50 psig and $Q_L = 0.75Q_{\mathrm{BEP}}$, (a) stage 3, (b) stage 5, (c) stage 7

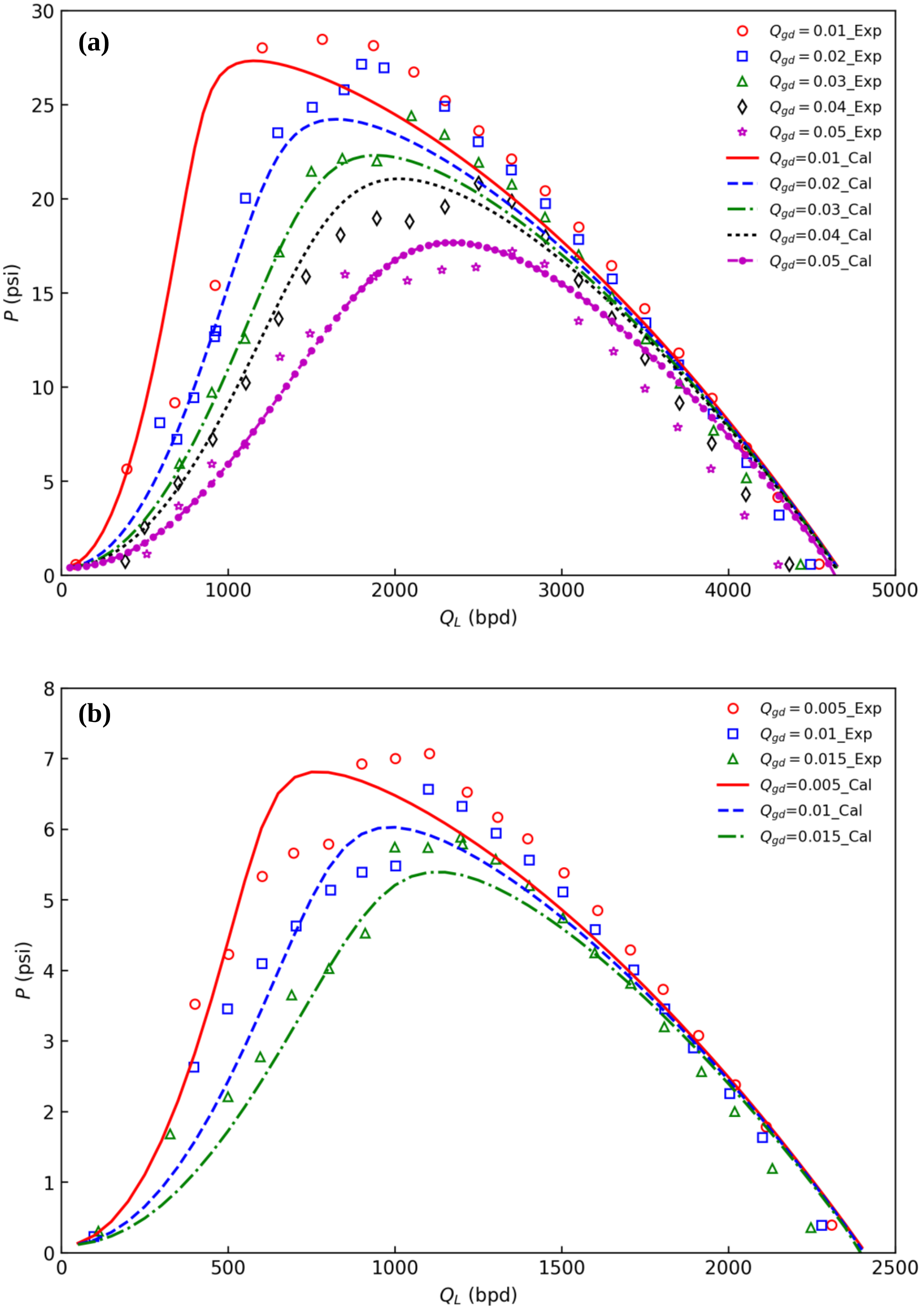

Figure E.7 Model comparison for mapping tests at stage 3 and P_{sep} = 150 psig, (a) N = 3500 rpm, (b) N = 1800 rpm

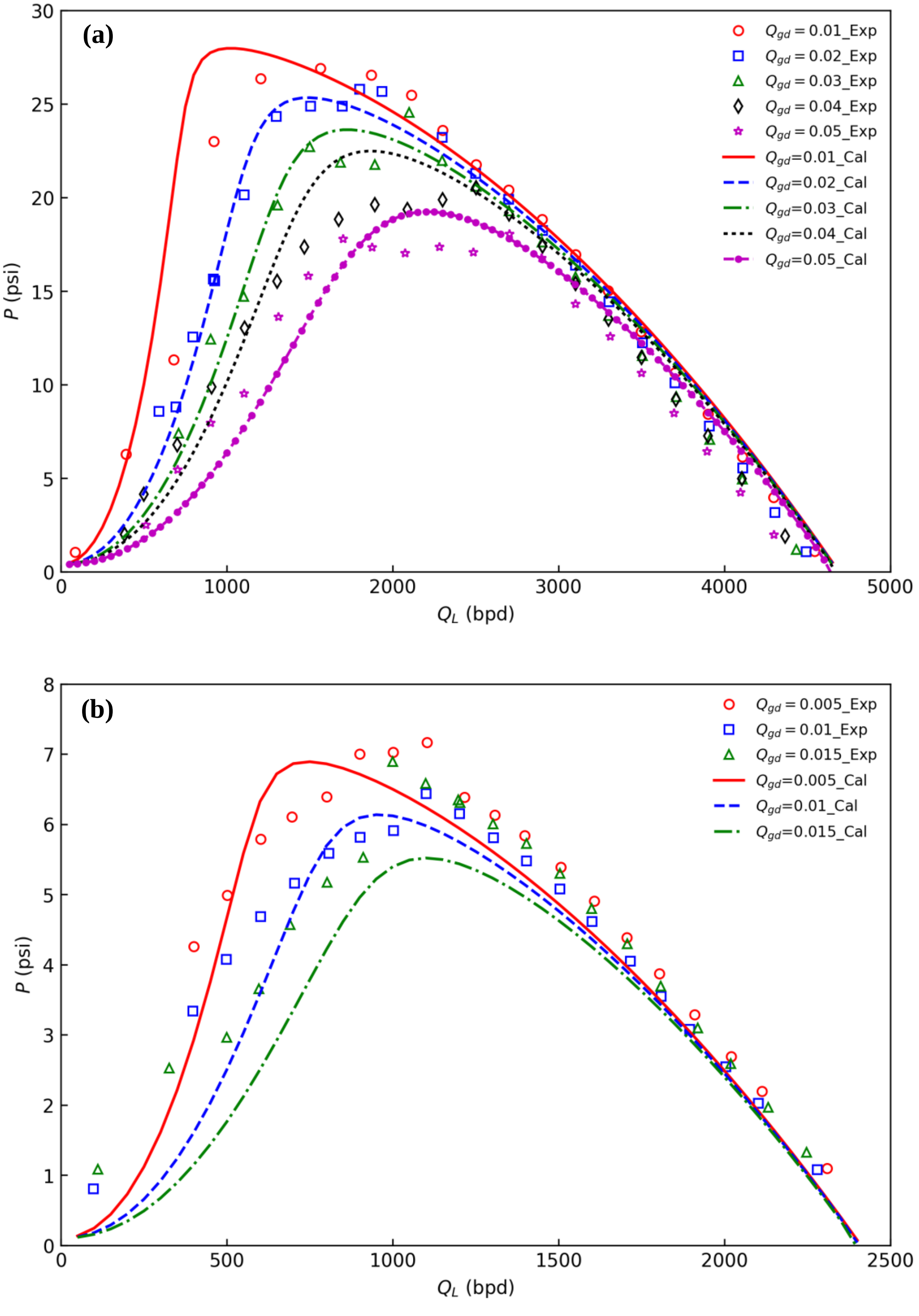

Figure E.8 Model comparison for mapping tests at stage 5 and P_{sep} = 150 psig, (a) N = 3500 rpm, (b) N = 1800 rpm

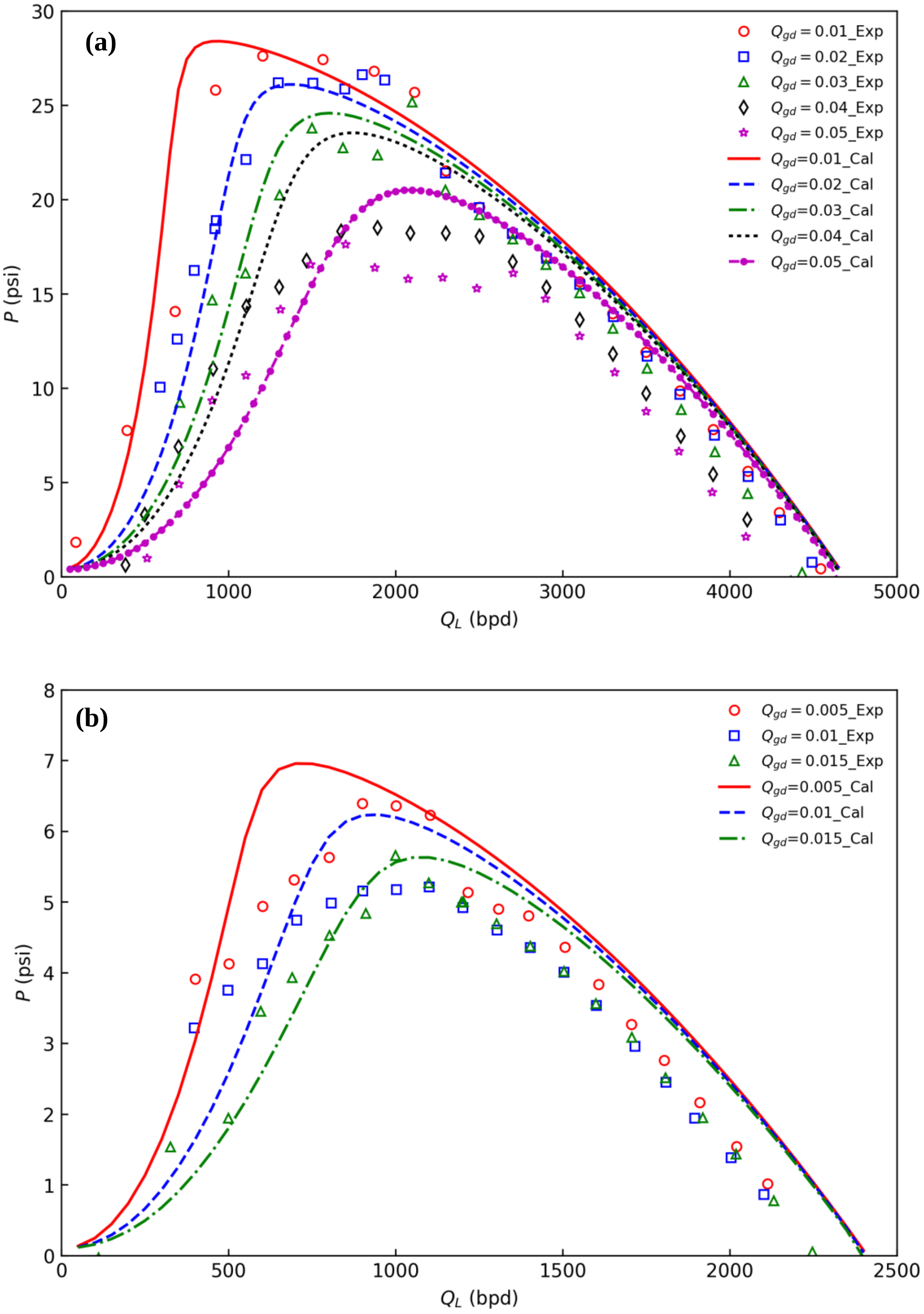

Figure E.9 Model comparison for mapping tests at stage 7 and P_{sep} = 150 psig, (a) N = 3500 rpm, (b) N = 1800 rpm

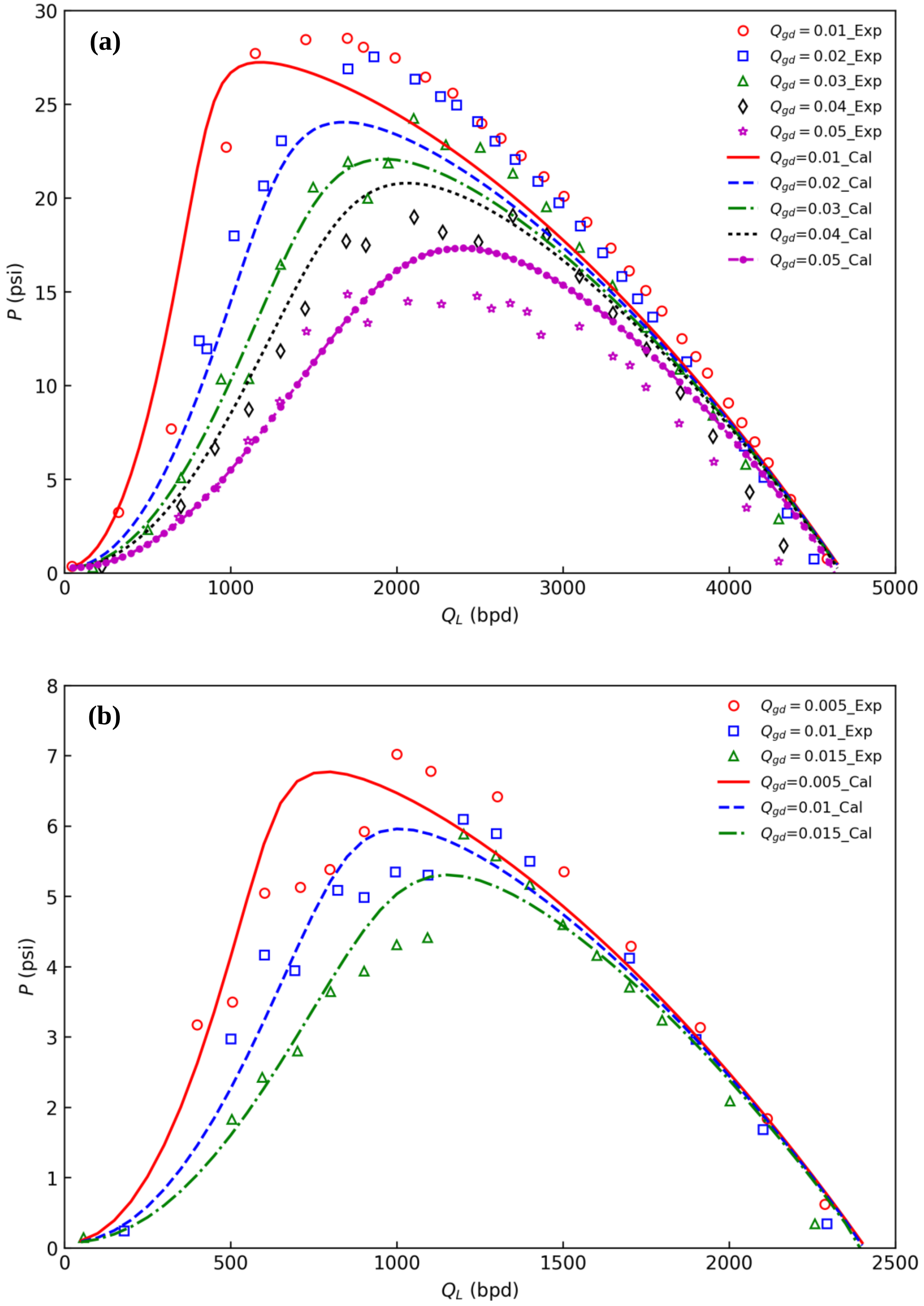

Figure E.10 Model comparison for mapping tests at stage 3 and P_{sep} = 100 psig, (a) N = 3500 rpm, (b) N = 1800 rpm

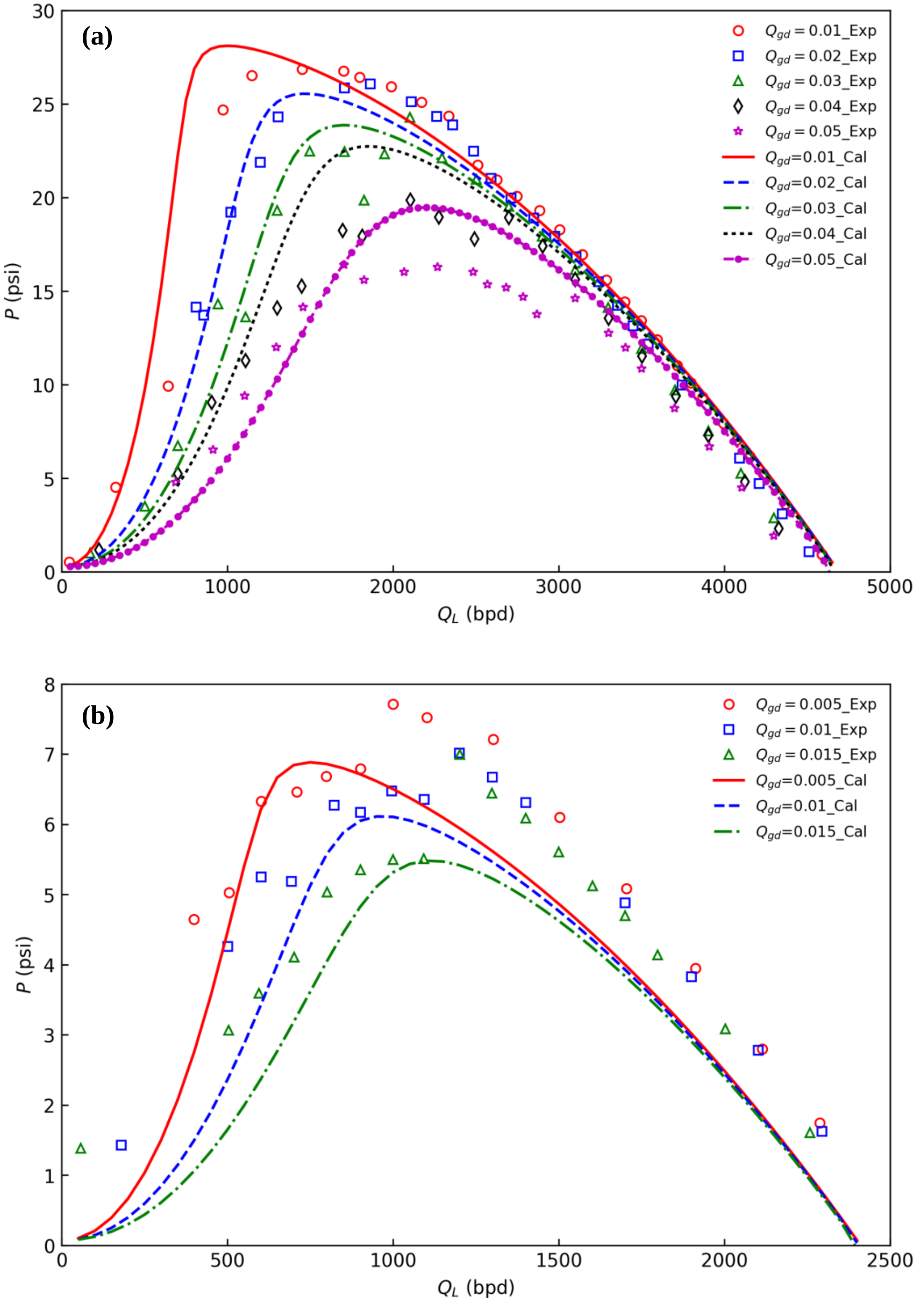

Figure E.11 Model comparison for mapping tests at stage 5 and P_{sep} = 100 psig, (a) N = 3500 rpm, (b) N = 1800 rpm

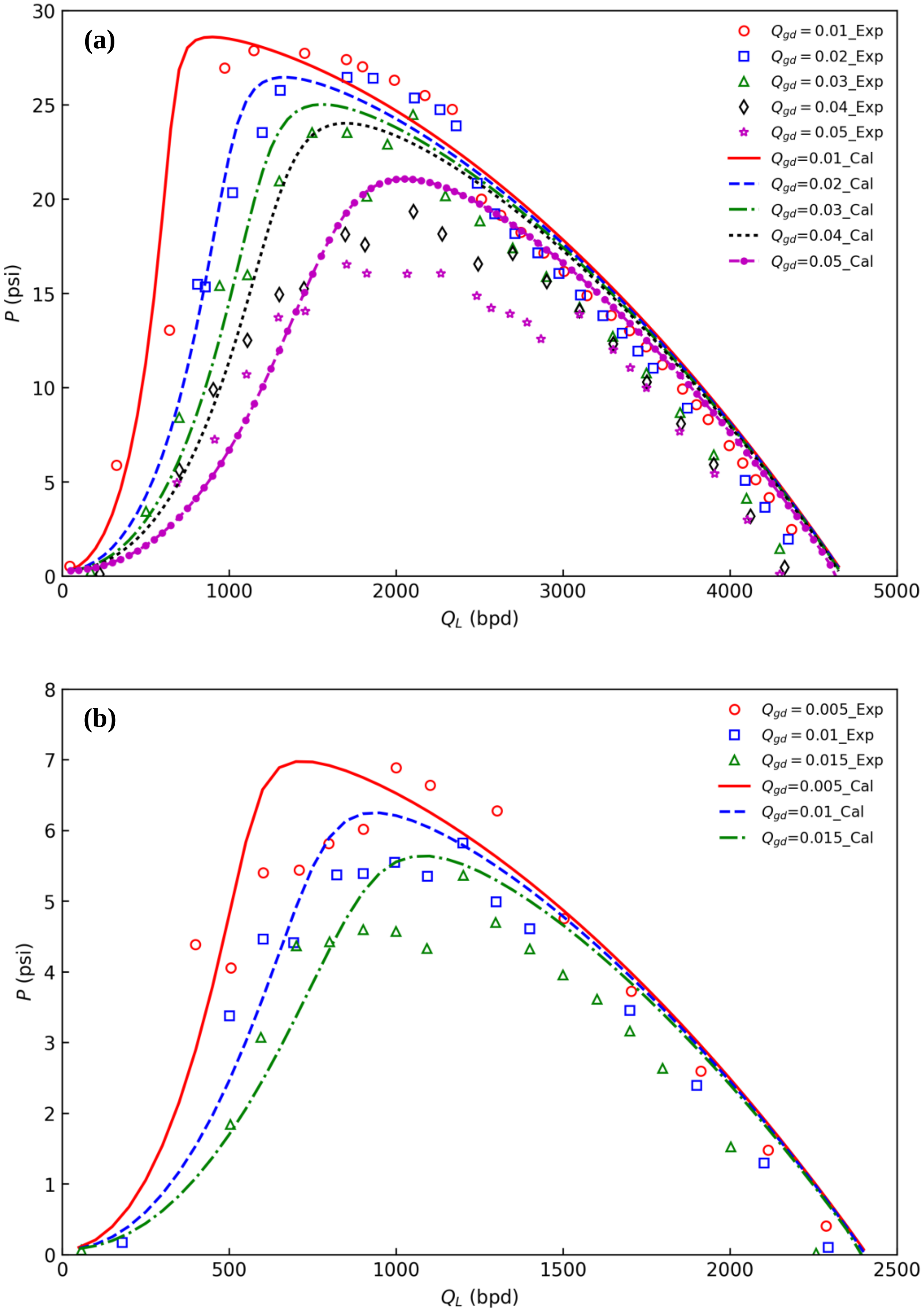

Figure E.12 Model comparison for mapping tests at stage 7 and P_{sep} = 100 psig, (a) N = 3500 rpm, (b) N = 1800 rpm

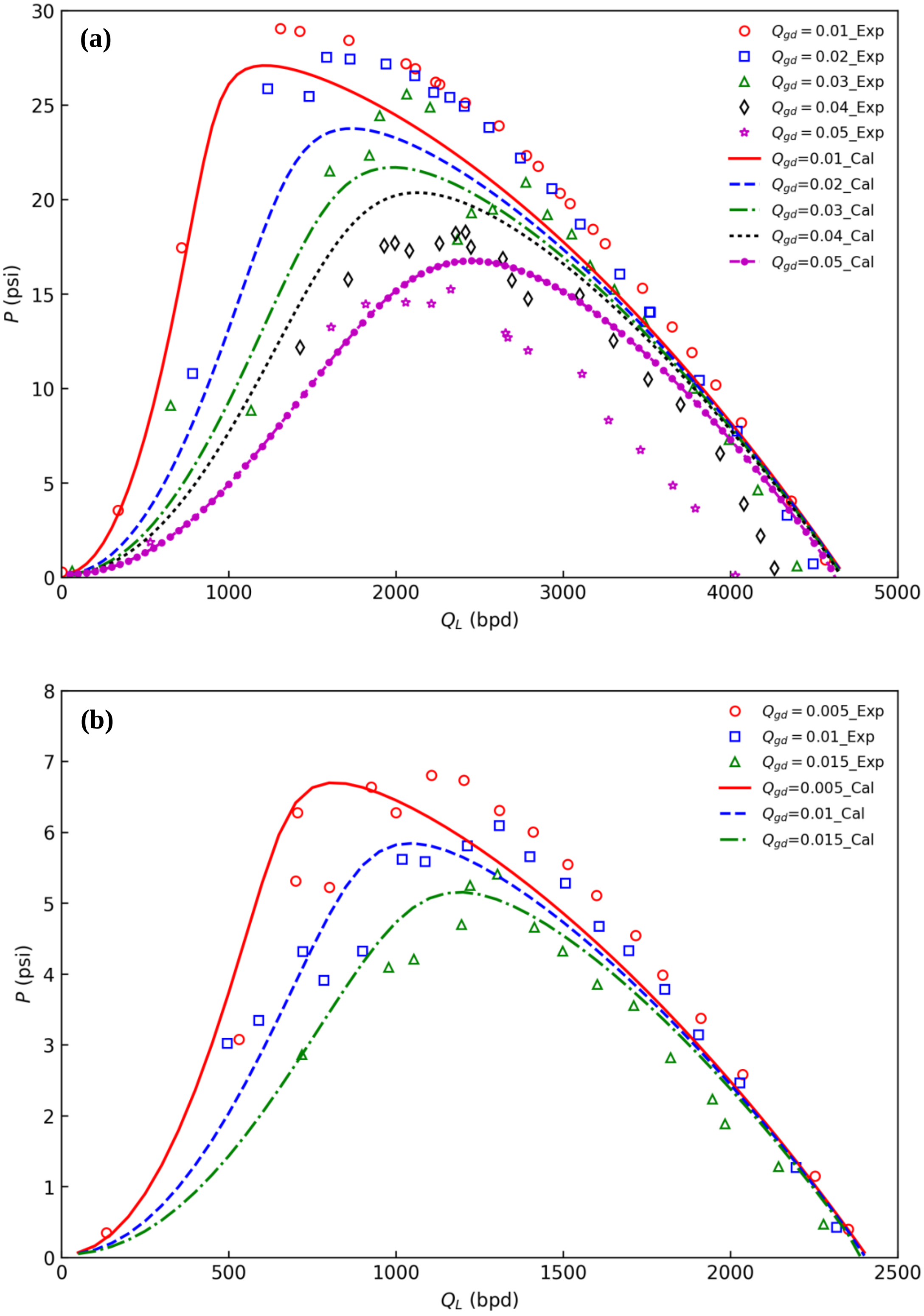

Figure E.13 Model comparison for mapping tests at stage 3 and P_{sep} = 50 psig, (a) N = 3500 rpm, (b) N = 1800 rpm

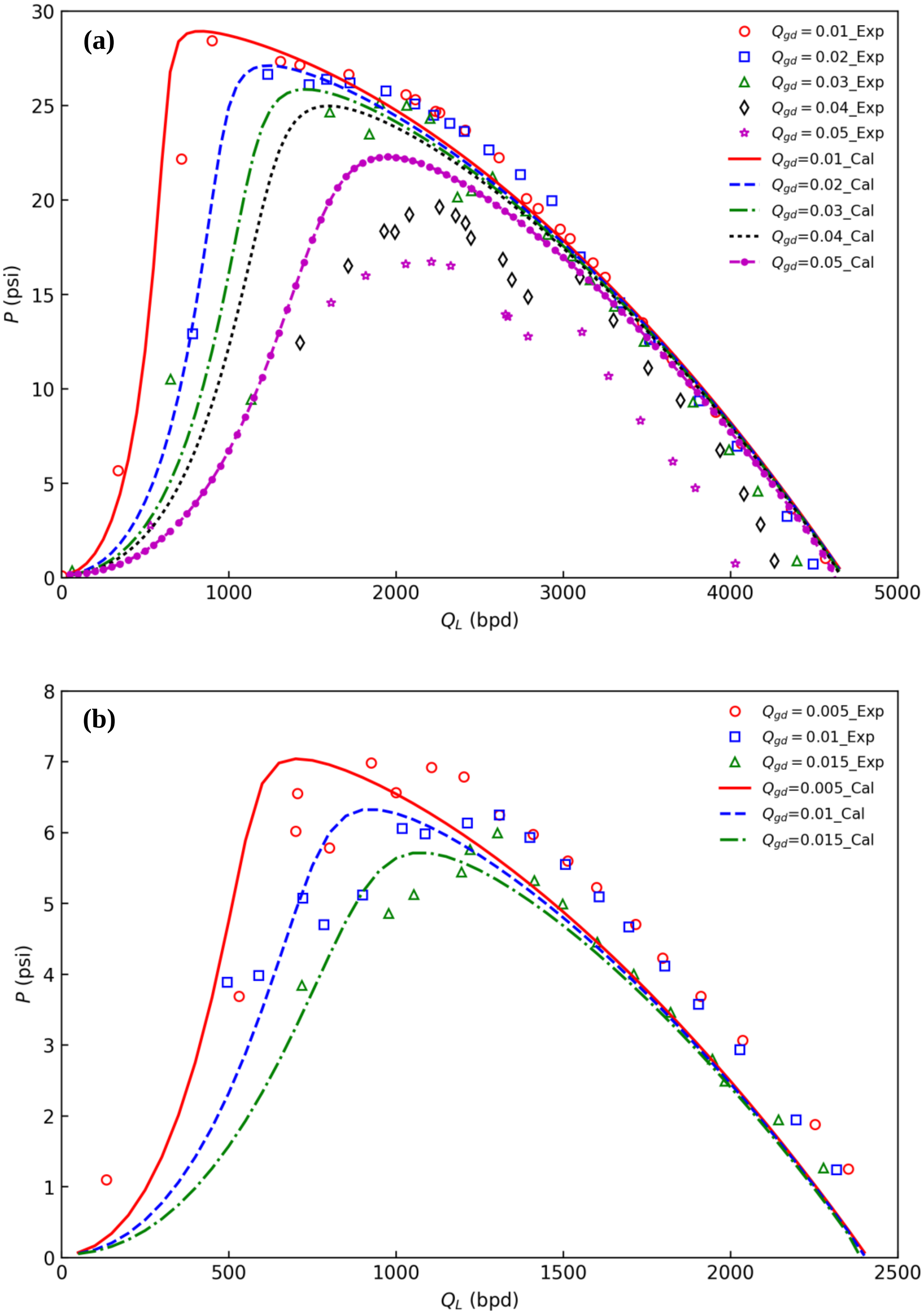

Figure E.14 Model comparison for mapping tests at stage 5 and P_{sep} = 50 psig, (a) N = 3500 rpm, (b) N = 1800 rpm

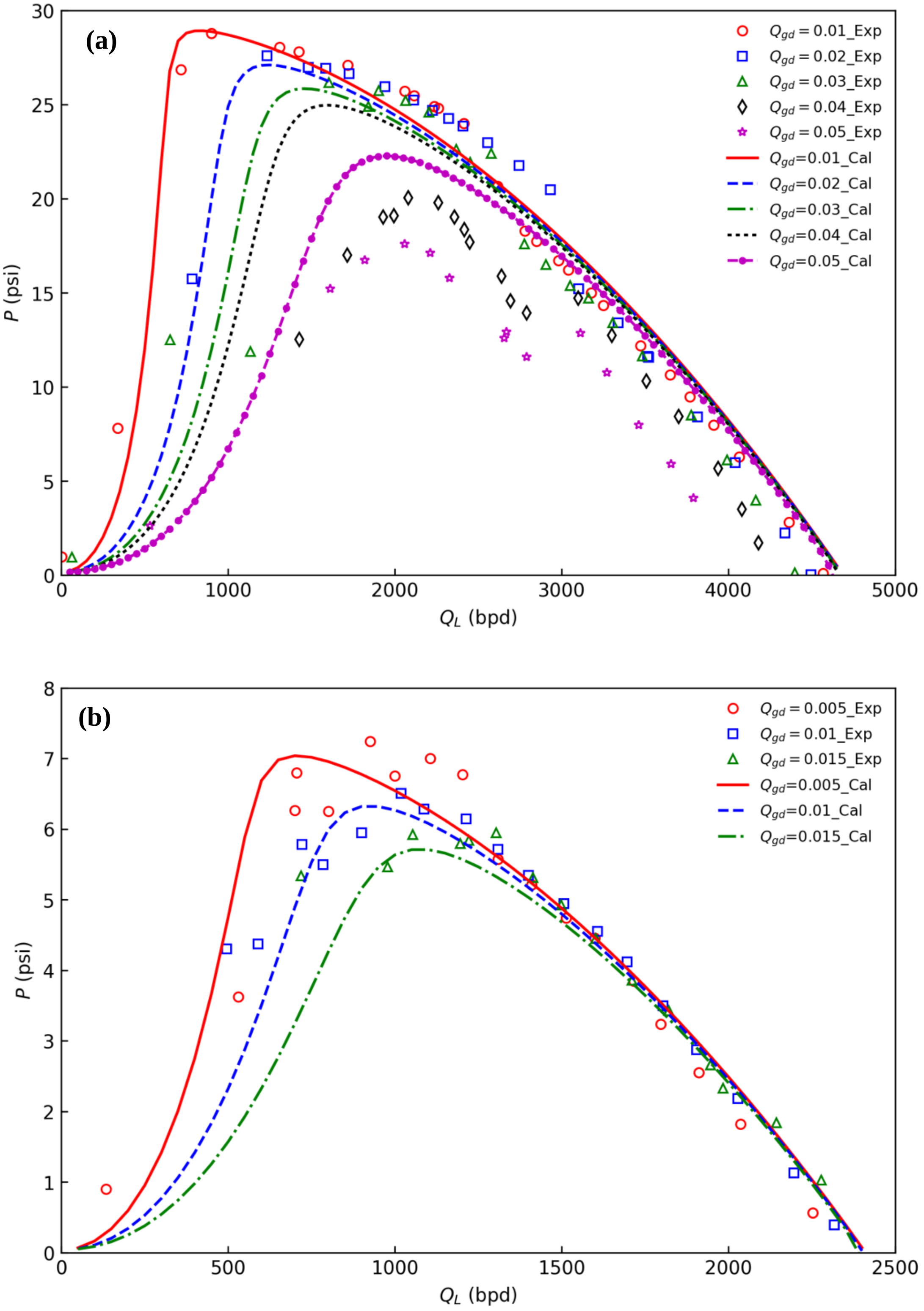

Figure E.15 Model comparison for mapping tests at stage 7 and P_{sep} = 50 psig, (a) N = 3500 rpm, (b) N = 1800 rpm

APPENDIX F

ERROR ANALYSIS

For single-phase measurement, the experimental error originates from instrument measurement errors, including pressure transducers, flowmeters, and temperature sensors etc. For differential pressure measurement, the instrument accuracy is ±0.25%. Thus, the uncertainty for differential pressure measurement is around ±0.25%.

For two-phase measurement, the error analysis should consider multiple factors since the gas properties are sensitive to the pressure and temperature. Table E.1 lists all the instruments and their measurement accuracies

Table E.1 Instrument specifications

Transducer	Model	Range	Accuracy
Temperature transmitter	Emerson Rosemount 3144	-50 °C to 85 °C	0.25%
Absolute pressure transmitter	Emerson Rosemount 2051S	0 to 500 psig	0.1%
Differential pressure transmitter	Emerson Rosemount 3051S	-10 to 50 psig	0.1%
Coriolis liquid flowmeter	Micro Motion CMF200	0 to 1600 lb/min	0.05%
Coriolis gas flowmeter	Micro Motion CMF025	0 to 40 lb/min	0.05%

The measurement accuracies for liquid/gas flow rates, pressure and temperature are 0.05%, 0.1% and 0.25%, respectively. Based on the error propagation theory, the error of GVF (λ) at each ESP stage intake is calculated by

$$\Delta\lambda = \sqrt{\left(\frac{\partial\lambda}{\partial T}\Delta T\right)^2 + \left(\frac{\partial\lambda}{\partial P}\Delta P\right)^2 + \left(\frac{\partial\lambda}{\partial \dot{m}_G}\Delta \dot{m}_G\right)^2 + \left(\frac{\partial\lambda}{\partial \dot{m}_L}\Delta \dot{m}_L\right)^2}\ , \tag{F.1}$$

where

$$\frac{\partial\lambda}{\partial T}=\rho_L\dot{m}_G\dot{m}_L\left(\rho_L\dot{m}_G+\rho_G\dot{m}_L\right)^{-2}\frac{pM_a}{ZRT^2}\left[1-x_v\left(1-\frac{M_V}{M_a}\right)\right], \tag{F.2}$$

$$\frac{\partial\lambda}{\partial P}=-\rho_L\dot{m}_G\dot{m}_L\left(\rho_L\dot{m}_G+\rho_G\dot{m}_L\right)^{-2}\frac{M_a}{ZRT}\left[1-x_v\left(1-\frac{M_V}{M_a}\right)\right], \tag{F.3}$$

$$\frac{\partial\lambda}{\partial\dot{m}_G}=\frac{1}{\rho_G}\left(\frac{\dot{m}_G}{\rho_G}+\frac{\dot{m}_L}{\rho_L}\right)^{-1}-\frac{\dot{m}_G}{\rho_G^2}\left(\frac{\dot{m}_G}{\rho_G}+\frac{\dot{m}_L}{\rho_L}\right)^{-2}, \tag{F.4}$$

$$\frac{\partial\lambda}{\partial\dot{m}_L}=-\frac{\dot{m}_G}{\rho_G\rho_L}\left(\frac{\dot{m}_G}{\rho_G}+\frac{\dot{m}_L}{\rho_L}\right)^{-2}. \tag{F.5}$$

In the equations above, $\dot{m}_G$ and $\dot{m}_L$ are mass flow rates of gas and liquid measured by Coriolis flowmeters, respectively. Substitute all the measurement errors listed in Table E.1 into Eq. (E-1), one can obtain the final error of calculated GVF below 5%.

CFD simulation errors contain modeling error and numerical error. Modeling errors, originated from mathematical representation of physical problem, are usually negligible in CFD simulation error analysis compared with numerical errors (Stern et al., 2011). In this study, the Richardson extrapolation (RE) is employed to analyze numerical error caused by coarse grids (Wilson et al., 2001).

Suppose coarse, medium and fine grids corresponding to numerical solutions: S_1, S_2 and S_3, respectively. Variances between medium-fine $\varepsilon_{21}=S_2-S_1$, and coarse-medium $\varepsilon_{32}=S_3-S_2$ are used to define the convergence ratio:

$$R=\frac{\varepsilon_{21}}{\varepsilon_{32}}. \tag{F.6}$$

R corresponds to three different convergence conditions. $0 < R < 1$ is monotonic convergence condition. Simulation uncertainties can be analyzed by generalized RE. $R <$

0 is oscillatory convergence condition. The oscillation maximum/minimum boundary is adopted to quantify numerical errors. $R > 1$ corresponds to divergence, whose errors and uncertainties cannot be estimated. Based on RE, the numerical solution with the first n terms of series expansion can be expressed as

$$S = S_C + \delta^* = S_C + \sum_{i=1}^{n} (\Delta x)^{p^{(i)}} g^{(i)}. \tag{F.7}$$

where Δx is the thickness of grid layer, $p^{(i)}$ is the order of accuracy, $g^{(i)}$ is series coefficient. For simplicity, $n = 1$ is analyzed in this study. Thus, δ^* can be estimated by

$$p = \frac{\ln(\varepsilon_{32}/\varepsilon_{21})}{\ln(r)}. \tag{F.8}$$

$$\delta^* = \frac{\varepsilon_{21}}{r^p - 1}. \tag{F.9}$$

where r is the ratio of grid layer thickness. To account for effects of higher-order terms and provide a quantitative metric to determine proximity of the solutions to the asymptotic range, the multiplication factor C is introduced,

$$C = \frac{r^p - 1}{r^{p_{est}} - 1}, \tag{F.10}$$

where p_{est} is an estimate for the limiting order of accuracy. C approaches 1 as spacing size goes to zero and asymptotic range is reached. Thus, the numerical uncertainty due to grid size can be obtained from:

$$\delta_C^* = C\left(\frac{\varepsilon_{21}}{r^p - 1}\right). \tag{F.11}$$

From the mesh independence check in Chapter 3, an estimation of the numerical error by Eq. (F-11) based on grid number of 62,755, 143,440 and 201,833 is below 3%. As mentioned above, the grids used in this study for performing CFD simulation contain more than 201,833 elements, which are sufficient to ensure the numerical accuracy.